Investigation of Interfaces Formed of High Workfunction Metal Oxides with Conjugated Polymers

by

Yanting Yin

Thesis
Submitted to Flinders University
for the degree of

Doctor of Philosophy

College of Science and Engineering

28/02/2019

Abstract

A range of proficient polymer-donor and fullerene acceptor materials for active layers used in solar devices, such as polymer-based solar cells have been developed and the hole transport layer (HTL)/anode buffer layer (ABL) such as MoO_3, works properly in such device and appropriate for solar materials engineering. However the charge transfer mechanism at the adjacent metal oxides/organic interfaces has not been fully understood due to the lack of technique to quantifying the dipole at the interfaces. Without a direct characterisation, the schematics of energy band shift and bending are ambiguous. Based on that, three main achievements will be shown in this research and can be applied in the solar cell fabricating and similar material engineering: (a) the technique of direct quantifying the dipole strength and its energetic distribution at the metal oxides/organics interfaces; (b) the working mechanism of charge transfer over the HTL/organics interfaces; (c) the characterisation of the changes upon dipole strength with different treatments, which occur in the device fabrication. To achieve the outcomes and a fundamental understanding of the materials properties and engineering of the interfaces formed with metal oxides and organics, a powerful combination of experimental techniques has been adopted to characterise the energetic and chemical properties of the materials and interfaces.

First, the nature of interface forming at MoO_3/P3HT:PC_{61}BM BHJ has been investigated. The mixing phase of components and formation of dipole at the interface are observed. Electron spectroscopy is employed to determine the strength of the dipole at the interface and the minimum deposition thickness to form a closed layer. The energy distribution at the interface is further exhibited. The work shows that upon evaporation of MoO_3, the strength of the dipole increases with a higher thickness of the MoO_3 layer and saturates at a thickness around 3nm at 2.2 eV. The methodology for a directly characterisation of dipole has been shown and the mechanism for charge transfer is discussed. As such the interfaces forming at V_2O_5/BHJ and WO_3/BHJ are further studied and the comparison in-between has been made.

A range of the value of electrical properties such as workfunction of MoO_3 has been reported once air exposure occurs. Investigation into the interface of MoO_3/P3HT:PC_{61}BM BHJ upon

exposure has been made and both the WF and the dipole forming at such interface are significantly influenced. Electron spectroscopy shows the adsorption of mainly H_2O on the metal oxide surface upon exposure, which also diffuses to the interface. The invasion of H_2O dielectric affects both the electrical properties of MoO_3 and the dipole formation at the interface by free- orientating and encountering the dipole direction. A comprehensive energy structure of the MoO_3/BHJ interface upon air exposure has been constructed. From which, the charge injection mechanism can be eliminated after exposure for 30min. The samples of V_2O_5 and WO_3 with conjugated P3HT:PC_{61}BM exposed to atmosphere have been further studied. The nature is similar to MoO_3/BHJ and the difference of energy structure construction upon exposure is illustrated. The finding is rather important for solar cell engineering due to the application of general fabrication.

A simulation of vacuum-annealing process of solar cell material engineering has been made on P3HT:PC_{61}BM BHJ and the MoO_3/BHJ interface, respectively. Our research shows that upon annealing of BHJ before deposition of MoO_3, a sharp interface with less mixing phase can be achieved. The mean dipole strength keeps constant so that the charge transfer would not be affected. On the other side, annealing upon MoO_3/BHJ interface causes the reduction of MoO_x and a heavier penetration into the BHJ. The interface region has been broadened, however the mean dipole strength is noticeably reduced. The charge injection transport is thus not energetically supported, leading to a conventional “HOMO-VB” transport and the device performance can be altered.

The methodology for characterising the dipole is also applied on the interface formed with MoO_3/TQ1:PC_{71}BM BHJ. The penetration of MoO_3 into BHJ is observed and the distribution of energy states at the interface is determined. It can be seen that a dipole with higher energy was formed at the MoO_3/TQ1:PC_{71}BM interface in comparison with that of MoO_3/P3HT:PC_{61}BM interface. The root of the difference has been addressed.

Table of Content

Declaration

I certify that this thesis does not incorporate without acknowledgment any material previously submitted for a degree or diploma in any university; and that to the best of my knowledge and belief it does not contain any material previously published or written by another person except where due reference is made in the text.

Yanting Yin

22/08/2018

Acknowledgements

I am always seeking opportunity to thank my principle supervisor-Professor. Gunther G. Andersson. He is such a dedicated professional in surface and interface characterisation, spectroscopy, material physical science, who guided me pass through the handicaps to get a slight breakthrough in the field. He supported me from many aspects. I had got opportunities to learn the experience maintaining the integrated UHV multi-spectroscopy, which other students probably did not get. I accomplished multiply research projects during the four years, gaining the knowledge to extend the use of spectroscopy to other fields, which was under his supports. He is also a so kind man, knowledgeable but keeping a low profile, earning respects from everyone.

I would also like to thank my associate supervisor- Professor. David A. Lewis. He is absolutely experienced in the field of organic materials, devices and commercialisation. He offers me precise suggestions from other perspectives, to go through the manuscripts.

My senior colleague Benjamin A. Chambers gave a systematic training on the equipment and taught me how to maintaining the apparatus. Alex Sibley helped me on the measurement of Scanning Auger Microscopy. I would like to thank them. All group members, Chris, Herri, Altaf, Gowri, Nahideh, Jesse, Liam and other colleagues, I really appreciate for your help and supports. Also, Chris and Andrew from workshop, you helped me a lot maintaining the rig.

Life would be hard and I could not achieve anything without the supports from my family, my wife Yan Wang, my parents Qinfang Yao and Hujian Yin. They deserve more thanks than I could ever give. They offered me unconditional love, encouragement and financial support.

Great thanks to the Scholarship (OSSA) from Chinese Government. I would also thank to Australian Nanotechnology Network, ANNF, AMMRF and Flinders Nanocentre.

I really appreciate everyone who provided me with love, reanimation and support. The years I spent in Flinders, in Australia, would be an unforgettable memory in my life.

Yanting Yin
22/08/2018

Published and Submitted Articles

1. Yanting, Y.; Alex, S.; Jamie, Q.; David, A. L.; Gunther, G. A., Dipole Formation at the MoO_3/Conjugated Polymer Interface. **Advanced Functional Materials** 2018, 28 (46), adfm.201802825R1 2018.

2. Yanting Yin, D. A. L. a. G. G. A., The Influence of Moisture on the Energy Level Alignment at the MoO_3/Organic Interfaces. **ACS Applied Materials & Interfaces**, 2018, 10 (50).

3. Yanting Yin, D. A. L. a. G. G. A., The Change of Dipole at MoO_3/P3HT:PC_{61}BM BHJ Interface for Various Thermal Treatments. (Close to submission) 2018.

4. Yanting, Y.; Alex, S.; Jamie, Q.; David, A. L.; Gunther, G. A., The Investigation of V_2O_5/WO_3-P3HT:PC_{61}BM Interface and the Characterisation of Dipoles Formation. (Close to submission) 2018.

5. Shrestha, A.; Yin, Y.; Andersson, G., G; Spooner, N. A.; Qiao, S. D., S, Versatile Pbs Quantum Dot Ligand Exchange Systems in the Presence of Pb-Thiolates. **Small,** 2017, 13.

6. Shrestha, A.; Batmunkh, M.; Shearer, C. J.; Yin, Y., Andersson; Gunther, G.; Shapter, J. G.; Qiao, S.; Dai, S., Nitrogen-Doped Cnx/Cnts Heteroelectrocatalysts for Highly Efficient Dye-Sensitized Solar Cells. **Advanced Energy Materials,** 2017, 7, 1602276.

7. Krishnan, G.; Al Qahtani, H. S.; Li, J.; Yin, Y.; Eom, N.; Golovko, V.; B, M.; F, G.; Andersson, G. G., Investigation of Ligand-Stabilized Gold Clusters on Defect-Rich Titania. **The Journal of Physical Chemistry C** 2017, 121, 28007-28016.

8. Worthington, M. J. H., et al., Sustainable Polysulfides for Oil Spill Remediation: Repurposing Industrial Waste for Environmental Benefit. **Advanced Sustainable Materials,** 2018, 2, 1800024.

9. Heping Shen; Etc; Yanting Yin; Gunther, A.; Kylie, C., In situ recombination junction between p-Si and TiO_2 enables high-efficiency monolithic perovskite/Si tandem cells. **Science Advances**, 2018, 4, 12.

10. Keyun, S.; Jun, K. H.; Elliot, S. W.; James, M. H.; Andrew, N.; Yanting, Y.; Gunther, A.;

Antonio, A.; Ullrich, S.; Chiara, N., Ultralow Surface Energy Self-Assembled Monolayers of Iodo-Perfluorinated Alkanes onto Silica driven by Halogen Bonding, . **Nanoscale**, 2019, 5.

11. Xun, P.; Anirudh, S.; Renee, K.; Desta, G.; Jonas, M. B.; Yanting, Y.; Gunther, G. A.; Mats, R. A., Ethanol Processable Donor Polymers with Functional Side Groups for Organic Photovoltaics. (close to submission) 2018.

Presentation Contributions

1. 10th International Conference on Hybrid and Organic Photovoltaics (HOPV 2018)

   June-2018, Spain, Oral Presentation

2. School Seminar

   Augest-2018, Australia, Oral Presentation

3. The 10th Research Symposium for Chinese PhD Students and Scholars (CAPS 2017)

   Nov-2017, Australia, Oral Presentation

4. Asia-Pacific Physics Conference/Australian Institute of Physics (APPC-AIP 2016)

   Dec-2016, Australia, Oral Presentation

5. International Conference on Nanoscience and Nanotechnology (ICONN-2018)

   Jan-2018, Australia, Poster Presentation

6. Nanocentre Annual Conference-Flinders

   2015/2016/2017/2018, Australia, Poster Presentation

List of Figures

Abbreviation List of Chemicals and Symbols

P3HT	*Poly(3-hexylthiophene-2,5-diyl*	FF	*Fill Factor*
$PC_{61}BM$	*Phenyl-C_{61}-butyric acid methyl ester*	R_s	*Series Resistance*
		R_{sh}	*Shunt Resistance*
TQ1	*Poly[[2,3-bis(3-octyloxyphenyl-5,8-quinoxalinediyl]-2,5-thiophenediyl]*	J-V	*Current Density-Voltage*
		PV	*Photovoltaics*
		OPV	*Organic Photovoltaics*
$PC_{71}BM$	*[6,6]-Phenyl C_{71} butyric acid methyl ester*	OLED	*Organic Light-emitting diode*
		BHJ	*Bulk Hetero-junction*
MoO_3	*Molybdenum Trioxide*	D-A	*Donor-Acceptor*
MoO_x	*Molybdenum Oxides(reduced)*	K.E.	*Kinetic Energy*
V_2O_5	*Vanadium Oxide*	B.E.	*Binding Energy*
VO_x	*Vanadium Oxide(reduced)*	EQE	*External Quantum Efficiency*
WO_3	*Tungsten Trioxide*	IQE	*Internal Quantum Efficiency*
WO_x	*Tungsten Oxide(reduced)*	A	*Absorption*
Ag	*Silver*	PCE	*Power Conversion Efficiency*
Al	*Aluminium*	T	*Transmittance*
Au	*Gold*	J_{SC}	*Short-circuit Current*
Si	*Silicon*	I_s	*Saturation Current*
a-Si	*Amorphous Silicon*	V_{OC}	*Open-circuit Voltage*
CB’	*Chlorobenzene*	λ(E)	*Electron mean free path*
ODCB	*1,2-Dichlorobenzene*	kB	*Boltzmann Constant*
F8BT	*Poly(9,9-dioctylfluorene-alt-benzothiadiazole)*	SVD	*Singular Value Decomposition*
		WSM	*Weighted Shifting Method*
PEDOT:PSS	*poly(3,4-ethylenedioxythiophene) polystyrene sulfonate*	DOS	*Density of State*
		TOF	*Time of Flight*
N_2		UHV	*Ultra-High Vacuum*
O_2		HV	*High Vacuum*

He	*Nitrogen*	PVD	*Physical Vapour Deposition*
ZnO	*Oxygen*	CVD	*Chemical Vapour Deposition*
ITO	*Helium*	PECVD	*Plasma Enhanced Chemical Vapour Deposition*
TiO_2	*Zinc Oxide*		
ABL	*Indium tin oxide*	QCM	*Quartz Crystal Microbalance*
CBL	*Titanium Oxide*	ASF	*Atomic Sensitive Factor*
WF/ϕ	*Anode Buffer Layer*	FWHM	*Full Width Half Maximum*
E_e	*Cathode Buffer Layer*	TMO(s)	*Transition Metal Oxide(s)*
E_f	*Workfunction*	E_{LUMO}	*Lowest Unoccupied Molecular Orbital Energy*
E_g	*Excitation Energy*		
CB	*Fermi Level Energy*	E_{HOMO}	*Highest Occupied Molecular Orbital Energy*
VB	*Band Gap*		
VL	*Conduction Band*	IE	*Ionisation Energy*
LUMO	*Valence Band*	EA	*Electron Affinity*
	Vacuum Level	HTL	*Hole Transport Layer*
HOMO	*Lowest Unoccupied Molecular Orbital*	ETL	*Electron Transport Layer*
E_{CB}	*Highest Occupied Molecular Orbital*		
E_{VB}	*Conduction Band Energy*		
	Valence Band Energy		
TG	*glass transition temperature*		

Chapter 1. Introduction and Research Aims

1.1. Review of the Polymer-Based Organic Photovoltaic

The section follows a structure that the solar cell of all categories will be discussed first. After which we will focus on organic solar cell and then subordinate polymer-based cell. The development and landmarks of such photovoltaic (PV) devices will be illustrated.

1.1.1. Solar Cell : Background

The demand for green energy has been highlighted in recent decades due to the fact that there are enormous drawbacks with conventional energy resources, such as fossil fuels and coals. These polluting, non-renewable resources can bring about the greenhouse effect and global warming, which are real with us and escalating constantly [1]. As a consequence the use of renewable energy, e.g. solar cells, is promoted and increasing in recent years.

Since the first applicable solar cell was designed in 1956 by the Alcatel-Lucent Bell Group [2], solar cells across a range of different types have been developed. Such cell devices are commonly capable of harvesting solar energy which can be transferred to electricity by PV effects [2, 3] that were initially discovered by Becquerel. The burgeoning industrialisation of solar cell panels, especially in Europe and Asia, has encouraged the investment in the research field of solar cell, and the researches are boosting its power conversion efficiency (PCE). For instance the certificated PCE of silicon-based solar cells made by Kaneka [4] has increased to 26.7% in 2017 due to the optimised passivation of front emitter and rear contact. The certificated PCE record of organic photovoltaic (OPV) device made by Toshiba is about 11.2% [4] in 2015. The cascade structure is based on a tandem cell with multi-donor and acceptor.

1.1.2. Organic Solar Cell : Background

The first organic semiconductor used for photovoltaic effect was achieved in the mid-20th century [5]. In comparison with silicon-based solar cells and other kinds of inorganic solar cells, organic cells are more flexible, convenient and low-cost, which makes them promising in a large field of application such as building-integrated photovoltaics (BIPV) and wearable electronic devices. A significant difference between the inorganic and organic solar cells is the

charge dissociation mechanism with absorbed photons. The inorganic PV is based on a typical homo- or hetero- PN junction while the mechanism for the latter one is excitonic PV effect. Different types of OPV have been developed. The category can be divided into: Dye-sensitised solar cells (DSSCs), polymer-based donor-acceptor solar cells and hybrid cells with inorganic/organic structure. The sensitiser of dye in DSSCs works as an oxidant, which is reduced by an electrolyte while further reduction occurs by a counter-electrolyte [6-9]. The hybrid solar cell, such as perovskites, works in a similar way with DSSCs. The certificated PCE of a single-junction perovskites solar cell made by KRICT [4, 10] has peaked at 20.9% in 2017. That is much higher than DSSCs due to the advantages in charge mobility and the diffusion length in perovskites materials (typically $CH_3NH_3PbX_3$, X indicates a variation of Halogen atom).

1.1.3. Polymer-Based Solar Cell : Background

This research is based on the structure of polymer-based solar cell. The history of polymer solar cell can be traced back to 1986. A bilayer small molecule organic solar cell was first invented by Tang [5, 11] with a PCE of 0.9%. In 1992 pioneering work blending soluble conjugated polymer and fullerene led to the fabrication of the first bulk heterojunction (BHJ) structure used for OPV. The electronic characterisation of such polymers and fullerenes was done in 1995 by Friend's group [5] which made remarkable progress in understanding the donor-acceptor working mechanism of polymer-fullerene heterojunctions.

Later work followed the achievements of the pioneers. The optimisation and substitution of applicable acceptor materials brought further success. The MEH-PPV: C_{60} as donor and acceptor heterojunction was applied in 1992. The solar cell made of such active layer materials achieved a PCE of 2%. In 1995, Yu's group [12] made a substitution of C_{60} by a modified derivative-Phenyl-C61-butyric acid methyl ester ($PC_{61}BM$) in 1995, resulting in an increase of the PCE to 2.9%. The advantage of acceptor $PC_{61}BM$ has been addressed to its higher solubility and appropriate electron affinity and ionisation potential for charge transfer. [6,6]-Phenyl-C71-butyric Acid Methyl Ester ($PC_{71}BM$) was synthesised based on C_{70} prototype, which produces 30% higher current density then $PC_{61}BM$ [5, 12] due to its optimised light absorption. Ongoing research on the fullerene-donor has commenced, essentially based on the modification of

benzene ring, carbon chain and the ester. For instance, the conjugated NHCS [13] has been tailored with $PC_{61}BM$ ester and named F-NHCS by John.A. The F-NHCS acceptor has wavelength absorption from 250-900 nm, which is much broader than conventional fullerene acceptors. The optimisation upon light absorption results in a boost in photon-current density (J_{sc}).

In 1993, Fred and Srdanov [14, 15] successfully synthetised the MEH-PPV, which served as donor materials. Since that time researchers have been improving the donor polymers for a better device performance. Enormous efforts have been put on the synthetic fabrication procedure and modification of the molecular chain of polymers. The enhancement of solubility, electrical and optical properties leads to a noticeable promotion of the cell PCE. Small molecular compounds also contributed to serve as donor organics however they do not work as well as polymer compounds, but novel research and modification of small-molecule compounds makes the use of donor. The release of polythiophene conjugated polymer donors- Poly(3-hexylthiophene-2,5-diyl) (P3HT) was considered as a landmark in achieving high-performance polymers. P3HT triumphs over contemporary products due to its high charge mobility, appropriate solubility and simple structure. The blending of P3HT and $IC_{70}BA$ has been adopted by Xiao.G for the active layer which achieves a PCE of 7.4% [5] of the device. Derivatives PTB7 and Poly [[2,3- bis(3-octyloxyphenyl)- 5,8-quinoxalinediyl]- 2,5-thiophenediyl] (TQ1) can be other alternatives. The energy structures are different from P3HT. The highest occupied molecular orbital (HOMO) energy is comparably higher, resulting in an optimised optical response. The absorption spectrum is significantly enhanced in the red-wavelength region as reported [16].

As overviewed by Antonio [11], the polymer donor–polymer acceptor (all-polymer) solar cells have been highlighted from 2012. Friend and Heeger [11] first adopted conjugated polymers of cyanate-poly (phenylenevinylene) PPV backbones. In the circumstance, the excitons generated from absorbed photons can be effectively dissociated to free charges at the blending interfaces of the polymers. MEH-PPV and C6-CN-PPV have been mixed by Friend [11]. The optical response can be enhanced by using such heterojunction, leading to a higher open-circuit voltage (V_{oc}) and external quantum efficiency (EQE). In 2017, Yikun [17] reported an achievement of

PCE of 8.48% by using the blend of PTB7-Th:NDP-V for donor and acceptor polymers. The promotion can be attributed to effective charge transfer over the interfaces and an enhancement upon the shorter-wavelength range response.

1.2. Mechanism of Polymer Based Solar Cell

In this section the typical structures of polymer solar cell is schematised including the inverted and conventional structure. The illustrated types are based on polymer-fullerene blended-bulk heterojunction active layer studied in the research. The working mechanism and characterisation of cell performance is elaborated.

1.2.1. Polymer-Based Solar Cell : Structure

Figure 1-1 shows the typical structure of polymer-based solar cells from laboratory and commercialisation, along with an energetic level diagram of the inverted schematic. The conventional structure is illustrated. In such device a transparent glass or plastic is used for substrate which is coated with ITO or FTO for a conductive contact with hole transport layer (HTL) or anode buffer layer (ABL). Organic adhesive poly (3,4-ethylenedioxythiophene) polystyrene sulfonate (PEDOT:PSS)[18, 19] can be a highlighted application for HTL due to its intensive interaction with the active layer. The photo-active layer is a blend of polymer-fullerene BHJ layer. The electron transport layer (ETL) /cathode buffer layer (CBL) is thus coated on the BHJ active layer. The typically-adopted material for electron interfacial layer is ZnO or TiO_2 because of the proper energy level alignment. Low workfunction (WF) conducting metal has been selected to ensure the proper electron transition over the interface and low resistance of the electrode. Ca, Li or Al and their alloys can be inserted.

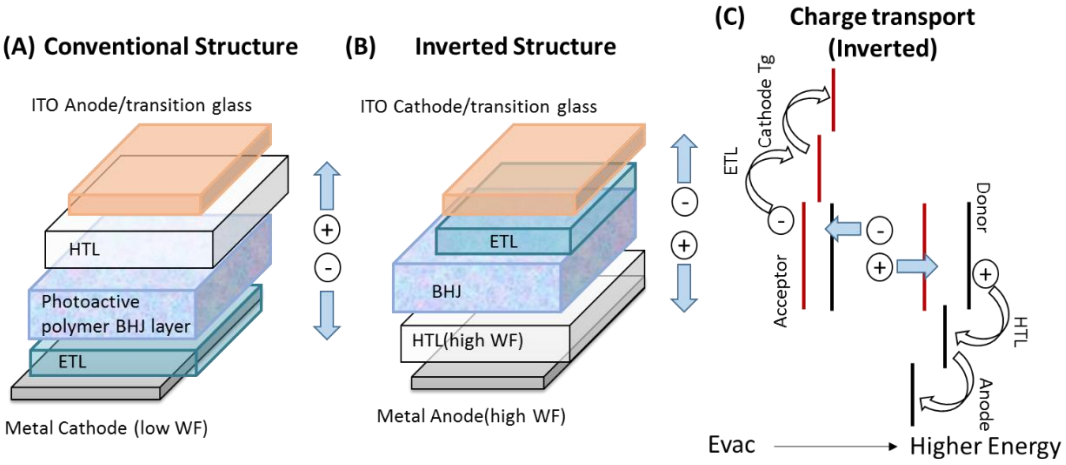

Figure 1- 1. The diagrams of conventional and inverted structure of polymer solar cell. The charge transfer based on inverted structure solar cells is shown

The schematic with an inverted structure (Figure 1-1 (B)) has been attracting attention for several years and significant effort has been exerted to improve the device performance. In the structure the concept for anode and cathode materials is reversed [9, 20, 21]. ITO or FTO coated glass serves as transition cathode while ZnO is typically used for ETL due to the alignment of energy structure at the interface [22, 23]. On the other side, high WF metal oxides, e.g. MoO_3, V_2O_5 and WO3, are commonly applied for HTL. The advantage has been determined [24-26], because these metal oxides are capable of extracting charge from either BHJ active layer or electrodes, thus enhancing the charge transfer over the interfaces. The materials for anode, however, needs to reconsider due to the alignment towards valence band (VB) of HTL. The WF of Ag and Au are relatively high, thus energetically favourable.

Given the circumstance, the energy level structure of inverted device results in a better Ohmic-contact for photo generated-charge transport and harvest. As reported by Zhicai [27], the device using an inverted structure yields a PCE of 10% while the one based on same active layer materials and conventional structure achieved a PCE of 8%.

1.2.2. Inverted Polymer-Based Solar Cell : Operation

The operation of an inverted polymer solar cell can be divided into three main processes (Fig 1-1(C)). (a) A radiating photon with an energy higher than the band gap (E_g) of active organic materials is capable of exciting an electron from the highest occupied molecular orbital

(HOMO) level to the lowest unoccupied molecular orbital (LUMO) level [11] to turn into an exciton. The photoelelctron generation process mostly occurs in the polymer BHJ layer due to the high transmittance of ITO cathode and ETL metal oxides. The exciton is defined as the bonded state of an excited electron and an associated hole [5, 28], which are mutually attracted by the electrostatic Coulomb force [28]. (b) The exciton diffuses to reach the interface of donor and acceptor, where excitons are dissociated into free charges (electrons and holes). The process can also be promoted by an electric field from interface dipole. Recombination may occur during the transfer of the exciton. Traps such as impurity defects [28, 29] and self-trapping eliminate the diffusion of excitons by recombination. Therefore, to achieve a maximised dissociation of exciton at the interface, a high diffusion length relative to thickness of layers and a thin layer of the polymer/fullerene are needed [6, 17, 28]. This is a trade-off with the thickness of the active layer, due to the fact that a high probability of light absorption can only be achieved with a thicker layer. Under these conditions, a blended donor and acceptor layer can be adopted which noticeably increases the rate of dissociation by increasing the interface area [17, 30]. (c) The split electron and hole (charges) transfer in different directions. The electron diffuses to the LUMO of acceptor while the hole transfers to the HOMO of donor. Due to the presence of an internal electric field, the charges move through the active layer towards the correspondent interfacial layers. Since the conduction band (CB) of ETL is favourable for electron transport, while the valence band (VB) of HTL is in alignment with the HOMO of donor, the charges are naturally migrating to the interfacial layers. The interfaces formed at electrodes/interfacial layers allow a further charge transfer, thus the individual electrodes serve as electron/hole collectors.

1.3. Interfacial Layer in an Inverted Polymer Solar Cell

The modification of molecular schematic and development of synthetic of the active organic layer vitally promote light absorption, charge lifetime and materials diffusion length. The blended donor-acceptor interfaces further enhance the charge dissociation. In addition, the use of interfacial buffer layers can be considered as essential for enhancing charge transfer and thus

harvesting free electrons and holes.

1.3.1. Electron Transport Layer: Mechanism and Materials

The ETL has a higher electron affinity (EA) than the acceptor and sufficient electron mobility supporting the electron transferring across the layer [31, 32]. Conversely, the hole is "obstructed" due to the ionisation energy (IE) which is not favourable for hole transport. The purpose for using ETL between the active layer and cathode is to minimise the charge recombination by diminishing the interface defects and buffering the energy levels at such interfaces [32, 33]. The chosen ETL materials always have a better compatibility with both the active layer and the electrode and can work as an interfacial barrier for moisture and oxygen residue [33, 34]. The degradation of the performance of a solar cell using the electron-transport interfacial layer is comparably less than the one without such a layer.

The most commonly used ETL material is ZnO because of its superior charge mobility and suitable EA [35]. In addition, Saltine Lithium Fluoride (LiF) was adopted by Kondakov [36] in 2005, as it has a better band alignment with adjacent polymer BHJ. Yang's group also tried Cesium carbonate (Cs_2CO_3) as ETL [37]. The Cs_2CO_3 shows better stability than LiF due to its capability to prevent moisture.

1.3.2. Hole Transport Layer: Mechanism

The aim of using HTL between the active layer and the electrode-anode is to energetically buffer the hole migrating over the adjacent interfaces [31, 38, 39]. The HTL usually has sufficient conductivity, thus the charge is able to transport across the layer. As reported by Sylvain [24], the HTL layer can further diminish the penetration of electrodes, such as Ag, that show a noticeable diffusion into the active layer by evaporation. The diffusion of Ag into organic bulk results in internal current leakage, reducing the shunt resistance (R_{sh}). Transmittance of the HTL materials is less important than ETL, but still worthy of consideration. A small chance of penetration of light across the active layer may occur, generally light with high wavelength. The HTL would allow the light to penetrate and reflection to happen due to the existence of metal electrodes [9] on the end. Here a second chance of light absorption in the bulk of active layer can occur. The photon loss during transition is proportionate to the transmittance of HTL.

1.3.3. Hole Transport Layer: Materials

In 2002, Kim [9, 40] first adopted PEDOT:PSS as the conductive electrode. Furthermore the poly-sulfonate material was modified as HTL in an inverted polymer solar cell and resulted in a wide use. Nowadays the PEDOT:PSS has a higher adhesion to the active layer due to the promotion of fabrication methods [18, 40]. The IE of PEDOT:PSS is rather equivalent (typically 5.1-5.2eV [19, 41, 42]) to the HOMO of the active layer. Such energy level structure at the interface of HTL and active organics yields a high hole affinity for transport. However, the acidity of PEDOT:PSS could cause corrosion on the electrode [5], which can be solved by inserting a thin layer of TiO_2 between them.

The history of using high WF metal oxides as interfacial layers, e.g. Molybdenum Trioxide (MoO_3), Vanadium Oxide (V_2O_5), Tungsten Trioxide (WO_3) and Rhenium dioxide (ReO_2), can be traced back to 2008. C. Tao's group [41] introduced MoO_3 as HTL by thermal evaporation. In this report the energy level diagram is shown. Incorporating MoO_3 prevents the flow of electron from the active layer towards the anode. The use of MoO_3 was determined to significantly increase the fill factor (FF) and current density (J_{sc}) of the solar cell. Since then a range of coating methods of MoO_3 on the polymer BHJ layer have been introduced. Vacuum nano-scale deposition such as physical and chemical vapour deposition (PVD and CVD) [43, 44], magnetron sputtering [45] and laser-controlled deposition [46]; solvent and gel processes such as solution coating [26, 47], sol-gel [47-49] and Nano-particles (NPs) ink [50] have been adopted. Interestingly, a variation of the WF and valence band states of MoO_3 have been reported [32], depending on the deposition methods. A series of treatments such as exposing MoO_3 to atmosphere [51, 52] and thermal-annealing [53] also result in difference of energy band structure. The cause will be studied in chapter 5 and 6.

Even though the transmittance of V_2O_5 is slight degraded from MoO_3 [32, 54], V_2O_5 has still been considered a substitution for MoO_3 due to their similar chemical and electrical features. However, the high toxicity [31] of V_2O_5 brought health issues to the operators which lowered the preference for this material. In 2011, Riedl [55] successfully used the thermal-evaporated and solution-processed V_2O_5 for HTL in a polymer solar cell. Comparisons were made and showed a lowered cell performance with a higher-concentrated precursor solution. Hancox and

other colleagues [56, 57] reported a hole-extracting mechanism of V_2O_x when it is used as the interfacial layer on a small molecule organic device (BCP/C60, non-polymer). The PCE increased to 2.5% from 2.0% of solely ITO on top without V_2O_x layer. The FF of the device increased to 0.45 and the J_{SC} achieved 0.66 mA cm^{-2}.

WO_3 was initially used in a device structured as an O_2 gas sensor [48] in 1999. The structure of WO_3 shares a cognate crystalline characterisation with MoO_3 and the electronic structure are similar. Given that, researchers have attempted applying WO_3 for HTL materials in an organic device. In 2012, James [58] worked on sol-gel WO_3, substituting for PEDOT:PSS. The energy level structure suited the hole transport, thus the device using WO_3 produced a similar efficiency with PEDOT:PSS. Further studies were implemented for using WO_3. A work by Maria in 2011 [59] revealed a usage of WO_3 as an organic light-emitting diode (OLED) interfacial layer. The reduced derivatives WO_x (x~2.5) offered a range of energy states across the valence structure towards the edge of conduction band. The occurrence of states acted as charge transfer reservoirs for both electrons and holes. In these conditions, the WO_x serves as either cathode or anode interfacial layer. However, in comparison with MoO_3, the lower formation rate of a closed WO_3 surface layer [31] and high temperature for operating WO_3 evaporation raised concerns about its usage in polymer solar cells. Therefore, WO_3 has hardly been adopted in polymer solar cells. In a report [60], WO_3 was applied as a modification of the electrode, rather than an individual layer. Even though using WO_3 as HTL in polymer solar cells is inappropriate at present, the preferable energy structure and transmittance are still promising for a hole transport layer with further modification.

1.4. Energy Level Alignment and Band Bending at Interface

In the section the charge transfer over the interfaces formed at the adjacent layers is described. First the interface is reviewed and energetic values of energy bands are illustrated. Methods such as photoelectron spectroscopy surveying the energetic levels are shown, including a direct measurement of WF, CB/LUMO and VB/HOMO.

1.4.1. Interfaces : Chemistry and Electronics

An interface is usually formed at the boundary of a contact of two distinct materials, which are conductive or semi-conductive. In a polymer solar cell, enormous investigations focusing on the interfaces formed at different layers have been implemented. These investigations offer an insight into the fundamental mechanism for the device operation. The chemical mixing phase and electrical properties alignment at the interface play a critical role on the charge transport and thus, overall series and shunt resistance (R_s and R_{sh}) of the devices.

By using Rutherford backscattering spectrometry (RBS), Sylvain [24] found a heavy diffusion of MoO_3 into the organic active layer with the proceeding of evaporation of MoO_3. At the interface, the compounds were mixed and such interface was uneven. Furthermore, the deposition of Ag onto MoO_3 incurs a diffusion of Ag into the MoO_3/active layer bulk. The mixing phase of the chemical distribution was also observed by Robin [61], which was diminished when the organic layer was inversely deposited onto the MoO_3. The deposition consequence resulted in a variation of chemical distribution at the interface. Such chemical distribution across the interface was due to the thermal Brownian motion of molecules [62] and the concentration gradient (CG). The adjacent materials tend to be physically mixed with each other, creating an interface of a few nanometres broadened. The diffusion flux of the compounds with a higher concentration is given by Fick's laws [63, 64].

$$\frac{\partial \emptyset(r,t)}{\partial t} = \nabla \cdot [D(\emptyset, r)\nabla\emptyset(r,t)] \qquad \text{Equation 1-1}$$

$\emptyset(r,t)$: the density of the diffusing materials;

r and t: location and diffusing time of the materials;

$D(\emptyset, r)$: the collective coefficient at given location and time;

∇ : the vector differential operator

In addition to the chemical distribution, the electrical characterisations at the interfaces are also of importance for the charge transfer and device operation. The energy band structures at the interface with distinct materials have been presented by many researchers. Different arguments were proposed and have been lasting until present. Researchers including Chen [65], Sun [66], Pietrick [67] and Kim [68], etc., assessed that the interfacial energy structure was from the

viewpoint of aligning the vacuum levels (E_{vac}) of each other. In the conditions the WF related to Fermi level did not shift in both of the contacting materials. The argument stands in inorganic devices such as silicon-based homo-junctions. However, two main questions were remaining unaddressed. a) The observation of interface electrostatic field was not characterised, thus, the dipole formation cannot be estimated; b) The working principle of high WF materials as the interfacial layers, such as MoO_3 (pristine WF as high as 6.8eV [69]), cannot be understood. This is due to the fact the IE of MoO_3 is normally 2eV larger than the HOMO of active layers, that is not favourable for hole transport.

In 1998, investigations into the interface of metals/long-chain alkane organic [70] by Professor Seki from Nagoya University raised a different model of the interface forming with organics and metals. Due to the energetic difference between the E_f of the metal and alkane organic, the equilibrium of the E_f occurred. Electrons transferred from the organic with a lower WF to the metal with a higher WF, creating an electrostatic field at the interface. Therefore, a shift of the energy levels presented at the interface. In the model, the E_{vac}, HOMO and LUMO of organics were shifted and a Schottky barrier was thus established. The model offered a prerequisite of the formation of interface dipole, which introduces an electrostatic field [70, 71]. The concept has been accepted by many other researchers, such as Meyer [72, 73], Hancox [39], Cappel [7] and Mark. T [74]. Figure 1-2 shows a general schematic of energy level alignment based on the conceptual model formed with two distinct materials. The difference in WFs of material (A) and (B) results in the flow of electrons due to the alignment of E_f. The electric field is thus established, forming an interfacial dipole. This dipole is capable of extracting charges, thus the energy bands within the dipole moment are either bent or shifted.

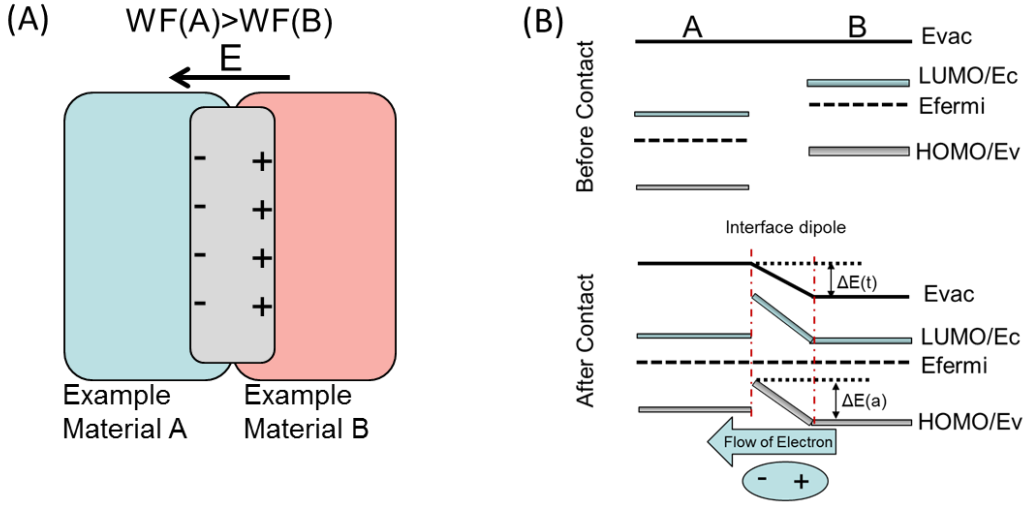

Figure 1- 2. (A) The illustration of different materials with various WF values; (B) After contact, the energy levels shown have been shifted significantly at the interface, Efermi indicates Ef (Fermi level energy)

Such energy bands alignment only presents at the conductive/semi-conductive interfaces. In an insulating material, the free-charge movement is obstructed. Electrons are not capable of redistributing at the interface, thus the energetic shift of bands structure does not exist.

1.4.2. Energy Band Parameters

The energy bands E_f, IE and EA described in Chapter 1.3 are the quantitative measures of the electric properties of materials. The theory based on an approximation to the quantum state of a solid, which derives the energies by examining the quantum mechanical wave functions [75] for charges in a model of many bonded atoms or molecules. The band theory successfully explains the electrical conductivity of given materials, the optical absorption, the photoelectric and the electroluminescent effects [75, 76]. It is also a milestone investigating the charge transfer over a range of interfaces.

Vacuum Level (E_{vac}) [28, 76]: The energy level where a free stationary electron locates with no binding force from the core level. It is outside or even infinitely distant from a solid. The other energy levels defined, are usually referred to the vacuum level.

Fermi Level (E_f) [77, 78]: The concept following Fermi-Dirac statistics describes the energy level of maximised-occupation of electrons in materials under absolute zero temperature.

According to Pauli Exclusion theory [78], Fermions such as electrons can only exist in certain states. Such level is with lowest energy, where electrons are able to occupy at absolute zero. The Fermi level plays an important role on the electrical and thermal characterisations of solid-state materials.

In terms of the Fermi-Dirac statistics, the probability of occupied state by an electron is given by equation 1-2 [77].

$$f(E) = \frac{1}{e^{(E-Ef)/kT}+1} \qquad \text{Equation 1-2}$$

E: the value or point on energy scale

Ef: Fermi Level on energy scale

kT : a product of Boltzmann constant and absolute temperature T (K)

Workfunction (WF): The value represents the energetic difference from E_f to E_{vac} in solids. As defined, the WF is the minimum thermodynamic energy that an electron requires to migrate from a solid surface to a vacuum zero outside the solid [78]. Given that, a semi-conducting interface would allow the alignment of E_f because thermodynamic energies must obey boundary conditions (probability of occupied states), so that the positions of Fermi levels must match at the boundary of two distinct materials.

It needs to be highlighted the WF can be significantly altered with a range of treatments. Mark. T [79] exhibited a work addressing the change of WF of the TMOs, such as MoO_3 and WO_3, as a consequence of the operation of thermal treatments. The work showed that the correlation of WF can be attributed to two aspects: the change in cation electronegativity, and the change in oxidation state of metal oxides. The overall change of WF are given by Equation 1-3.

$$Wf' = Wf + \Delta Wf = Wf + \Delta\theta_e + \Delta\theta_d \qquad \text{Equation 1-3}$$

Wf: original WF of a given metal oxide

$\Delta\theta_e$: the change of WF due to the change of cation electronegativity

$\Delta\theta_d$: the change of WF due to the change of oxidation state of a given metal oxide

In a pristine MoO_3 sample, the reduction of MoO_3 to a MoO_x (x~2.5) was determined in the work due to the thermal annealing at a given temperature (> 150 ℃). According to Nethercott's postulate of the geometric mean [80], since the electronegativity of Mo^{5+} is lower than Mo^{6+}, the WF of the partially-reduced MoO_3 can be increased with the increasing concentration of Mo^{5+} and the O-deficiency. The expression for Fermi dependence on the proportion of Mo^{5+} and the non-stoichiometry of the Mo^{6+}, Mo^{5+} and O^{2-} can be written as Equation 1-4.

$$\Delta\theta_e = 2[((X_{mo6+})^{1-2x}(X_{Mo5+})^{2x}(X_{O2-})^{3-x})^{1/(4-x)} - ((X_{Mo6+})(X_{O2-})^3)^{1/4}] \quad \text{Equation 1-4}$$

x: proportion of the part of Mo^{5+}

x_{mo6+}: non-stoichiometry electronegativity of Mo^{6+}

x_{mo5+}: non-stoichiometry electronegativity of Mo^{5+}

x_{o2-}: non-stoichiometry electronegativity of O^{2-}

From the valence electron spectra of photoelectron spectroscopy, the O-vacancies of MoO_3 due to the increase of entropy, breaching the O bond was stated, generating donor states approaching the E_f. Such states could further increase the density of charges near the CB because the given states could easily cause the ionisation of the CB. Overall, the E_f would shift upwards to the E_{vac} due to the occurrence of free charges flowing across the states. The conductivity of MoO_3 can be enhanced. The second change of WF is proportionate to the occurrence of O-vacancies. The formula is given:

$$\Delta\theta_d = [-\frac{1}{2} kt \ln(\frac{x}{x_0})] \quad \text{Equation 1-5}$$

kT: a sum product of Boltzmann constant and given temperature

$\frac{x}{x_0}$: the concentration of O-vacancies (for example, MoO_x, x~2.5 indicates that the concentration of O- defected MoO_x within MoO_3 is 0.5/3)

Secondary-electron Cascade (2nd electron Cascade): The WF can be derived from the cut-off of secondary electron peak by conducting UV-light photoelectron spectroscopy (UPS) [81] and Kelvin probe microscopy (KPM or KP) [82]. The secondary electrons are emitted from the

surface layer of a sample and lose energy on their way through the sample. These low kinetic energy (k.e.) electrons are excited by the initial electron avalanche [83]. A work by Anirudh [83] in 2015 shows that secondary electrons have a large electron mean free path, which allows the migration of the secondary electrons across a heterogeneous sample. These electrons carrying information of correspondent components contribute to the secondary electron peak cascade. However the peak cut-off derived from spectroscopy is dominated by either the material at the outermost layer or the material has a lower WF[83]. Using WF examining the energetic characteristics from the interface and quantifying the compounds is inappropriate.

Conduction Band, Lowest Unoccupied Molecular Orbital and Electron Affinity (CB, LUMO and EA): The CB has been defined as the lowest range where vacant electronic states exist. Electrons with sufficient energy can jump from the valence band to CB. These energy orbitals allow the electrons to move freely in the materials, generating an electric current. The term LUMO is normally used in organic solids, which has a similar meaning as CB. From the perspective of organic chemistry, a linear combination of atomic orbitals is considered and electrons arrive at molecular orbitals for the entire molecules. On this basis, the energy difference from the CB or LUMO to the E_{vac} is defined as EA.

Valence Band, Highest Occupied Molecular Orbital and Ionisation Energy/Potential (VB, HOMO and IE): The VB is the outermost energetic orbital in which electrons are present at absolute zero temperature. Such band is located below the E_f in a semi-conductor. In the field of organic materials, the HOMO energies are defined with a similar meaning. The term "IE" represents the energy difference from the VB or HOMO to the E_{vac} in a solid-state material.

Band gap (E_g): The concept E_g only occurs in semi-conductors and insulators, which is defined as the energy difference between the lowest unoccupied state of the CB/LUMO and the highest occupied state of the VB/HOMO. In semimetals, these two bands overlap, thus no E_g presents. No energetic states exist in the region of E_g. A large E_g means a higher energy is required to excite the electrons from VB/HOMO to CB/LUMO, while the probability of free electrons existing in conduction states is lower [84]. Given that a larger E_g normally indicates a lower conductivity across the solid, thus the R_s can be increased. On the contrary, the intrinsic current can be diminished in a PV device [85] due to the less chance of intrinsic recombination[86]. In

the circumstances the open-circuit voltage (V_{oc}) can be promoted with a larger E_g.

1.4.3. Interface: Metal/Organic

Professor Seki has shown a range of researches covering the interfaces formed with long-chain alkane/metal [70], C60/metal [82] and TPD/Au [87], respectively. Two models depicting the energy level diagrams were proposed. In both of the models, the E_f of metal and organic was aligned. The traditional (Mott-Schottky) model illustrated an effect of band bending with abundant free charges. The LUMO and HOMO of the organic were curved at the interface, creating a Schottky barrier. On the other side, the actual measurements from UPS and KPM led to another schematic. The E_{vac} of organics was shifted while only a small degree of band bending was observed. Such band structure was assigned to the lower charge mobility in organic materials that the charges were not capable of redistributing sufficiently at the interface. However, due to the lack of quantifying methods, the LUMO and HOMO of organic at the interface were not deduced.

In 2009, Slawomir [85] reported a work using the UPS to illustrate the energy bands at the polymer/metal interface. The E_f was aligned with no band-bending shown. The charge transfer follows the rule of energy level alignment, i.e. HOMO level of BHJ to VB level of MoO_3, CB level of MoO_3 to LUMO level of BHJ. Other reseachers [71] have doubted the existence of band bending at the interface formed with organic solids, but until now both of the models operate and are shown in publicaitons.

1.4.4. Interface: Organic/Organic

Due to the lack of technique approaching the interfaces forming at conjugate organic layers without any destruction, the organic/organic interfaces have not been thoroughly investigated. A BHJ interface is even harder to quantify because the chemical phases are heavily mixed. The energy bands structures shown in a range of published work [65, 88] were based on the alignment of E_{vac}, which is improper with the contact of distinct organic materials. A recent work published by Soohyung [89] exhibited a potential energy level structure at the interface forming with PTB7/$PC_{71}BM$ and P3HT/$PC_{71}BM$ (polymer-fullerene). The alignment of E_f in the work resulted in the band bending of energy bands of P3HT. The charge transfer was discussed.

Besides, the dipole formation at the interface of P3HT/$PC_{71}BM$ was highlighted due to the energy difference of the WF, which essentially shifted the energy levels. The dipole was not found in PTB7/$PC_{71}BM$ BHJ due to the fact the WF of the two materials are same.

1.4.5. Interface: ETL/Organic

The interfaces forming at ETL metal oxides/organics are of great interests to researchers because the interfacial layers are supposed to offer a smoother electron transport. Meanwhile, the energy bands structure could be a barrier for inverse electron transferring. Yang's group [33] successfully employed the RGO/TiO_x composite film as ETL, illustrating a promotion of the PCE of devices. In 2005, the reduced MoO_x and V_2O_x were used by Xinchen [34] for ETL, because the reduction significantly decreased the WF of these transition metal oxides (TMOs). The modified EA level was thus suitable for electron reservoir. The interface with energy level structure was estimated.

1.4.6. Interface: HTL/Organic- Conventional Concept

The interfaces forming with HTL metal oxides and organics are granted with an avalanche of attention. There are still several unsolved concerns about the hole transport, energy level positioning and dipole formation at such interfaces. All these factors are in relevance to the ultimate performance of polymer solar cells. Therefore, ongoing investigations are implemented by researchers. In Chen.T's [41], Katsuyuki's [90] and Hancox [91]'s work, conventional energy level diagrams at MoO_3/organic interface were shown. Aligning E_{vac} of MoO_3 and organics resulted in a feasible hole migration from the HOMO of active layer to the VB of MoO_3. However there were two questionable points need to be stated: (a) The Fermi level equilibrium due to the contact of distinct materials was not taken into account. Thus the formation of interface dipole was ambiguous. No band shift or bending can be estimated. As a matter of fact, the alignment of E_f of organics/MoO_3 can be exactly seen from the spectra from photoelectron spectroscopies, which has been demonstrated by other researchers[61]; (b) The energy bands of MoO_3 were referred to others' studies. The EA of MoO_3 is 2.3eV; the IE is 5.3eV across a range of reports. It was hard to trace the origins, but the newly reported WF of evaporated MoO_3 levelled higher than 6eV [61] while the IE was more than 9eV [32, 61]. The sol-

gel or solution processed MoO_3 still had a WF higher than 5eV while the IE was around 7.5eV [32]. Such electronic values were based on MoO_3 target, powder and paste with a high purity. Moreover, Yuzheng [38] assigned the origin of high WF of MoO_3 to intrinsic properties of crystalline materials by a thoroughly research.

Similar results on the interface of V_2O_5/organic can be referred to Gerardo's and Hai-Qiao's work [88]. The energy level diagrams and mechanism of charge transfer at the interfaces were based on the alignment of E_{vac}. The estimation of the diagrams was questionable because aligning E_{vac} is normally applied before the contact of two materials.

Even though a boost of PCE of OPV has been demonstrated by inserting the high WF metal oxides as HTL, the mechanism and electronic structure at such interfaces are still unclear. The measured energy levels of MoO_3, such as VB, are energetically unfavourable for hole transport because the VB of MoO_3 is far below the HOMO of organic layer. This has been determined by many scientists [54, 57, 69, 79, 92-94].

1.4.7. Interface: HTL/Organic- Unique Charge Transfer

Since early 2000, the WF of a neat MoO_3 film with sufficient thickness has been determined as 6.7-6.8eV [32]. The WF of V_2O_5 [56] ranged from 6.8 to 7.0eV and for WO_3, it was about 6.7eV [32]. Based on the values, Hamwi and Meyer [93] noticed a p-type doping effect of MoO_3 on an organic layer when it served as HTL. A conclusion was deduced, that the WF of the complex of CBP/MoO_3 increased with the increasing amount of MoO_3. The energy band structure at the interface was shown as a function of sufficient MoO_3 deposition. Kroger [72]-a colleague of Meyer, addressed the functions of the deep-lying energy states of MoO_3 at an organic interface by using UPS technique. The energy level diagram at the interface of MoO_3/α-NPD was illustrated with the energy shift of E_{vac} upon the α-NPD. In terms of the high WF of MoO_3, the CB of MoO_3 was close to the HOMO of α-NPD with a minor difference of 0.6eV. Direct hole transport from the HOMO of α-NPD to the CB of MoO_3 was thus proposed, which was defined as hole injection mechanism. As a consequence of the injection of holes, electrons were extracted inversely towards the HOMO of α-NPD. Positive charge and negative charge are physically equivalent. Such charge migrations occurred because the energy bands,

including HOMO/VB and LUMO/CB, offered the energy states as reservoirs for the charges. However, the HOMO and LUMO of α-NPD at the interface was unclear due to the lack of characterisation of the interface dipole. Further investigation and modelling have been done by Meyer [73, 95]. From 2010 to 2014, Meyer and his group schematised the energy band structures at the interfaces of MoO_3/organic[72], MoO_3/graphene[54] and V_2O_5/organic[55]. The models of charge injection/extraction were presented, which explained the working mechanism of these high WF TMOs as HTL. The architecture of the energy levels and assumed charge transfer over the interface are shown in Figure 1-3.

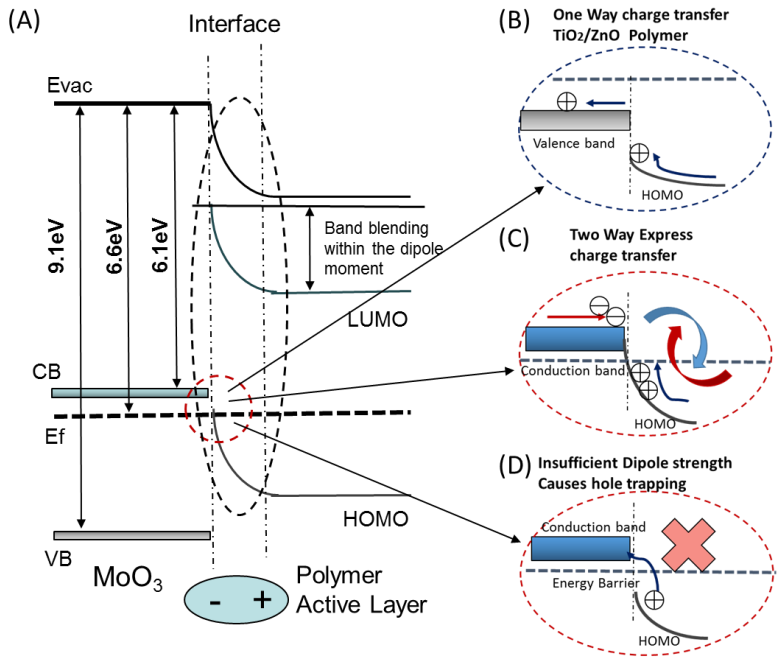

Figure 1- 3. (A) The energy level diagram at the interface of MoO_3/polymer active layer; (B) The conventional hole transport over a TiO_2/active layer interface; (C) The "express" charge transfer over a MoO_3/active layer interface; (D) Insufficient dipole strength causes obstruction to the charge injection/extraction

The schematic is based on the interface of MoO_3/organic active layer. The alignment of E_f results in the shift of E_{vac} on the side of active layer approaching the interface. Meanwhile, within the interface region, the bending of energy levels can be observed. This is due to the formation of a dipole at the interface a consequence of the energetic equilibrium of electrons. Such dipole is capable of biasing the energy bands of the organic within the dipole moment. The curvature of bands shown in the figure is determined by the dipole strength. In Figure 1-

3(B), the VB of TiO_2 is in proximity to the HOMO of organic. Given that, a conventional hole transport form the HOMO of organic to VB of TiO_2 is illustrated. In Figure 1-3(C), the hole transfers from the active layer, along the HOMO bending at the interface, to the CB of MoO_3. With a sufficient dipole strength, the energy gap between the HOMO of organic and the CB of MoO_3 at such interface can be eliminated. Besides, the bending of the LUMO of organic can further block the electrons flowing to the MoO_3 HTL due to the presence of a Schottky barrier. A two-way charge transfer defined by quantum dynamics [54, 96-98] over the interface is thus established. With an insufficient dipole strength shown in Figure 1-3(D), the energy gap between the HOMO of organic and the CB of MoO_3 occurs. The transport efficiency can be consequently reduced.

The concept of charge extraction/injection mechanism and the energy level structure have been echoed by other researchers. Similar diagrams at the TMOs/organic interfaces were delivered by Wang [99] and Irfan [92, 99]. In these pioneering works, a key element has drawn attention from the researchers. The dipole formation and its strength are vital to reduce the energy gap between the correspondent energy bands. How to characterising the dipole strength forming at the adjacent solids, especially the high WF metal oxides and organics, are of great importance.

1.5. Interface Electrical Dipole

The formation of a local electric dipole and an interface dipole is elaborated in this section. The difference between an interface dipole and a surface dipole is described.

1.5.1. Local Dipole Formation

The dipole investigated in the work is formed at the interfaces of distinct materials. The vector sum of an interface dipole can be defined as an accumulation of the individual dipolar vectors orientating in parallel with others, pointing to a given direction. The definition of a single local dipole can be simplified as the dissociation and interaction of a positive and negative charges[100], which is shown in Figure 1-4(A). The dissociation of the charges is the consequence of the flow of electrons due to the Fermi level alignment of two adjacent different

molecules. Therefore, the sum for a dipole between two distinct molecules is a sum of vectors of these local dipoles. For example, the WF of MoO_3 is much higher than that of P3HT. Therefore, at the molecular level, a certain number of electrons flow from the P3HT molecule to the MoO_3 side. The electrons are depleted in that P3HT molecule and oppositely concentrated in the MoO_3. The P3HT molecule is thus defined as a cation. Electric potential at the boundary of the two molecules are established. Such potential working as a dipole between two molecules is assigned to an accumulation of the single local dipoles based on the equilibrium of E_f.

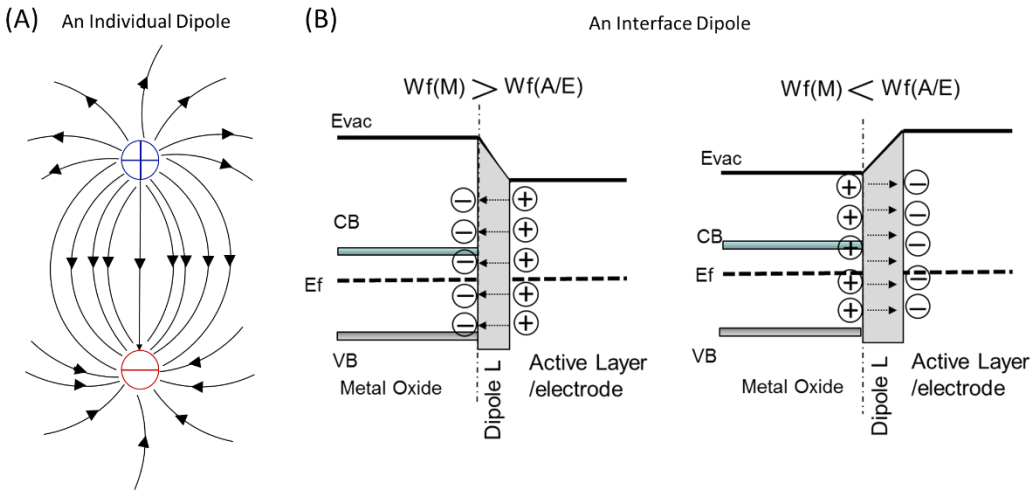

Figure 1- 4. (A) A local electric dipole; (B) The formation of an interface dipole layer, the direction of such dipole is based on the difference of WF of the district materials. The illustration of the amount of charges is an indication, not a real number of the local dipoles

The term-dipole moment is defined as the characterisation or quantities of the electric vector distribution of a dipole from positive to negative end, depending on the charge and distance. Here the calculation of dipole moment and the electric field are shown. The moment[100, 101] of a single dipole can be given as Equation 1-6

$$P(r) = \int_V^0 \rho(r_0)(r_0 - r)d^3r_0 \qquad \text{Equation 1-6}$$

r_0- r: difference in charge density

d^3r_0: an elementary volume in V

V: volume definition

For counting a dipole moment with the charges in an array, the moment follows the equation 1-7[102, 103].

$$P(a) = \sum_{i=1}^{N} q_i \cdot d_i \qquad \text{Equation 1-7}$$

q_i: charges volume

d_i: distance between charges related to the position of a charge

In the following step, the electric field and potential of a dipole can be calculated. Considering a pair of opposite charges which are close, the potential at position r follows the Equation 1-8[102].

$$\emptyset(r) = \frac{q}{4\pi\varepsilon_0|r-r_+|} - \frac{q}{4\pi\varepsilon_0|r-r_-|} \qquad \text{Equation 1-8}$$

q: charge volume

ε_0: permittivity of free space [100, 102]

$|r - r_+|,\ |r - r_-|$: vector distance in absolute from the positive and negative charge

Where at position r_0, the general electrostatic potential is proportionate to an electric dipole at the origin is given by Equation 1-9 [104, 105].

$$\emptyset(r_0) = \frac{P\cdot\hat{R}}{4\pi\varepsilon_0 R^2} = -P \cdot \nabla \frac{1}{4\pi\varepsilon_0 R} \qquad \text{Equation 1-9}$$

$\hat{R}$: a unit vector in the direction of r_0

P: the (vector) dipole moment from Equation 1-6

∇: Del operator

1.5.2. Interface Dipole and the Characteristics

The interface dipole at the boundary of two distinct materials consisting of a number of dipoles between the molecules. The dipoles at the molecular level is a vector sum of the individual local dipoles, and can be distributed at an interface. The accumulation of the specified local dipoles, which orientate parallel and point towards the surface normal, leads to the formation of an interface dipole. The schematic of an interface dipole forming at the adjacent metal oxide

(MoO_3) and polymer active layer (BHJ) is shown in Figure 1-4(B). The electrons are depleted from the material (BHJ) with a lower WF, flowing to the material (MoO_3) with a higher WF. The formed electrostatic field at the interface is assigned to the interface dipole.

Eisuki [70] reported in 1998 about the estimation of a dipole formed at the interface of metal and organic, which had been known as a concept generally expressed in the field of inorganic materials. The consequence of the dipole formation was assigned to the change of WF of the Ag covered with organic layer. Hisao and Seki [71] further explained, that the chemical interaction of two distinct materials at the interface would cause the rearrangement of the electronic cloud, altering the interface dipole. Such changes led to the formation of the interfacial states, working as a buffer for the charge transferring. The vector orientation of the molecules resulted in a permanent interface dipole. The dipole formed at Ag/CH_x CF_y function groups was further characterised. The dipole strength was in proportion to the change of WF.

In 2012, the interface between the TiO_2 layer and the electrolyte in a DSSC was investigated by Cho [6]. An interface layer was estimated and the dipolar moment was derived as a function of the difference of the WF. It was determined, that a dipole with a negative dipolar moment towards the layer of TiO_2 resulted in the shift of the conduction band (CB) of TiO_2. Consequently the V_{oc} was increased, which was in line with the increase of energy difference between the CB of TiO_2 and the redox energy of electrolyte. Beside, Cappel [7] has also revealed the similar findings.

As shown in a work by Jens Meyer [54] in 2014, the dipole formed at the interface formed with MoO_3 and p-doped graphene electrode was characterised using the UPS method. The MoO_3 was evaporated on the graphene and an increase in the WF from 4.7eV of 1.5 Å MoO_3 to 6.6eV of 130 Å MoO_3 was observed. Such increase in WF was further used for determining the dipole strength at the interface, which levelled at 1.9eV. The dipole strength was significant, thus it was capable of energetically supporting the charge injection/extraction transport over the interface. In 2017, Zhanhao [106] exhibited a work examining the dipole strength formed at the interface of Al and MEH-PPV. The methods employed in the work were based on a combination of X-ray photoelectron spectroscopy (XPS) and KP. The increase of the deposition amount of Al on MEH-PPV was precisely controlled by an angled mask and measured with

XPS. It was shown, that upon the increase of Al thickness, the WF of the sample derived from the KP increased. The dipole strength was thus in line with the change of WF.

A work by Soohyung [89] in 2014 showed the characterisation of a dipole forming between two distinct organics- the interface formed with PTB7 and $PC_{71}BM$. The change of the WF of $PC_{71}BM$ with PTB7 across a range of thicknesses was observed from the secondary electron cascade of UPS. The change of the HOMO level derived from the valence electron peak of UPS was also illustrated. The dipole was consequently determined from the energy difference of the shift of HOMO and change of WF at a certain deposition thickness.

1.5.3. Drawbacks of Conventional Characterisation of Interface Dipoles

Further studies about the characterisation of interface dipoles have been carried out by other researchers such as Hayashi [82]. The dipole strength in agreement with the change of the measured WF was frequently reported. However, several drawbacks using the WF measurement for determining the interface dipole strength can be addressed and presented below:

a) Characterisations based on the changes in WF are not directly related to the formation of the dipoles at the interfaces. Instead, they are the speculation for a dipole forming at such interfaces. This is due to the properties of secondary electrons described in Chapter 1.4.2. The secondary electrons are collected by either UPS or KPM detectors and contributed to the measured electron cascade, which are carrying the energetic information of a complex of different components. This is because the secondary electrons have a large mean free path, allowing them to migrate between the distinct components [83]. A direct measurement of the dipole needs a consideration of the changed or unchanged chemical characterisation. Based on that, further decomposition can be processed, leading to a quantitative definition of dipole.

b) The emission of secondary electrons contributing to the spectrum comes from the surface layer of a sample due to its large cross-section. However, the range of the interface dipole is relatively deep below the surface that the secondary electron does not carry information directly from such interfaces. The change of WF upon the

interface is the characterisation of the material at the outermost layer, but electrically affected by the interface dipole, i.e. biased within the interface dipole moment. Such influence is in proportion to the distance of the interface dipole, rather than a direct examination of the interface dipole strength. The calculation of a dipole moment is shown in Equation 1-6.

c) The secondary electrons carrying information about the outermost layer can be easily influenced by the impurities or adsorbates on the surface. This is due to the characterisation of the secondary electrons, which is based on a further alignment with the vacuum/air. As a consequence, a surface dipole is formed. The electrical property of the surface dipole can be interfered due to the occurrence of the surface adsorbates. A further alignment with the WF of the calibration sample of detectors is processed. The calibration sample used in UPS and KPM is usually a highly oriented pyrolytic graphite with a determined WF [82]. The formation of a surface dipole and the alignment with the detector calibration sample is shown in Figure 1-5 and the calibration with the WF of the calibration sample is given by Equation 1-10. Examining the WF of a sample, such as MoO_3, in a non-high vacuum condition can be easily influenced by surface impurities and adsorbate, e.g. moisture or hydro-carbon. In the conditions, the measured WF is not a pristine characteristic of the sample.

$$E_{bin} = hv - E_{kin'} - \emptyset_{sample} = hv - E_{kin} - \emptyset_{spectrometer} \qquad \text{Equation 1-10}$$

E_{bin}: binding energy scale(eV)

hv: induced photon energy (eV)

$E_{kin'}$: kinetic energy (eV) aligning with the spectrometer

E_{kin}: kinetic energy (eV) of the sample as a function of induced photon

$\emptyset_{sample}$: WF of given sample

$\emptyset_{spectrometer}$: WF of the calibration sample of spectrometer

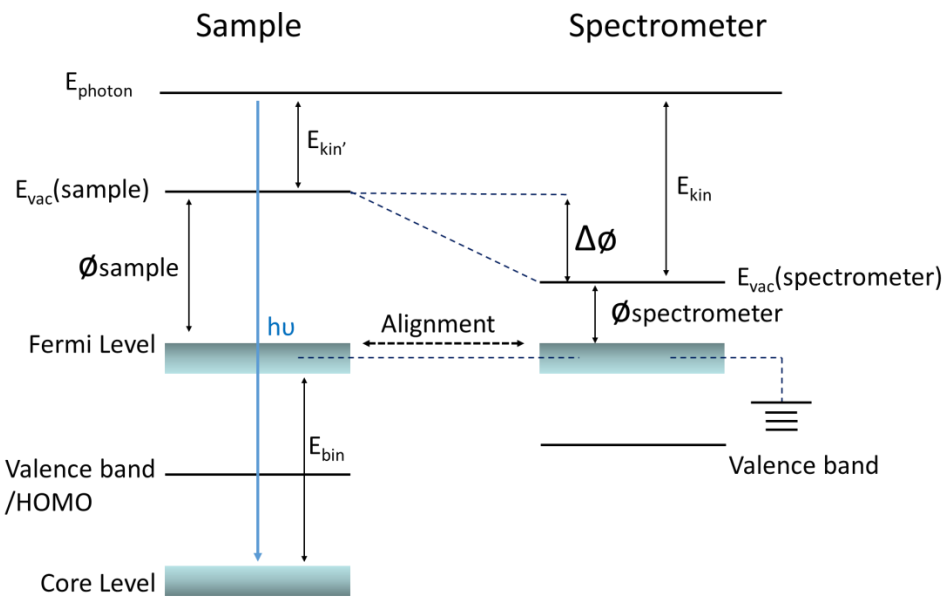

Figure 1- 5. The establishment of a surface dipole of a sample related to the WF of the spectrometer

d) The range of energy band shift with a certain thickness of distinct materials cannot be acquired from the WF and HOMO/valence band energy. Thus, the distribution of dipole strength at the adjacent interfaces is not derived from such analysis. In terms of the single electronic values given by the WF and HOMO energy, the structural model based on the WF to explain the prior results can only be schematised with band bending. The energy shift of the band structure at the interfaces and the energy distribution within the dipole moment are not clear.

The depth of the emission of valence electron from UPS is relatively large, which is approaching the exact interface. The measured valence electron spectra is a linear combination of the valence states from distinct materials [107-109] at the interface. By conducting a decomposition method, the constitution of the components can be identified. The nature will be described in detail in Chapter 2. Furthermore, a combination of the analysis of the secondary electron spectra and ion scattering energy loss spectra leads to a better understanding of the chemical and energetic characteristics at the interfaces.

1.6. Research Aims

In this research, a systematic analysis of the results from the photoelectron spectroscopy and ion scattering spectroscopy will be carried out. The fact of a dipole forming at the high WF TMOs/polymer BHJ interface will be demonstrated in a novel but legitimate way. The valence electron spectra and secondary electron spectra derived from UPS will be investigated in detail and analysed by two different decomposition algorithms. Therefore, the distribution of energy shift, mean and maximised energy shift of BHJ due to the formation of dipole will be shown. Given the results, a complete energy level structure at the interfaces can be modelled and the mechanism of charge transfer will be fully studied.

Further studies will be proceeded on the interface and dipole, under the conditions of external treatments, such as air contamination and thermal annealing.

1.6.1. Dipole Forming at the Interface of High WF TMOs and Polymer BHJ

It is assumed that the CB of MoO_3 and the HOMO of functional polymer/fullerene [110, 111] align due to a range of electronic properties of MoO_3 [52, 73, 92] amongst them the WF of pristine MoO_3 which was reported as 6.7eV [32, 94, 112]. The alignment of the CB of MoO_3 and the HOMO of conducting polymer BHJ is considered as favourable for the charge transfer [113], following the charge injection/extraction mechanism [93, 95, 114]. However, the band structure at the interface and the energy level alignment for the charge transfer are not clear due to a lack of technique for characterising. The WF and IE of MoO_3 have been reported to change in proportion to the thickness of the deposited layer [94, 115]. A speculation can thus be proposed, that a dipole can form at the MoO_3/BHJ interface [6, 112, 116] due to the noticeable difference in the WF of MoO_3 and polymer. The formation of dipoles can strongly impact on the charge transfer over the interface[61]. The energy of a single dipole can be calculated [71, 103], however in the condition of an interface, dipoles may encounter with each other, thus either enhances or cancels each out. The interface dipole energy may conduct a significant difference from the theoretical value of an individual one. The exact interface dipole strength has not been characterised. The intermediate energy states forming at the interface is yet to known and the prediction of charge transferring over the interface lacks of evidence.

The aim of this work is to address two main findings. a) A minimum deposition thickness of

MoO_3 is required to form a closed layer, the amount of MoO_3 will be quantified and shown using a combination of spectroscopy. b) It will be demonstrated that the dipole energy can alter significantly across the variation of deposition amount, influencing the way of charge transfer over the interface.

Further investigations will be implemented on the interfaces forming with V_2O_5/WO_3 and conjugate polymer. Such TMOs have a similar electrical properties as MoO_3. The difference of surface coverage and interface dipoles among these TMOs will be shown. The interface formed with MoO_3 and TQ1:$PC_{71}BM$ BHJ will be further studied.

1.6.2. Influence of Air Exposure on the Interface Dipole Forming at TMOs/BHJ Interface

Detailed understanding of the properties of interfaces in electronic devices is critical for the correct selection of materials to improve device performance and lifetime. A range of quantities are used to characterise the electronic properties of metal oxides such as WF, IE, EA, all three of which are comparatively large for the metal oxides MoO_3, V_2O_5 and WO_3 [6, 24, 32, 55, 59, 114, 117]. The WF is, by definition, a measure of the dipole between the top surfaces and vacuum, however, it is often assumed that this value also reflects the energy levels at the MoO_3/polymer interface. Importantly, these two dipoles are actually independent of each other and the change in WF at the vacuum interface cannot be taken as a measure for the change in the dipole at the MoO_3/BHJ interface, especially if there is intermixing of MoO_3 with the organic layer. The latter dipole must be measured independently.

It has been observed that the electronic properties of the surface of MoO_3 change strongly upon exposure to air, for example, the WF of MoO_3 shifts from 6.7 eV to 5.2 eV[51] when MoO_3 is exposed to atmosphere. Similar results have been found for the other high WF metal oxides as well [88, 118]. Further, the WF of TMOs [26, 88, 119, 120], for instance MoO_3 processed with sol-gel method and solution process[121], was characterised to be 5.3 eV[122]. Rempel [123] et al. have shown that a gaseous hydrated complex of the type of MoO_3/nH_2O is formed when samples are exposed to moisture. The occurrence of WF change has also been reported [30] to deteriorate the polymer device performance by significantly increasing the Rs.

Variations in the WF of MoO_3 of 1.6 eV have been reported in literature for MoO_3 surfaces generated under a variety of conditions. From the range of values for the WF it can be expected that other quantities like IE and EA will also strongly depend on the conditions of fabricating MoO_3 layers and conditions of exposure to air. During the fabrication of organic electronic devices exposure to air depends on the conditions for the fabrication of the devices and post fabrication exposure. However, as stated above, it is unclear how these changes to the WF, IE and EA correlate to changes of the electronic properties at the MoO_3/BHJ interface, in particular to the change in the dipole at this interface. Thus it is important to distinguish between the WF change and the change of the dipole at the MoO_3/BHJ interface as the aging mechanisms may be different leading to reversible or irreversible changes to the chemistry and ultimately the electronic energy levels across the interface.

The aim of this work is to understand the mechanism of the change of the electronic properties of the interface of MoO_3 with the BHJ formed by P3HT and PCBM. In particular it will be shown that the level of moisture to which the MoO_3/BHJ interface is exposed subsequent to its formation is crucial for the strength of the dipole at the interface. Depending on the conditions used in device fabrication handling, these findings have strong implications for the efficiency of the devices, the reproducibility of their functioning and on their lifetime.

Further investigation into the influence of exposure of the interfaces forming with V_2O_5/WO_3 and conjugate polymer will be commenced. Thus, the difference of the effects on these distinct metal oxides and conjugate polymer will be stated.

1.6.3. Influence of Thermal Annealing on the Interface Dipole Forming at TMOs/BHJ Interface

During the fabrication of a polymer solar cell, the annealing procedure has been adopted [24, 46, 124] . The process has been applied to either the BHJ [125-129], or on the deposited MoO_3 [24, 130]. The elimination of amorphous phase of polymer BHJ [68, 125, 131] leads to a boost in charge mobility [132-134], which is produced by performing the annealing upon BHJ at a temperature exceeding the glass transition temperature (T_g) of the polymers[135]. Meanwhile, the crystallisation in the polymer structure [125, 126, 135, 136] can also be achieved and the optical

response [68] is enhanced. These benefits contribute to the increase of the PCE of solar cell.

On the other side, the crystallisation nature of MoO_3[130] is reported to be promoted with the conducting of annealing upon MoO_3, which also benefits the interfacial contact for a better electron extraction[136]. Other findings including a variation of MoO_3 distribution into BHJ were reported [24] due to the annealing. Greiner found a reduction of MoO_x[53] at 150 °C. Such reduction caused the decrease of the WF of MoO_x by 1.1eV. A decline of WF by 1.1eV will certainly cause a change of the dipole formation. The variation of potential change of dipole has not been investigated. Besides, the dipole and the energy level structure at MoO_3/polymer BHJ interface under the thermal treatment has not been studied due to the interface mixing phase and the lack of technique for approaching the interface without destructing the layers. Therefore the mechanism of charge transfer is unpredictable under the condition of annealing.

The aim of this work is to deeply investigating the chemical distribution at the MoO_3/BHJ interface and quantifying the energy levels at such interface with the annealing proceeded. Various thermal annealing treatments will be performed upon the interface. The charge transferring over the interface as a consequence of annealing will be estimated.

1.7. Thesis Outline

The work presented and result discussed here is focused on the interfaces formed with incorporating high WF metal oxides and conjugated polymer layer and the characterisation of dipole at given interfaces. The metal oxides are used as transition anode buffer layers/hole transport layers. The constitution of polymer BHJ is a blending of the thiophene polymer and the small molecule fullerene.

In **Chapter 3**, the energy level of MoO_3 and P3HT:$PC_{61}BM$ BHJ is investigated and the formed interface is studied. A novel method using a combination of multi-spectroscopy for analysing the surface coverage and valence electron states is shown and a breakthrough of directly quantifying the dipole strength at the interface is achieved.

In **Chapter 4**, we show the influence of moisture and other residuum from atmosphere on the

chemical and electrical properties of MoO_3 and the interface formed with BHJ. The change upon dipole as a consequence of moisture invasion has been identified by analysing the valence spectra. Therefore, the schematic of energy levels at the interface of MoO_3/ P3HT:$PC_{61}BM$ BHJ after exposure is shown.

In **Chapter 5**, a simulation of annealing process has been applied in vacuum on either P3HT:$PC_{61}BM$ or the interface adjacent with MoO_3. The characterisation has been done for identifying the changes of chemical and energy level properties under the circumstances of annealing.

Chapter 6 is focused on the use of the multi-spectroscopy and the mathematical algorithm on the interfaces formed with alternative HTL materials-V_2O_5 or WO_3 and P3HT:$PC_{61}BM$ BHJ. The given dipole formations have been studied with the characterisation of full energy level diagram. Besides, the surface coverage as a function of deposition thickness of V_2O_5 and WO_3 has been investigated.

In **Chapter 7**, study of the air-exposed interfaces of V_2O_5 and WO_3 with P3HT:$PC_{61}BM$ BHJ was carried out. The cause of the change upon both energy levels of V_2O_5 /WO_3 and the interface dipole strength has been attributed to the invasion of moisture. Therefore, the charge transfer under the condition of air exposure is illustrated.

In **Chapter 8**, a new polymer-fullerene BHJ (TQ1:$PC_{71}BM$) is used as active layer substrate. MoO_3 is adopted as anode buffer layer and the interface of MoO_3/TQ1:$PC_{71}BM$ is studied. The chapter further validates the methodology used for decomposing the valance electron spectra and identifying the comprising components. The air exposure has also been processed on such interface. As such the change upon dipole strength has been quantified.

Reference

1. Anderson, T.R., E. Hawkins, and P.D. Jones, *CO2, the greenhouse effect and global warming: from the pioneering work of Arrhenius and Callendar to today's Earth System Models.* Endeavour, 2016. **40**(3): p. 178-187.
2. Fraas, L., *Low Cost Solar Electric Power.* Book, 2014.
3. Anderson, W.W. and Y.G. Chai, *Becquerel effect solar cell.* Energy Conversion, 1974. **15**(3-4): p. 85-94.
4. Green, M., A, et al., *Solar cell efficiency tables (version 52).* Prog Photovolt Res Appl., 2018. **26**: p. 427–436.
5. Kim, H., et al., *Organic solar cells based on conjugated polymers : History and recent advances.* Korean Journal of Chemical Engineering, 2014. **31**(7): p. 1095-1104.
6. Cho, C., et al., *Molecular modification on dye-sensitized solar cells by phosphonate self-assembled monolayers.* J. Mater. Chem., 2012. **22**(7): p. 2915-2921.
7. Cappel, U.B., et al., *Energy alignment and surface dipoles of rylene dyes adsorbed to TiO2 nanoparticles.* Phys Chem Chem Phys, 2011. **13**(32): p. 14767-14774.
8. Yang, X., et al., *Coordinated shifts of interfacial energy levels: insight into electron injection in highly efficient dye-sensitized solar cells.* Energy & Environmental Science, 2013. **6**(12): p. 3637.
9. Hoppe, H. and N.S. Sariciftci, *Organic solar cells: An overview.* Journal of Materials Research, 2011. **19**(07): p. 1924-1945.
10. Yang, W., J. Noh, and N. Jeon, *High‐performance photovoltaicperovskite layers fabricated through intramolecular exchange.* Science, 2017. **348**(6240): p. 1234-1237.
11. Facchetti, A., *Polymer donor–polymer acceptor (all-polymer) solar cells.* Materials Today, 2013. **16**(4): p. 123-132.
12. Cho, S., et al., *Role of additional PCBM layer between ZnO and photoactive layers in inverted bulk-heterojunction solar cells.* Scientific Reports, 20147. **4**(4306).
13. Mikroyannidis, J.A., et al., *A Simple and Effective Modification of PCBM for Use as an Electron Acceptor in Efficient Bulk Heterojunction Solar Cells.* Advanced Functional Materials, 2010. **21**(4).
14. Marletta, A., V. Gonçalves, and D.T. Balogh, *Photoluminescence of MEH-PPV/PS blends.* Brazilian Journal of Physics, 2004. **34**(2b).
15. Chen, S.H., et al., *Aging of Poly(2-methoxy-5-(2′-ethylhexyloxy)-1,4-phenylenevinylene)/Toluene Solutions and Subsequent Effects on Luminescence Behavior of Cast Films.* Langmuir, 2004. **20**: p. 8909-8915
16. Zhu, H., M.B. Johansson, and E.M.J. Johansson, *The Effect of Dopant‐Free Hole Transport Polymers P3HT, P3TI and TQ1 on Charge Generation and Recombination in Cesium‐Bismuth‐Iodide Solar Cells.* ChemSusChem, 2018. **11**(6).
17. Guo, Y., et al., *Improved Performance of All-Polymer Solar Cells Enabled by Naphthodiperylenetetraimide-Based Polymer Acceptor.* Adv Mater, 2017. **29**(26).
18. Maniruzzaman, M., et al., *MoO3/Au/MoO3–PEDOT:PSS multilayer electrodes for ITO-free organic solar cells.* Materials Science in Semiconductor Processing, 2014. **27**: p. 114-120.
19. Sharma, A., G. Andersson, and D.A. Lewis, *Role of humidity on indium and tin migration in organic photovoltaic devices.* Phys Chem Chem Phys, 2011. **13**(10): p. 4381-4387.
20. Yu, B., et al., *Efficient inverted solar cells using TiO2 nanotube arrays.* Nanotechnology, 2008. **19**(25).

21. Tao, C., et al., *Role of tungsten oxide in inverted polymer solar cells.* APPLIED PHYSICS LETTERS, 2009. **94**.
22. Jeon, I., et al., *Air-processed inverted organic solar cells utilizing a 2-aminoethanol-stabilized ZnO nanoparticle electron transport layer that requires no thermal annealing.* J. Mater. Chem. A, 2014. **2**: p. 18754-18760.
23. Sharma, A., et al., *Effect of Annealing Temperature of ZnO on the Energy Level Alignment in Inverted Organic Photovoltaics (OPVs).* Energy Technology, 2014. **2**(5): p. 462-468.
24. Chambon, S., et al., *MoO3 Thickness, Thermal Annealing and Solvent Annealing Effects on Inverted and Direct Polymer Photovoltaic Solar Cells.* Materials, 2012. **5**(12): p. 2521-2536.
25. Murase, S. and Y. Yang, *Solution processed MoO3 interfacial layer for organic photovoltaics prepared by a facile synthesis method.* Adv Mater, 2012. **24**(18): p. 2459-2462.
26. Wu, J., et al., *Role of solution-processed V2O5 in P3HT:PCBM based inverted polymer solar cells.* Synthetic Metals, 2013. **170**: p. 7-10.
27. He, Z., et al., *Enhanced power-conversion efficiency in polymer solar cells using an inverted device structure.* Nature Photonics, 2012. **6**: p. 591–595.
28. Choy, W.C.H., *Organic Solar Cells.* Book, 2013.
29. BORSENBERGER, P.M. and W.T. GRUENBAUM, *Hole Trapping in Molecularly Doped Polymers.* BORSENBERGER ET AL, 1998(352).
30. Litzov, I. and C. Brabec, *Development of Efficient and Stable Inverted Bulk Heterojunction (BHJ) Solar Cells Using Different Metal Oxide Interfaces.* Materials, 2013. **6**(12): p. 5796-5820.
31. Lattante, S., *Electron and Hole Transport Layers: Their Use in Inverted Bulk Heterojunction Polymer Solar Cells.* Electronics, 2014. **3**(1): p. 132-164.
32. Meyer, J., et al., *Transition metal oxides for organic electronics: energetics, device physics and applications.* Adv Mater, 2012. **24**(40): p. 5408-5427.
33. Zhang, Y., S. Yuan, and W. Liu, *Inverted organic solar cells employing RGO/TiOx composite films as electron transport layers.* Electrochimica Acta, 2014. **143**: p. 18-22.
34. Li, X., et al., *MoOx and V2Ox as hole and electron transport layers through functionalized intercalation in normal and inverted organic optoelectronic devices.* Light: Science & Applications, 2015. **4**(4): p. 273.
35. Vasilopoulou, M., et al., *Organic photovoltaic performance improvement using atomic layer deposited ZnO electron-collecting layers.* Solid-State Electronics, 2014. **101**: p. 50-56.
36. Kondakov, D.Y., *Voltammetric study of Bphen electron-transport layer in contact with LiF／Al cathode in organic light-emitting diodes.* Journal of Applied Physics, 2006. **99**(024901).
37. Xin, Y., et al., *UV-Ozone Treatment on Cs2CO3 Interfacial Layer for the Improvement of Inverted Polymer Solar Cells.* Journal of Nanomaterials, 2013. **2013**(104825).
38. Guo, Y. and J. Robertson, *Origin of the high work function and high conductivity of MoO3.* Applied Physics Letters, 2014. **105**(22): p. 222110.
39. Hancox, I., et al., *The effect of a MoOx hole-extracting layer on the performance of organic photovoltaic cells based on small molecule planar heterojunctions.* Organic Electronics, 2010. **11**(12): p. 2019-2025.
40. Kim, H., et al., *Effects of pentacene-doped PEDOT:PSS as a hole-conducting layer on the performance characteristics of polymer photovoltaic cells.* Nanoscale Res Lett, 2012. **7**(1): p. 5.
41. Tao, C., et al., *Performance improvement of inverted polymer solar cells with different top electrodes by introducing a MoO3 buffer layer.* Applied Physics Letters, 2008. **93**(19): p. 193307.
42. Maniruzzaman, M., et al., *ITO free MoO3/Au/MoO3 structures using Al2O3 as protective barrier between MoO3 and PEDOT:PSS in organic solar cells.* Renewable Energy, 2014. **71**: p. 193-199.

43. Mattox, D.M., *Physical vapor deposition (PVD) processes.* Metal Finishing, 2001. **99**(1): p. 409-423.
44. Zhao, M., et al., *Effect of nitrogen atomic percentage on N+-bombarded MWCNTs in cytocompatibility and hemocompatibility.* Nanoscale Res Lett, 2014. **9**(1): p. 142.
45. Fu, F., et al., *Low-temperature-processed efficient semi-transparent planar perovskite solar cells for bifacial and tandem applications.* Nat Commun, 2015. **6**(8932).
46. Pardo, A. and J. Torres, *Substrate and annealing temperature effects on the crystallographic and optical properties of MoO3 thin films prepared by laser assisted evaporation.* Thin Solid Films, 2012. **520**(6): p. 1709-1717.
47. Zilberberg, K., J. Meyer, and T. Riedl, *Solution processed metal-oxides for organic electronic devices.* Journal of Materials Chemistry C, 2013. **1**(32): p. 4796.
48. Galatsis, K., et al., *Sol-Gel prepared MoO3-WO3 thin-films for O2 gas sensing.* Sensors and Actuators B, 2001. **77**: p. 478-483.
49. Meulenkamp , E.A., W.V. Klinken , and A.R. Schlatmann, *In-situ X-ray diffraction of Li intercalation in sol-gel V2O5 film.* Solid State Ionics, 1999. **126**: p. 235–244.
50. Etman, A.S., et al., *Facile Water-Based Strategy for Synthesizing MoO3−x Nanosheets:Efficient Visible Light Photocatalysts for Dye Degradation.* ACS OMEGA, 2018. **3**: p. 2201−2209.
51. Irfan, et al., *Energy level evolution of air and oxygen exposed molybdenum trioxide films.* Applied Physics Letters, 2010. **96**(24): p. 243307.
52. Irfan, et al., *Work function recovery of air exposed molybdenum oxide thin films.* Applied Physics Letters, 2012. **101**(9): p. 093305.
53. Greiner, M.T., et al., *Transition Metal Oxide Work Functions: The Influence of Cation Oxidation State and Oxygen Vacancies.* Advanced Functional Materials, 2012. **22**(21): p. 4557-4568.
54. Meyer, J., et al., *Metal oxide induced charge transfer doping and band alignment of graphene electrodes for efficient organic light emitting diodes.* Sci Rep, 2014. **4**: p. 5380.
55. Meyer, J., et al., *Electronic structure of Vanadium pentoxide: An efficient hole injector for organic electronic materials.* Journal of Applied Physics, 2011. **110**(3): p. 033710.
56. Hancox, I., et al., *Utilizing n-type vanadium oxide films as hole-extracting layers for small molecule organic photovoltaics.* Applied Physics Letters, 2011. **99**(1): p. 013304.
57. Hancox, I., et al., *Optimization of a High Work Function Solution Processed Vanadium Oxide Hole-Extracting Layer for Small Molecule and Polymer Organic Photovoltaic Cells.* The Journal of Physical Chemistry C, 2012. **117**(1): p. 49-57.
58. Hill, J.C. and K.-S. Choi, *Effect of Electrolytes on the Selectivity and Stability of n-type WO3 Photoelectrodes for Use in Solar Water Oxidation.* J. Phys. Chem. C, 2012. **116**(14): p. 7612–7620.
59. Vasilopoulou, M., et al., *Reduction of Tungsten Oxide: A Path Towards Dual Functionality Utilization for Efficient Anode and Cathode Interfacial Layers in Organic Light-Emitting Diodes.* Advanced Functional Materials, 2011. **21**(8): p. 1489-1497.
60. Chen, Y. and S. Ruan, *Highly efficient ITO-free polymer solar cells based on metal resonant microcavity using WO3/Au/WO3 as transparent electrodes.* Organic Electronics, 2014. **15**(7): p. 1545-1555.
61. White, R.T., E.S. Thibau, and Z.H. Lu, *Interface Structure of MoO3 on Organic Semiconductors.* Sci Rep, 2016. **6**: p. 21109.
62. Layton, D., *The original observations of Brownian motion.* J. Chem. Educ, 1965. **42**(7): p. 367.
63. Shire, S.J., *The molecular basis of high viscosity of monoclonal antibodies (mAbs) at high concentration.* Monoclonal Antibodies, 2015. **Chapter 2**.
64. *http://hyperphysics.phy-astr.gsu.edu/hbase/Kinetic/henry.html.*

65. Chen, L., et al., *Interface investigation and engineering – achieving high performance polymer photovoltaic devices.* Journal of Materials Chemistry, 2010. **20**(13): p. 2575.
66. Sun, Y., et al., *Efficient, air-stable bulk heterojunction polymer solar cells using MoO(x) as the anode interfacial layer.* Adv Mater, 2011. **23**(19): p. 2226-2230.
67. Hudhomme, P., *An overview of molecular acceptors for organic solar cells.* EPJ Photovoltaics, 2013. **4**: p. 40401.
68. Kim, J.Y., et al., *Analysis of Annealing Process on P3HT:PCBM-Based Polymer Solar Cells Using Optical and Impedance Spectroscopy.* Journal of Nanoscience and Nanotechnology, 2013. **13**(5): p. 3360-3364.
69. Zhang, M., et al., *Organic Schottky barrier photovoltaic cells based on MoOx/C60.* Applied Physics Letters, 2010. **96**(18): p. 183301.
70. Eisuke, I., et al., *Interfacial electronic structure of long-chain alkanermetal systems studied by UV-photoelectron and metastable atom electron spectroscopies.* Chemical Physics Letters, 1998. **287**: p. 137-142.
71. Ishii, H., et al., *Energy Level Alignment and Interficial Electronic Structures at Organic/Metal and Organic/Organic Interfaces.* Advanced Materials, 1999. **11**(8).
72. Kröger, M., et al., *Role of the deep-lying electronic states of MoO3 in the enhancement of hole-injection in organic thin films.* Applied Physics Letters, 2009. **95**(12): p. 123301.
73. Meyer, J., et al., *Charge generation layers comprising transition metal-oxide/organic interfaces: Electronic structure and charge generation mechanism.* Applied Physics Letters, 2010. **96**(19): p. 193302.
74. Greiner, M.T., et al., *Universal energy-level alignment of molecules on metal oxides.* Nat Mater, 2011. **11**(1): p. 76-81.
75. Hou, J. and X. Guo, *Active Layer Materials for Organic Solar Cells.* Book, 2013: p. 17-42.
76. Ma, H., et al., *Interface Engineering for Organic Electronics.* Advanced Functional Materials, 2010. **20**(9): p. 1371-1388.
77. Goldsmid, H.J., *The Physics of Thermoelectric Energy Conversion.* Book Chapter 4, 2017: p. 4-11.
78. Verhoeven, J.W., *Glossary of terms used in photochemistry* IUPAC 1996.
79. Greiner, M.T., et al., *Universal energy-level alignment of molecules on metal oxides.* Nature Materials, 2012. **11**(1): p. 76-81.
80. Nethercot, H.J., *Prediction of Fermi Energies and Photoelectric Thresholds Based on Electronegativity Concepts.* Phys. Rev. Lett, 1974. **3**: p. 1088.
81. Ozawa, R., et al., *Angle-resolved UPS study of the oxygen-induced 2 × 1 surface of Cu(110).* Surface Science, 1996. **346**: p. 237-242.
82. Hayashi, N., et al., *Examination of band bending at buckminsterfullerene (C60)/metal interfaces by the Kelvin probe method.* Journal of Applied Physics, 2002. **92**(7): p. 3784-3793.
83. Sharma, A., et al., *Invisible high workfunction materials on heterogeneous surfaces.* Applied Surface Science, 2015. **327**: p. 22-26.
84. Benramache, S., O. Belahssen, and H.B. Temam, *Effect of band gap energy on the electrical conductivity in doped ZnO thin film.* Journal of Semiconductors, 2014. **35**(7).
85. Braun, S., W.R. Salaneck, and M. Fahlman, *Energy-Level Alignment at Organic/Metal and Organic/Organic Interfaces.* Advanced Materials, 2009. **21**(14-15): p. 1450-1472.
86. Augusto, A., et al., *Analysis of the recombination mechanisms of a silicon solar cell with low bandgap-voltage offset.* Journal of Applied Physics, 2017. **121**(205704).
87. kazuhiko, S., et al., *Organic/Metal systems studied by electron spectroscopies and other techniques.* Synthetic Metals, 2001. **119**: p. 19-24.

88. Wang, H.-Q., et al., *Nanocrystal V2O5 thin film as hole-extraction layer in normal architecture organic solar cells.* Organic Electronics, 2012. **13**(12): p. 3014-3021.
89. Park, S., et al., *The origin of high PCE in PTB7 based photovoltaics: proper charge neutrality level and free energy of charge separation at PTB7/PC71BM interface.* Sci Rep, 2016. **6**: p. 35262.
90. MORII, K., et al., *Enhanced Hole Injection in a Hybrid Organic–Inorganic Light-Emitting Diode.* Japanese Journal of Applied Physics, 2008. **47**(9): p. 7366–7368.
91. Hancox, I., et al., *Increased efficiency of small molecule photovoltaic cells by insertion of a MoO3hole-extracting layer.* Energy Environ. Sci., 2010. **3**(1): p. 107-110.
92. Irfan, et al., *Strong interface p-doping and band bending in C60 on MoOx.* Organic Electronics, 2011. **12**(9): p. 1588-1593.
93. Hamwi, S., et al., *p-type doping efficiency of MoO3 in organic hole transport materials.* Applied Physics Letters, 2009. **94**(25): p. 253307.
94. Nakayama, Y., et al., *Origins of Improved Hole-Injection Efficiency by the Deposition of MoO3on the Polymeric Semiconductor Poly(dioctylfluorene-alt-benzothiadiazole).* Advanced Functional Materials, 2009. **19**(23): p. 3746-3752.
95. Meyer, J. and A. Kahn, *Electronic structure of molybdenum-oxide films and associated charge injection mechanisms in organic devices.* Journal of Photonics for Energy, 2011. **1**(1): p. 011109.
96. Kohler, A., *Organic semiconductors: No more breaks for electrons.* Nat Mater, 2012. **11**(10): p. 836-837.
97. Grasselli, F., A. Bertoni, and G. Goldoni, *Exact two-body quantum dynamics of an electron-hole pair in semiconductor coupled quantum wells: a time-dependent approach.* Phys.Rev.B, 2016. **93**: p. 195310.
98. Hoff, D.A., R.d. Silva, and L.G.C. Rego, *Coupled Electron–Hole Quantum Dynamics on D–π–A Dye-Sensitized TiO2 Semiconductors.* J. Phys. Chem. C, 2012. **116**(40): p. 21169–21178.
99. Wang, C., et al., *Role of molybdenum oxide for organic electronics: Surface analytical studies.* Journal of Vacuum Science & Technology B, Nanotechnology and Microelectronics: Materials, Processing, Measurement, and Phenomena, 2014. **32**(4): p. 040801.
100. Talman, R., *The Electric Dipole Moment Challenge.* Book, 2017.
101. Debye, P., *The Dipole Moment And Chemical Structure.* Book, 1931.
102. Gross, L. and C. Herrmann, *Local electric dipole moments: A generalized approach.* J Comput Chem, 2016. **37**(25): p. 2260-2265.
103. Allahyarov, E., H. Lowen, and L. Zhu, *Dipole correlation effects on the local field and the effective dielectric constant in composite dielectrics containing high-k inclusions.* Phys Chem Chem Phys, 2016. **18**(28): p. 19103-19117.
104. Hirose, K., et al., *First-Principles Calculations in Real-Space Formalism.* Book, 2005: p. 18.
105. Dugdale, D.E., *Essentials of Electromagnetism.* Book, 1993: p. 80–81.
106. Hu, Z., et al., *Dipole formation at organic/metal interfaces with pre-deposited and post-deposited metal.* NPG Asia Materials, 2017. **9**(5): p. 379.
107. Yin, Y., et al., *Dipole Formation at the MoO3/Conjugated Polymer Interface.* Advanced Functional Materials, 2018. **28**(46): p. 1802825-1802835.
108. Berlich, A., Y. Liu, and H. Morgner, *Growth of nickel nanoparticles on NiO/Ni(001): Evidence of adsorbed oxygen on metal particles by metastable induced electron spectroscopy (MIES).* Surface Science, 2008. **602**(24): p. 3737-3744.
109. Berlich, A., Y.C. Liu, and H. Morgner, *Evaporation of Ni and carbon containing species onto NiO/Ni as case study for metal support catalysts investigated by Metastable Induced Electron Spectroscopy (MIES).* Radiation Physics and Chemistry, 2005. **74**(3-4): p. 201-209.

110. Kröger, M., et al., *Role of the deep-lying electronic states of MoO3 in the enhancement of hole-injection in organic thin films.* Applied Physics Letters, 2009. **95**(12): p. 123301.
111. Meyer, J., *Electronic structure of molybdenum-oxide films and associated charge injection mechanisms in organic devices.* Journal of Photonics for Energy, 2011. **1**(1): p. 011109.
112. Yi, Y., et al., *The interface state assisted charge transport at the MoO(3)/metal interface.* J Chem Phys, 2009. **130**(9): p. 094704.
113. Meyer, J., et al., *Charge generation layers comprising transition metal-oxide/organic interfaces: Electronic structure and charge generation mechanism.* Applied Physics Letters, 2010. **96**(19): p. 193302.
114. Zhao, Y., et al., *Poly(3,4-ethylenedioxythiophene):poly(styrenesulfonate)/MoO3 composite layer for efficient and stable hole injection in organic semiconductors.* Journal of Applied Physics, 2012. **111**(4): p. 043716.
115. Wu, Q.-H., et al., *Electronic structure of MoO3−x/graphene interface.* Carbon, 2013. **65**: p. 46-52.
116. Steim, R., F.R. Kogler, and C.J. Brabec, *Interface materials for organic solar cells.* Journal of Materials Chemistry, 2010. **20**(13): p. 2499.
117. Baek, W.H., et al., *Effect of P3HT:PCBM concentration in solvent on performances of organic solar cells.* Solar Energy Materials and Solar Cells, 2009. **93**(8): p. 1263-1267.
118. Papaefthimiou, S., G. Leftheriotis, and P. Yianoulis, *Study of electrochromic cells incorporating WO3, MoO3, WO3-MoO3 and V2O5 coatings.* Thin Solid Films, 1999. **343–344**: p. 183-186.
119. Galatsis, K., et al., *Sol-Gel prepared MoO3-Wo3 thin-films for O2 gas sensing.* Sensors and Actuators B, 2001. **77**: p. 478-483.
120. Chen, C.C., et al., *An efficient triple-junction polymer solar cell having a power conversion efficiency exceeding 11%.* Adv Mater, 2014. **26**(32): p. 5670-5677.
121. Ho, P., et al., *The effects of MoO3 treatment on inverted PBDTTT-C:PC71BM solar cells.* Solar Energy Materials and Solar Cells, 2013. **119**: p. 235-240.
122. Fu, Q., et al., *Room-temperature sol-gel derived molybdenum oxide thin films for efficient and stable solution-processed organic light-emitting diodes.* ACS Appl Mater Interfaces, 2013. **5**(13): p. 6024-6029.
123. Rempel, K.U., A.A. Migdisov, and A.E. Williams-Jones, *The solubility and speciation of molybdenum in water vapour at elevated temperatures and pressures: Implications for ore genesis.* Geochimica et Cosmochimica Acta, 2006. **70**(3): p. 687-696.
124. Chang, W., et al., *Post-deposition annealing control of phase and texture for the sputtered MoO3 films.* CrystEngComm, 2011. **13**(16): p. 5125.
125. Ng, A., et al., *Annealing of P3HT:PCBM blend film--the effect on its optical properties.* ACS Appl Mater Interfaces, 2013. **5**(10): p. 4247-4259.
126. Lu, Y., et al., *Temperature-dependent morphology evolution of P3HT:PCBM blend solar cells during annealing processes.* Synthetic Metals, 2012. **162**(23): p. 2039-2046.
127. Holmes, N.P., et al., *Nano-pathways: Bridging the divide between water-processable nanoparticulate and bulk heterojunction organic photovoltaics.* Nano Energy, 2016. **19**: p. 495-510.
128. Gartner, S., et al., *Eco-friendly fabrication of 4% efficient organic solar cells from surfactant-free P3HT:ICBA nanoparticle dispersions.* Adv Mater, 2014. **26**(38): p. 6653-6657.
129. Pan, X., et al., *Environmentally friendly preparation of nanoparticles for organic photovoltaics.* Organic Electronics, 2018. **59**: p. 432-440.
130. Dhanasankar, M., K.K. Purushothaman, and G. Muralidharan, *Effect of temperature of annealing on optical, structural and electrochromic properties of sol–gel dip coated molybdenum oxide films.* Applied Surface Science, 2011. **257**(6): p. 2074-2079.

131. Abramavicius, V., et al., *Carrier motion in as-spun and annealed P3HT:PCBM blends revealed by ultrafast optical electric field probing and Monte Carlo simulations.* Phys Chem Chem Phys, 2014. **16**(6): p. 2686-2692.
132. Abbas, M. and N. Tekin, *Balanced charge carrier mobilities in bulk heterojunction organic solar cells.* Applied Physics Letters, 2012. **101**(7): p. 073302.
133. Xiang, D., et al., *Gap states assisted MoO3 nanobelt photodetector with wide spectrum response.* Sci Rep, 2014. **4**: p. 4891.
134. Yang, Q., et al., *The improved performance of solution-processed SQ:PC71BM photovoltaic devices via MoO3 as the anode modification layer.* Applied Surface Science, 2013. **284**: p. 849-854.
135. Sharma, A., et al., *Unravelling the Thermomechanical Properties of Bulk Heterojunction Blends in Polymer Solar Cells.* Macromolecules, 2017. **50**(8): p. 3347-3354.
136. Xu, X., et al., *High efficient inverted polymer solar cells with different annealing treatment.* Materials Science and Engineering: C, 2012. **32**(4): p. 685-691.

Chapter 2. Methodology

2.1. Experimental Instruments

The incident photon energy (hU) of all photoelectron spectroscopy applied in this work follows a relationship of the kinetic energy ($K.E$), the binding energy ($B.E$) and WF of the spectrometer (ϕsp), which is described in following equation. Where ϕsp (4.15eV) is calibrated with a graphite calibration sample.

$$K.E = hv - B.E - \phi sp \qquad \text{Equation 2-1}$$

The non-monochromatic multiple-photoelectron spectroscopy shares a similar photon in-electron out mechanism: a) Photons are absorbed from the radiation and thus momentum conserving electrons transition vertically between an occupied and unoccupied state; b) Subsequently, electrons migrate to sample surface and then escape from the sample; c) The escaped electrons pass through the lens and energy filter and thus electrons with given energy can be amplified by the channeltrons and reordered by detector channel plates.

The multiply spectroscopy is performed under an ultrahigh vacuum (UHV) chamber with an essential pressure of a few 10^{-10} mbar. The deposition chamber was kept in high vacuum (HV) and samples deposited with metal oxides can be directly transferred to the analysis chamber to avoid exposure and contamination. Thus, the sample properties are considerably close to their pristine forms. The schematic of the insitu-deposition and spectroscopy apparatus are shown in Figure 2-1. The probing depths of the spectroscopies are illustrated.

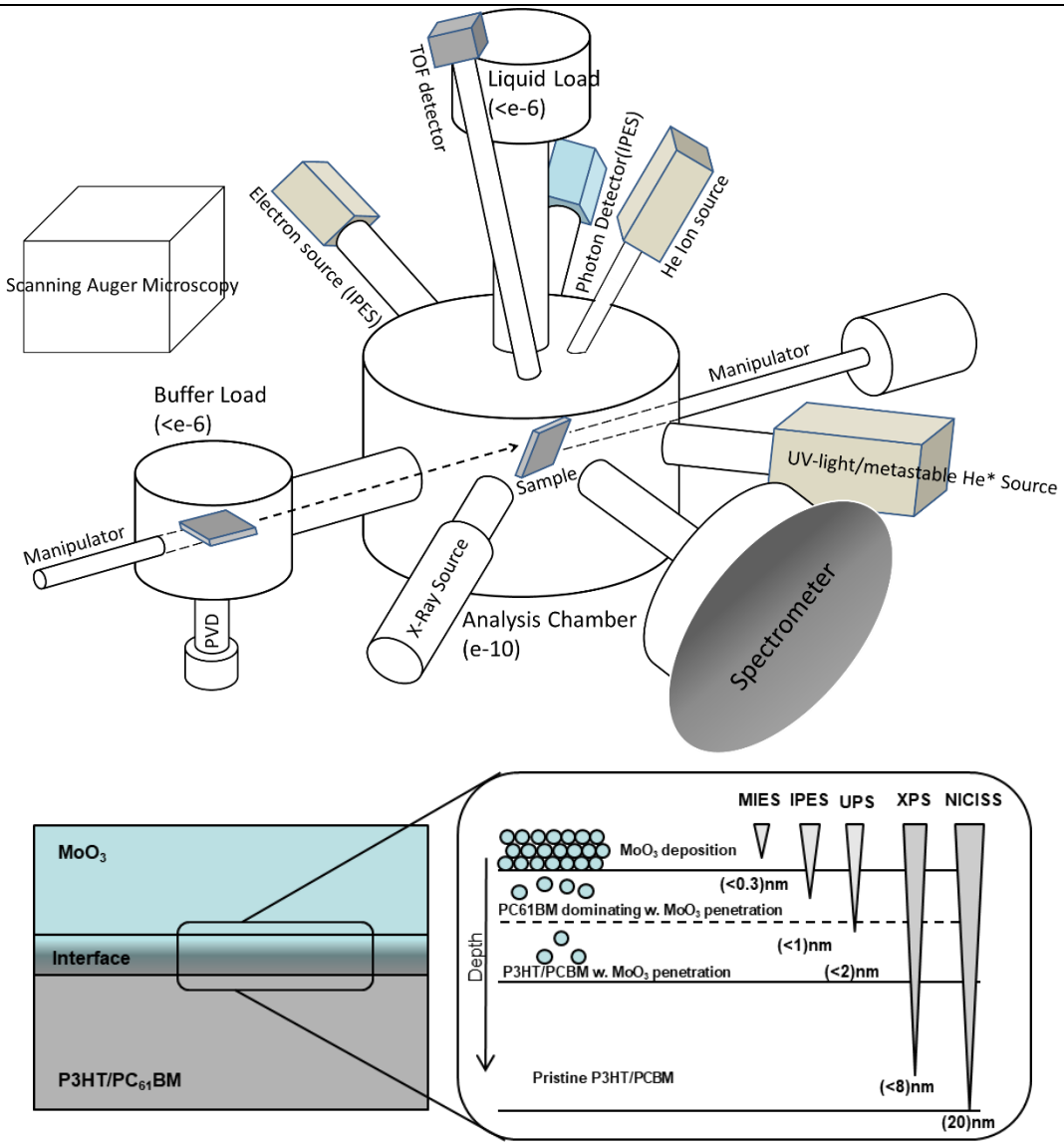

Figure 2- 1. The schematic of the insitu-evaporator and multi-spectroscopy, the SAM is excluded but the samples made are transferred to SAM in short time; The probing depth of spectroscopies is illustrated, the pressure indicated here has a unit of mbar.

2.1.1. X-Ray Photoelectron Spectroscopy (XPS)[1, 2]

The XPS spectra are acquired using an UHV apparatus provided by SPECS (Berlin). An UHV no-monochromatic X-ray source (12kV-200 W) with Mg anode was used for the measurements. Electrons are first emitted with Thoria-coated Tungsten filaments, which are accelerated onto anode, generating X-ray emission. Consequently, X-ray passes through vacuum tube and projects on sample surface. The intense photon of X-ray excites the electron from inner shell core level (S, P electronic orbits, etc) due to the excitation energy (1153.6eV for Mg anode) of

sample, which is illustrated in Figure 2-1, causing the transition of photoelectron across the whole energy bands. The nature of electron excitation energy thus can be used for identifying the sample elements and binding form [3] and the relative composition constituents within certain depth can also be quantified. Given the electron energy loss [4], the intensity of electron attenuated in the bulk is given by:

$$I\,(E,\alpha,d) = Io\exp(-\frac{d}{\cos(\theta).\lambda(E)}) \qquad \text{Equation 2-2}$$

d : The measuring depth

θ : The angle between the direction to the detector and the surface normal

$\lambda(E))$: the electron mean free path [5]

Io : The maximum intensity (at outermost surface)

Besides, the angle between the X-ray irradiation and the analyser is 54 °. Survey scans were processed with a pass energy of 40eV while high-resolution scans at a pass energy of 10 eV were recorded. A typical XPS survey scan of V_2O_5 on P3HT:PCBM BHJ is shown in Figure 2-2.

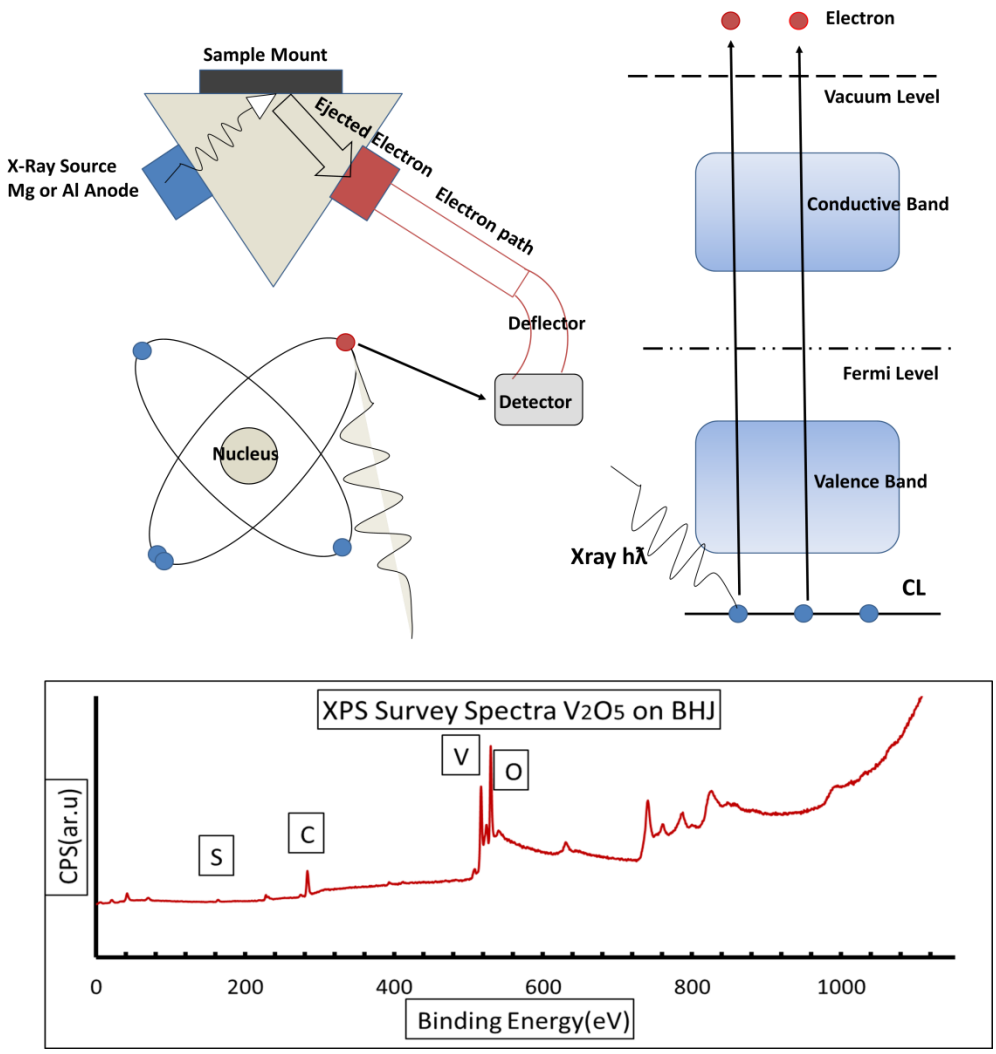

Figure 2- 2. The excitation of X-ray photoelectron from elemental core level and the XPS Survey scan of a V_2O_5/BHJ sample

The XPS can also be used for determining valence electron states[6] and WF of the samples. However, there are several drawbacks: a) The core-hole lifetime broadening results in a high uncertainty of the measured arbitrary counts precision, which is described with Heisenberg's uncertainty principle; b) The momentum of x-ray photons is higher by order of magnitude than that of electrons thus it generates relatively-high background noise; c) The X-ray radiation leads to a disparity in the cross-section[7], thus the valence electron states and calculated density of states (DOS) are not in agreement. For the purpose of acquiring valence and secondary-electron states of a sample with a decent resolution, the Photoelectron Spectroscopy using UV-light is introduced.

2.1.2. Ultra-violet Photoelectron Spectroscopy and Metastable Impact Electron Spectroscopy (UPS and MIES)

The HeI UV light and metastable helium atoms (He*$3S_1$) are simultaneously emitted by a cold cathode two-stage discharger (MFS, Clausthal-Zellerfeld, Germany) and separated by a chopper. A bias voltage of 10V has been imposed on sample stage for collecting UP and MIE spectra. Comparing with UPS, from which, the spectrum consists of emitting electrons from a depth of up to ~ 3nm, the MIES only observes outermost layer due to the surface sensitive probing. The excitation energy of He I UV radiation is 21.218 eV while it is 19.218 eV for MIES. The technique bases on a single photon generating electron process. In contrast to XPS, the advantage of applying UV radiation is the controllable narrow line width. Under UV radiation electrons are ionised from the valence levels, electrons do not undergo inelastic scattering within the material are primary photoelectrons, which construct the valence region and illustrate Density of States (DOS) [8], leading to the definition of the energy of valence band (E_{VB}) or highest occupied molecular orbital (E_{HOMO}). Those undergo-inelastic scattering when transiting in-between components are called secondary electrons [9], which are superimposed with the distinct features from primary electrons. The onset of secondary electron peak can be used for determining WF/ϕ. Figure 2-3 shows the typical UP spectrum and the definition of electrical parameters. It is important to emphasise that the determination of WF is related to the dipole at the surface of a sample. This dipole is established due to the E_f alignment with the detector analyser.

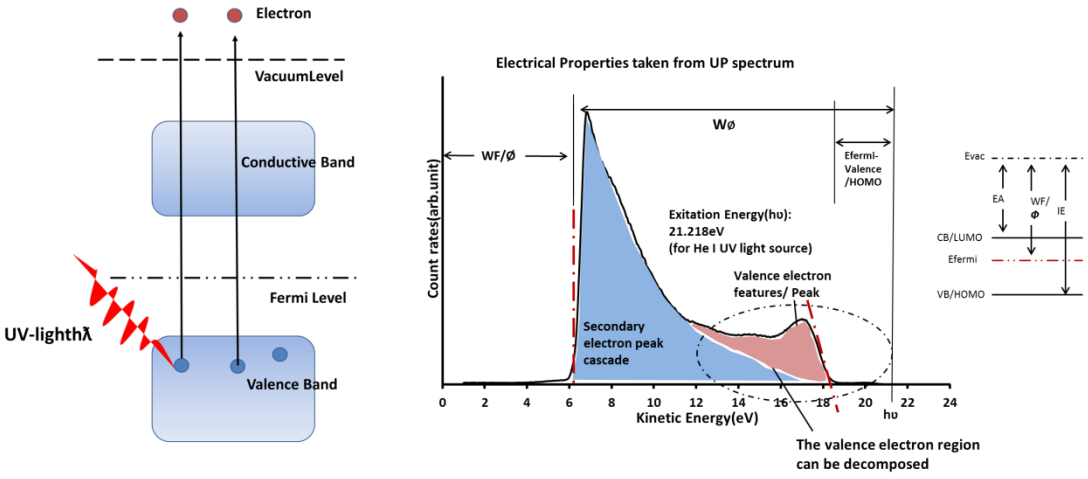

Figure 2- 3. The excitation of photoelectron from valence level and the parameters collected

from UP spectrum

He* atom ($1s2s^3S_1$) has an excitation energy of 19.818 eV which is employed for metastable induced source. The performance of He* when ejected to a sample surface consists of three major mechanisms [10]. The interaction of metastable He* is based either on the combination of the processed resonant ionisation (RI) and Auger neutralisation (AN) or based on the Auger de-excitation (AD) process. For instance, the AD process normally happens at surfaces, which have a band gap and are semiconducting. Given that, an electron from the sample can tunnel into the He 1s level. The energy difference transfers to the He 2s and subsequently an electron is emitted. RI and AN processes take place at surfaces with valence electron density close to the Fermi level which typically is given for metal surfaces. The He* 2s electron tunnels into the valence states of a sample due to the low band gap by resonance ionising [11], releasing a positive He ion. Therefore, an electron from the sample surface fills the He 1s orbital and neutralises the positive ion. Energy difference occurs during the procedure, which is from the energy level of electron filling He 1s and the level of another electron where the He 1s is transferred (sample surface). A following electron is then emitted for the ionisation and neutralisation circle. MIES characterises the energy shifts over valence region within approximately 0.2nm depth[12, 13], which is used to observe the TMO formation on the top surface and identify the surface coverage. The features of spectra acquired using AD process are relatively sharp. In the work, the AD process dominates both the P3HT:$PC_{61}M$/TQ1:$PC_{71}BM$ BHJ as well as the TMOs surfaces.

2.1.3. Neutral Impact Collision Ion Scattering Spectroscopy (NICISS) [14, 15]

The illustration of NICISS shows in Figure 2-4, which is applied to obtain the concentration depth profiles of the elements at a soft-matter surface with a maximum depth of 20nm and a depth resolution of a few Å close to the surface. In this research, we aim to identify the distributions and penetrations of MoO_3, V_2O_5, and WO_3 into a polymer BHJ bulk and the regions of mixing chemical phase.

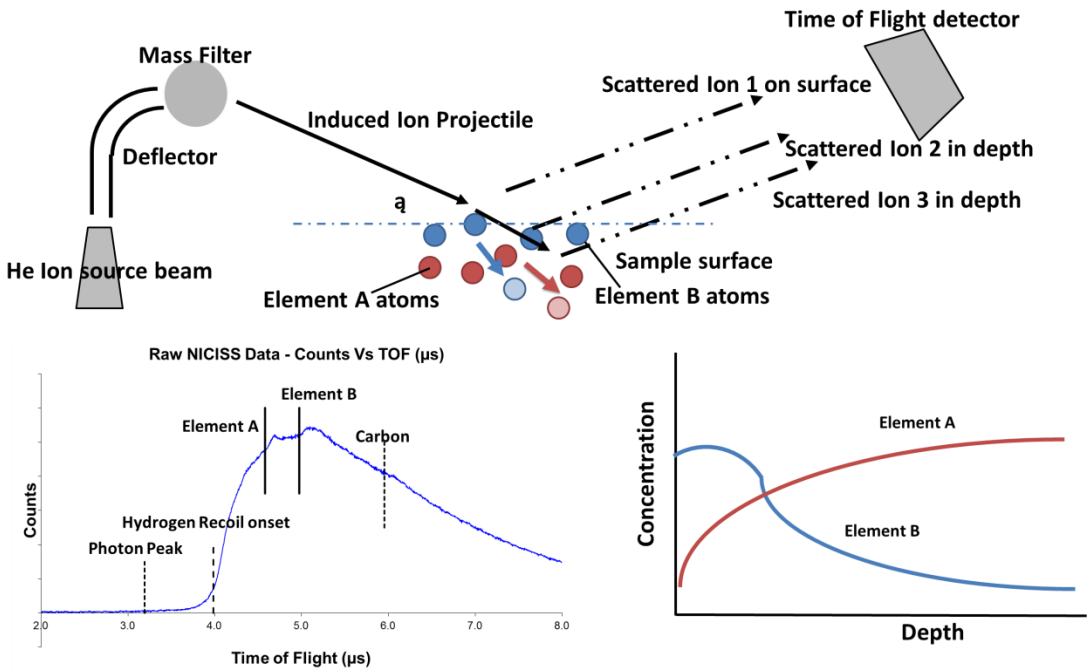

Figure 2- 4. The diagram of NICISS operation; the raw NICISS spectrum and the extraction of depth profile

Helium ions in a pulsed beam with a few K eV kinetic energy are directed onto a sample. The kinetic energy of scattered projectiles is determined by their time of flight (TOF) from the target to the detector. The energy loss of the projectiles occurs due to backscattering and the target atom mass determines the energy transfer, which can be used for distinguishing the elements forming the sample from the peak position on TOF scale. Because of the energy loss caused by small-angle-scattering and electronic excitations (stopping power [16]) on the trajectory of the projectiles when passing through the sample is used to determine the depth, that the projectile is backscattered. The combination of the two types of energy loss is used to determine the elemental concentration depth profiles. In a NICISS measurement the dose is kept below $5 \cdot 10^{13}$ ions/cm^2 in order to avoid damage of the sample due to sputtering. The analysis of depth profile of certain components contains the identification of elements on scale, which needs to be extracted from Hydrogen recoil background first and the calibration of depth from TOF scale. A typical conversion of spectrum of NICISS from energy loss spectrum is shown in Figure 2-4. In the present work the zero mark of the depth scale has not been calibrated as in report[17] but rather calculated from the TOF length and energy of the incident He ion. The accuracy of the position of the zero mark of the depth scale thus is not as good as reported[17] but sufficient

for the work. Subsequently the relative concentration is derived from NICISS spectra as a function of dual x-axis (energy loss and depth).

2.1.4. Inverse Photoelectron Spectroscopy (IPES) [18, 19]

The technique bases on an inverted mechanism of photoelectron emission. From which, the electrons with well-defined energy are directed by a BaO filament electron gun onto the sample surface and the energy relates to the equilibrated Fermi level of sample components. The electrons directly transit into the unoccupied states below kinetic energy once imprinted on the sample and synchronously recombination takes place that releases the photons. The photons are consequently detected by a Geiger-Mueller [20] isochromatic tube detector, which is operated in isochromatic detecting mode with a UV band pass energy of 10eV. The tube is filled with a mixing gas ambient of Ar and Acetone while the latter is used for ionising gas, which is thus ionised by incident photon radiation. The flux of Acetone ions is thus recorded and converted to incident photons flux. Which is further processed as a function of the kinetic energy (K.E) of the electron beam. Finally, a record of unoccupied states of a sample can be achieved. By approximating energy peak onset, the energy of conduction band (E_{CB}) or lowest unoccupied molecular orbital (E_{LUMO}) can be identified and the details will be described later. The states below Fermi level are inaccessible for IPES (no emission of photons). Thus, by combining the insitu-UPS and IPES, a complete energy band structure of the samples containing WF, E_{VB}/E_{HOMO} and E_{CB}/E_{LUMO} is illustrated. Moreover, it is worthwhile to note that the duration of radiation of the electron gun towards a sample surface has to be limited. The reason is due to the flux of low kinetic energy electrons from the source, which can easily cause the molecular resonance of a sample surface, especially on organics. Thus, the sample composition can be destructed.

2.1.5. Scanning Auger Microscopy (SAM)

The technique combines Scanning Electron Microscopy (SEM) [21, 22] and Auger Electron Spectroscopy (AES) [23, 24]. SEM provides the visual analysis over the sample surface, which has been used for determining the surface coverage with evaporated amount of metal oxides, observing the layer forming in this work. A beam of electrons is generated in an electron column at the initial stage by metal emission filament and then induced onto the sample surface.

The incident beam focus can be controlled by an array of electromagnetic lens, which scans over the surface in a pattern and images as raster graphics with required resolution. Emitted electrons from target are collected by the electron detector with the information of each position. To clarify the digital image, the signal of displayable brightness actually indicates the intensity of the elections over the scanning range, which is changeable across variation of surface topography. The insitu-AES then assists to identify the elemental information within the pointed range in a SEM image. Auger process[23] has been initiated by creating of a core hole with high-energy electron beam (2-10K eV). The ionised atom after the removal of core hole electron immediately relaxes back to a lower energy state from higher excited state. Thus, the energy liberated in the process is transferred to a second electron, which allows overpassing the binding energy of the second electron. The emitted Auger electron retains the reminder as kinetic energy, which has been measured for composing spectra. By combining SEM and AES, a mapping identification of elements over the ranged surface can achieved.

2.2. Fabrication Methods

2.2.1. Spin-Coating

Spin-coating process is a cost-effective method to establish a uniform think layer of nanoparticles on a substrate. The process has been commonly used in fabricating experimental-scale polymer solar cells and other organic devices[25]. The schematic of spin-coating process is shown in Figure 2-5. The substrate (Si in our work) is held on a vacuum plate by a rotary or scroll pump. The solution is then dispensed onto the substrate surface by a pipette. Subsequently the rotation of plate is accelerated and forms certain rotating speed (up to 3000 round/min). By which, the solution distributes and comes across the surface due to the centripetal forces. The solution is left on the substrate for approximately 2min for evaporating the solvent used in the work. The samples are then sent to oven for further removing the solvent residue. Thus, a uniform thin film coating the whole substrate is left. The rotating speed, accelerating speed and rotating duration have been carefully optimised, so that the required uniformity and thickness of the layer can be achieved.

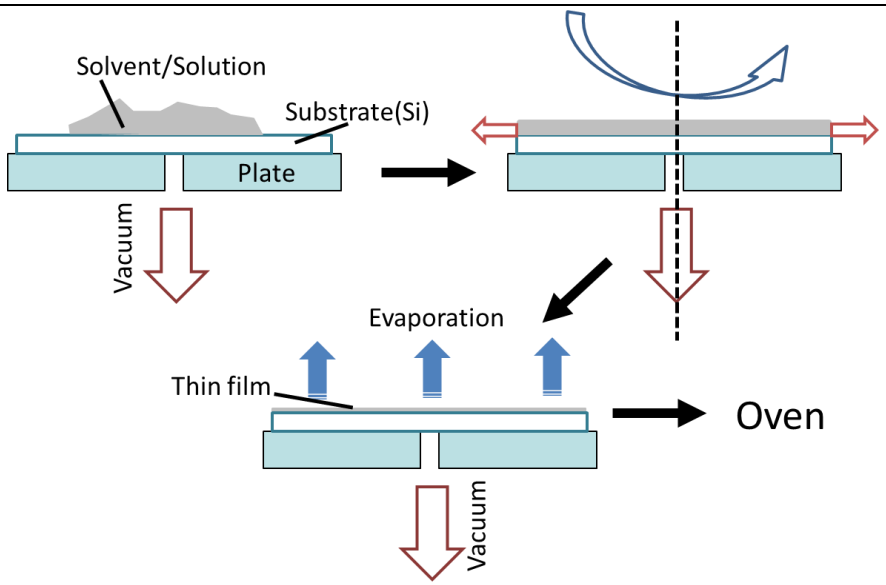

Figure 2- 5. Schematic of the spin-coating process to form a thin layer film

2.2.2. Physical Vapour Deposition (PVD)

The physical vapour deposition[26] has been employed in the work for depositing metal oxides and electrode materials, which has been widely used to deposit such materials during the fabrication of organic devices. The method has been proceeded in high vacuum (<e^{-6} mbar) with a thermal source up to 1500^{o} C and a crucible containing evaporating materials. The deposition is performed by a process[27], which changes the materials from a condensed phase to a vapour phase first. The symbol of phase change arises that the out-gassing of vapour chase has significantly increased the pressure (up to $2e^{-6}$). The condition of out-gas has been held for 10min before opening the target shutter for a constant pressure and deposition rate of the materials. The vapour-phased atoms hit the substrate surface and thus deposited in their condensed phase. A thin film is thus achieved and the thickness of the film is controlled by the deposition rate, duration, conduct angle and the distance from the target substrate. Each material has a certain vapour pressure under given temperate. The film thickness is monitored by a Quartz Crystal Microbalance (QCM), which is based on piezoelectricity phenomenon of a quartz. A resonator crystal is biased first, thus a frequency of shearing deformation has been recorded. By depositing certain materials with a given amount, the resonance frequency stiffens and shifts, resulting in a change of the resistance of the resonator. The change has been recorded which is proportionate to the mass dissipation. It needs to point out that the deposited layer,

however, does not necessarily form a layer of even thickness because of the random distribution of particles and the measuring mechanism of QCM. The QCM only monitors the accumulated mass, rather than a uniformly distributed film. The difference of actual thickness and the measured one is important due to the formation of metal oxide layers in this work does not completely cover the surface with minor deposition thickness. The QCM technique is based on a linear relationship between the frequency shift and the mass change. The formula is given by:

$$\Delta f = -\frac{2 f_0^2}{A\sqrt{\mu_q \rho_q}} \Delta m = -S_f \Delta m \qquad \text{Equation 2-3}$$

Δf : Frequency shift

f_0^2 : Base frequency

A : Area of the surface

μ_q : Shear modulus

ρ_q : Density of quartz crystal

S_f : Integral mass sensitivity

Δm : Mass shift/change

2.3. Characterisation of Energy Bands and Mathematical Algorithm for Data Evaluation

2.3.1. Characterisation of Energy Band Properties

In order to determine the WF, the secondary electron cut-off of the UP spectra have been deconvoluted individually with a Gaussian function reflecting the energy resolution of the electrostatic energy analyser which is explained in detail in reference[28] and a Fermi distribution function describing the occupation of electron energy state [29]. The deconvolution

follows given formula below:

$$I(E) = \int_0^E \frac{1}{e^{(E-Ef)/kT} + 1} \times \frac{1}{\sqrt{2\pi\sigma}} e^{\frac{-(e-\mu)^2}{2\sigma^2}} d(E) \qquad \text{Equation 2-4}$$

$I(E)$: The measured spectrum

E : The value on energy scale

kT : A product of Boltzmann constant and absolute temperature T(K)

σ : The Gaussian width, which is related to the analyser resolution, which has been determined[28].

μ : The Gaussian distribution centre (on energy scale)

Subsequent to the deconvolution the cut-off was fitted with a linear function. The energy at the intersection of the linear function with the energy axis is taken as the WF of the individual sample.

The E_{CB} and lowest unoccupied molecular orbital (E_{LUMO}) can be determined by approximating the base line and the onset of peak of IPE spectrum with a linear curve and determining their intersections [18]. The same procedure can be allied for determining the energy of valence band (E_{VB}) and highest occupied molecular orbital (E_{HOMO}) in UPS [30]. The energy difference between E_{CB}/E_{LUMO} and E_{VB}/E_{HOMO} can be taken as energy of band gap (E_g). The calculation of E_g is given by:

$$E_{CB} + E_{VB} = E_g \qquad \text{Equation 2-5}$$

$$E_{LUMO} + E_{HOMO} = E_g$$

The E_{CB} and E_{LUMO} are originally negative on the energy scale thus an absolute value is needed. It is to be noted the E_{VB}/E_{CB}, E_{LUMO}/E_{HOMO} represent the energy difference from the Fermi level, not from the vacuum level.

2.3.2. Decomposition of UP/MIE Spectra: Singular Value Decomposition(SVD)

The samples investigated here are composed of various components. The valence electron

region of measured UP and MIE spectra can be considered as a linear combination of the spectra due to the presence of the individual components, which illustrates as component X, Y and Z in Figure 2-6 for example. To analyse and identify the constituents, we apply the method Singular Value Decomposition (SVD) [31-33] that is explained here.

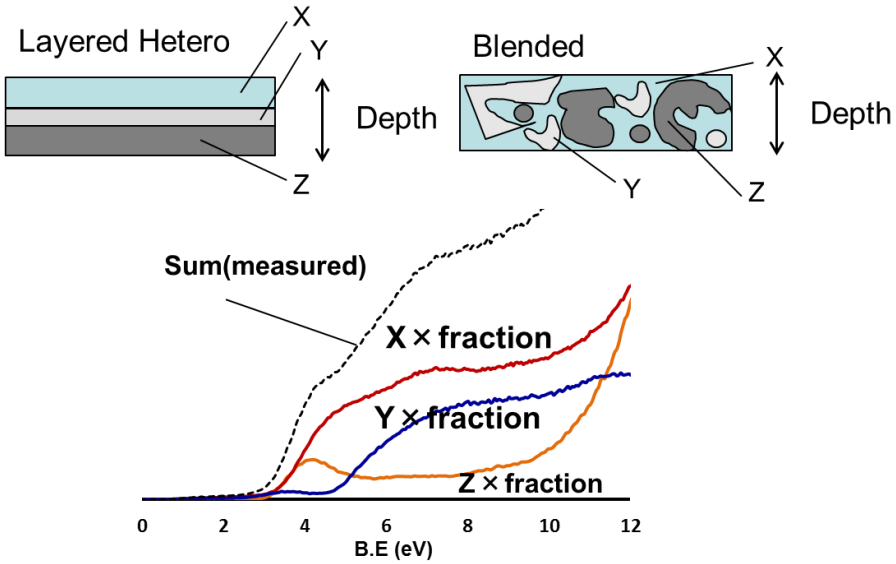

Figure 2- 6. Linear combination of various spectra from components, showing as measured one in MIES/UPS

The series of UP and MIE spectra of samples with a gradual change, e.g. gradual increase of TMO evaporation amount on BHJ, can be considered as a matrix. In the first step of SVD the dimension of these matrices are analysed which means determining how many base spectra are required to reconstruct the series of measured spectra. This analysis results not only in the number of base spectra required for reconstruction but also yields the base spectra. The base spectra are not necessarily representing physical meaningful reference spectra but have only a mathematical meaning. As an example, the base spectra could be negative which has no meaning for measured spectra. In a second matrix operation, the base spectra are converted into meaningful reference spectra. This second operation is not a mathematically rigorous procedure. The operation is applied with the boundary condition that the resulting reference spectra are non-negative and that the set of measured spectra has to be fitted by

$$S^{i}_{meas} = \sum_{j} a_j^{(i)} \times S_{ref,j} \qquad \text{with} \qquad \sum_{j} a_j^{(i)} = 1 \qquad \text{Equation 2-6 (A)}$$

$S_{meas}^{(i)}$: The measured spectrum i

$S_{ref,j}$: The j[th] reference spectrum and

$a_j^{(i)}$: The weighting factors used in the fitting procedure

The sum of the weighting factors has to be unity within experimental uncertainty, but an error of about 0.1 for $\sum_j a_j^{(i)}$ is acceptable. SVD method offers a sight into the hidden spectra $S_{ref,j}$ which constitute the measured ones. Besides, the weighting factors of $S_{ref,j}$ is achievable. Here we define the series of measured spectra as initial matrix (S)-an x × y matrix with a rank of r, which follows a matrix conversion:

$$S = U \times W \times V^T \qquad \text{Equation 2-6 (B)}$$

U: orthogonal m × n matrix

W: r × r diagonal matrix, contains the square roots of eigenvalues from U or V in descending order

V: square n × n matrix

Operation of this mathematical matrix conversion allows a deconvolution of content covering a variety of constituent data set, converting the correlated variables into uncorrelated ones. The singularity of the maximum variation can be determined while identification of dimensions can be achieved. The measured spectra are thus transformed to a linear combination of base spectra. Here S indicates a column vectors with rows defined as energy channel (En). Further analysis can be performed:

$$S_{ni} = A_i(E_n) \qquad \text{Equation 2-6 (C)}$$

n: number of channels in the spectra A_i

E_n: energy related to channel n

The base spectra Bi can be obtained through an operation:

$$B_i(E_n) = U_i(E_n) \times w_i \qquad \text{Equation 2-6 (D)}$$

The conversion the Bi to a series of meaning spectra S'_i shows below:

$$S'_i(E_n) = \sum_{k=1}^{I'} B_k(E_n) v_{ki}^T \qquad \text{with I'} \leq \text{I} \qquad \text{Equation 2-6 (E)}$$

Here S'_i represents the reference spectra indicating a variation of components. Thus, we are capable of identifying the change of compositions and their proportions across a variation of sample. Nevertheless, the limits of SVD method processing the spectra needs to be pointed out that it only distinguishes a reference spectrum of average shifting energy on the X-axis (energy scale) when one of reference spectra keep shifting across variation of energy. To achieve a complete energy band diagram containing energy bands with quantified energy shift, we will apply Weighted Shifting Method for the decomposition of the spectra.

2.3.3. Decomposition of UP/MIE Spectra: Weighted Shifting Method (WSM)

The application of Weighted Shifting Method (WSM) [34] is based on the evidence of the occurrence of spectra with energy shift, which fits the analysis of interfacial dipoles. The existence of shifting spectra caused by dipole can be determined by initialising SVD upon the spectra set where the treated metal oxides can be identified as well in this work. A TMO/polymer BHJ interface in the method consists of several base spectra that can be fitted as linear combination, which result in the measured spectra: a) The pristine polymer BHJ spectrum which shows no shift on energy scale ; b) The spectrum of a pristine TMO with enough thickness deposited onto the substrate; c) The spectrum of treated (e.g. exposed and heated) TMO; d) A set of spectra by the shape of the pristine BHJ but shifted on the binding energy scale by using the equation:

$$S^i_{meas} = \sum_{j=0}^{n} a^i_j \times S_{BHJ}(E + j \cdot \Delta E) + b \cdot S_{MTO} + c \cdot S_{t-MTO} \quad \text{with} \quad \sum_j a^i_j + b + c = 1 \qquad \text{Equation 2-7}$$

$$\Delta E^i_{mean} = \sum_{j=0}^{n} a^i_j \cdot j \cdot \Delta E$$

S^i_{meas}: The measured spectrum i,

S_{BHJ} : The spectrum of the pristine BHJ layer

S_{MTO} : The spectrum of pristine TMO

S_{t-MTO} : The spectrum of treated TMO

a_j^i, b, c : The weighting factors used in the fitting procedure

ΔE^i_{mean} : The mean shift for spectrum

ΔE : The stepwise shifting energy (0.1eV)

j : The energy steps

The sum of the weighting factors has to be unity within experimental uncertainty, but an error of about 0.1 for $\sum_j a_j^i + b + C$ is considered acceptable. However, in the case of the MIE spectra the sum of the weighting factors differs from unity by more than 0.1. The reason for this finding is that the He* can be easily redirected by electric fields originating from lateral potential differences at the sample surface, which will be discussed below in more detail. For MIES normalisation is required here.

2.3.4. Normalisation of UP/MIE Spectra and XPS Relative Concentration

It has been noted that the weighting factor for the reference spectra had to be normalised in the present case. Usually this is not required for UP spectra. However, in the present case of MIES the sensitivity for the interaction of He* with the samples is changing with the coverage of the surface considerably. The reason for this observation is most likely that the sensitivity for the interaction of He* with one type of surface represented by one of the reference spectra is changing with the coverage of the surface with the other type of surface represented by the other reference spectrum. The normalisation can be performed by inserting a reference P3HT sample, which was examined before and after the sample measurements.

When quantifying the peaks of XPS spectra, the intensity of peaks of various elements needs to be normalised with Atomic sensitive factor (ASF) [35, 36]. The intensity of peaks on energy scale is comprised with ejected electrons with certain energy. The variation of energy represents elements with their atomic core level information, which also has respective photoelectron cross-sections[7, 37]. Subsequently, the contribution of electrons intensity can be influenced by the cross-sections, thus a normalisation with ASF has to be processed to scale the measured

peak intensity, so that variations of peak intensity are representative of the actual amount of elements.

2.4. Chemical Compounds Used in the Work

The chemical structures of polymer-thiophene donor and fullerene acceptor materials used in this work are illustrated in Figure 2-7.

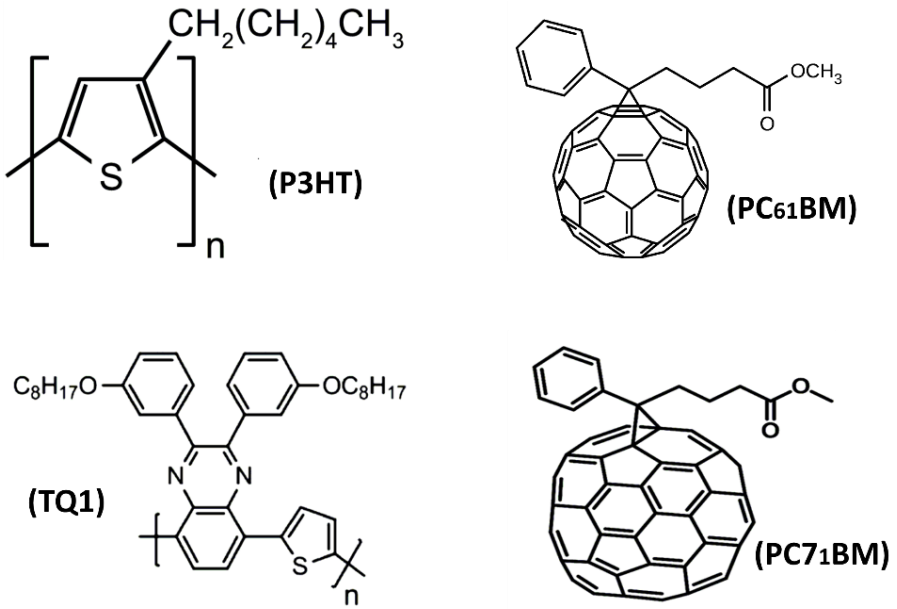

Figure 2- 7. The chemical structure of donor (P3HT and TQ1) and acceptor ($PC_{61}BM$ and $PC_{71}BM$))[38]

a) Polymer : (P3HT) Poly(3-hexylthiophene-2,5-diyl

The chemical form of P3HT is shown as $(C_{10}H_{14}S)_n$. The molar mass is 744.54 g/mol and the density is 1.1g/cm^3. The solid electronic grade P3HT was purchased from Rike Metals (U.S.) as 99.99% purity with 90K molecular weight. The P3HT is in strip-type bulk form with a melting point of approximately 238 ℃.

b) Organic-fullerene: ($PC_{61}BM$ or [60]PCBM) Phenyl-C_{61}-butyric acid methyl ester

The chemical form of solid $PC_{61}BM$ has been identified as $C_{72}H_{14}O_2$ with a molar mass of 910.88 g/mol. The density ranges from 1.3g/cm^3 to 1.5g/cm^3. The solid $PC_{61}BM$ was purchased from Solenne BV (Netherlands), 99.9% purity as solid electronic grade. The $PC_{61}BM$ is in

powder form. The melting point of $PC_{61}BM$ ranges from 215 ℃ ~225 ℃.

c) Polymer: (TQ1) Poly[[2,3-bis(3-octyloxyphenyl)-5,8-quinoxalinediyl]-2,5-thiophenediyl]

TQ1 is an up-to-date polymer donor material, structuring as $(C_{40}H_{46}N_2O_2S)_n$. The molar mass is 586.82 g/mol. The solid TQ1 was acquired as donor sample from research group of Mats Andersson [39-41], Flinders University. The TQ1 is in powder form with a purity of 99.5%. The melting point of TQ1 is not clear. We have revealed the range of melting point of TQ1 in our work as 170 ℃ ~190 ℃.

d) Organic- fullerene: ($PC_{71}BM$ or [70]PCBM) [6,6]-Phenyl C71 butyric acid methyl ester

$PC_{71}BM$ shares a similar chemical structure and feature as $PC_{61}BM$. In comparison, $PC_{71}BM$ has a larger phenyl ring and the regular chemical form is $C_{82}H_{14}O_2$. The molar mass has been measured as 1030.99 g/mol and the bulk density ranges from 1.4g/cm^3 to 1.6g/cm^3. The material was purchased from Solenne BV (Netherlands) as 99.99% purity electronic grade. The $PC_{71}BM$ is in powder form with a melting point ranging from 215 ℃ ~225 ℃

e) Solvent: (CB) chlorobenzene

Liquid form CB structures as C_6H_5Cl. The molar mass is 112.56g/mol and the density is 1.11g/cm^3.The solvent was obtained from Sigma-Aldrich with a purity of 99.99%. The boiling point for CB is 131 ℃, which has a solubility of organic-polymer materials. The CB can be easily blended with ODCB and used for modifying evaporation and boiling point of the solvent.

f) Solvent: (ODCB) 1,2-Dichlorobenzene

Liquid form ODCB has a chemical structure of $C_6H_4Cl_2$. The molar mass is 147.01g/mol with a density of 1.3g/cm^3. The solvent was obtaniend from Sigma-Aldrich, the purity of the liquid levels at 99.95%. The solvent ODCB used in this work has a higher solubility of solid thiophene and Fullerenes materials such as P3HT and PCBM. The boiling point for ODCB is 180 ℃.

g) Transition Metal Oxide: (MoO_3) Molybdenum Trioxide

High purity MoO_3 (99.95%) was purchased from Sigma-Aldrich. The MoO_3 was in solid

powder form with a density of 4.68g/cm^3. The melting point of pristine MoO_3 is 795 ℃.

h) Transition Metal Oxide: (V_2O_5) Vanadium Oxide

High purity V_2O_5 (99.9%) was gained from Sigma-Aldrich. The V_2O_5 was in solid powder form with a density of 3.36g/cm^3. The melting point of pristine V_2O_5 is 690 ℃. The temperature of required vapour pressure for evaporation is higher than the melting point. Therefore, during the process of PVD, V_2O_5 is in liquid non-Newtonian fluid form.

i) Transition Metal Oxide: (WO_3) Tungsten Trioxide

High purity WO_3 (99.95%) was purchased from Sigma-Aldrich. The WO_3 was in solid powder form with a density of 7.16g/cm^3. The melting point of pristine WO_3 is 1473 ℃.

j) Substrate: (Si) Silicon

The Si (111-crystal orientation) wafer substrates for depositing polymer BHJ were purchased from MTI corp. (U.S.) as a prime-semiconductor level. The Si was heavily doped with As (Arsenic). Thus, the base resistivity was low as 0.001-0.005 ohm/cm and the Si wafer features an N-type electronic property.

2.5. Fundamental Sample Preparations

2.5.1. Cleaning of Si substrate

The sample substrate of Si had been cleaned before deposition. Subsequent to a procedure slicing the Si wafer into 1cm×1cm pieces, the Si was immersed in a blended solvent of HCl and HF (3:1 wt%) for 10min. The concentration of the solution was 10%wt with deionised water. After which, the Si substrates were rinsed for 10min and then dried in oven condition.

2.5.2. Bulk Heterojunction (BHJ) Sample Preparation

As described, the BHJ of P3HT/$PC_{61}BM$ [42] was first investigated due to its typical application in organic solar cell and also in other organic devices. The TQ1/$PC_{71}BM$ BHJ was subsequently studied. The new organic donor-acceptor (D-A) BHJ represents an up-to-date blending of polymer-fullerene. A better OPV performance was thus proposed. The investigation upon

transition metal oxides involves MoO_3 and its alternatives: V_2O_5 and WO_3.

High purity $PC_{61}BM$ and P3HT were blend in solvent. We used CB and ODCB (1:1 wt%) as solvent for the P3HT/$PC_{61}BM$ solution. The P3HT to $PC_{61}BM$ was blend at a ratio of 1:1 and the concentration was processed as 2.5 wt.% to simulate a high active layer performance [43]. Eventually ODCB is suitable for dissolve the P3HT and $PC_{61}BM$ and subsequently a blended solution is prepared. The boiling point of ODCB is relatively high. Thus, the polymer-fullerene materials can be reoriented and mixed well before the solvent is evaporated. The addition of CB in the solvent leads to a modification of the boiling point of mixed solvent; as such, the process of drying solvent can be accelerated to avoid potential contamination to the materials. The solvent was stir-mixed for more than 7 hours at 50℃. Low-resistance (less than 0.005Ω/cm) As-doped Si wafers (1cm × 1cm) were used as substrates. The solution was spin-coated at 2000rpm for 60s, resulting in a thick BHJ layer. Subsequently samples were heated to 120℃ for 10min for evaporating the solvent.

Similarly, $PC_{71}BM$ and TQ1 were blended in a mixed solution of CB and ODCB (1:1 wt%). The ratio of TQ1 to $PC_{71}BM$ was 1:2.5 2.5 wt% [39]. The solvent had been stirred for homogenisation at 60℃ for 12 hours before being drop-casted on to Si substrate. After which, the samples were sent to oven and heated at 130℃ for 15min. The processed BHJ substrates are thus sent to vacuum chamber within 2 hours for applying metal oxide deposition to minimise the oxidation and contamination of BHJ.

2.5.3. Metal Oxides Deposition

Physical Vapour Deposition (PVD) [44] in vacuum has been applied with a base pressure of ~ 10^{-7} mbar. First, these high purity metal oxides were loaded into quartz crucibles. The crucibles are subsequently sent to a thermal-evaporator. After which, the thermal couple [45] reflecting the temperature of crucibles was positioned. The MoO_3 was processed at 480~510 ℃, while the deposition temperature for V_2O_5 and WO_3 were respectively 740 ℃ and 1070 ℃. Thermal-evaporation was conducted at an angle of 45 ° between the direction of the sample surface normal and the direction to the detector. The deposition rates have been precisely controlled for all metal oxides at about 0.02nm/s and measured by a QCM [46, 47]. All the work consists of a substrate of polymer BHJ and a deposition of metal oxides. The treatments upon BHJ and

metal oxides are described in individual chapters.

Reference

1. Metson, J.B., *Charge compensation and binding energy referencing in XPS analysis.* Surface and interface analysis, 1999. **27**(12): p. 1069-1072.
2. Shircliff, R.A., et al., *Angle-Resolved XPS Analysis and Characterization of Monolayer and Multilayer Silane Films for DNA Coupling to Silica.* Langmuir, 2013. **29**(12): p. 4057–4067.
3. Silversmit, G., et al., *Determination of the V2p XPS Binding Energies for Different Vanadium Oxidation States (V5+ to V0+).* Journal of Electron Spectroscopy, 2004. **135**: p. 167-175.
4. Fuggle, J.C., D.J. Fabian, and L.M. Watson, *Electron energy loss processes in X-ray photoelectron spectroscopy.* Journal of Electron Spectroscopy and Related Phenomena, 1976. **9**(2): p. 99-109.
5. Gall, D., *Electron mean free path in elemental metals.* Journal of Applied Physics, 2016. **119**(085101).
6. Ilton, E.S., et al., *XPS determination of Mn oxidation states in Mn (hydr)oxides.* Applied Surface Science, 2016. **366**(475-485).
7. iJo, M., *An almost knowledge-free approach to XPS intensity evaluation where use of atomic photoemission cross sections suffices for yielding material-specific inelastic background.* Journal of Electron Spectroscopy and Related Phenomena, 2017. **215**(36-56).
8. Schmerl, N.M., et al., *Valence band structure of PDMS surface and a blend with MWCNTs: A UPS and MIES study of an insulating polymer.* Applied Surface Science, 2015. **353**: p. 693-699.
9. Qi, D., et al., *Tuning the Electron Affinity and Secondary Electron Emission of Diamond (100) Surfaces by Diels-Alder Reaction.* Langmuir, 2007. **23**(19): p. 9722-9727.
10. Chambers, B.A., et al., *The direct measurement of the electronic density of states of graphene using metastable induced electron spectroscopy.* 2D Materials, 2017. **4**(2): p. 025068.
11. Monreal, R.C., *Auger neutralization and ionization processes for charge exchange between slow noble gas atoms and solid surfaces.* Progress in Surface Science, 2014. **89**: p. 80-125.
12. Krischok, S. and H.V. Kempter, *The chemisorption of H2O and CO2 on TiO2 surfaces: studies with MIES and UPS (HeI/II).* Surface Science, 2002. **507-510**: p. 69-73.
13. Volgmann, K., F. Voigts, and W. Maus-Friedrichs, *The interaction of H2O molecules with iron films studied with MIES, UPS and XPS.* Surface Science, 2012. **606**: p. 858-864.
14. Andersson, G.G. and H. Morgner, *Impact collision ion scattering spectroscopy (ICISS) and neutral impact collision ion scattering spectroscopy (NICISS) at surfaces of organic liquids.* Surface Science, 1998. **405**: p. 138-151.
15. Ridings, C. and G.G. Andersson, *Deconvolution of NICISS profiles involving elements of similar masses.* Nuclear Instruments and Methods in Physics Research Section B: Beam Interactions with Materials and Atoms, 2014. **340**: p. 63-66.
16. Andersson, G.G. and H. Morgner, *Determing the stopping power of low energy Helium in alkanethiolates with Netual Imapct Collision Ion Scattering Spectroscopy* Nuclear Instruments and Methods in Physics Research Section B: Beam Interactions with Materials and Atoms, 1999. **155**: p. 357-368.
17. Andersson, G.G., H. Morgner, and D. Schulze, *Surface properties of electrolyte solutions studied with ion beam analysis.* Nuclear Instruments and Methods in Physics Research Section B: Beam Interactions with Materials and Atoms, 2002. **190**(1-4): p. 222-225.
18. Meyer, J. and A. Kahn, *Electronic structure of molybdenum-oxide films and associated charge injection mechanisms in organic devices.* Journal of Photonics for Energy, 2011. **1**(1): p. 011109.

19. Irfan, et al., *Strong interface p-doping and band bending in C60 on MoOx.* Organic Electronics, 2011. **12**(9): p. 1588-1593.
20. Amandeep, K., S. Sharma, and B. Mittal, *Comparison of sensitivity of Geiger Muller counter and ionization chamber based survey meters.* J Nucl Med 2012. **53**: p. 2607.
21. Ko, Y.H., et al., *Diffuse light-scattering properties of nanocracked and porous MoO3films self-formed by electrodeposition and thermal annealing.* physica status solidi (a), 2012. **209**(11): p. 2161-2166.
22. Acres, R.G., et al., *Molecular Structure of 3-Aminopropyltriethoxysilane Layers Formed on Silanol-Terminated Silicon Surfaces.* The Journal of Physical Chemistry C, 2012. **116**(10): p. 6289-6297.
23. Sato, M., et al., *Analysis of Insulating Materials and Deep Interfaces by Auger Electron Spectroscopy.* FUJITSU Sci. Tech. J., 2010. **46**(3): p. 257–262.
24. López-Carreño, L.D., et al., *Oxidation of molybdenum surfaces by reactive oxygen plasma and O2+ bombardment: an auger and XPS study.* Surface and interface analysis, 1998. **26**(4): p. 235–241.
25. Chibane, L., et al., *Development of Molybdenum Trioxide (MoO3) by Spin Coating Method for Photovoltaic Application.* Journal of Materials Science and Engineering B, 2013. **3**(7): p. 418-422.
26. Mattox, D.M., *Physical vapor deposition (PVD) processes.* Metal Finishing, 2001. **99**(1): p. 409-423.
27. Uribe, E., et al., *Development of Al oxide PVD coatings against metal dusting.* Surface Engineering, 2015. **31**(2).
28. Sharma, A., et al., *Invisible high workfunction materials on heterogeneous surfaces.* Applied Surface Science, 2015. **327**: p. 22-26.
29. Sammut, E., et al., *Quantitative Assessment of Perfusion – Where Are We Now?* Cardiac Magnetic Resonance, 2014. **7**: p. 9278.
30. Vasilopoulou, M., et al., *The influence of hydrogenation and oxygen vacancies on molybdenum oxides work function and gap states for application in organic optoelectronics.* J Am Chem Soc, 2012. **134**(39): p. 16178-16187.
31. Oberbrodhage, J., *Determination of a solute electron energy spectrum not accessible experimentally by means of Singular Value Decomposition.* Journal of Electron Spectroscopy and Related Phenomena, 2000. **170**: p. 231–238.
32. Berlich, A., Y. Liu, and H. Morgner, *Growth of nickel nanoparticles on NiO/Ni(001): Evidence of adsorbed oxygen on metal particles by metastable induced electron spectroscopy (MIES).* Surface Science, 2008. **602**(24): p. 3737-3744.
33. Berlich, A., Y.C. Liu, and H. Morgner, *Evaporation of Ni and carbon containing species onto NiO/Ni as case study for metal support catalysts investigated by Metastable Induced Electron Spectroscopy (MIES).* Radiation Physics and Chemistry, 2005. **74**(3-4): p. 201-209.
34. Yin, Y., et al., *Dipole Formation at the MoO3/Conjugated Polymer Interface.* Advanced Functional Materials, 2018. **28**(46): p. 1802825-1802835.
35. Wagner, C.D., et al., *Empirical atomic sensitivity factors for quantitative analysis by electron spectroscopy for chemical analysis.* Surface and interface analysis, 1981. **3**(5): p. 211-225.
36. Wagner, C.D., *Sensitivity factors for XPS analysis of surface atoms.* Journal of Electron Spectroscopy and Related Phenomena, 1983. **32**(2): p. 99-102.
37. Verma, H.R., *Atomic and Nuclear Analytical Methods: XRF, Mössbauer, XPS, NAA and Ion-Beam Spectroscopic Techniques.* Book, 2007.
38. Aldrich, S., *https://www.sigmaaldrich.com/*.
39. Sharma , A., et al., *Unravelling the Thermomechanical Properties of Bulk Heterojunction Blends in Polymer Solar Cells.* Macromolecules, 2017. **50**(8): p. 3347-3354.

40. George, Z., et al., *Two-in-one: cathode modification and improved solar cell blend stability through addition of modified fullerenes.* Journal of Materials Chemistry A, 2016(7).
41. Lindqvist, C., et al., *Fullerene mixtures enhance the thermal stability of a non-crystalline polymer solar cell blend.* Applied Physics Letters, 2014. **104**: p. 153301.
42. Lu, Y., et al., *Temperature-dependent morphology evolution of P3HT:PCBM blend solar cells during annealing processes.* Synthetic Metals, 2012. **162**(23): p. 2039-2046.
43. Baek, W.H., et al., *Effect of P3HT:PCBM concentration in solvent on performances of organic solar cells.* Solar Energy Materials and Solar Cells, 2009. **93**(8): p. 1263-1267.
44. Saji, V.S. and C.W. Lee, *Molybdenum, molybdenum oxides, and their electrochemistry.* ChemSusChem, 2012. **5**(7): p. 1146-1161.
45. Machin, G. and J. Pearce, *Step change improvements in high-temperature thermocouple thermometry.* Proceedings of 2012 UKACC International Conference on Control, 2012(13075187).
46. Hagihara, T., et al., *Electrochemical Quartz Crystal Microbalance Study of the Electrodeposition of Platinum.* Electrochimica Acta, 2015. **176**: p. 65-69.
47. Mecea, V.M., *From Quartz Crystal Microbalance to Fundamental Principles of Mass Measurements.* Analytical Letter, 2005. **38**: p. 753-767.

Chapter 3. Observation and Characterisation of Dipole forming at MoO_3/P3HT:$PC_{61}BM$ BHJ Interface

3.1. Abstract

MoO_3 is used as HTL/ABL in organic based solar cells because of its capability to extract electrons and inject holes from the active layer due to its high work function. Here we use UV-photoelectron spectroscopy and metastable induced electron spectroscopy to determine the strength of the dipole at the MoO_3/polymer interface and the minimum MoO_3 thickness required to form a closed metal oxide layer. Neutral impact collision ion scattering spectroscopy is used to determine how deep the MoO_3 penetrates into the polymer. Our investigation shows, that upon deposition of the MoO_3, a strong dipole is formed at the interface between the active layer and the MoO_3. The strength of the dipole increases with increasing thickness of the MoO_3 layer and saturates at a thickness around 3nm at 2.2 eV.

3.2. Introduction and Research Aim

Transition metal oxides, such as MoO_3[1, 2] ,V_2O_5 and WO_3, are frequently used as HTL/ABL [3-6] in organic solar cell and other organic devices. The reason why MoO_3 is used as ABL is its high work function. It is assumed that the CB of MoO_3 and the HOMO of functional polymer/fullerene [2, 7] align due to a range of electronic properties of MoO_3 [8-10] amongst them the high WF/ϕ of pristine MoO_3 which was reported as 6.7eV [11-13]. The alignment of the CB of MoO_3 and the HOMO of conducting polymer/fullerene is considered as favourable for the charge transfer over the ABL/active polymer-fullerene BHJ interface[14], and could contribute to the increase in solar cell efficiency. The charge transfer has been assigned to charge injection/extraction mechanism [1, 15, 16]. However, the energy levels, the band structure, energy level alignment and barriers for the charge transfer at the MoO_3/BHJ interface are not well known due to a lack of characterisation. It has been reported that the WF and IE of MoO_3 change with the thickness of the deposited MoO_3 layer [12, 17]. It can be speculated, that the large difference in the electrical properties of MoO_3 and polymer BHJ could result in the formation

of dipoles at the MoO_3/BHJ interface [13, 18, 19]. The formation of dipoles at the MoO_3/BHJ interface and the related electric field could generate intermediate energy states and strongly impact on the charge transfer over the interface[20]. The dipole energy has been assumed as the difference of the WF of materials at the interface [8, 9]. The energy of a single dipole can be calculated [21, 22] however in an interface, dipoles may encounter with each other thus either enhances or cancels each out. The interface dipole energy may endure a significant difference from the theoretical value of an individual one which has not been precisely characterised. Subsequently, the intermediate energy states forming at the interface are yet to known and the prediction of charge transferring over the interface lacks of evidence.

Our work will point out two main findings. Firstly, it will be quantified and shown that a minimum deposition thickness of MoO_3 is required to form a closed layer. Secondly, it will be demonstrated that the dipole energy can alter significantly across the variation of deposition amount. Thus the way of charge transferring over the MoO_3/BHJ interface would be changed. Electron spectroscopy is employed in the work for analysing the electronic properties of the interface and Neutral impact collision ion scattering spectroscopy for determining concentration depth profiles of all materials. Microscopy assists to obtain a topology of surface and how the MoO_3 particles forming on BHJ.

3.3. Sample Preparation

The methods of blending P3HT and $PC_{61}BM$ and the deposition of metal oxides are described in experimental section. The sample preparation in this work is illustrated in Figure 3-1.

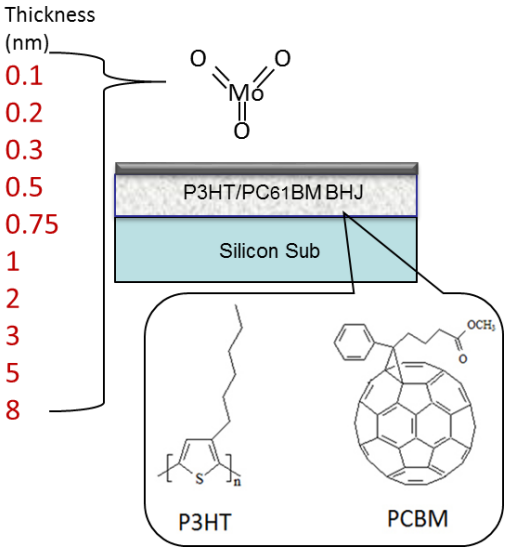

Figure 3- 1. Sample preparation of MoO_3 deposited onto polymer BHJ across a range of thickness

Layers of various MoO_3 thicknesses (0.1, 0.2, 0.3, 0.5, 0.75, 1, 2, 3, 5 and 8 nm) were separately made upon BHJ. Subsequently the samples were transferred from PVD vacuum chamber directly into the analysis UHV chamber for applying measurements. The samples were kept pristine because no reaction with oxygen and moisture can happen during the transport.

3.4. Results and Discussion

3.4.1. Chemical Composition of MoO_3/P3HT:$PC_{61}BM$ Interface

In Figure 3-2 high-resolution XP spectra of (Molybdenum) Mo, (Sulphur) S, (Carbon) C and (Oxygen) O are shown and the plots of relative concentration and fraction of certain elements are illustrated in Figure 3-2(D) and (E). The high resolution elemental peaks have been fitted. Figure 3-2(A) shows that the Mo $3d_{5/2}$ peak is found for all MoO_3 layer thicknesses at 232.8 ± 0.15 eV which corresponds to Mo^{6+} [23]. The fact that the Mo $3d_{5/2}$ does not shift is a strong indication that the samples are not charging when MoO_3 is deposited thus justifying the energy calibration procedure as described. From the same figure the S $2p_{3/2}$ peak is found at 164.0 ± 0.15 eV[24] and shows no variation in peak position within error bars. In Figure 3-2(B) it can be seen, that in the C 1s spectra one peak is found at 285 ± 0.15 eV, a second peak at

approximately 287.2 ± 0.3 eV and a further peak (tagged in shadow) at the position across 283.5 to 284.1 (±0.15) eV. The intensity of the low binding energy C peak also increases with the amount of MoO_3 deposited, which is illustrated in Figure 3-2(E). The peak at 285 ± 0.15 eV can be identified as representing the C-C bond while the C-O bond peaks at 287.2 ± 0.3 eV. Based on the energy calibration procedure outlined above it can be concluded that origin of the low binding energy C peak is not due to charging of the samples and also not due to the formation of a chemical species involving C upon evaporation of MoO_3, such as Molybdenum carbonate, which requires a higher temperature to form and would have shown up as new specimen in Mo peak. The particular C peak contains a range of peaks from 283.5 eV to 284.1 eV and they vary in fraction upon different MoO_3 deposition amount. The nature of the low binding energy C peak will be discussed below.

As the fitting of O 1s is shown in Figure 3-2(C). The O 1s spectrum of the pristine fullerene can be fitted with two peaks with one of them found in the range of 532-533.5 (±0.15 eV) and the second at 530.8 ± 0.25 eV. They can be identified as due to the polymer BHJ [24, 25] and MoO_3[26], respectively. With increasing amount of deposited MoO_3, the O from MoO_3 reveals a slight shift around 0.5eV as the position of the O 1s peaks and the Oxygen peaks from polymer BHJ shift 1.5eV to the lower binding energy, which is shown in Figure 3-2(D). The nature is rather similar as C peak.

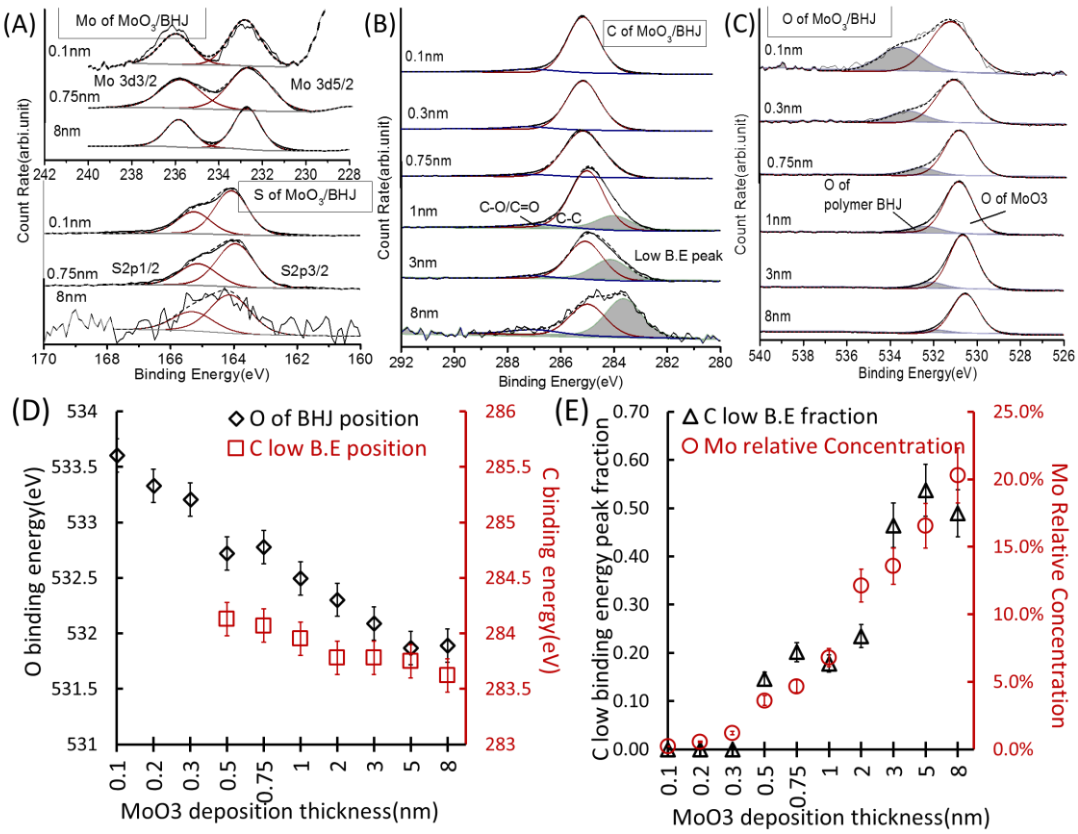

Figure 3- 2. (A) Molybdenum Mo_{3d} and Sulfur S_{2p} peaks related to various MoO_3 layer thicknesses; (B) Carbon C_{1s} fitting of high-resolution XP spectra; (C) Oxygen O_{1s} fitting of high-resolution XP spectra; (D) Peak position of low binding energy C and O peak related to the polymer/fullerene; (E) The fraction of C low binding energy peak and the concentration of Mo upon variation of deposition

The nature of low binding energy C peak (283.5~284.1eV) can be further discussed here. A chemical shift as reason for the occurring of this component can be excluded. Moreover, the deposition was processed in high vacuum to avoid any potential chemical reactions. Thus it is assumed that the C_{1s} peak of the BHJ layer experiences an electric potential at the MoO_3/BHJ interface, which relates to the deposition amount of MoO_3.

3.4.2. Elemental Depth Distribution

The relative concentration of Mo derived from the NICIS spectra is shown as function of the energy loss and depth in in Figure 3-3. We show here both scales because the stopping power

of He^+ in MoO_3 has not yet been determined and the nature will be similar in following chapters. The concentration depth profiles towards the side of the larger depth of the profiles show a gradient, which is much lower than the gradient on the side of the lower depth. This is an indication that there is a distribution of MoO_3 into BHJ and that the MoO_3 layer is not a compact layer. This can be seen from comparing with a profiling of MoO_3/SiO_2. The spectrum of a sample with 4nm MoO_3 deposited onto a Si substrate is also shown. The gradient of the Mo concentration at the side of the MoO_3/SiO_2 interface (large depth) is much larger than the gradient at the MoO_3/BHJ interface, indicating that MoO_3-SiO_2 forms a sharper interface than MoO_3-BHJ. The finding of difference of gradients of MoO_3 upon two types of substrate interface is due to the straggling of the stopping power which increases with the depth[27]. After evaporating 0.1 nm of MoO_3 on BHJ, Mo can be found over a depth range of ~ 3 nm. Thus the MoO_3 particles tend to be merged into BHJ bulk even with minor MoO_3 deposition. After deposition of 1 nm Mo can be found over a depth range of more than 8 nm. The distribution of MoO_3 in the concentration depth profile can have various reasons. One option is that MoO_3 particles with a range of sizes are formed. They could be located on top of the polymer BHJ or just below the BHJ surface. The alternative option is that small MoO_3 particles (or even single MoO_3 molecules) are formed and that they have a concentration depth profile into the BHJ layer. The real distribution could be a combination of both options. Below we will combine the information from the concentration depth profiles with the information of the composition of the outermost layer and decide which of the two options is applicable. Besides, it can be noted that the concentration of Mo at the surface layer does not show a significant change after 1nm deposition but rather the width of the Mo profile is increasing and maintaining constant at the outermost surface of BHJ. This is an indication that the MoO_3 forms a closed layer from about 1 nm thickness and growth in thickness with further evaporation of MoO_3, which can be seen at the MoO_3 side from the figure. The depth of MoO_3 diffusion into BHJ also keeps constant after a closed layer is formed.

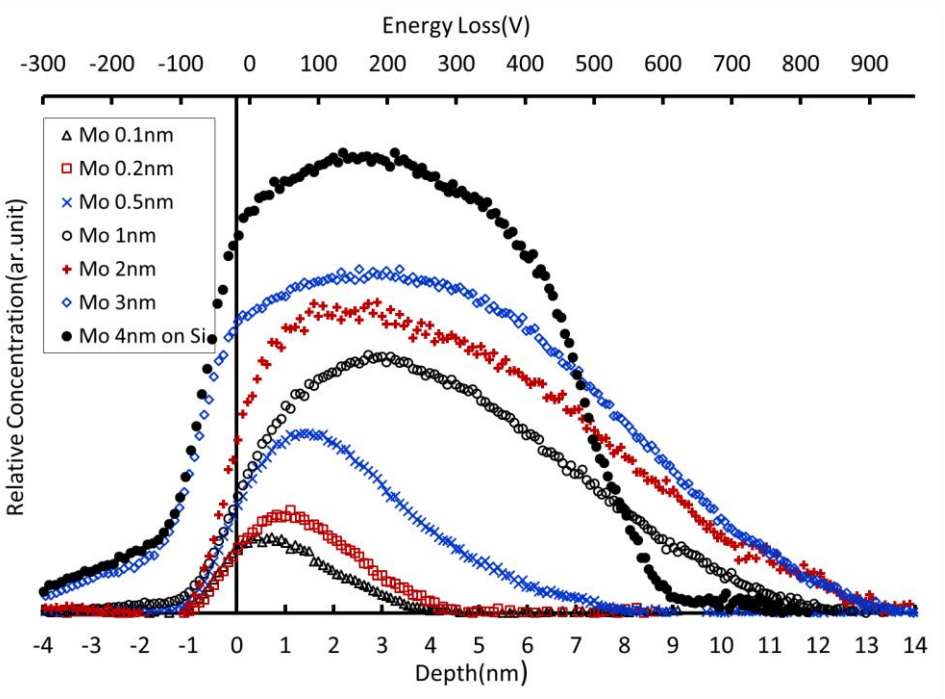

Figure 3- 3. Concentration depth profile of Molybdenum showing the distribution of Mo onto the polymer BHJ layer with the zero mark indicating the very surface of samples. A spectrum of pristine 4nm MoO_3 deposited on Si substrate has been included for comparison

3.4.3. Observation of MoO_3 Distribution upon BHJ Surface

The surface topography as analysed with SEM and the distribution of the elements across the surface as analysed with AES of the 0.3nm MoO_3/BHJ sample are shown in Figure 3-4. The lateral resolution for both methods is ~ 5nm. Figure 3-4(A) illustrates a randomly selected area of the sample surface and the AES analysis upon spot (a) and (b) shows differences in Mo concentration. This is an indication that upon deposition of 0.3nm MoO_3, the surface has not been fully covered. The SEM image lacks information whether MoO_3 island have been formed on the BHJ layer. However, In Figure 3-4(B) it is clear that the distribution of MoO_3 onto polymer BHJ surface is uniform.

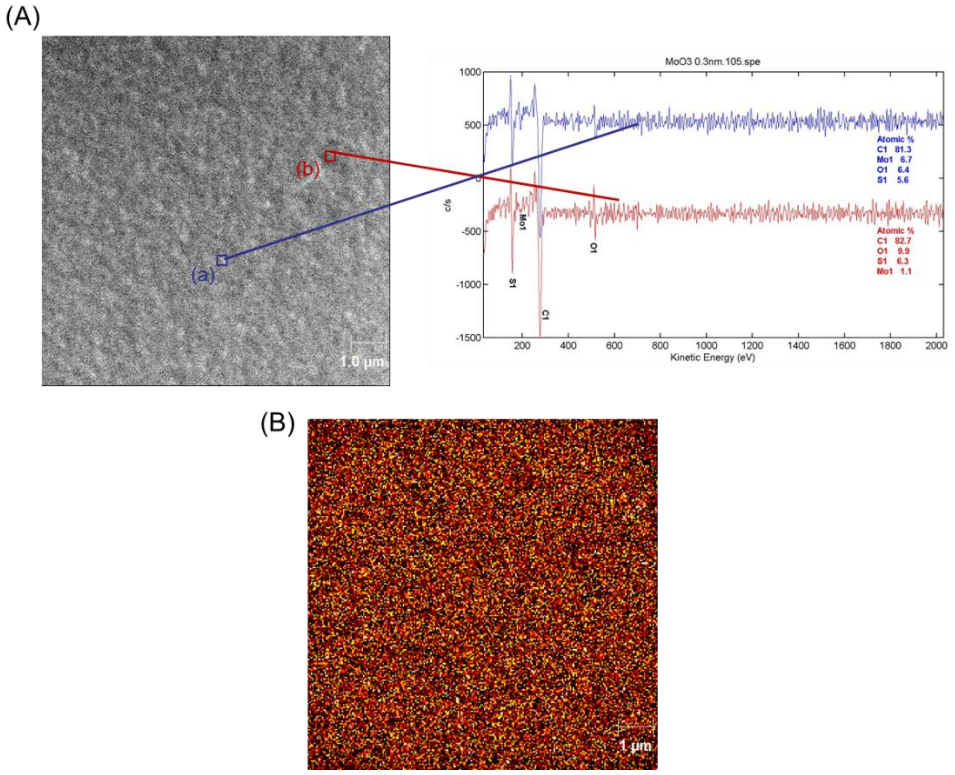

Figure 3- 4. (A) AES survey spectra on the selected spots of sample and SEM image of 0.3nm MoO_3/BHJ sample; (B) The mapping of Mo determining MoO_3 distribution over the 10×10 μm^2 area of SEM image, the scale on figure is 1 υm

3.4.4. Decomposition and Analysis of MIES/UPS Spectra

a) The Observation and Analysis of MIES/UPS of the MoO_3/BHJ Samples

The MIE/UP and IPE spectra and the plot of WF are shown in Figure 3-5. In both the MIE and UP spectra a gradual change of the shape of spectra can be seen from the pristine BHJ to the highest coverage with MoO_3. In Figure 3-5(A) the secondary electron cut-off of UPS shifts negatively on binding energy scale with increasing amount of MoO_3, indicating an increase in the WF of the samples with increasing amount of deposited MoO_3. The energy onset declines from approximately 16.7eV to 14.6eV. In Figure 3-5(B) it can be seen in valence electron region of UPS that a feature peaking at ~ 4eV increases with escalating deposition, which can be assigned to the occurrence of MoO_3. Meanwhile the energy peak onset at ~7eV declines due to the decreasing fraction of polymer BHJ. The same nature has been found in valence region of MIE spectra, which is shown in Figure 3-5(C). It can be seen that the features of ~9.5eV in MIES related to the BHJ decrease and the changes in valence region of both MIES and UPS

occurred gradually. The Figure 3-5(D) shows the WF of the samples. The WF was taken from secondary electron cut-off of the UP spectra, which follows the procedure described in methodology section. The WF increases from 4.5 ± 0.1eV of 0.1nm deposition to 6.8 ± 0.1eV of 8nm MoO_3 on BHJ in Figure 3-5(D). The overall change in WF is 2.3 ± 0.2eV.

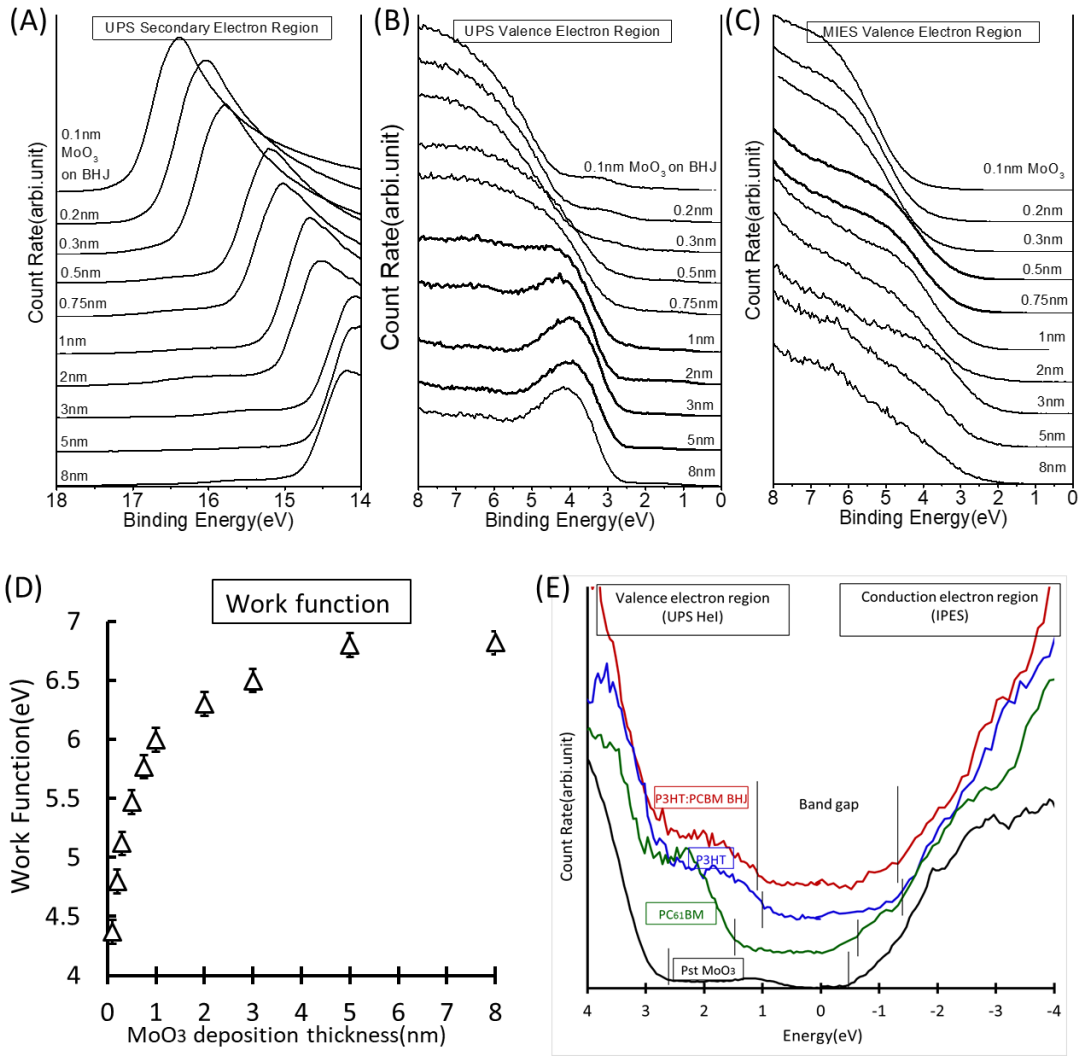

Figure 3- 5. (A) secondary electron region and (B) Valence electron region of the UP spectra of samples with a range of MoO_3 layer thicknesses; (C) MIE valence spectra of the same samples; (D) The plot of WF of the samples; (E) conduction/valence electron region of pristine MoO_3, P3HT, $PC_{61}BM$ and Blended BHJ

In order to gain an understanding of the energy band structure at the MoO_3/BHJ interface and accurately characterisation of the band energy of either MoO_3 or polymer BHJ, the samples including P3HT, $PC_{61}BM$, blended BHJ, 8nm MoO_3 have been investigated with IPES and

UPS, which have been made on Si substructure and measured as pristine. The UPS valence electron and IPE spectra are shown in Figure 3-5(E) the WF, E_{HOMO}, E_{LUMO}, E_{VB}, E_{CB} and band gap (E_g) of these samples are plotted in table 3-1 with an error bar of $\pm$0.1eV. The calculation of following electrical properties is described in methodology section. The WF/ϕ, E_{VB} and E_{HOMO} we obtained for MoO_3/BHJ are corresponds to Kroger[2], Meyer[11] and Burak's work[28].

Sample	**WF/ϕ(eV)±0.1**	**E_{HOMO}/ E_{VB} (eV) ±0.1**	**E_{LUMO}/ E_{CB} (eV) ±0.1**	**E_g (eV) ±0.2**
P3HT	3.6	1.1	1.6	2.7
$PC_{61}BM$	3.9	1.6	1.0	2.6
P3HT/$PC_{61}BM$	3.7	1.2	1.5	2.7
MoO_3	6.9	2.6	0.4	3.0

Table 3-1. The plots of WF, E_{HOMO}, E_{LUMO}, E_{VB}, E_{CB} and band gap (E_g) of pristine samples, note that the all energies are indicated with a zero point at Fermi Level (E_f)

The spectra of pristine components are measured also for comparison in decomposition section and the electrical parameters will be used for reconstructing the energy bands.

b) Decomposition of Valence Electron Region of MIE/UP Spectra

The occurrence and growth of energy states in Figure 3-5(B) across the valence electron region have been observed. The UP/MIE spectra of escalating amount of MoO_3 on BHJ surface consists of a linear combination of at least MoO_3 and polymer BHJ spectra, which is further processed and proved as following.

To identify the components within the measuring depth which construct the spectra, the valence electron region of MIES and UPS has been processed by applying SVD in subsequent groups (e.g. pristine BHJ, pristine MoO_3, 0.1, 0.2, 0.3nm MoO_3 on BHJ as one group). The outcome reveals gradual changes. From MoO_3/BHJ samples, three reference spectra have been distinguished in both UPS and MIES to fit the spectra, which are shown in Figure 3-6 (A-F). The comparison with pristine BHJ and MoO_3 are included as Figure 3-6 (G) and (H). The first reference spectrum (Ref. A) is similar to the spectrum of a layer of 8 nm of MoO_3 layer

deposited directly onto the silicon base, thus it has been assigned to pristine MoO_3. The second reference spectrum (Ref. B) is almost identically featured as the spectrum of pristine BHJ. Moreover, the shape of spectrum (Ref. C) is related to the second reference spectrum (pristine BHJ) but shifted by a range from 1.0~ 1.8 eV to lower binding energy depending from different groups. Similar observations can be made when analysing with SVD other subsets of MIE spectra. The natures are rather similar with UP spectra. It is important to note that distribution of secondary electron occurs with a binding energy more than 8 eV. Thus the feature presenting more than 8 eV is a complex of valence and secondary electron, which is not appropriate for analysis of spectra.

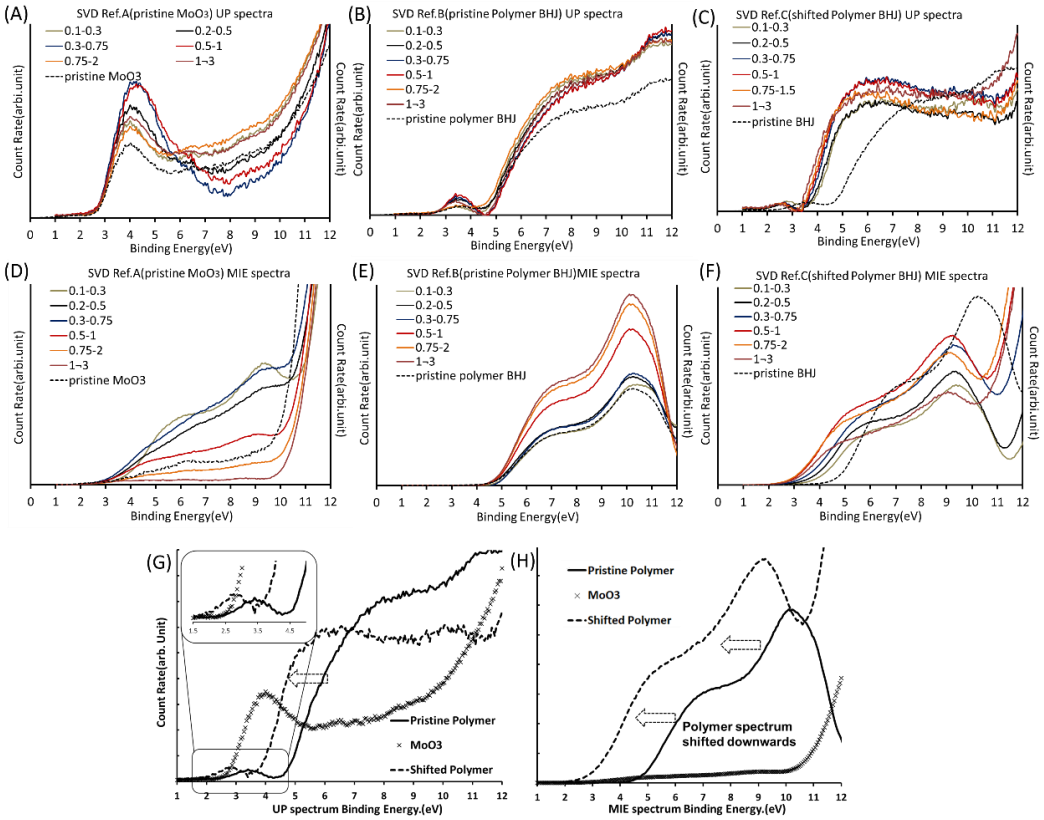

Figure 3- 6. (A) (B) (C) the decomposed UP spectra of grouped MoO_3/BHJ samples results in three reference spectra in different sample group. (D) (E) (F) the reference spectra in different group from the decomposition of MIES; (G) (H) the comparison of reference spectra of UPS and MIES (0.5nm, 0.75nm, 1nm MoO_3/BHJ sample group) which manifests a BHJ spectrum but shifts to lower binding energy axis

The question arises what the physical meaning of the shift of the spectrum of the BHJ is (Ref.

C). The BHJ spectral component in the measured spectra, which is shifted relative to the pristine BHJ layer, is a BHJ layer. However, this BHJ layer is subject to a dipole. The dipole is forming between the bulk BHJ and the evaporated MoO_3 and the shifted BHJ component is physically located in the dipole thus subject to a shift on the electron energy scale. The shifted spectral component is found at a lower binding energy which means that the positive end of the dipole is from BHJ, which points towards the outermost layer thus towards the MoO_3. It is also important to note that the Ref. C only represents the average shifted BHJ spectrum in individual groups, rather than a necessarily existing spectrum with physical meaning. Given the fact from UPS the difference of shifting energy of Ref. C ranges about 0.8eV across various groups, the Ref. C is thus comprised of a series of BHJ spectra with a variation of energy shift on the scale. The difference among the spectra is their weighing factors.

Based on the analysis of SVD, a revised procedure of weighted shifting method (WSM) for fitting the measured spectra has been developed, which allows spectra to shift on energy scale. From which, the series of spectra with different energy shift can be accurately characterised. The decomposition method has been described in experimental part and the equation is performed as following:

$$S_{meas}^{(i)} = \sum_{j=0}^{n} a_j^{(i)} \times S_{BHJ}\left(E + j \cdot \Delta E\right) + b \cdot S_{MoO_3} \quad \text{with} \quad \sum_j a_j^{(i)} + b = 1$$

$$\Delta E_{mean}^{(i)} = \sum_{j=0}^{n} a_j^{(i)} \cdot j \cdot \Delta E$$

Equation 3-1

$S_{meas}^{(i)}$: the measured spectrum i

S_{BHJ} : the spectrum of the pristine BHJ layer

S_{MoO3} :the spectrum of the sample after evaporating 8 nm of MoO_3, i.e. the thickest MoO_3

$a_j^{(i)}$: the weighting factors used in the fitting procedure

$\Delta E_{mean}^{(i)}$: the mean shift for spectrum i

ΔE : The stepwise energy shift, which was set to 0.1eV

The sum of the weighting factors has to be unity within experimental uncertainty, but an error of about 0.1 for $\sum_j a_j^{(i)} + b$ is considered acceptable. In Figure 3-7 the fitting of MIE and UP spectra of a 0.75nm MoO_3/BHJ sample is shown based on WSM method. The fitting residuum is relatively small and all other spectra sets can be fitted at least as good as both spectra.

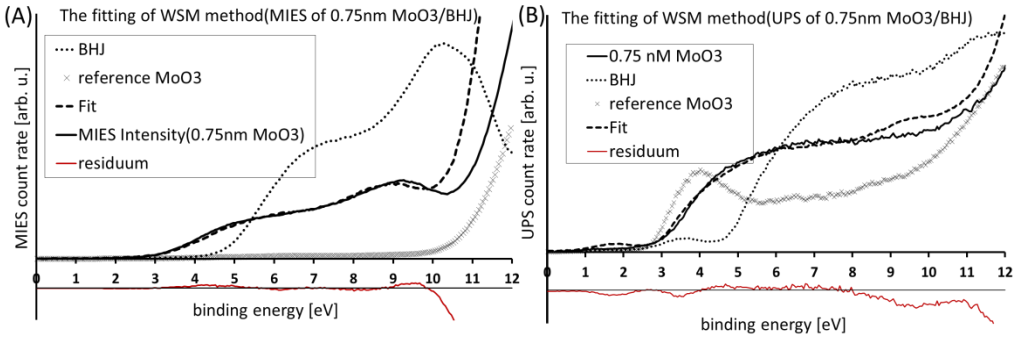

Figure 3- 7. (A) The fitting using WSM method on MIES of 0.75 MoO_3/BHJ sample; (B) The fitting using WSM method on UPS of 0.75 MoO_3/BHJ sample; The residuum is exhibited

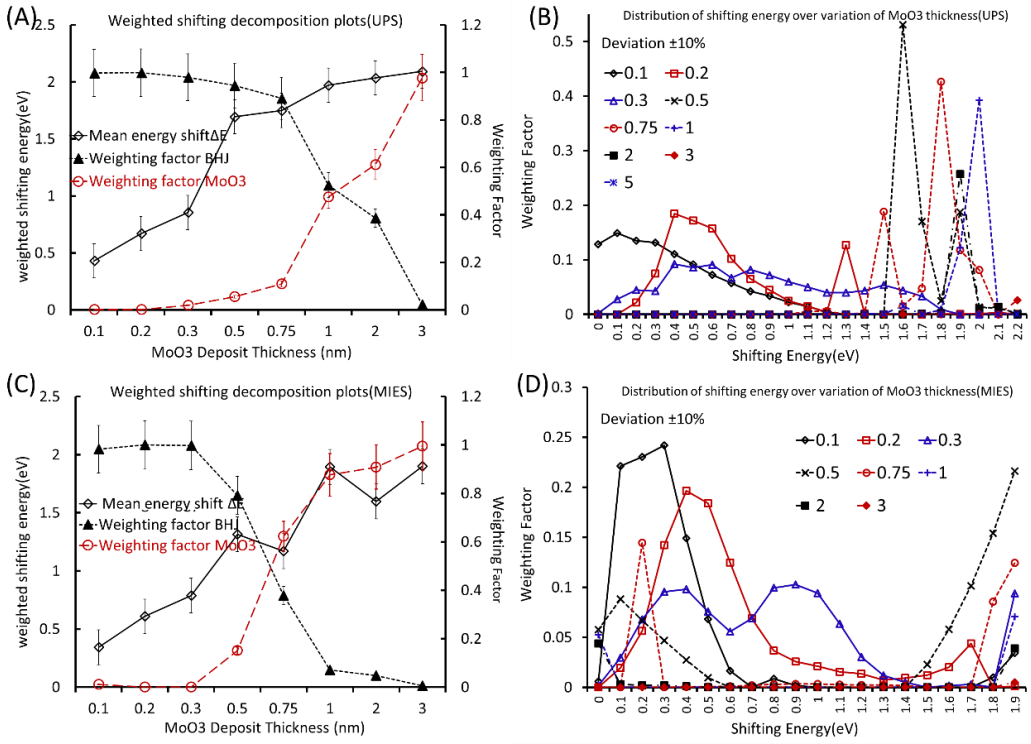

Figure 3- 8. (A)(C)The weighting factors of the whole set of UP and MIE spectra; (B)The weighted energy shift of UPS for the samples from 0.1nm to 3nm MoO_3 deposition along with the fraction of the shifted-BHJ spectrum; (D) The weighted energy shift of MIES for the samples

from 0.1nm to 3nm MoO_3 deposition along with the fraction of the shifted-BHJ spectrum

The decomposed weighting factor for the shifting UP and MIE spectra are shown in Figure 3-8(A) and 3-8(C), which distributes a variety of energy due to the probing depth of these two methods. It can be seen that up to a thickness of 2 nm a fraction of BHJ spectra at least 0.25 can be seen in the UP spectra and the mean energy shift of the BHJ spectrum levels at 1.8 ±0.1 eV. The shift of the BHJ spectrum component also occurs when fitting the MIE spectra in Figure 3-8(C) but is 1.6 ±0.1 eV at 2nm MoO_3 and thus smaller than for the UP spectra. The shift for the UP and the MIE spectra are the same within error bar. From the same figure, the MoO_3 has not shown up with the deposition amount less than 0.5nm because the MoO_3 has diffused into BHJ, thus no MoO_3 can be observed at the outermost layer. The weighting factor then approaches unity around 1~2 nm thickness of MoO_3 which means that at this thickness full coverage of the BHJ with MoO_3 is reached. The conclusion is also supported by NICISS results. In Figure 3-8(B) and (D), BHJ spectra across a variety of energy shift have been obtained from the decomposition of both UP and MIE spectra. The range of energy shifts to a higher energy distribution with escalating amount of MoO_3 on BHJ. The distribution of energy shift of UPS reveals the existence and characterisation of intermediate energy states of BHJ at the interface.

The mean energy shift of the UP and MIE BHJ spectrum is increasing with increasing amount of MoO_3 and thus is induced by the deposition of the MoO_3. As outlined above, the shift is caused by the formation of a dipole between the bulk BHJ and the evaporated MoO_3. Both P3HT and $PC_{61}BM$ from the BHJ are affected by the dipole in terms of the third spectrum, which has been identified in SVD, featuring a similar shape with pristine BHJ. The dipole formation as a function of deposition amount and the diagram of an individual dipole are shown in Figure 3-9. A distribution of dipoles is located at the interface between MoO_3 and BHJ. This means that the individual dipoles at the interface have most likely the same strength but that they have a distribution in orientation relative to the surface normal. The energy of a single dipole can be calculated as the difference of WF, levelling as high as 3.3eV between MoO_3 and BHJ due to the fact the WF for MoO_3 is 6.9 eV while for BHJ it is 3.6 eV. This has been shown in Table 3-1. However in an interface, dipoles may encounter with each other thus cancel out,

resulting in relatively-lower interface dipole energy. Besides, an individual dipole oriented perpendicular to the surface normal does not contribute to a shift of the BHJ spectrum because the dipoles encounter with each other perpendicularly and the contribution is cancelling each out. It needs to point out that the observation of dipole from UPS does not fully cover the interface due to the probing depth. However, the peaking strength of such interface dipole normally presents at the surface layer, which bases on the distribution of MoO_3. The concentration of distribution of MoO_3 into BHJ peaks at the surface region, which is within the probing depth of UPS. The reason for the formation of the dipole has been attributed to the flow of electron from the BHJ to the MoO_3 due to energy level alignment[29]. The BHJ within dipole thus gains electrons and shifted to a lower binding energy.

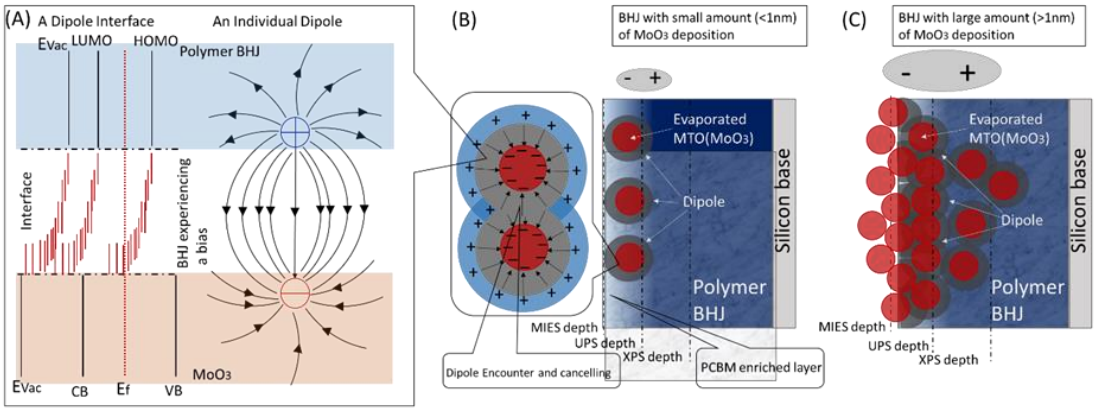

Figure 3- 9. The illustration of Dipole forming at the BHJ/MoO_3 interface under two circumstances: with minor and high MoO_3 coverage upon BHJ, the dipole affected on MoO_3 is mostly cancelling out because the MoO_3 particles diffuse into BHJ and are surrounded

The dipole formation is also supported by the XPS data, which shows the occurrence of a C_{1s} component at 283.5~284.1 eV. The C in the BHJ layer at the BHJ/MoO_3 interface locating within the dipole layer experiences an electric potential relative to the bulk of the BHJ layer. The position of the O_{1s} peak at binding energy 532 – 535.5 eV shows a similar shift of 1.7 eV as the above discussed C_{1s} peak and can be assigned to O_{1s} in $PC_{61}BM$. The O_{1s} peak related to MoO_3 is shifted only by 0.5eV. Although both P3HT and $PC_{61}BM$ are subjected to the dipole, the S peak related to the thiophene rings the P3HT does not show an obvious shift because the surface of the $PC_{61}BM$/P3HT BHJ layer is strongly enriched in $PC_{61}BM$ [30-32]. Thus the shift upon S is hard to identify due to the low relative concentration. Given the fact the MoO_3 does

not show shift in either XPS or UPS. With a high amount of deposition, energy shift of MoO_3 may occur on the MoO_3 particles which are close to polymer surface. Meanwhile the pristine MoO_3 particles accumulate on the surface. Thus the spectrum is dominated with pristine MoO_3 and the energy shift is difficult to identify. Another option can be discussed: the MoO_3 keeps constantly biased with all deposition thickness and even directly evaporated on Si substrate due to its high WF. However the hypothesis is beyond proving with the existing instruments.

3.4.5. Work Function Reconstitution and Reconstruction of Energy Levels at the MoO_3/BHJ Interface

The analysis of the UP and MIE spectra show that three different components contribute to the formation of the outermost layer: the BHJ, the BHJ but subject to be shifted electronically through the formation of a dipole at the surface and the MoO_3. All three components will contribute to the WF as measured by the UV-photoelectron spectra. The WF of samples formed by such materials has previously been reconstructed by Berlich et al. [33] using

$$WF_{fit}^{i} = \sum_{j=0}^{n} a_j^i \times \left(WF_{BHJ} + j \cdot \Delta E\right) + b \cdot WF_{MoO_3} \qquad \text{Equation 3-2}$$

WF_{BHJ} : the WF of the pristine BHJ

WF_{MoO_3} : the WF of pristine MoO_3

$j \cdot \Delta E$: the shift of the BHJ spectrum as shown on the x-axis of Figure 3-8(B)

a_j^i : the weighting factor of the shifted BHJ spectrum as shown in Figure 3-8(B)

b : the weighting factor for the MoO_3 reference spectrum

The reconstructed WF is shown in Figure 3-10 with comparison to the measured WF, yielding a close fitting to each other within error bars. Note that none of the parameters used in Equation 3-2 are parameters for fitting the WF but are all parameters are either measured or taken from fitting procedures of quantities other than the WF. The WF of BHJ within the dipole exhibits an increase due to the energy shift, the nature will be shown later in Figure 3-11. As such the

close matching of the measured WF with the reconstructed one gives further evidence that the fitting procedure of the UP and MIE spectra through Equation 3-1 is adequate. Due to the fact the weighting factors for fitting the WF are from the decomposition of valence electron region. The change upon WF is thus parallel to that of the valence band energy. Subsequently, the conclusion that the modification of WF is due to the interface dipole[17] has been demonstrated.

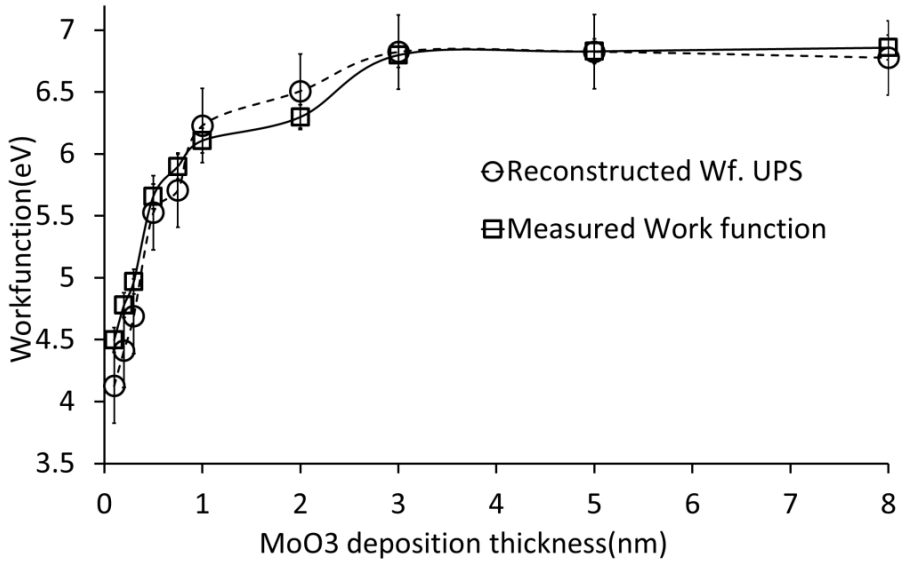

Figure 3- 10. Measured and reconstructed WF for MoO_3 thicknesses as measured by UPS

We have now determined all quantities for a full consideration of the energy levels at the MoO_3/BHJ interface in Table 3-1 and Figure 3-8(B) as a function of the variation of the thicknesses of the evaporated MoO_3 upon BHJ. The energy levels at the interface for the range of MoO_3 layer thicknesses are summarised in Figure 3-11. The zero-mark on the horizontal axis represents no deposition of MoO_3 and thus the surface of the BHJ layer and the zero mark on the vertical axis the position of the Fermi level. On the horizontal axis, the left side represents the inner part of the pristine polymer BHJ. The direction to the right from the zero mark on the horizontal axis represents the interface of the MoO_3 layer to the BHJ layer with increasing distance from the BHJ. The meaning of the layer thickness is that the value for an energy level is shown after deposition of a MoO_3 layer with a specific layer thickness. It is important to note that the MoO_3/BHJ interface, there is a mixed MoO_3/BHJ region, which is considered as dipole moment. The E_{HOMO} shown for the BHJ layer within the moment is given by the BHJ layer shifted energetically due to the formation of the dipole at the interface. This

energy level is indicated as an upwards bended curve extending to the right from the zero mark on the horizontal axis.

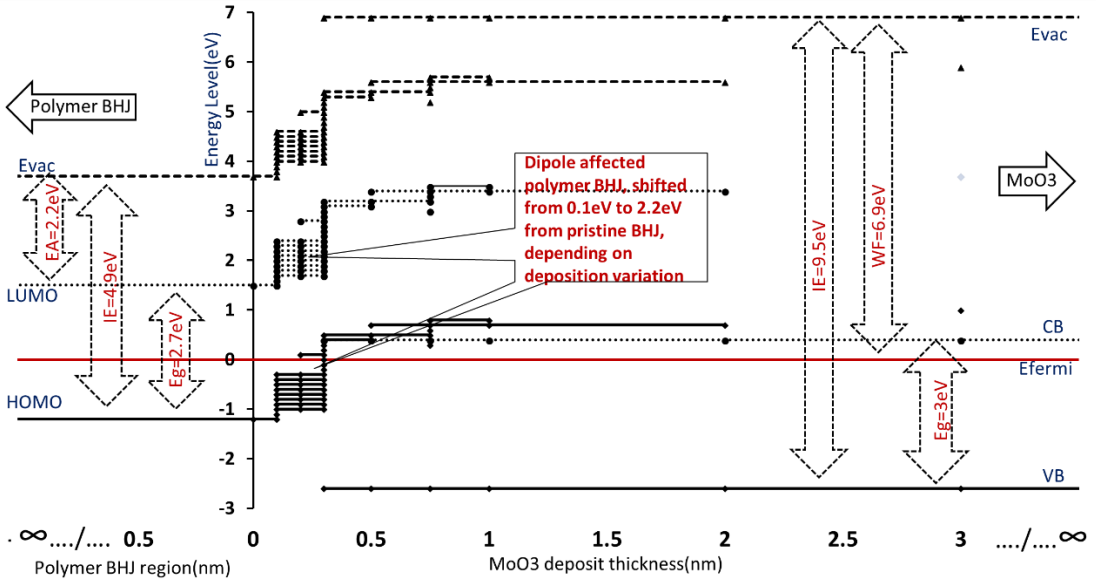

Figure 3- 11. The reconstruction of interface energy bands of pristine polymer BHJ, energy-shifted BHJ and pristine MoO_3 upon variation of MoO_3 deposition

3.4.6. Implication for the Operation of Charge Transport over the Interface

In a given polymer based solar cell a specific amount of MoO_3 will be deposited. Thus, we here will discuss also the electronic energy levels and the charge transfer of the combinations of the BHJ with two different MoO_3 layer thicknesses, namely 0.3nm and 2nm. The energy level schematics are shown in Figure 3-12. A series of intermediate energy states have been found upon deposition of 0.3nm MoO_3 with a range of energy shifts from 0.2-1.5eV see Figure 3-8(B). As has been described above, at this MoO_3 thickness the surface has not been covered. The transfer of charge carriers across the MoO_3/BHJ interface can be described as follows. Subsequently the hole transfers to the range of intermediate HOMO levels in the BHJ formed by the deposition of the MoO_3. It can be assumed that in the statistical average over many hole transfer processes the hole will transfer first to the lowest intermediate energy level and then proceed to the intermediate level with the highest energy shift. However, the energy level with the largest energy shift is at a shift of 1.5eV, resulting in an energy gap of approximately 0.2eV to the conduction band (CB) of MoO_3. Thus, in this case a barrier for the hole transfer exists at the MoO_3/BHJ interface which can result in a loss of charge carriers [34], yielding a fact of hole

trapping [35, 36]. In general the situation is the same when the MoO_3 the evaporated layer has a thickness of 2nm on BHJ. The only difference is that the energy level with the highest energy shift is now at a shift 2.1eV which exceeds the energy barrier of E_{CB} of MoO_3 and E_{HOMO} of BHJ. Thus, a continuous energy ladder from HOMO of pristine BHJ to shifted the energetically BHJ can be identified. The charge transfer over the interface thus abides by hole injection/electron extraction mechanism [1] and potentially improves the charge transfer efficiency.

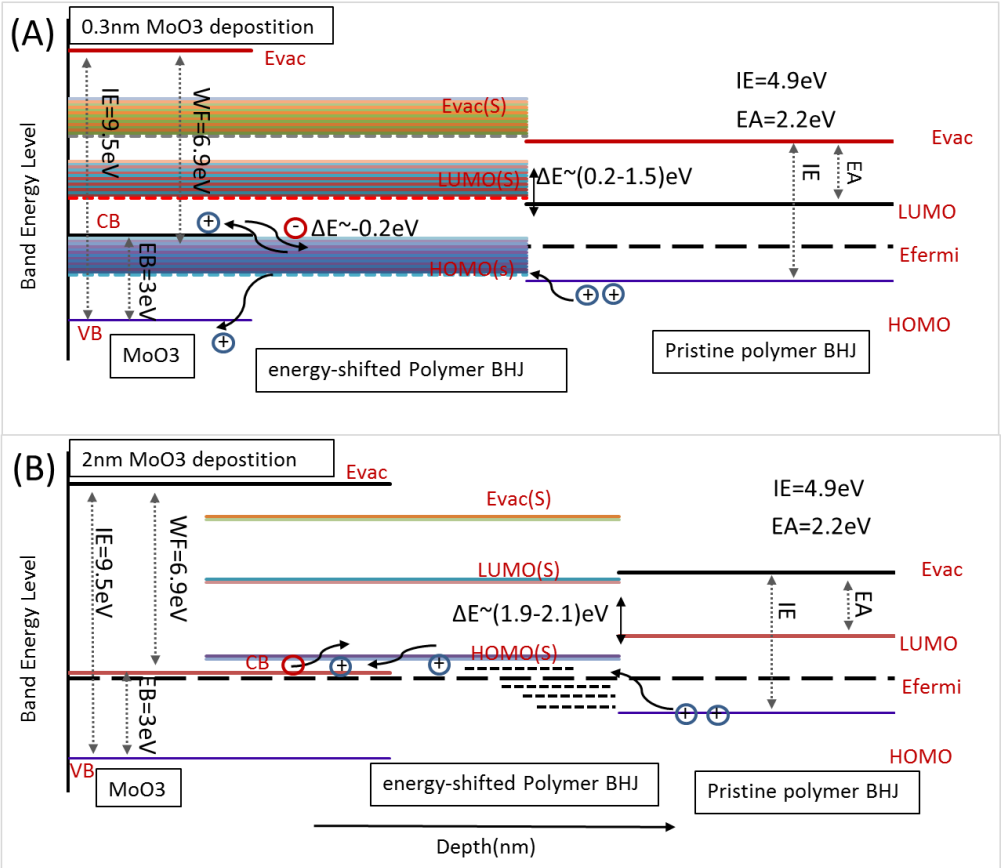

Figure 3- 12. The interface energy level structure of (A) 0.3nm and (B) 2nm MoO_3 on polymer BHJ and the illustration of charge transfer

It can be seen that the gap decreases with increasing MoO_3 thickness. While in the present work full devices have not been tested it can be expected that the device performance of a real photovoltaic cell will improve with increasing MoO_3 thickness due to the advancement of the hole injection mechanism [1]. A closed MoO_3 layer onto BHJ surface is also required otherwise the direct contact of electrode and polymer BHJ will cause current leakage. On the opposite, for a consideration of lower R_s of the device, a thinner MoO_3 layer is proposed. The choosing

of MoO_3 thickness as anode buffer layer in an organic device needs a thoughtful consideration under all circumstances

3.5. Conclusion

Upon evaporation of MoO_3 onto the BHJ formed by P3HT and $PC_{61}BM$, no chemical change of all chemical components is observed. The analysis of core and valence electron spectra show that a dipole is formed at the MoO_3/BHJ interface. When evaporated, the MoO_3 penetrates into the BHJ, and the penetration depth increases with increasing amount of evaporated MoO_3. The strength of the dipole at the MoO_3/BHJ interface increases with increasing MoO_3 layer thickness. The energy level of the unoccupied states has also been determined experimentally and thus a full picture of the electronic states at the MoO_3/BHJ interface has been developed.

The formation of the dipole at the MoO_3/BHJ interface influences the charge transfer over the interface. It can be calculated that thicker MoO_3 layers would be beneficial for charge transport. However, it would deteriorate the light absorption. This assumption will have to be tested with real devices. With a closed MoO_3 layer on BHJ surface, which is more than ~1nm deposition, the dipole strength at the interface is adequate for charge extraction/injection transport. The methodologies used in this chapter provide with a technique for the characterisation of dipole and intermediate energy levels at the interface. The change of dipole with a variety of treatment upon either the BHJ or the MoO_3 can be observed and quantified as well, which will be discussed in following chapters.

Reference

1. Hamwi, S., et al., *p-type doping efficiency of MoO3 in organic hole transport materials.* Applied Physics Letters, 2009. **94**(25): p. 253307.
2. Kröger, M., et al., *Role of the deep-lying electronic states of MoO3 in the enhancement of hole-injection in organic thin films.* Applied Physics Letters, 2009. **95**(12): p. 123301.
3. Ho, P., et al., *The effects of MoO3 treatment on inverted PBDTTT-C:PC71BM solar cells.* Solar Energy Materials and Solar Cells, 2013. **119**: p. 235-240.
4. Debecker, D.P., et al., *Total oxidation of benzene and chlorobenzene with MoO3- and WO3-promoted V2O5/TiO2 catalysts prepared by a nonhydrolytic sol–gel route.* Catalysis Today, 2010. **157**(1-4): p. 125-130.
5. Maniruzzaman, M., et al., *MoO3/Au/MoO3–PEDOT:PSS multilayer electrodes for ITO-free organic solar cells.* Materials Science in Semiconductor Processing, 2014. **27**: p. 114-120.
6. Ma, H., et al., *Interface Engineering for Organic Electronics.* Advanced Functional Materials, 2010. **20**(9): p. 1371-1388.
7. Meyer, J., *Electronic structure of molybdenum-oxide films and associated charge injection mechanisms in organic devices.* Journal of Photonics for Energy, 2011. **1**(1): p. 011109.
8. Meyer, J., et al., *Charge generation layers comprising transition metal-oxide/organic interfaces: Electronic structure and charge generation mechanism.* Applied Physics Letters, 2010. **96**(19): p. 193302.
9. Irfan, et al., *Work function recovery of air exposed molybdenum oxide thin films.* Applied Physics Letters, 2012. **101**(9): p. 093305.
10. Irfan, et al., *Strong interface p-doping and band bending in C60 on MoOx.* Organic Electronics, 2011. **12**(9): p. 1588-1593.
11. Meyer, J., et al., *Transition metal oxides for organic electronics: energetics, device physics and applications.* Adv Mater, 2012. **24**(40): p. 5408-5427.
12. Nakayama, Y., et al., *Origins of Improved Hole-Injection Efficiency by the Deposition of MoO3on the Polymeric Semiconductor Poly(dioctylfluorene-alt-benzothiadiazole).* Advanced Functional Materials, 2009. **19**(23): p. 3746-3752.
13. Yi, Y., et al., *The interface state assisted charge transport at the MoO(3)/metal interface.* J Chem Phys, 2009. **130**(9): p. 094704.
14. Meyer, J., et al., *Charge generation layers comprising transition metal-oxide/organic interfaces: Electronic structure and charge generation mechanism.* Applied Physics Letters, 2010. **96**(19): p. 193302.
15. Meyer, J. and A. Kahn, *Electronic structure of molybdenum-oxide films and associated charge injection mechanisms in organic devices.* Journal of Photonics for Energy, 2011. **1**(1): p. 011109.
16. Zhao, Y., et al., *Poly(3,4-ethylenedioxythiophene):poly(styrenesulfonate)/MoO3 composite layer for efficient and stable hole injection in organic semiconductors.* Journal of Applied Physics, 2012. **111**(4): p. 043716.
17. Wu, Q.-H., et al., *Electronic structure of MoO3−x/graphene interface.* Carbon, 2013. **65**: p. 46-52.
18. Cho, C., et al., *Molecular modification on dye-sensitized solar cells by phosphonate self-assembled monolayers.* J. Mater. Chem., 2012. **22**(7): p. 2915-2921.
19. Steim, R., F.R. Kogler, and C.J. Brabec, *Interface materials for organic solar cells.* Journal of Materials Chemistry, 2010. **20**(13): p. 2499.
20. White, R.T., E.S. Thibau, and Z.H. Lu, *Interface Structure of MoO3 on Organic Semiconductors.* Sci Rep,

2016. **6**: p. 21109.

21. Ishii, H., et al., *Energy Level Alignment and Interficial Electronic Structures at Organic/Metal and Organic/Organic Interfaces.* Advanced Materials, 1999. **11**(8).
22. Allahyarov, E., H. Lowen, and L. Zhu, *Dipole correlation effects on the local field and the effective dielectric constant in composite dielectrics containing high-k inclusions.* Phys Chem Chem Phys, 2016. **18**(28): p. 19103-19117.
23. Cattin, L., M. Morsli, and J. Bernède, *Improvement in the Lifetime of Planar Organic Photovoltaic Cells through the Introduction of MoO3 into Their Cathode Buffer Layers.* Electronics, 2014. **3**(1): p. 122-131.
24. Scudiero, L., Y. Shen, and M.C. Gupta, *Effect of light illumination and temperature on P3HT films, n-type Si, and ITO.* Applied Surface Science, 2014. **292**: p. 100-106.
25. Cheng, P., Y. Li, and X. Zhan, *A DMF-assisted solution process boosts the efficiency in P3HT:PCBM solar cells up to 5.31%.* Nanotechnology, 2013. **24**(48): p. 484008.
26. Shakir, I., M. Shahid, and D.J. Kang, *MoO3 and Cu0.33MoO3 nanorods for unprecedented UV/Visible light photocatalysis.* Chemical Communications, 2010(24).
27. Andersson, G.G., *Energy-loss straggling of helium projectiles at low kinetic energies.* Physical Review A, 2007. **75**(3).
28. Kadem, B., A. Hassan, and W. Cranton, *Efficient P3HT:PCBM bulk heterojunction organic solar cells; effect of post deposition thermal treatment.* Journal of Materials Science: Materials in Electronics, 2016. **27**(7): p. 7038-7048.
29. Vourdas, N., et al., *Omnidirectional antireflective properties of porous tungsten oxide films with in-depth variation of void fraction and stoichiometry.* Optics Communications, 2012. **285**(24): p. 5229-5234.
30. Schmerl, N. and G. Andersson, *A layered structure at the surface of P3HT/PCBM blends.* Phys Chem Chem Phys, 2011. **13**(33): p. 14993-15002.
31. Ng, A., et al., *Annealing of P3HT:PCBM blend film--the effect on its optical properties.* ACS Appl Mater Interfaces, 2013. **5**(10): p. 4247-4259.
32. Lu, Y., et al., *Temperature-dependent morphology evolution of P3HT:PCBM blend solar cells during annealing processes.* Synthetic Metals, 2012. **162**(23): p. 2039-2046.
33. Berlich, A., Y. Liu, and H. Morgner, *Growth of nickel nanoparticles on NiO/Ni(001): Evidence of adsorbed oxygen on metal particles by metastable induced electron spectroscopy (MIES).* Surface Science, 2008. **602**(24): p. 3737-3744.
34. Stolterfoht, M., et al., *Charge Transport without Recombination in Organic Solar Cells and Photodiodes.* The Journal of Physical Chemistry C, 2015. **119**(48): p. 26866-26874.
35. Harding, M.J., et al., *Variations in Hole Injection due to Fast and Slow Interfacial Traps in Polymer Light-Emitting Diodes with Interlayers.* Advanced Functional Materials, 2010. **20**(1): p. 119-130.
36. Ohkita, H., et al., *Direct observation of the carbazole hole trap in polymer solid films by the charge-resonance band.* Chemical Physics Letters, 1996. **263**: p. 602-606.

Chapter 4. Influence of Moisture on the Energy Level Alignment at the MoO_3/P3HT:$PC_{61}BM$ BHJ Interfaces

4.1. Abstract

In this work, a dramatic change in WF of MoO_3 and influence to the dipole forming at the interface of MoO_3/P3HT:$PC_{61}BM$ BHJ was observed when it is exposed even for short times to atmosphere. Valence electron spectroscopy shows that the mainly H_2O molecules diffuse to the MoO_3/organic interface and affect the electronic properties of the MoO_3/P3HT:$PC_{61}BM$ interface by forming a strong dipole. Moreover, further change simultaneously occurs in conduction and valence band energy of MoO_3, which has been addressed as a result of dielectric-H_2O attaching on MoO_3. The E_g of MoO_3 after exposure has been broadened, resulting in a potential decrease of the conductivity of metal oxide layer. The electron spectroscopy data is used to construct a comprehensive energy structure of the MoO_3/P3HT:$PC_{61}BM$ interface. From which, the charge injection mechanism has been determined to be ineffective after air exposure.

4.2. Introduction and Research Aim

Interfaces between organic and metal oxide materials commonly lead to the formation of dipoles at the respective interface[1]. Such interfaces are found and demonstrated in chapter 3 which is based on MoO_3/P3HT:$PC_{61}BM$ BHJ. The dipole plays a critical role for the charge transfer in the device[2]. Additionally to the strength of the dipole at the interface, it is also important to understand, which factors during creating the interface influence the dipole, how stable the dipole is and which conditions affect the dipole during operation of the devices after the interface has been established. Understanding of the strength and stability of the dipole are vital for fabricating photovoltaic devices because variation in the conditions of fabrication and operation could lead to substantially different results in device performance [3, 4].

MoO_3 feature a high WF, IE and EA [3, 5-10]. As an example, the WF of pristine MoO_3 is reported to be 6.7 eV [5, 11, 12], the IE about 9.7 eV [13] and the EA 6.5 eV. In our work, the electric properties are rather similar. Thus, it has been proposed [13-15] that the barrier between the CB of MoO_3 and the HOMO of polymer BHJ is small enough for efficient electron transfer [16, 17], which boosts the charge transfer over the interface and ultimately enhances the solar cell performance. The alignment of the energy levels affects the performance of other electronic

devices in a similar way.

However, in literature a range of values is reported for the electronic properties of metal oxides. A noticeable change of the electrical properties of MoO_3 was reported during the fabrication of device with the WF shifting to 5.1 eV [18] when MoO_3 is exposed to atmosphere. Further, the WF of TMOs [19-22], for instance MoO_3 processed with sol-gel method and solution process[23], was characterised to be 5.3 eV[24]. Thus, variations in the WF of MoO_3 of 1.6 eV have been reported in literature. When MoO_3 is used as ABL/HTL in a polymer-based photovoltaic device, a variation of the WF of 1.6 eV will influence the energy level alignment in the solar cells and consequently influence strongly the device performance. Exposure of the MoO_3/organic interface to moisture can occur for various reasons. Subsequent to the evaporation of MoO_3 onto the BHJ layer, samples are often exposed to air in the solar cell fabrication process. Exposure can also occur when MoO_3 layers are fabricated through sol-gel processes. Rempel [25] et al. have shown that a gaseous hydrated complex of the type of MoO_3/nH_2O is formed when samples are exposed to moisture. JianQiang [26] et al. have attributed the changes to a reduction of Mo^{6+}, occurring as Mo^{5+}. The occurrence of WF change has also been reported [27] to deteriorate the polymer device performance by significantly increasing the series resistance (R_s). In summary, exposure to air of cells fabricated with MoO_3 is known to influence the performance of solar cells but so far, it is unclear in which way exposure of the MoO_3/BHJ interface to air influences the energy levels of the materials at this interface.

In this work, firstly the strong dipole forming at the MoO_3/organic interface will be shown in case the interface is formed at ultra-high vacuum (UHV) conditions thus in the absence of water. Secondly, it will be demonstrated that the dipole also changes strongly in case the interface is exposed to moisture subsequently to fabrication. Depending on the condition of device fabrication and handling the devices after fabrication, these findings have strong implication on the efficiency of the cell devices, the reproducibility of their functioning and on their lifetime. Electron spectroscopy is employed in the work for analysing the chemical and electronic properties of the interface and neutral impact collision ion scattering spectroscopy for determining concentration depth profiles of all materials.

4.3. Sample Preparation and Treatment

The methods of blending P3HT and $PC_{61}BM$ and the deposition of metal oxides are described in experimental section. The sample preparation in this work is illustrated in Figure 4-1:

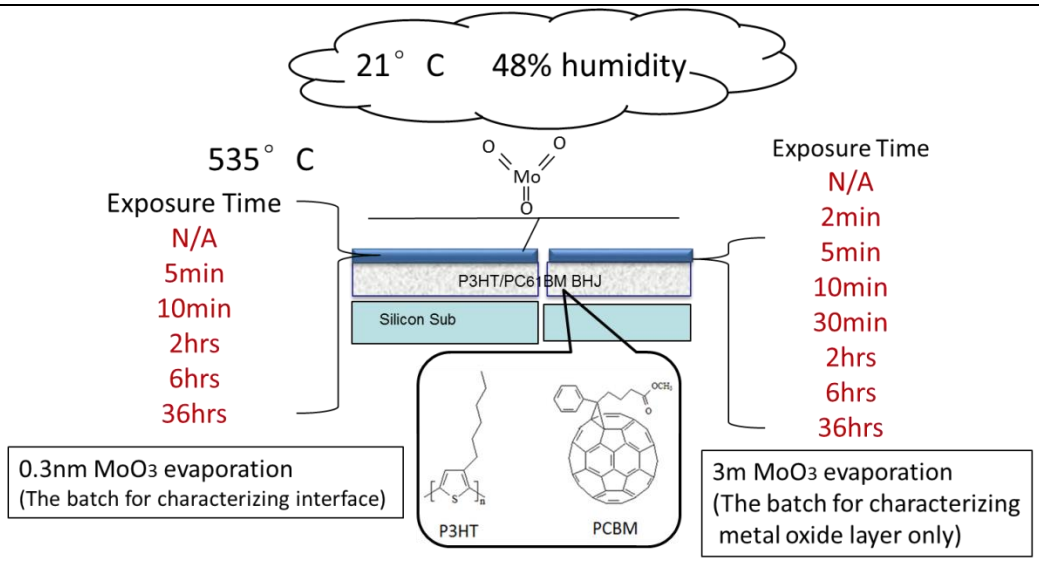

Figure 4- 1. Sample structure and air exposure treatments

All samples were made in the same batch and processed together. The MoO_3/BHJ samples were exposed to air for a range of time up to 168 hours in order to mimic conditions that could occur during the fabrication processes of the organic photovoltaic devices. Samples were prepared with two kinds of MoO_3 layer thicknesses. Samples with 3 nm MoO_3 layers were fabricated to investigate the properties of the MoO_3 only. At a layer thickness of 3 nm the underlying BHJ layer is not visible in UP spectra probing the valence electron properties. Investigating samples with a thickness of 0.3 nm MoO_3 allows probing the changes at the MoO_3/BHJ interface as a consequence of the exposure to air. The second batch of samples with 0.3nm of deposited MoO_3 were exposed to air only for 5min, 2 hours and 6 hours respectively and measured with MIE/UP spectroscopy. The exposure condition was set to 21 ºC and 47% humidity in a laboratory condition. Subsequently the samples were transferred to analysis chamber under UHV condition ($<10^{-9}$) for applying spectroscopies. Therefore, further air contamination and reaction are prohibited.

4.4. Results and Discussion

4.4.1. Chemical Characteristics and Valence States Shift of the Air-exposed MoO_3/BHJ interface

The high-resolution XP spectra of Molybdenum(Mo), Sulphur(S), Carbon(C) and Oxygen(O) of the samples of 3nm MoO_3 thickness at various exposure times to air are shown in Figure 4-2. The relative concentration of C, Mo and O and the energy shift of C and O are shown in

Figure 4-3 (A), (B). The relative concentration calculated for the adsorption of H_2O and O_2 is shown in Figure 4-3 (C).

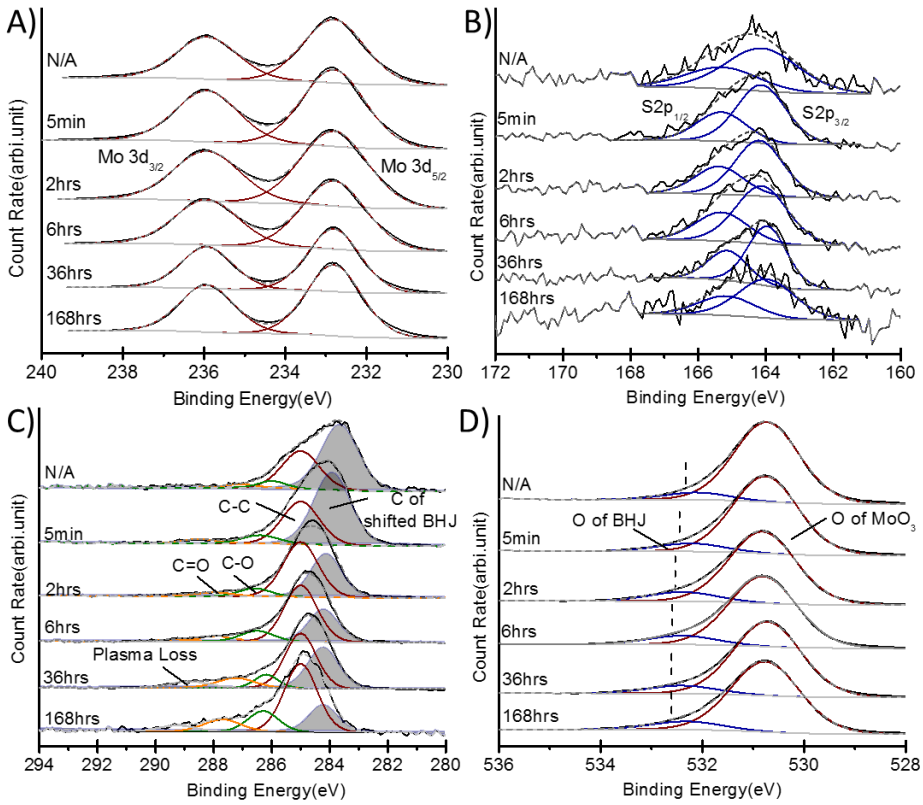

Figure 4- 2. Fits of the high resolution XP spectra of (A) Mo, (B) S, (C) C and (D) O. The changed and shifted peaks are tagged with shadow

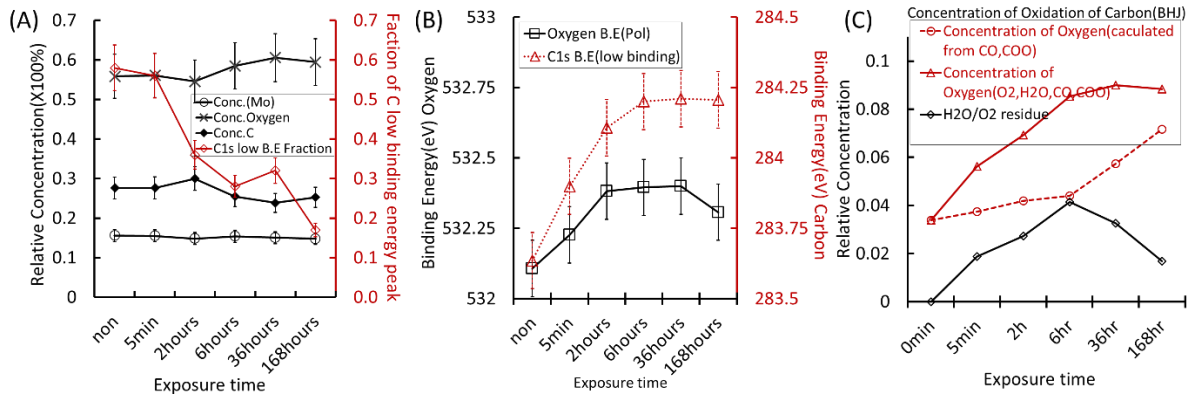

Figure 4- 3. (A) The change of relative concentration of O, C and Mo and the fraction of low binding energy C peak during air exposure; (B) The energy shift of low binding energy C and O peaks of polymer BHJ; (C) The relative concentration of H_2O and O_2 adsorbed on the sample as a function of exposure time

In Figure 4-2(A) and (B), the energy positions of the Mo and S peak are shown. All Mo high

resolution spectra could be fitted with a doublet with the Mo $3d_{5/2}$ peak found at 232.8 ±0.15 eV, and can be assigned as Mo^{6+}[28]. Upon exposure to air, there is no shift in the position or FMHW of Mo in the XP spectra compared to the pristine MoO_3 spectrum indicating no change in the oxidation state of the Mo due to exposure to air. Other previous work report a shift of the Mo peak of MoO_3 upon 30min air exposure but did not outline the calibration procedure of the reported XP spectra[26]. The S peak does not show a shift upon increasing air exposure time, indicating the P3HT was not significantly affected during air exposure.

Four individual peaks are found when fitting the C1s spectrum of the unexposed sample as can be seen in Figure 4-2 (C). The C peak with the lowest binding energy is found at 283.6 ±0.15 eV and is attributed to the formation of a dipole at the interface as described in detail in chapter 3 [29]. The respective C species is then attributed to a fraction of the polymer, which is electronically biased in the dipole field formed at the MoO_3/BHJ interface.

There is also evidence of oxidation of C in the BHJ, with C1s peaks at 286.3 ±0.15 eV and 288.0 ±0.15 eV attributed to C-O and C=O, respectively. This result shows that the BHJ after deposition of MoO_3 is oxidised due to the exposure to O and moisture, but importantly as described above, there is no evidence of reduced Mo in the XPS. Such oxidation of the BHJ does not occur if the BHJ only is exposed to air, which compares a BHJ sample that is freshly prepared with one that has been exposed to air for 36 hours(spectra not shown here). The oxidation of the polymer after describing the XPS results of O will be discussed.

Two peaks are found that are attributable to O species as shown in 错误!未找到引用源。(D). One peak has a position at 530.8 ±0.15 eV[30] which is attributed to the O in MoO_3 and does not shift during the air exposure, supporting that the MoO_3 is not changing oxidation states due to the exposure to moisture.

The binding energy of the second peak is 532.1 ±0.15 eV for the non-exposure sample and can be attributed to O of the BHJ. At the same position also O of H_2O and adsorbed O_2 would occur. The O content slightly increases with exposure time to air as can be seen in Figure 4-3 (A). As can be seen in Figure 4-2(D) and 4-3 (B), the O peak related to the BHJ shifts slightly during the air exposure to 532.4 ±0.15 eV over the period of 36 hours, a change of 0.3 eV.

The change in intensity and in binding energy of the C peaks due to air exposure can be seen in Figure 4-3 (A) and (B): the fraction of the 283.6 eV peaks decreases with increasing duration of the air exposure while the energy position shifts to higher binding energy. After 168 hours exposure the fraction is merely 0.17 which positions at 284.2 ±0.15 eV. The binding energy

shift and fraction decrease of C low binding energy peak and O peak of polymer BHJ indicates that the BHJ was affected by the interfacial dipole in a similar way as the C of the BHJ. The shift of the O peak initially positioned at 532.1 eV peak is attributed to the weakening of the dipole at the MoO_3/BHJ interface upon exposure to air. The fact that the shift of the 532.1 eV O 1s is lesser than that of the 283.6 eV C 1s peak could be a result of the O containing functional group being located further away from MoO_3 at the MoO_3/BHJ interface.

In Figure 4-3 (C) the change in concentration of C related to the oxidation of the BHJ and the change in O related to the H_2O/O_2 at the interface and the oxidation of the BHJ are shown. For C the 286.3 and 288.0 eV peaks are considered reflecting the oxidation of the BHJ and for O the 532.1 eV peak is considered reflecting the oxidation of the BHJ as well as the adsorption of H_2O and potentially of O_2. The increase in O related to water and adsorption of H_2O and potentially O_2 (solid red line) increases faster with exposure to air than the increase in oxidation products of the BHJ (dashed red line). The black solid line shows the difference in both graphs. The difference shows that exposure to air causes two changes. The first change is the adsorption of H_2O and potentially of O_2. The second and later change is the oxidation of the BHJ. Electron transfers from BHJ to MoO_3 at the interface due to the energy level alignment, which decreases the oxidation potential of BHJ. Therefore the BHJ at the interface is more likely to be oxidised.

4.4.2. Elemental Depth Distribution

NICISS has been applied to determine the relative concentration of Mo evaporated onto the BHJ as a function of both depth and energy loss. The result is shown in Figure 4-4. A distribution of MoO_3 thicknesses on the polymer BHJ can be identified. With the ongoing air-exposure process, the concentration of Mo at the surface decreases slightly and a shift of Mo to larger depth can be observed. The reason for this shift is that either MoO_3 penetrates deeper into the polymer BHJ or that components from the atmosphere have adsorbed onto the MoO_3. The former is the more likely reason.

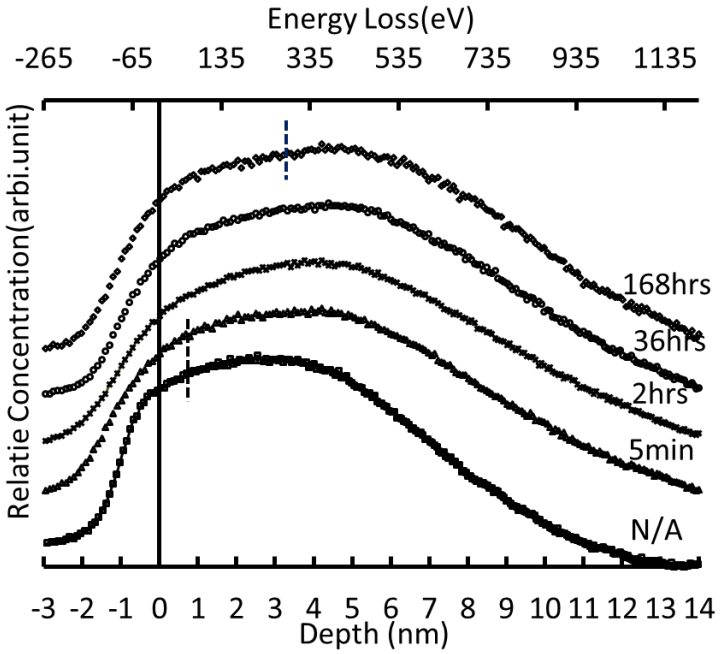

Figure 4- 4. NICISS result shows Molybdenum depth profile during the various exposures, the relative concentration is via two axis-energy loss and depth scale

4.4.3. Decomposition and Analysis of MIES/UPS Spectra

a) The Analysis of MIES/UPS of the Samples with Exposure

To understand the implications of the observations from the XPS – that there is evidence for the strength of the dipole at the interface changing, but no change in oxidation state of the MoO_3 - the UP spectra of all samples discussed in the XPS section and further samples exposed for 2 min, 10 min and 30 min to air are shown in Figure 4-5 (A) and (B). IPES has been applied to samples which have been exposed to air for 5 min, 30 min, 2 h and 6 h. The results are shown in Figure 4-5 (B). In Figure 4-5 (C) the valence electron region in the MIE spectra and in Figure 4-5 (D) the values are plotted.

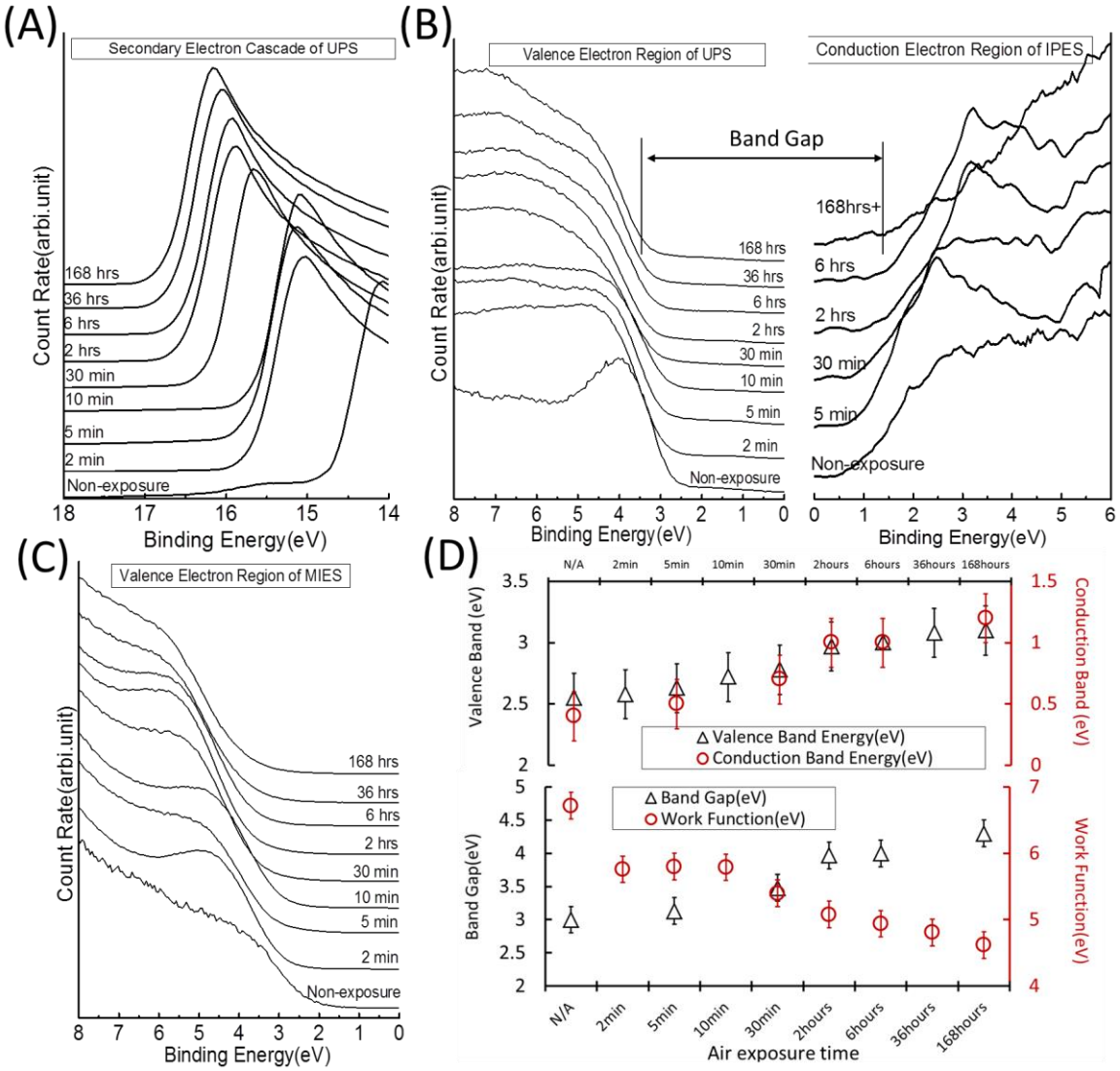

Figure 4- 5. (A) The secondary electron cut-off in the UP spectra of the samples from non-exposure to 168-hour exposure; (B) The valence electron region of UP spectra and the conduction electron region of IPES of selected samples; (C) The valence electron region of the MIE spectra of all exposed samples; (D) Up: The plots of change upon E_{CB} and E_{VB}; Below: The plots of change upon WF and E_g as function of length of exposure to air

The plot of work function (WF) is shown in Figure 4-5(D) which decreases with increasing exposure time of the samples to air and for the non-exposed sample; it is 6.7 $\pm$ 0.1eV and then dramatically decreases to 5.7 $\pm$ 0.1 eV after merely 2-min exposure. After exposure to air for 168hrs, the WF of the sample levels at 4.6 $\pm$ 0.1 eV. The valence band energy (E_{VB}) of the samples is illustrated as well which exhibits a gradual increase from 2.6 $\pm$ 0.1eV of non-exposed sample to 3.1 $\pm$ 0.1eV after 168-hour exposure. Meanwhile an increase in conduction

band energy (E_{CB}) was observed. The E_{CB} initiates at 0.4 ± 0.1eV and increases to 0.5 ± 0.1eV after 5-min exposure, then peaks at 1.2eV ± 0.1eV. Therefore, the band gap energy (E_g) was calculated. The E_g of pristine MoO_3 levels at 3.0 ± 0.2eV, which escalates with exposure time and peaks at 4.3 ± 0.2eV after 168-hour exposure. The E_g has been broadened by 1.3eV in all, as such it can be concluded the conductivity of MoO_3 layer will be declined due to the fact a broadened band gap normally indicates such change [31, 32]. The finding of changes upon WF and E_{CB} is instructive which would affect the charge transfer over the interface. The nature will be discussed later.

To determine if the changes in WF and the electronic properties were due to O_2 or moisture in the air, three conditions were examined: normal laboratory atmosphere (21℃, 42% humidity), dry N_2 (99.99%) and dry air (H_2O<25ppm)) individually for 40 minutes each. The secondary electron cut-off in the respective UP spectra is shown in Figure 4-6. Exposure the samples to humid air decreases the WF from 6.7 ±0.1 eV to 5.5 ±0.1 eV thus by 1.2 ±0.2 eV. Exposure to N_2 decreases the WF by 0.1 ±0.2 eV and by exposure to dry air by 0.2 ±0.2 eV. This gives evidence that the decrease in WF upon exposure to laboratory air is due to the moisture content in the air and not due to exposure to N_2 or O_2. The very small changes in WF upon exposure to N_2 and dry air are most likely related to the rest humidity content of the N_2 and dry air used. Irfan et al. reported [33] that O_2 influences the samples as well but the impact is limited and inferior to the effect of H_2O because the H_2O is more likely to stick on surface and diffuse into bulk.

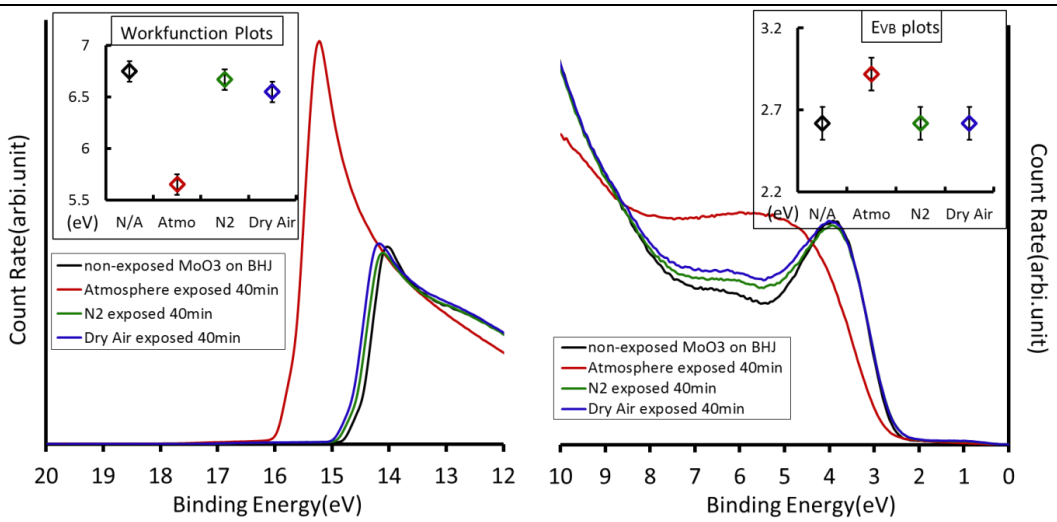

Figure 4- 6. MoO_3/BHJ samples exposed to atmosphere/N_2/dry-air and the UPS results. Left: secondary electron region with WF plots; Right: valence electron region with E_{VB} plots

The heating upon air-exposed MoO_3 leads to the recovery of the WF to some degree. As reported [17], the WF increases back to 6.3 eV with 500 ℃ heating, which, however, is not realistic for interfaces involving organic compounds to their lack of stability at such high temperatures. Heating to elevated temperatures like 300 ℃ causes reduction of MoO_3[28]. Temperatures below 200 ℃ only cause reduction of MoO_3 and no recovery of WF can be observed.

b) Decomposition of Valence Electron Region of MIE/UP Spectra

Examination of the valence electron region (0-10 eV) of the MIE and UP spectra indicated a complex system made up of two reference spectra. SVD was used to analyse by decomposing the spectra and identifying the reference ones. In Figure 4-7 (A), the two reference spectra required to fit the MIE spectra and a comparison with pristine MoO_3 and long-time exposed MoO_3 are shown. It is reasonable to assign Ref. A to pristine MoO_3 because of the high coverage with MoO_3 and similar features. The exact nature of the other reference spectrum (Ref. B) is not known and for this reason denoted as a complex MoO_3 affected by H_2O (MoO_3•H_2O) [34-36]. The normalised weighting factors of both reference spectra are given in Figure 4-7 (B). With increasing exposure time a sharp increase of the weighting factor of MoO_3•H_2O (Ref. B) can be observed. The weighting factor for Ref. B increases from 0 to 0.68 within the first 5-minute of exposure and to 0.94 within the first 2 hours. The weighting factor then stays rather constant. The weighting factor of Ref. A shows the opposite trend.

The decomposition of the UP spectra also results in two reference spectra. One of the reference spectra (Ref. A) is rather similar to the non-exposed MoO_3 spectrum (dark dash line) in Figure 4-7(C). Thus, the Ref. A represents approximately the non-exposed MoO_3. The Ref. B is then related to MoO_3 being exposed to H_2O. The weighting factor for Ref. B in fitting the UP spectra shows a similar trend as the weighting factor for Ref. B of the MIE spectra in Figure 4-7(D), the Ref. B (MoO_3•H_2O) increases dramatically from 0.17 to 0.69 after merely 5 min exposure and then and then becomes the by far dominating weighting factor. The weighting factor of the unexposed sample is 0.17. It could be expected that this weighting factor is 0 rather than 0.17. The discrepancy is most likely due to the fact that the SVD algorithm can result in a small degree of mixing of the reference spectra rather than finding the reference of the pristine substances. The nature of the weighting factors for the MIE and UP spectra is rather similar.

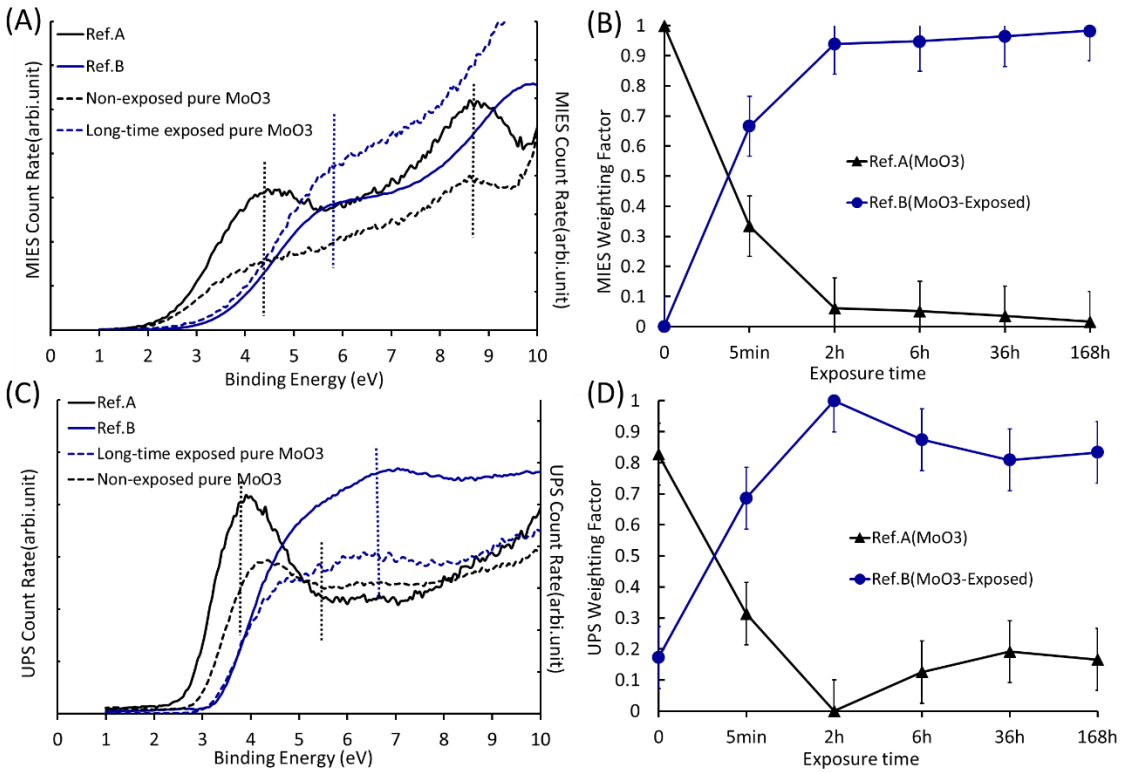

Figure 4- 7. (A)(C) The decomposed MIE and UP spectra using SVD method and the comparison with non-exposed MoO_3 and long-time exposed MoO_3 spectra; (B) (D) The weighting factors of individual reference spectra of analysed MIES and UPS

c) The influence of moisture on dipole forming at MoO_3/BHJ interface

To understand more details of the influence of air exposure of the BHJ/MoO_3 interface of samples with 0.3 nm of MoO_3 evaporated onto the BHJ layer were investigated with UPS and MIES. The reason for choosing a MoO_3 layer of 0.3 rather than 3 nm for these experiments is that the probing depth of UPS and MIES is less than that of XPS.

The 0.3nm MoO_3 on polymer BHJ samples were exposed for 5min, 2 hours and 6 hours individually. In this set of spectra, a new component in the MIE and UP spectra can be identified. This new component corresponds to the BHJ layer and cannot be seen in the UP and MIE spectra of the 3 nm MoO_3 samples. MoO_3 cannot be seen in the MIE spectra at such thickness because the MoO_3 forms a closed layer on the BHJ.

When evaporating an increasing amount of MoO_3 it is found that the UP and MIE spectra gradually shift to lower binding energy. From these results the weighted shifting method (WSM) described and used in chapter 3 for fitting the spectra can be modified. The weighted shifting method is applied by using the following procedure:

$$S^{(i)}_{meas} = \sum_{j=0}^{n} a^{(i)}_j \times S_{BHJ}\left(E + j \cdot \Delta E\right) + b \cdot S_{MoO_3} + c \cdot S_{e-MoO_3} \quad \text{with} \quad \sum_j a^{(i)}_j + b + c = 1$$

$$\Delta E^{(i)}_{mean} = \sum_{j=0}^{n} a^{(i)}_j \cdot j \cdot \Delta E$$

Equation 4-1

S_{BHJ} : the spectrum of the BHJ layer

S_{MoO3} : the spectrum of MoO_3

$S_{e\text{-}MoO3}$: the spectrum of MoO_3 exposed, which is identified from SVD

ΔE : an energy increment

$j \cdot \Delta E$: an integer multiple of the energy increment for which S_{BHJ} is shifted in applying Equation 4-1

$\Delta E^{(i)}_{mean}$: the mean shift for spectrum i. $\Delta E^{(i)}_{mean}$ is a consequence of the dipole formed at the BHJ/MoO_3 interface with evidence for such diploe formation. The first term in equation reflects the fact that the spectrum of the BHJ layer is shifted by a range of energy differences and the weighting factor $a^{(i)}_j$ reflects which fraction of the BHJ is affected by the energy shift $j \cdot \Delta E$. The graph of the weighting factors of the shifted BHJ spectra in MIES and UPS is shown in Figure 4-8 and the fraction of reference exposed MoO_3 is included.

The distributions of weighting factors for the energy shift move to lower binding energies with increasing exposure time for both MIES and UPS. The same holds for the mean energy shift calculated via the procedure described in chapter 3. The mean energy shift is shown in the insets. In MIES, the mean energy shift moves from 1.0 ± 0.1 eV to 0.6 ± 0.1 eV within 6 hours of exposure time. Oxidation of BHJ may consequently change the feature of spectra of BHJ. However it only occurs after exposure for more than 2 hours. The change of energy shift is mainly found within 2 hours exposure. In UPS, the weighted average shows a shift from 1.3 ± 0.1 eV to 1.1 ± 0.1 eV. The decrease in the mean energy shift demonstrates that the dipole at the BHJ/MoO_3 interface decreases upon exposure to air. In conjunction with the XPS results and the change of WF it can be concluded that the change in the change in dipole at the BHJ/MoO_3 interface is a consequence of the humidity of air. It is important to note that the change in dipole at the BHJ/MoO_3 interface upon exposure to air is different than the change in WF. This illustrates that conclusions of the change in energy levels at the interface cannot be derived from analysing the change in WF but require investigating the energy levels at the BHJ/MoO_3 interface directly.

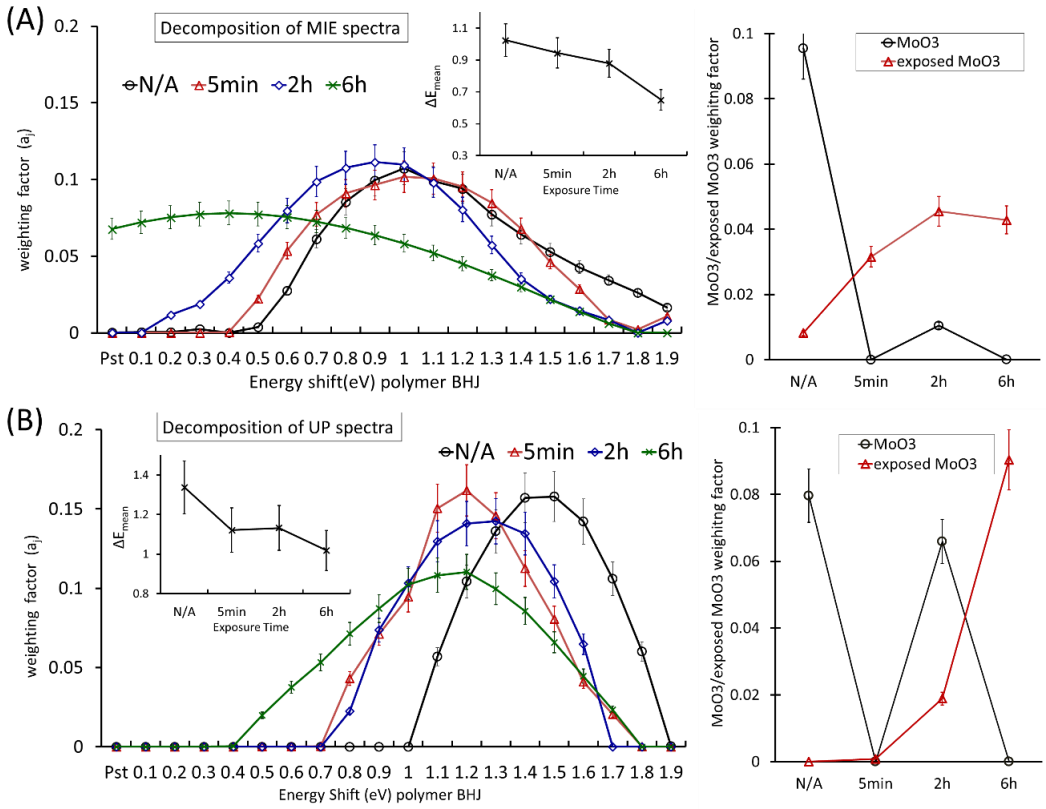

Figure 4- 8. (A) Weighting factor of the shifted polymer BHJ spectra of MIES; (B) weighting factor of the shifted polymer BHJ spectra of UPS; the insets show the weighted shifted energy of polymer BHJ spectra as function of exposure time; the Figures at the right side illustrate the weighting factor of MoO_3 and exposed MoO_3 •H_2O

4.4.4. Model for the Change in BHJ/MoO_3 Interface Dipole

The formation of dipole at the interface has been demonstrated in previous chapter. Upon exposure to air, this dipole decreases as the shifted species in the UPS and MIES of the 0.3nm MoO_3 decreases with exposure time to air.

The likely explanation of the decrease in the strength of the dipole at the BHJ/MoO_3 interface upon exposure to air is that H_2O diffuses to the MoO_3/polymer BHJ interface as illustrated in Figure 4-9 (A). In the upper part of the Figure the situation of the interface between MoO_3 and BHJ is illustrated with the interface layer between the two substances. In the lower part the schematic shows that H_2O molecules have diffused to the MoO_3/BHJ interface. H_2O has such a strong dipole and is free to orient at the interface. A dielectric such as H_2O will always orient at the interface such that it will counter the existing dipole by generating a bias under the effect of electrostatic potential, countering the dipole direction, redirecting and confines the charge.

This results in a decrease of the diploe formed at the pristine BHJ/MoO_3 interface.

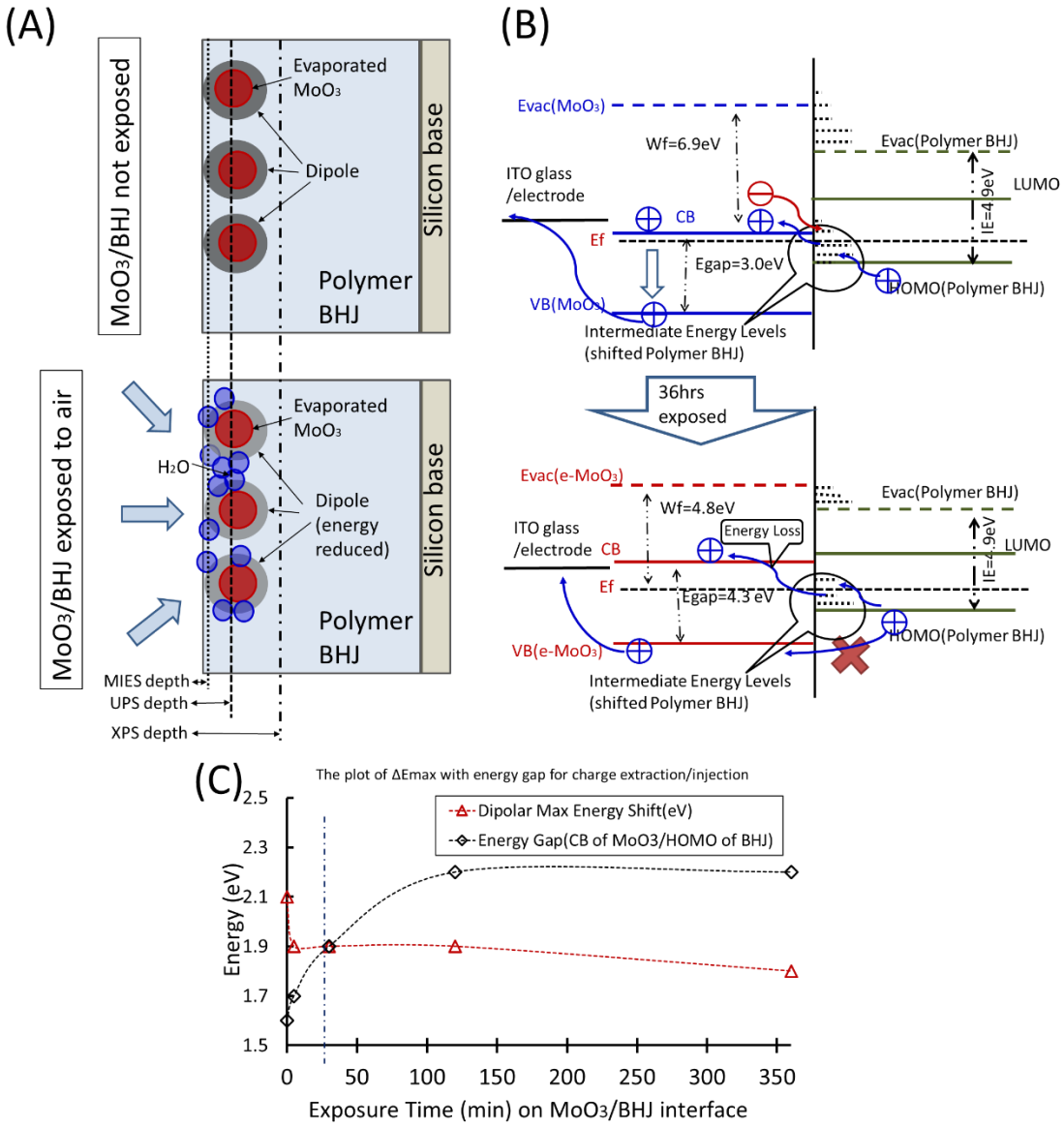

Figure 4- 9. (A) The illustration of the diffusion of H_2O from atmosphere to the MoO_3/Polymer BHJ interface. H_2O diffusion to the interface is a possible reason for the reduction in dipole at the MoO_3/BHJ interface. The choice of the shape of the MoO_3 particles is arbitrary and not important for the illustration of the mechanism. (B) The energy level model for the MoO_3/polymer BHJ interface before and after exposure to air. The position of the energy levels of MoO_3, BHJ and the intermediate energy levels is based on the measurements with UPS; (C) The plot of the maximum energy shifts and the growth of energy gap as a consequence of exposure

The finding of this work has strong implications for devices using MoO_3 or similar metal oxides to form interfaces with organics such as polymer or fullerene and the blended BHJ. The

energy level diagram of the MoO_3/BHJ interface unexposed to moisture can be described such that the charge transfer follows the charge injection mechanism as described in reference[5, 14]. The reason is that the positioning of energy bands of MoO_3 and BHJ due to the dipole formed at the interface results in the alignment of the HOMO of the BHJ with the CB of MoO_3. The diagram is illustrated in the top part of Figure 4-9 (B) and the energy positions are derived from the evaluation of UPS/IPES measurements.

The first implication of air exposure is that the energy level alignment between MoO_3 and BHJ is changing and creates an energy barrier between the air exposed-MoO_3 and HOMO of BHJ. The energy level diagram of the interface which has been exposed for 36 hours to moisture is shown in the lower part of Figure 4-9 (B). In Figure 4-9 (C) the change of the dipole strength at the MoO_3/BHJ interface and the gap between HOMO of BHJ and CB of MoO_3 are shown as function of the time of exposure to moisture The energy gap levels at 1.6 eV while in chapter 3[14] the maximum energy shift due to the dipole formation of BHJ $\Delta E_{Max}^{(i)}$ has been found to be 2.1 eV. At this condition the $\Delta E_{Max}^{(i)}$ exceeds the energy gap thus the charge transfer can be referred to the top part of Figure 4-9 (B). With ongoing exposure of the sample to moisture, the energy gap increases due to the increase of E_{CB} of MoO_3 while the $\Delta E_{Max}^{(i)}$ decreases. The change of $\Delta E_{Max}^{(i)}$ (the change of value can be referred to Figure 4-8 (B)) is shown in Figure 4-9 (C) with the corresponding change of the energy gap as derived from Figure 4-5 (D). It can be seen that after 30min exposure to moisture the energy gap exceeds $\Delta E_{Max}^{(i)}$, and the energy levels of HOMO and BHJ are no longer aligned. As a consequence, a decrease of the charge transfer over the interface can be expected. The misalignment of the energy levels becomes even worse with increasing exposure time to moisture. This means that the interface is expected to turn into a hole-trap [37-39], deteriorating the charge transfer efficiency.

A second consequence of the exposure to air is also illustrated in Figure 4-5 (D). H2O acts as a dielectric, significantly broadening the E_g, which could reduce the conductivity of MoO_3. Both impacts together increase the R_s within a photovoltaic and thus decrease the overall performance of the device.

It needs to be noted here that the findings of the present work go far beyond the MoO_3/BHJ interface investigated in the chapter. As outlined, most organic/inorganic interfaces will form diploes at their interface. The influence of moisture invasion upon V_2O_5 and WO_3-BHJ interfaces will be studied later. Most importantly, the strength of the dipole is likely to change in case the interface is exposed to moisture. The exposure to moisture could cause the dipole

to be eliminated. If the interface is part of an electronic device, the function of the device can strongly change.

4.5. Conclusion

The interface between MoO_3 and a BHJ formed by P3HT and $PC_{61}BM$ has been investigated with electron spectroscopy. The dipole formation at the MoO_3/BHJ interface has been further proved. The dipole decreases when the interface is exposed to air. The decrease in the strength of the dipole is most likely caused by the diffusion of mainly H_2O to the interface during exposure to air. The implication for the performance of photovoltaic devices is discussed.

Reference

1. Ishii, H., et al., *energy level alignement at model interfaces of organic electroluminescent devices studied by UV photoemission: trend in the deviation from traditional way of estimating the interfacial electyronic structure.* IEEE Journal of Selected Topics in Quantum Electronics, 1998. **4**: p. 24.
2. Zhang, M., et al., *Organic Schottky barrier photovoltaic cells based on MoOx/C60.* Applied Physics Letters, 2010. **96**(18): p. 183301.
3. Vasilopoulou, M., et al., *Reduction of Tungsten Oxide: A Path Towards Dual Functionality Utilization for Efficient Anode and Cathode Interfacial Layers in Organic Light-Emitting Diodes.* Advanced Functional Materials, 2011. **21**(8): p. 1489-1497.
4. Schubert, S., et al., *Oxide Sandwiched Metal Thin-Film Electrodes for Long-Term Stable Organic Solar Cells.* Advanced Functional Materials, 2012. **22**(23): p. 4993-4999.
5. Meyer, J., et al., *Transition metal oxides for organic electronics: energetics, device physics and applications.* Adv Mater, 2012. **24**(40): p. 5408-5427.
6. Meyer, J., et al., *Electronic structure of Vanadium pentoxide: An efficient hole injector for organic electronic materials.* Journal of Applied Physics, 2011. **110**(3): p. 033710.
7. Chambon, S., et al., *MoO3 Thickness, Thermal Annealing and Solvent Annealing Effects on Inverted and Direct Polymer Photovoltaic Solar Cells.* Materials, 2012. **5**(12): p. 2521-2536.
8. Chen, S., et al., *Metal oxides for interface engineering in polymer solar cells.* Journal of Materials Chemistry, 2012. **22**(46): p. 24202.
9. Cho, C., et al., *Molecular modification on dye-sensitized solar cells by phosphonate self-assembled monolayers.* J. Mater. Chem., 2012. **22**(7): p. 2915-2921.
10. Baek, W.H., et al., *Effect of P3HT:PCBM concentration in solvent on performances of organic solar cells.* Solar Energy Materials and Solar Cells, 2009. **93**(8): p. 1263-1267.
11. Yi, Y., et al., *The interface state assisted charge transport at the MoO(3)/metal interface.* J Chem Phys, 2009. **130**(9): p. 094704.
12. Nakayama, Y., et al., *Origins of Improved Hole-Injection Efficiency by the Deposition of MoO3on the Polymeric Semiconductor Poly(dioctylfluorene-alt-benzothiadiazole).* Advanced Functional Materials, 2009. **19**(23): p. 3746-3752.
13. Kröger, M., et al., *Role of the deep-lying electronic states of MoO3 in the enhancement of hole-injection in organic thin films.* Applied Physics Letters, 2009. **95**(12): p. 123301.
14. Hamwi, S., et al., *p-type doping efficiency of MoO3 in organic hole transport materials.* Applied Physics Letters, 2009. **94**(25): p. 253307.
15. Meyer, J., et al., *Charge generation layers comprising transition metal-oxide/organic interfaces: Electronic structure and charge generation mechanism.* Applied Physics Letters, 2010. **96**(19): p. 193302.
16. Meyer, J. and A. Kahn, *Electronic structure of molybdenum-oxide films and associated charge injection mechanisms in organic devices.* Journal of Photonics for Energy, 2011. **1**(1): p. 011109.
17. Irfan, et al., *Work function recovery of air exposed molybdenum oxide thin films.* Applied Physics Letters, 2012. **101**(9): p. 093305.
18. Cattin, L., M. Morsli, and J. Bernède, *Improvement in the Lifetime of Planar Organic Photovoltaic Cells through the Introduction of MoO3 into Their Cathode Buffer Layers.* Electronics, 2014. **3**(1): p. 122-131.
19. K.Galatsis, Y.X.L., W.Wlodarski, K.Kalantar-zadeh, *Sol-Gel prepared MoO3-Wo3 thin-films for O2 gas sensing.* Sensors and A ctuators, 2001. **B 77**: p. 478-483.
20. Chen, C.C., et al., *An efficient triple-junction polymer solar cell having a power conversion efficiency exceeding 11%.* Adv Mater, 2014. **26**(32): p. 5670-7.
21. Wu, J., et al., *Role of solution-processed V2O5 in P3HT:PCBM based inverted polymer solar cells.* Synthetic Metals, 2013. **170**: p. 7-10.
22. Wang, H.-Q., et al., *Nanocrystal V2O5 thin film as hole-extraction layer in normal architecture organic solar cells.* Organic Electronics, 2012. **13**(12): p. 3014-3021.
23. Ho, P., et al., *The effects of MoO3 treatment on inverted PBDTTT-C:PC71BM solar cells.* Solar Energy Materials and Solar Cells, 2013. **119**: p. 235-240.
24. Fu, Q., et al., *Room-temperature sol-gel derived molybdenum oxide thin films for efficient and stable solution-processed organic light-emitting diodes.* ACS Appl Mater Interfaces, 2013. **5**(13): p. 6024-9.
25. Rempel, K.U., A.A. Migdisov, and A.E. Williams-Jones, *The solubility and speciation of molybdenum in*

water vapour at elevated temperatures and pressures: Implications for ore genesis. Geochimica et Cosmochimica Acta, 2006. **70**(3): p. 687-696.
26. Zhong, J.Q., et al., *Ionization potential dependent air exposure effect on the MoO3/organic interface energy level alignment.* Organic Electronics, 2012. **13**(12): p. 2793-2800.
27. Litzov, I. and C. Brabec, *Development of Efficient and Stable Inverted Bulk Heterojunction (BHJ) Solar Cells Using Different Metal Oxide Interfaces.* Materials, 2013. **6**(12): p. 5796-5820.
28. Greiner, M.T., et al., *Transition Metal Oxide Work Functions: The Influence of Cation Oxidation State and Oxygen Vacancies.* Advanced Functional Materials, 2012. **22**(21): p. 4557-4568.
29. Yin, Y., et al., *Dipole Formation at the MoO3/Conjugated Polymer Interface.* Advanced Functional Materials, 2018. **Under Revirew**.
30. Gajardo, P., et al., *Characterization of molybdenum-platinum catalysts supported on γ-alumina by X-ray photoelectron spectroscopy.* J. Electron Spectrosc. Relat. Phenom, 1979. **17**: p. 121-135.
31. Benramache, S., O. Belahssen, and H.B. Temam, *Effect of band gap energy on the electrical conductivity in doped ZnO thin film.* Journal of Semiconductors, 2014. **35**(7).
32. Shaheen, A., W. Zia, and M.S. Anwar, *Band Structure and Electrical Conductivity in Semiconductors.* Phd Thesis, 2010.
33. Irfan, et al., *Energy level evolution of air and oxygen exposed molybdenum trioxide films*. Applied Physics Letters, 2010. **96**(24): p. 243307.
34. Krischok, S., O. Höfft, and V. Kempter, *The chemisorption of H2O and CO2 on TiO2 surfaces: studies with MIES and UPS (HeI/II).* Surface Science, 2002. **69**(73): p. 507-510.
35. Volgmann, K., F. Voigts, and W. Maus-Friedrichs, *The interaction of H2O molecules with iron films studied with MIES, UPS and XPS.* Surface Science, 2012. **606**(9-10): p. 858-864.
36. Krischok, S., et al., *H2O interaction with bare and Li-precovered TiO2: studies with electron spectroscopies(MIES and UPS(HeI and II)).* Surface Science, 2001. **495**: p. 8-18.
37. BORSENBERGER, P.M. and W.T. GRUENBAUM, *Hole Trapping in Molecularly Doped Polymers.* Journal of Polymer Science: Part B, 1999. **37**: p. 349–356.
38. Ohkita, H., et al., *Direct observation of the carbazole hole trap in polymer solid films by the charge-resonance band.* Chemical Physics Letters, 1996. **263**: p. 602-606.
39. Harding, M.J., et al., *Variations in Hole Injection due to Fast and Slow Interfacial Traps in Polymer Light-Emitting Diodes with Interlayers.* Advanced Functional Materials, 2010. **20**(1): p. 119-130.

Chapter 5 . Change of Dipole at MoO_3/P3HT:$PC_{61}BM$ BHJ Interface for Various Thermal Treatments

5.1. Abstract

The benefit of annealing process during the fabrication of polymer-based optical/electrical devices has been widely accepted. The process is performed on individual P3HT:$PC_{61}BM$ BHJ and the MoO_3/BHJ dual layer in the work and the chemical and electronic changes of the interface under such circumstances have been studied. Upon annealing on BHJ before deposition of MoO_3, a sharp interface with less mixing phase can be achieved. The dipole strength slightly declines but the charge transfer has not been noticeably affected. On the other side, annealing upon MoO_3/BHJ dual layer causes the reduction to MoO_x and a heavier penetration into the BHJ. The interface has been broadened however the dipole strength was significantly declined due to the occurrence of MoO_x, which possesses a lower WF and higher metallic feature. The charge injection transport cannot be energetically supported, leading to a HOMO-valence band transport and the device performance can be altered.

5.2. Introduction and Research Aim

The inverted type [1, 2] of polymer-based solar cell consists of a sandwiched structure of anode ABL/polymer-fullerene (donor and acceptor)/ CBL [3, 4]. High WF TMOs such as MoO_3, V_2O_5 and WO_3 are used as ABL, which have been known for boosting the charge transfer efficiency [4, 5]. Our previous research[6], Meyer's[7] and Wang's group[8] have assigned the charge transfer at such interfaces to a charge injection/extraction mechanism, which bases on the alignment of the HOMO of the organic layer and the CB of the MTOs. The energy alignment highly relies on the dipole forming at the interface which has been revealed[6].

Annealing of the MoO_3/polymer BHJ has been routinely employed for the fabrication of OPVs [2, 9, 10] . It has been reported that thermal annealing has been applied to either the BHJ [11-15], or on the deposited MoO_3 [2, 16] by the sol-gel method, laser deposition[10] or evaporation. The elimination of amorphous phase of polymer BHJ [11, 17, 18] results in a higher charge mobility

[19-21] which can be produced by annealing upon BHJ at a temperature exceeding the glass transition temperature (T_g) of conjugated polymers[22]. Further benefits such as the promotion of crystallisation in the polymer structure [1, 11, 12, 22] and the enhancement of optical response [17] have also been observed. It has been reported that the power conversion efficiency (PCE) of the devices increase upon annealing on BHJ [1, 2, 9, 12, 17]. The annealing upon MoO_3 leads to the promotion of crystallisation nature of MoO_3[16] and the interfacial contact for a better electron extraction[1]. Other findings including a variation of MoO_3 distribution into BHJ were reported [2] due to the annealing while Greiner found a reduction of MoO_x[23] at 150 °C which also decreases the WF by 1.1eV. However the dipole and the energy level structure at such metal oxide/polymer BHJ interface under the thermal treatment has not been studied due to the interface mixing phase and lack of technique for approaching the interface without destructing the layers. A decline of WF by 1.1eV will certainly cause a dramatic change of the dipole formation but the variation of potential change of dipole has not been investigated. Therefore the mechanism of charge transfer is unclear under the condition of annealing.

In the work, a systematic analysis of the chemical distribution and quantification, valence states and electrical characterisation at an interface formed with MoO_3 and P3HTPC_{61}BM BHJ will be shown. The interface will be processed with various thermal treats and the changes upon these properties will be investigated using a powerful combination of electron spectroscopy and mathematical decomposition algorithm.

5.3. Sample Preparation and Treatment

P3HT and PC_{61}BM are blended as described and the depositions of metal oxides are discussed in experimental section. Here the thermal processes of the samples are illustrated in Fig 5-1. A list including the brief sample information is shown.

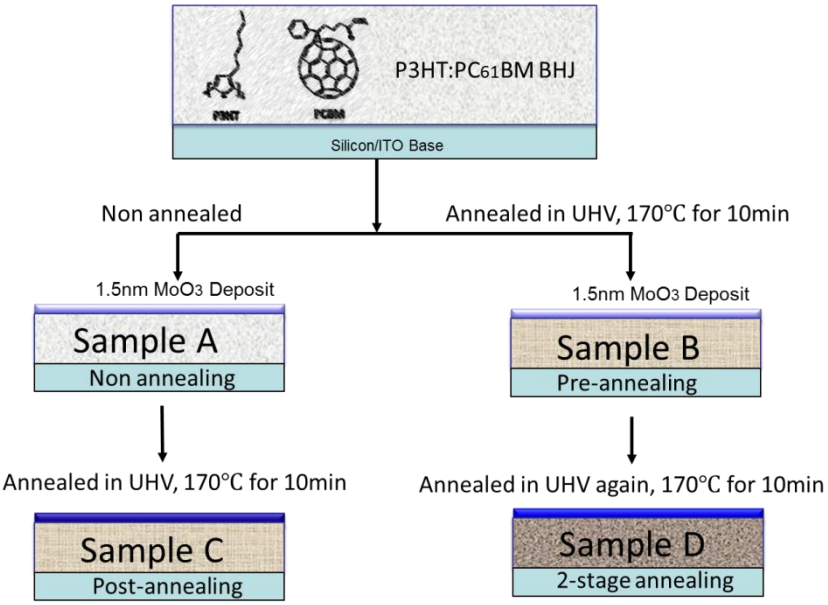

Figure 5- 1. Annealing of MoO_3/P3HT:$PC_{61}BM$ and the samples preparation

Sample A, not annealed BHJ with 1.5nm MoO_3 deposited in high vacuum

Sample B, Pre-annealed (BHJ) at 170 °C/10min, after which the MoO_3 was deposited

Sample C, not annealed BHJ with MoO_3 deposited, then annealed together 170 °C/10min

Sample D, subsequently annealed, BHJ pre-annealed and with MoO_3 deposited, after which, the sample was annealed again.

5.4. Results and Discussion

5.4.1. Chemical Distribution and Characterisation of the MoO_3/BHJ Interface upon Annealing

Concentration depth profiles as measured with NICISS of Molybdenum are shown in Figure 5-2(A) as a function of both energy loss and depth. The evaporation of MoO_3 on polymer surface yields a heavy penetration into the BHJ. On a pristine MoO_3/BHJ sample, the deposition of 1.5nm MoO_3 leads to a gradient distribution of Mo over a depth range of at least 8nm, which peaks at approximately 1.7nm. The gradient of the distribution towards the surface shows a much steeper slope than the gradient at the side towards the polymer BHJ. Upon the annealing of BHJ, the diffusion of MoO_3 has been significantly reduced as shown of the pre-

annealed sample due to the energy distribution peaking at about 0.6nm. In contrast, the Mo concentration peaks at a much higher depth into BHJ of the post-annealed sample which is the same as for the subsequent 2 stage-annealed sample. MoO_3 tends to penetrate into the polymer BHJ bulk.

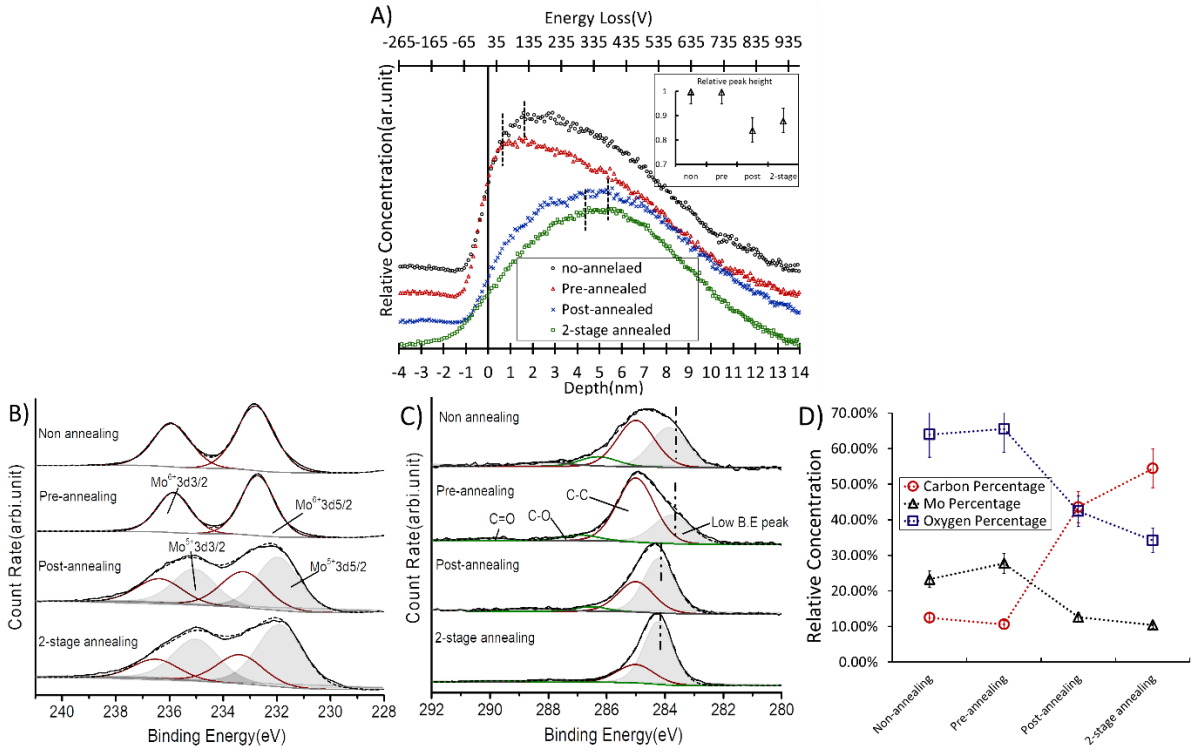

Figure 5- 2. (A) The depth profile of Mo derived from NICISS under different conditions of annealing treatment, the sub-figure illustrates relative peak height;(B) (C) The fittings of Mo and C spectra of XPS, the occurrence of Mo^{5+} is remarked as shadow; (D) The relative concentration of C, Mo and O as a function of annealing conditions

In Figure 5-2(B) and (C) the high resolution XP spectra of Mo $3d_{5/2}$ and C1s are shown including fitting of the spectra. Relative concentrations of Mo, C and O can be seen in Figure 5-2(D). The spectra of O and S are not shown. A pristine polymer BHJ sample was measured before and after annealing under same condition. Annealing did not change noticeably the spectra.

The $Mo3d_{5/2}$ peak was found at 233.0 ±0.15eV [20, 24] for the non- and pre-annealed samples. Post-annealed samples with two $Mo3d_{5/2}$ contributions at positions of 233.1 ±0.15eV and 231.7 ±0.15eV[25] were found. The change in binding energy corresponds to the reduction of Mo in

MoO_3 from Mo^{6+} to Mo^{5+}. The fraction of Mo^{5+} after annealing is in the range of 0.6~0.7. In the fitting of the C peak four individual components can be identified The C-C sp2, C-O and C=O/C=O-H peaks are found at 285.0eV, 286.7eV and 288.0eV (±0.15eV)[26, 27]. The energy distribution peaking at low binding energy and ranging from 283.7eV to 284.2eV has been discussed in our previous chapter[6]. This is due to the formation of a dipole at the MoO_3/BHJ interface, which electrically biases the energy of polymer BHJ within the potential gradient generated by the dipole. The fraction of C found at binding energies < 285 eV in non- and pre-annealed sample is less than for samples post-annealed and 2-stage annealed sample. However, the position of the contribution at < 285 is lower by 0.5eV compared to the latter two samples. The reason for this difference is a consequence of the strength of the dipole energy which will be discussed later.

In Figure 5-2(D) the relative concentration of C shows a dramatic increase from about 10% (（non and pre-annealing） to 50% (post and 2-stage annealing) after the annealing processed upon MoO_3/BHJ interface, while the O and Mo decline by contrast. This finding is in line with the NICISS results which show a shift of the Mo distribution to larger depth. Such a shift results in a decrease of the relative intensity in XPS of the respective elements even if the total amount of the respective element in the samples is constant.

5.4.2. Analysis of Electrical Properties of MoO_3/BHJ Interface upon Annealing

a) Analysis of UPS of the MoO_3/BHJ interface with various annealing treatments

The secondary electron cut-off for the samples and the valence electron region derived from UPS are shown in Figure 5-3(A) and (B). The WF is shown in Figure 5-3(C). A sample of 6nm MoO_3 on Si was processed under the same annealing condition and the combined result of UPS and IPES is included in Figure 5-3(D). A pristine BHJ reference sample has been processed with annealing. Neither the secondary electron spectra nor the valence electron spectra of BHJ changes after annealing, indicating no energy level structure of BHJ has been altered. From Figure 5-3(D) in prominent contrast the WF of MoO_3 declines from 6.8 ±0.1 eV to around 4.8 ±0.1eV and a distribution of energy states across the valence electron region can be seen approaching the zero mark (E_f) on energy scale. It is a representation of distinct metallic feature

of MoO_x (x~2.5) contributing to a higher conductivity [23, 28-30]. No significant change of the onset of the IPE spectrum can be seen, indicating that the E_{CB} of both pristine MoO_3 and annealed MoO_x stay constant at 0.4eV. The E_g of MoO_3 descends from 3.0eV to 1.4eV (±0.2). It is worthwhile to point out that before annealing the 6nm MoO_3 forms a closed layer on Si. Such MoO_3 layer can be aggregated and becomes uneven after annealing because of the higher surface energy of MoO_3 in comparison to Si[31]. Under the circumstance the valence electron spectrum of annealed MoO_3 can be considered as a mix of Si spectrum which was carried out in a fraction. Since the substrate is As-doped N-type Si, the growth of energy states across valence spectra which is close to Fermi level is mainly assigned to MoO_x.

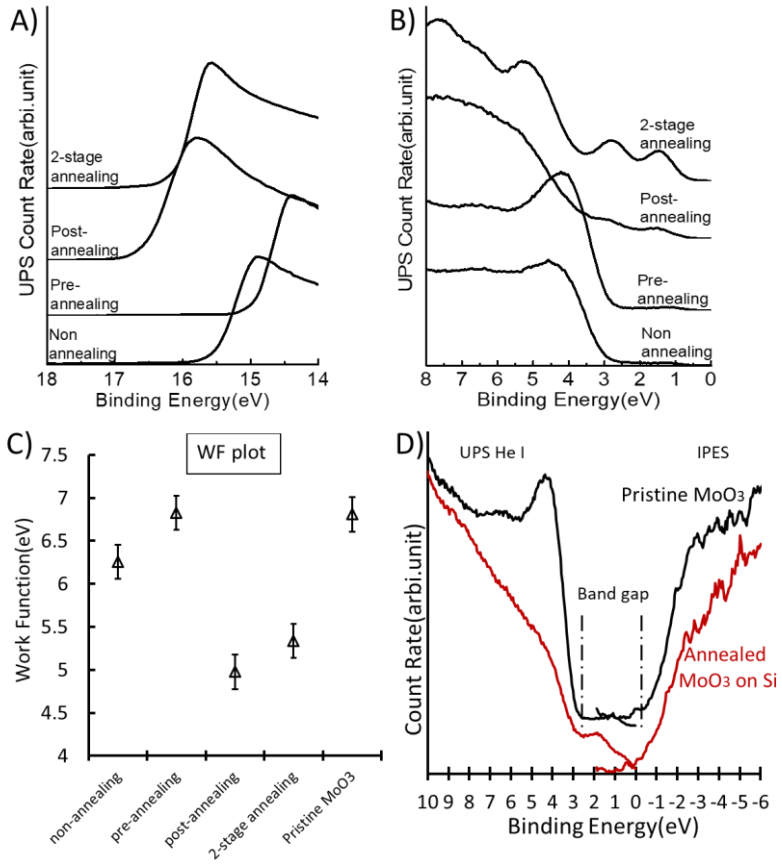

Figure 5- 3 (A) Secondary electron cascade of UP spectra; (B) Valence electron region of UP spectra; (C) WF plot of the samples; (D) Conduction electron region of IPE spectra with UP spectra before and after annealing of a pure 6nm MoO_3 layer on Si.

In Figure 5-3(A) a dramatic shift of the secondary electron peak onset upon the energy scale has been observed as a function of different annealing treatment. Meanwhile in Figure 5-3(B)

energy peaks at about 1.8eV and 2.8eV have established in post- and 2-stage annealed samples. The spectrum of the annealed MoO_3/BHJ sample in Figure 5-3(B) shows features different to those in the spectrum of the annealed pure MoO_3 in Figure 5-3(D). This is an indication the valence electron spectrum of MoO_3/BHJ interface is a complex combination of both annealed MoO_3 and polymer BHJ, which will be analysed further below.

The WF of the non-annealed sample is 6.4 ± 0.1eV. The WF of the pre-annealed sample is 6.8 ± 0.1eV, which is close to the WF of pristine MoO_3 [32]. After annealing the WF decreases to 4.8 ± 0.1eV and 5.3 ± 0.1eV, respectively for latter two samples. The measured WF of the annealed MoO_3 on Si sample was 4.8 eV. In terms of the proportion of reduced MoO_x due to annealing, a calculation by using Equations 1-8, 1-9, 1-10 was performed. The WF using theoretical calculation levels at 5.0eV for the annealed MoO_3 on Si, which is in agreement with the measured one within the error bar.

b) Decomposition of valence electron region of UP spectra

SVD has been applied on the valence electron region of the UP spectra of the non-annealing, pre- and post-annealing and 2-stage annealing samples to identify the constituting components of the measured spectra. The reference spectra representing the constituting components and the corresponding weighing factors are shown in Figure 5-4. The comparison of reference spectra found by decomposition with pristine MoO_3 and polymer BHJ is included in Figure 5-4(A) insets below the main figure.

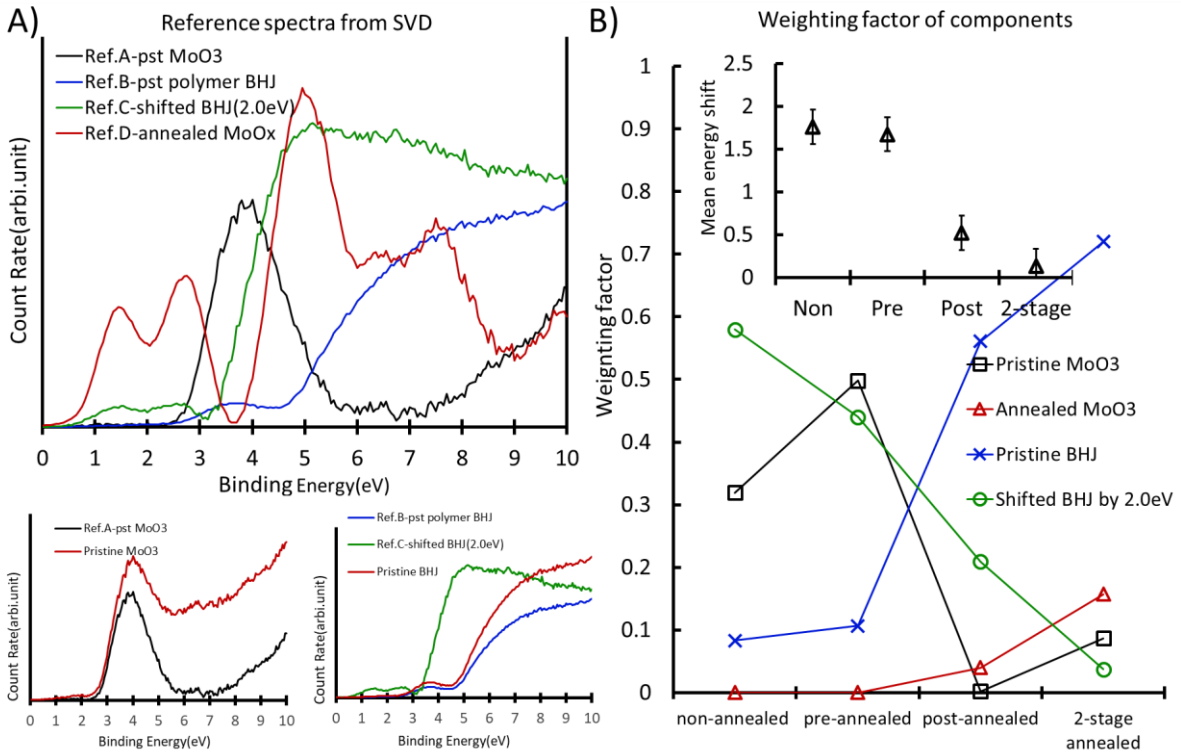

Figure 5- 4. (A) The UP reference spectra identified applying SVD, the insets below illustrating a comparison with pristine MoO_3 and BHJ sample; (B) The weighting factor of reference spectra, the inset shows the calculated mean energy shift shown as equation 5-1

Fig 5-4(A) shows the four reference spectra required to fit the whole set of the measured spectra. It is in the nature of SVD that the reference spectra resulting from the applying the algorithm not necessarily are identical with the spectra of a surface formed by a specific substance. The reason is that the SVD algorithm can lead to a small degree of intermixing of the spectra of the plain substance or adding or removing the secondary electron background. Ref. A has very similar features as the spectrum of a pristine MoO_3 sample and is thus assigned to pristine MoO_3. The peak at 4eV is characteristic for MoO_3[33].

By comparing in Figure 5-4(A), Ref. B can clearly be attributed to the pristine BHJ. Ref. C is very similar in shape to Ref. B but is subject to a shift to lower binding energy region by around 2.0eV. Such a reference spectrum had been identified in our earlier work[6] and represents the BHJ being subject to a shift on the energy scale due to the formation of the strong dipole between the BHJ and MoO_3. Ref. C also seems to show to a small degree a contribution from Ref. D. The reason of a small proportion of mixing of spectra has been described.

Concerning Ref. D which has a number of characteristic peaks, namely at 1.5eV, 2.6eV, 5eV and 7.6eV. The peaks at 1.5 eV and 2.6 eV are in the gap between HOMO and LUMO of the BHJ and the band gap of MoO_3 and change the semiconducting nature of both MoO_3 and the BHJ. They can lead to enhanced charge transfer but also act as recombination sites for electrons and holes or as trap states for either charge carrier. The exact nature of the substance represented by Ref. D is not entirely clear. It could be reduced MoO_3 with oxygen vacancies and Mo at lower oxidation states than 6. It could also be a chemical modification of the BHJ.

The weighting factors of the four reference spectra for fitting the measured spectra are displayed in Figure 5-4(B). The non-annealed sample and the pre-annealed sample show mainly contributions of MoO_3 and the shifted BHJ spectrum. This finding is the same as showed in chapter 3 before for deposition of MoO_3 onto the BHJ [6].The post-annealed sample shows a decrease of the shifted BHJ spectrum and a very strong contribution of the pristine BHJ spectrum while the contribution of the pristine MoO_3 has disappeared. This finding is in agreement with the finding of NICISS and XPS which had shown that the MoO_3 moves to deeper layers when the samples are annealed. A small contribution of the Ref. D can also be identified showing that the annealing has led to a change in the MoO_3 and the BHJ. The same trend can be seen also for the two stage annealed sample with the reference spectrum reflecting the change in the BHJ and the MoO_3 becoming stronger. Also a small contribution of the pristine MoO_3 is indicated.

Oppositely a large fraction BHJ with minor energy shift can be seen by post-annealing the MoO_3/BHJ sample however the dipole strength can be dramatically deteriorated. The mean energy shift (ΔE_{mean}) being illustrated as inset in Figure 5-4(B) can be carried out by following the equation 5-1. The calculation of ΔE_{mean} has been adopted in previous chapter with a similar form[6].

$$\Delta E_{mean} = \frac{(j_a \cdot \Delta E_a + j_b \cdot \Delta E_b)}{j_a + j_b} \qquad \text{Equation 5-1}$$

ΔE : the energy shift found for reference spectra

ΔE_a : pristine polymer BHJ, which shows zero energy shift

ΔE_b: BHJ with an energy shift of approximately 2.0eV to lower binding energy

j_a and j_b: the individual weighting factors

The ΔE_{mean} is thus calculated as 1.7eV for pre-annealed sample, which declines from pristine sample by 0.1eV, and for sample post-annealing and 2-stage annealing it levels at 0.5eV and 0.2eV. The decrease in dipole strength can be due to either the change in local strength of the dipole at the MoO_3/BHJ interface or a decrease in the intensity of the BHJ component shifted on the energy scale because of a dipole related to the diffusion of the MoO_3 to a deeper layer in the BHJ. Only in case the BHJ has been annealed before depositing the MoO_3 (pre-annealed) the diffusion of MoO_3 into the BHJ is stopped and the strong dipole at the MoO_3/BHJ interface retained.

5.4.3. Diagram of Chemical Distribution and Dipole Formation at the Interface upon Annealing

The valence electron spectroscopy through UPS in combination with the chemical analysis through XPS and measuring the concentration depth profiles of the elements with NICISS allows getting a comprehensive understanding of the chemical and energy structure of the MoO_3/BHJ interface which is illustrated in Figure 5-5.

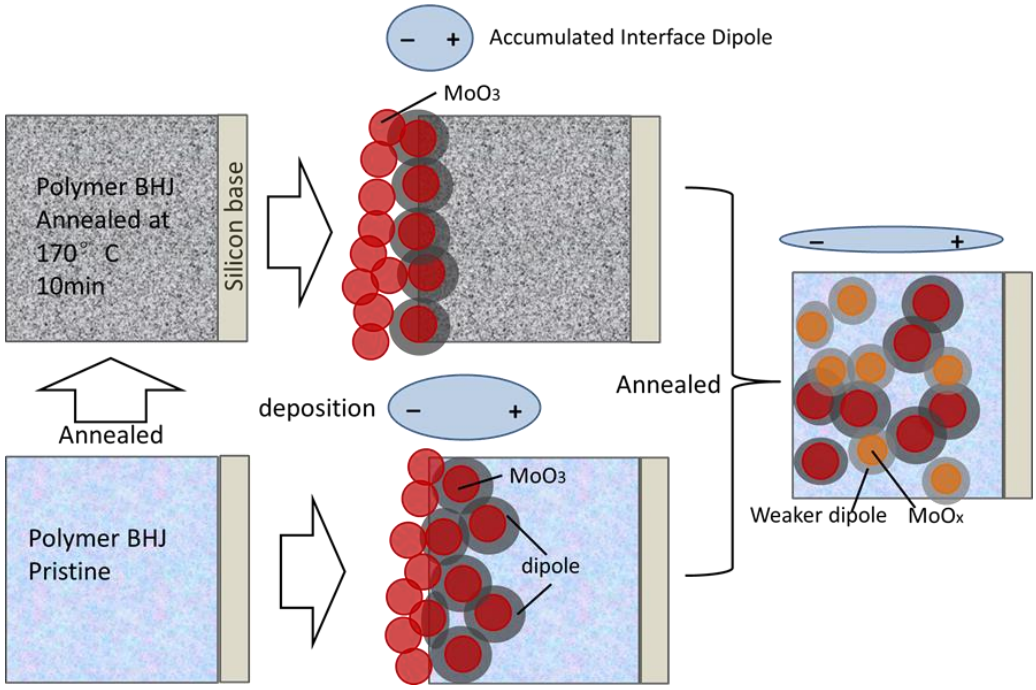

Figure 5- 5. Illustration of the MoO_3/BHJ interface after annealing of the BHJ layer (top part) and before annealing (bottom part). At the very right the interface of both the non-pre- and the pre-annealing are sketched which result in a similar distribution of the MoO_3. Note that the thickness of interface dipole on the vertical direction indicates the dipole strength, while the distance on parallel direction is the interface depth

The distribution of MoO_3 in the polymer BHJ as function of the depth has been analysed with NICISS. After annealing the MoO_3 particles are redistributed at a larger depth. The two reasons most likely are that the surface energy of MoO_3 is larger than that of the polymer, driving the MoO_3 particles to larger depth. And also the entropy of mixing phase increases, resulting in an increase of the mobility of MoO_3 particles [34, 35]. Via XPS, reduction of MoO_3 was found. The WF of the samples decreases upon annealing due to both the decrease in concentration of MoO_3 at the surface and the reduction of MoO_3 to MoO_x. In comparison with the non-reduced MoO_3, the latter has a lower intrinsic WF.

The dipole as measured with UPS at the interface between MoO_3 and BHJ decreases due to annealing which is discussed below:

a) If the BHJ is pre-annealed, diffusion of MoO_3 into the BHJ is not promoted by deposition and the distribution of the MoO_3 in the BHJ as function of the depth does not shift deeper.

In this case, the dipole at the MoO_3/BHJ interface retains compared to the previously reported dipole strength [6].

b) Whether the BHJ is not pre-annealed or pre-annealed, diffusion of MoO_3 into the BHJ is promoted by the post-annealing and the distribution of the MoO_3 in the BHJ as function of the depth changes. In this case, the dipole at the MoO_3/BHJ interface strongly changes compared to the dipole strength shown in chapter 3[6]. The reasons are (a) the decrease in MoO_3 concentration at the surface due to the further diffusion of MoO_3 into the BHJ; (b) the reduction of MoO_3 and formation of MoO_x, producing a reduced WF; and (c) that the MoO_x does not form a closed layer anymore but is more spread out. In the latter case the dipole orientation between the MoO_x and the BHJ is distributed in all directions due to the increase in the number of isolated MoO_{x+} particles.

5.4.4. Estimation of Charge Transfer over the Interface upon Various Annealing Treatments

In Figure 5-6 a model based on the electron spectroscopy data of the MoO_3/BHJ interface is shown. The schematic illustrates the energy levels and their relative positions and also indicates implication for the charge transfer over the interface after applying annealing at the various conditions investigated. The energy levels Fermi level (E_f), E_{CB} or E_{LUMO}, E_{VB} or E_{HOMO} are taken from the electron spectroscopy measurements directly or from the analysis of the spectra based on the component identification. The value for ΔE_{mean} is from Figure 5-4(B). The left and right sides are representing the region of MoO_3 and polymer BHJ, respectively. The middle region is the interface with mixed phases formed. In that region, the dash lines are representing the energy levels of polymer BHJ and their shift on the energy scale. The values for MoO_3, annealed MoO_x and polymer BHJ are taken from direct measurements. The CB of annealed MoO_x is rather close to E_f.

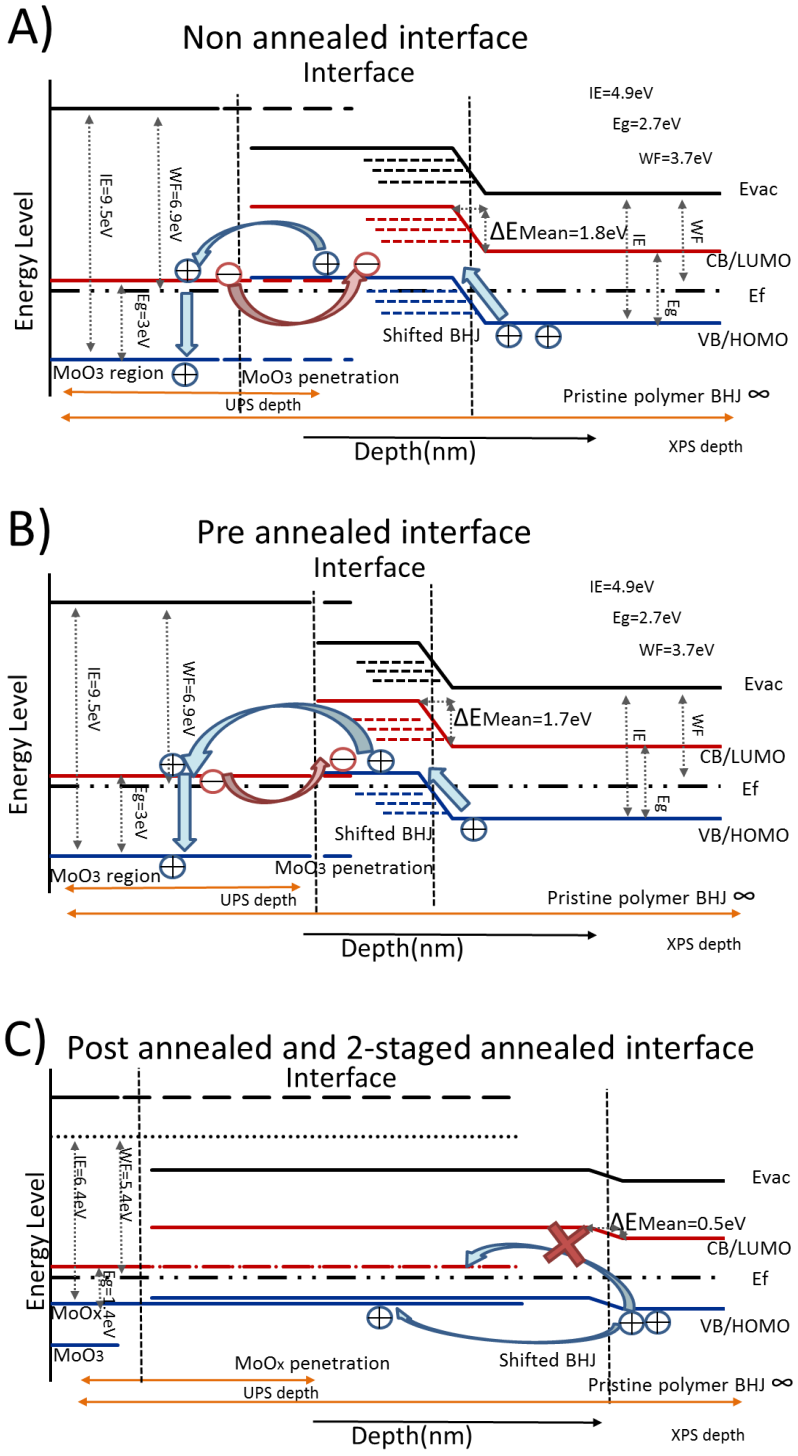

Figure 5- 6. The energy level diagram of an interface with various annealing treatments, the assumed charge transfer is included

In Figure 5-6(A) the charge transfer of an untreated MoO_3/BHJ interface follows then electron extraction/hole injection mechanism as described elsewhere [7, 8, 32] due to the position of the LUMO of the BHJ just above the HOMO of the polymer. Energetic support from interface

dipole, which shifts the energy levels of polymer BHJ within the moment. The energy level positions do not change upon annealing. The ΔE_{mean} levels at 1.7eV and is still sufficient for charge transition.

For the post-annealed and 2-stage annealed sample, E_{mean} is merely around 0.5eV which is not sufficient for an effective charge transfer across the MoO_3/BHJ interface. The reason is that the energy levels do not align well as the CB of MoO_3 and HOMO of polymer BHJ with energy shift are not matching. Therefore the extraction/injection as for the non-annealed and pre-annealed sample cannot be carried out. Under these energy level conditions, the hole can only transfer from the HOMO of BHJ to the VB of MoO_x based on the relative positioning of the energy levels.

In the fabrication of a polymer-based photovoltaic device such as a solar cell using MoO_3 as hole transport layer, the annealing process needs to be considered carefully. The pre-annealing of polymer BHJ hindering the diffusion of MoO_3 particles into deeper layers in the BHJ would benefit achieving a favourable the R_{sh} in most case. The post-annealing, however, is double-edged. The promotion of conductivity and interaction at the interface can be beneficial while the heavier penetration of MoO_3 could potentially causes current leakage, resulting in a decrease in R_{sh}. Finally, the decrease of the dipole strength at the interface between MoO_3 and the BHJ leads to a variation of charge transfer, which based on the energy level diagrams in Figure 5-6, can be predicted to reduce the polymer based solar cell efficiency.

5.5. Conclusion

Annealing has been applied at different stages of interface forming between MoO_3 and a BHJ (blended with P3HT and $PC_{61}BM$). It was found that the annealing conditions strongly influence the distribution of MoO_3 along the depth scale. Pre-annealing of the BHJ effectively inhibits the diffusion of the deposited MoO_3, leading to an interface which is sharper than that of the samples which were not pre-annealed. With the operation of post-annealing, the MoO_3 diffuses deeper into the BHJ. The interface between MoO_3 and the BHJ is redistributed over a larger depth, diluting the concentration of MoO_3 and leading to a decrease in alignment of the

orientation of the dipole parallel to the surface normal at the MoO_3/BHJ interface. The implication of the annealing conditions on the charge transfer has been estimated. The overall outcome of the present work is that the annealing conditions for real devices have to be carefully optimised in order to avoid detrimental effects of the diffusion of MoO_3 into the BHJ upon annealing.

Reference

1. Xu, X., et al., *High efficient inverted polymer solar cells with different annealing treatment.* Materials Science and Engineering: C, 2012. **32**(4): p. 685-691.
2. Chambon, S., et al., *MoO3 Thickness, Thermal Annealing and Solvent Annealing Effects on Inverted and Direct Polymer Photovoltaic Solar Cells.* Materials, 2012. **5**(12): p. 2521-2536.
3. Lin, R., et al., *Optimisation of the sol–gel derived ZnO buffer layer for inverted structure bulk heterojunction organic solar cells using a low band gap polymer.* Thin Solid Films, 2014. **566**: p. 99-107.
4. Itoh, E. and S. Nakagoshi, *Impedance analysis of the multilayered organic solar cells with and without hole buffer layer.* Japanese Journal of Applied Physics, 2014. **53**(4S): p. 04ER15.
5. Lu, H.-I., et al., *New Molecular Donors with Dithienopyrrole as the Electron-Donating Group for Efficient Small-Molecule Organic Solar Cells.* Chemistry of Materials, 2014. **26**(15): p. 4361-4367.
6. Yin, Y., et al., *Dipole Formation at the MoO3/Conjugated Polymer Interface.* Advanced Functional Materials, 2018. **28**(46): p. 1802825-1802835.
7. Kröger, M., et al., *Role of the deep-lying electronic states of MoO3 in the enhancement of hole-injection in organic thin films.* Applied Physics Letters, 2009. **95**(12): p. 123301.
8. Wang, C., et al., *Role of molybdenum oxide for organic electronics: Surface analytical studies.* Journal of Vacuum Science & Technology B, Nanotechnology and Microelectronics: Materials, Processing, Measurement, and Phenomena, 2014. **32**(4): p. 040801.
9. Chang, W., et al., *Post-deposition annealing control of phase and texture for the sputtered MoO3 films.* CrystEngComm, 2011. **13**(16): p. 5125.
10. Pardo, A. and J. Torres, *Substrate and annealing temperature effects on the crystallographic and optical properties of MoO3 thin films prepared by laser assisted evaporation.* Thin Solid Films, 2012. **520**(6): p. 1709-1717.
11. Ng, A., et al., *Annealing of P3HT:PCBM blend film--the effect on its optical properties.* ACS Appl Mater Interfaces, 2013. **5**(10): p. 4247-4259.
12. Lu, Y., et al., *Temperature-dependent morphology evolution of P3HT:PCBM blend solar cells during annealing processes.* Synthetic Metals, 2012. **162**(23): p. 2039-2046.
13. Holmes, N.P., et al., *Nano-pathways: Bridging the divide between water-processable nanoparticulate and bulk heterojunction organic photovoltaics.* Nano Energy, 2016. **19**: p. 495-510.
14. Gartner, S., et al., *Eco-friendly fabrication of 4% efficient organic solar cells from surfactant-free P3HT:ICBA nanoparticle dispersions.* Adv Mater, 2014. **26**(38): p. 6653-7.
15. Pan, X., et al., *Environmentally friendly preparation of nanoparticles for organic photovoltaics.* Organic Electronics, 2018. **59**: p. 432-440.
16. Dhanasankar, M., K.K. Purushothaman, and G. Muralidharan, *Effect of temperature of annealing on optical, structural and electrochromic properties of sol–gel dip coated molybdenum oxide films.* Applied Surface Science, 2011. **257**(6): p. 2074-2079.
17. Kim, J.Y., et al., *Analysis of Annealing Process on P3HT:PCBM-Based Polymer Solar Cells Using Optical and Impedance Spectroscopy.* Journal of Nanoscience and Nanotechnology, 2013. **13**(5): p. 3360-3364.
18. Abramavicius, V., et al., *Carrier motion in as-spun and annealed P3HT:PCBM blends revealed by ultrafast optical electric field probing and Monte Carlo simulations.* Phys Chem Chem Phys, 2014. **16**(6): p. 2686-2692.
19. Abbas, M. and N. Tekin, *Balanced charge carrier mobilities in bulk heterojunction organic solar cells.*

Applied Physics Letters, 2012. **101**(7): p. 073302.

20. Xiang, D., et al., *Gap states assisted MoO3 nanobelt photodetector with wide spectrum response.* Sci Rep, 2014. **4**: p. 4891.
21. Yang, Q., et al., *The improved performance of solution-processed SQ:PC71BM photovoltaic devices via MoO3 as the anode modification layer.* Applied Surface Science, 2013. **284**: p. 849-854.
22. Sharma, A., et al., *Unravelling the Thermomechanical Properties of Bulk Heterojunction Blends in Polymer Solar Cells.* Macromolecules, 2017. **50**(8): p. 3347-3354.
23. Greiner, M.T., et al., *Transition Metal Oxide Work Functions: The Influence of Cation Oxidation State and Oxygen Vacancies.* Advanced Functional Materials, 2012. **22**(21): p. 4557-4568.
24. Kumar, P., et al., *Reaction mechanism of core–shell MoO2/MoS2nanoflakes via plasma-assisted sulfurization of MoO3.* Materials Research Express, 2016. **3**(5): p. 055021.
25. Bai, S., et al., *Facile synthesis of α-MoO3 nanorods with high sensitivity to CO and intrinsic sensing performance.* Materials Research Bulletin, 2015. **64**: p. 252-256.
26. Andreoli, E. and A.R. Barron, *CO2 Adsorption by para-Nitroaniline Sulfuric Acid-Derived Porous Carbon Foam.* C-Journal of Carbon research, 2016. **2**(4): p. 25.
27. Zhu, H., et al., *A Novel Metal–Organic Framework Route to Embed Co Nanoparticles into Multi-Walled Carbon Nanotubes for Effective Oxygen Reduction in Alkaline Media.* Catalysts, 2017. **7**(12): p. 364.
28. Vasilopoulou, M., et al., *Reduction of Tungsten Oxide: A Path Towards Dual Functionality Utilization for Efficient Anode and Cathode Interfacial Layers in Organic Light-Emitting Diodes.* Advanced Functional Materials, 2011. **21**(8): p. 1489-1497.
29. Yuan, N., J. Li, and C. Lin, *Valence reduction process from sol-gel V2O5 to VO2 thin films.* Applied Surface Science, 2002. **191**: p. 176-180.
30. Dang, J., G. Zhang, and K. Chou, *Phase Transitions and Morphology Evolutions during Hydrogen Reduction of MoO3 to MoO2.* High Temperature Materials and Processes, 2014. **33**(4).
31. Ma, W., et al., *Impacts of Surface Energy on Lithium Ion Intercalation Properties of V2O5.* ACS Appl Mater Interfaces, 2016. **8**(30): p. 19542–19549.
32. Meyer, J., et al., *Transition metal oxides for organic electronics: energetics, device physics and applications.* Adv Mater, 2012. **24**(40): p. 5408-5427.
33. Greiner, M.T., et al., *Universal energy-level alignment of molecules on metal oxides.* Nat Mater, 2011. **11**(1): p. 76-81.
34. Howard, J.B., et al., *Fine Tuning Surface Energy of Poly(3-hexylthiophene) by Heteroatom Modification of the Alkyl Side Chains.* ACS Macro Letters, 2015. **4**(7): p. 725-730.
35. Papakondylis, A. and P. Sautet, *Ab Initio Study of the Structure of the α-MoO3 Solid and Study of the Adsorption of H2O and CO Molecules on Its (100) Surface.* J. Phys. Chem. B, 1996. **100**(25): p. 10681–10688.

Chapter 6. Observation and Characterisation of Dipoles forming at V_2O_5/BHJ and WO_3/BHJ Interfaces

6.1. Abstract

The formation of dipole at V_2O_5/P3HT:PC_{61}BM BHJ and WO_3/BHJ interfaces is determined and characterised by applying electron spectroscopy. The minimum deposition thickness of V_2O_5 and WO_3 for a closed layer on the BHJ surface has also been identified. Neutral impact collision ion scattering spectroscopy was used to profile the concentration of metal oxides within a certain depth and a mixing region of metal oxides/polymer was observed. Upon the evaporation of V_2O_5 and WO_3, intermediate energy levels of polymer BHJ with relative energy shift were characterised by decomposing the valence electron spectra. Subsequently, the reconstructing of energy bands at the interface was accomplished. The mean energy shift due to the dipole increases with increasing amount of the transition metal oxide (TMO) deposition. For V_2O_5/BHJ, it saturates at 2.4 eV with 3 nm, which levels at ~1.6 eV for a WO_3/BHJ interface.

6.2. Introduction and Research Aim

The application of an anode buffer layer (ABL) in traditional and inverted structure polymer-based solar cells [1-4] and a variety of organic devices is highlighted in this thesis. Solar cell efficiency is improved by enhancing device shunt resistance[5, 6] and facilitating charge transfer at the interface[7, 8]. The regularly used materials for ABL are MoO_3 and similar metal oxides, such as V_2O_5, WO_3 and ReO_2—all have the common characteristics of high WF/ϕ[3, 7, 9], suitable conductivity[10] and transmittance[11, 12]. Research has revealed the WF of pristine MoO_3, V_2O_5 and WO_3 as 6.7 eV[13], 6.9 eV and 6.6 eV respectively[14]. Subsequently, the alignment of energy levels at the interface of these TMOs and polymer/fullerene active layer leads to a strong dipole[15]. Thus, the dipole formation provides energy shift for a highly effective charge transfer. The process has been reported as charge injection/extraction[16, 17] mechanism, as described in previous chapters.

In Chapter 3, the change of energy levels including WF, E_{VB}, E_{CB} and E_g at a MoO_3/P3HT:$PC_{61}BM$ BHJ interface across a range of MoO_3 deposition amount was characterised. Most importantly, a method to quantify the intermediate energy states at the interface was demonstrated with multi-spectroscopy. Thus, the dipole energy and the energy level structure at the interface were characterised.

In this thesis, V_2O_5 and WO_3 with P3HT:$PC_{61}BM$ BHJ will be investigated with a range of deposition amounts. As an alternative high WF metal oxide, V_2O_5 features electrical properties[14] and surface energy[18] similar to MoO_3. Using V_2O_5 as a buffer layer in polymer solar cells has been previously reported [7, 19, 20]. Considering WO_3, pristine WF has been reported as lower than that of MoO_3 while surface energy is higher. WO_3 has been occasionally applied in polymer solar cells[21, 22], but is commonly used in OLEDs[14]. In fact, the characterisation of the interface of V_2O_5/conjugate organic and WO_3/conjugate organic and the dipole formation are not clear from the literature. However, these mechanisms can significantly influence the charge transfer efficiency over the interfaces. In this thesis, V_2O_5 and WO_3 with P3HT:$PC_{61}BM$ BHJ are investigated with a range of deposition amounts and the characterisation of dipole locating at V_2O_5/BHJ and WO_3/BHJ interfaces to achieve a deep understanding of the energy level structure. Electron spectroscopy will be used to analyse the chemical and electronic properties and ion scattering spectroscopy used to profile concentration depth of the materials. Microscopy will assist in obtaining a topology of surface and how the TMO particles forming on BHJ.

6.3. Sample Preparation

The methods of blending P3HT and $PC_{61}BM$ and the V_2O_5 and WO_3 evaporation are described in the Chapter 2. The sample preparation in this work is illustrated in Figure 6-1.

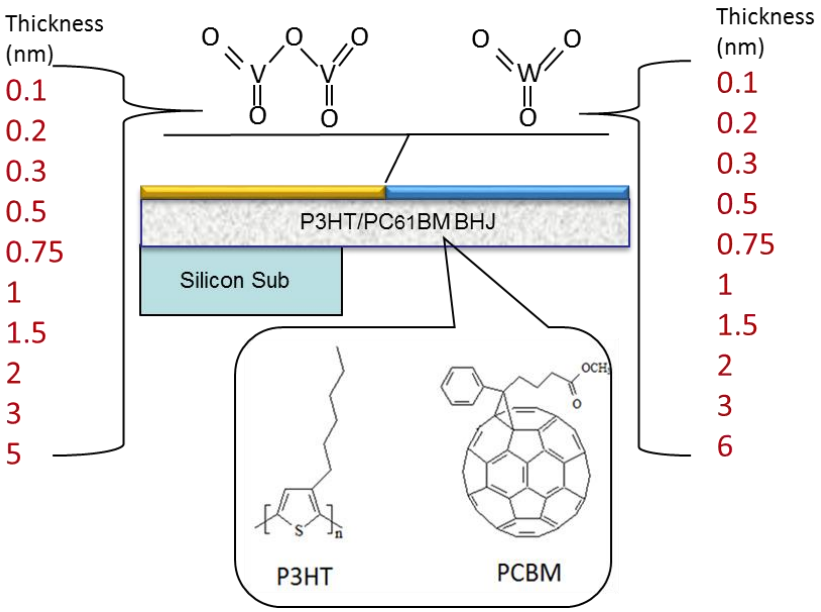

Figure 6- 1. The sample structure: blended P3HT and $PC_{61}BM$ deposited with V_2O_5 and WO_3 across a variation of thickness

A series of V_2O_5 layer thickness (0.1, 0.2, 0.3, 0.5, 0.75, 1, 1.5, 2, 3 and 5 nm) onto polymer BHJ was achieved. Samples were then directly transferred into the analysis chamber for measuring with electron and ion scattering spectroscopy under an ultra-high vacuum (UHV) ambient ($<10^{-9}$ mbar). Thus, exposure to air and contamination were avoided. The WO_3 samples (0.1, 0.2, 0.3, 0.5, 0.75, 1, 1.5, 2, 3 and 6 nm) onto BHJ were subsequently achieved and characterised under the same condition.

6.4. Results and discussion

6.4.1. Chemical Composition of V_2O_5/P3HT:$PC_{61}BM$ Interface

The fittings of the high-resolution x-ray scans of Vanadium (V) and Sulphur (S) of the 0.1, 0.75 and 5 nm V_2O_5/BHJ samples are shown in Figure 6-2(A), and those of the Carbon (C) and Oxygen (O) of the 0.1, 0.75, 3 and 5 nm V_2O_5/BHJ samples are shown in Figure 6-2(B) and (C). The energy position of O and S of polymer BHJ are shown in Figure 6-2(D). The fraction of low binding energy C peak is shown in Figure 6-2(E).

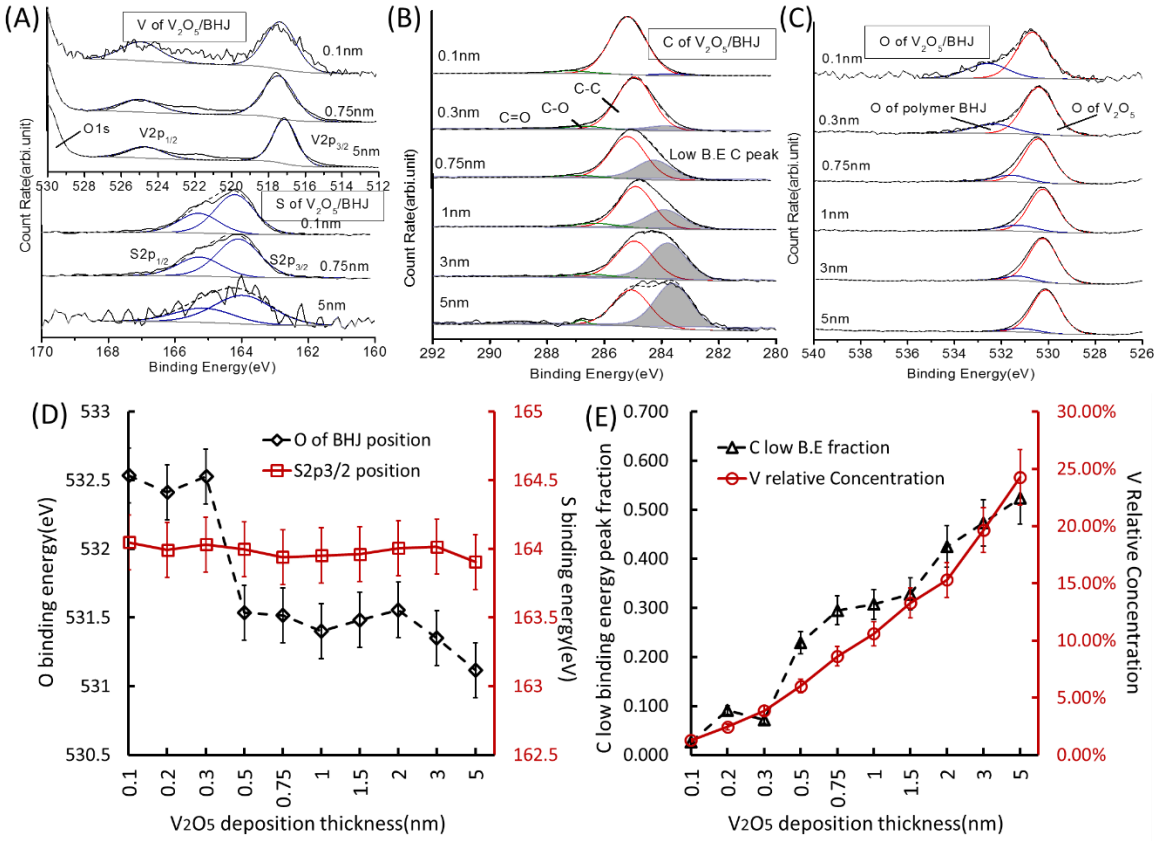

Figure 6- 2. (A)(B)(C) High-resolution scans of V, S, C and O and fitting of peaks; (D) The binding energy plots of individual O and S peak; (E) The fraction and concentration plots of individual C and V peak

No chemical or valence state change of V was observed in Figure 6-2(A), as the V^{5+} $2p_{3/2}$ peak is found at 517.1 ±0.15 eV[23, 24]. Either energy shift or formation of multimodal was observed. Thus, the energy scale has not been calibrated. In Figure 6-2(A), The S 2p3/2 representing the thiophene of P3HT $(C_{10}H_{14}S)_n$[25] peaked at 164.0 ±0.15 eV with no obvious change in peak position. It was determined that P3HT was underlying $PC_{61}BM$[26] in the blended BHJ and the latter dominates the outermost layer of BHJ.

In terms of C, the C1s spectra indicating the occurrence of $PC_{61}BM$ and P3HT were shown. C-C binding peak was found at 285 ±0.15 eV, while the C-O bond peaks at 286.7 ±0.15 to 287.2 ±0.15 eV[25]. Slight oxidation of BHJ was observed on the V_2O_5 deposition due to the increase of C=O bond, identified at 288.2 ±0.15 to 288.6 ±0.15 eV[27]. In addition, a peak at 283.6 ± 0.15 eV is identified to fit the spectra, which increases in intensity with V_2O_5 deposition[28] and is similar to the findings in Chapter 3. The fraction of the low binding energy C peak overtakes

the C-C bond with more than 5 nm V_2O_5 deposited onto BHJ, as shown in Figure 6-2(E). The fitting of O1s spectra results in two individual peaks. The first level at 530.4 ± 0.15 and the second is fitted at 531.2–532.6 ± 0.15 eV. The first was assigned to the O fraction of V_2O_5[29], while the second was identified as the occurrence of $PC_{61}BM$ of BHJ[30]. In Figure 6-2(D), the position of the O peak from polymer BHJ shifts by 1.4 eV to the lower binding energy. The shift of the O peak is in alignment with the shift of the low energy C peak. Such an energy shift of C and O peaks and increase in the proportion of the low binding energy C peak can be attributed to the proportion of polymer BHJ that subjects to the dipole forming at the interface, bearing an electric potential. The cause is similar to that described in Chapter 3.

6.4.2. Chemical Composition of WO_3/P3HT:$PC_{61}BM$ Interface

The high-resolution scan spectra of Tungsten (W), Sulphur (S), Carbon (C) and Oxygen (O was fitted and is shown in Figure 6-3(A), (B), (C) for the 0.1, 0.75, 2 and 6 nm WO_3/BHJ samples.

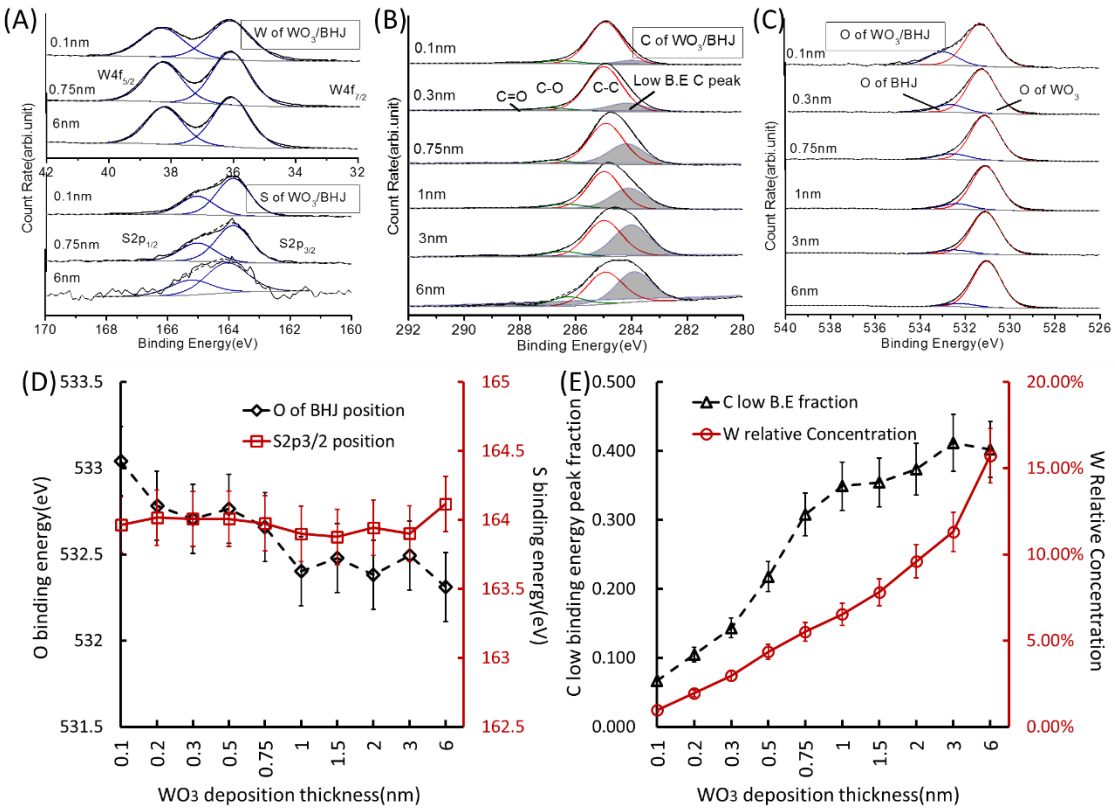

Figure 6- 3. (A)(B)(C) High-resolution scans of W, S, C and O and fitting of peaks; (D) The binding energy plots of individual O and S peak; (E) The fraction and concentration plots of

individual C and W peak

Similar to the nature of V_2O_5 on BHJ, there was no change observed for the chemical and valence state of W and S in Figure 6-3(A). $W4f_{7/2}$ was found at 36.0 ± 0.15 eV in all samples, corresponding to W^{6+}[31], while $S2p_{3/2}$ peaked at 164.0 ± 0.15 eV. The dipole that was discussed forming at the WO_3/BHJ interface electrically affected the polymer BHJ, yielding an energy shift. Therefore, an increase of low binding energy peak of C was observed, situated at 283.8 ± 0.15 eV with a fraction of 0.4 in the 6 nm WO_3 sample. In Figure 6-3(E), the binding energy of O of polymer BHJ within the dipole moment shifted from 533.0 ± 0.155 eV to 532.3 ± 0.155 eV. The indication of dipole forming at the WO_3/BHJ interface is similar to that of V_2O_5/BHJ.

Due to the energy shift being higher than 1 eV, the dipole at such a TMO/BHJ interface can be energetically significant enough to affect the electrical potential of interface. Consequently, further investigation into the interface was performed.

6.4.3. Elemental Depth Distributions of V_2O_5 and WO_3 on Polymer BHJ

NICISS profiling the distributions of V and W are shown in Figure 6-4, which exhibits the relative concentration as a function of both energy loss and depth. The samples included (0.1, 0.2, 0.5, 1, 2 and 3 nm) V_2O_5 and (0.1, 0.2, 0.5,1, 2, 3 and 6 nm) WO_3 on BHJ.

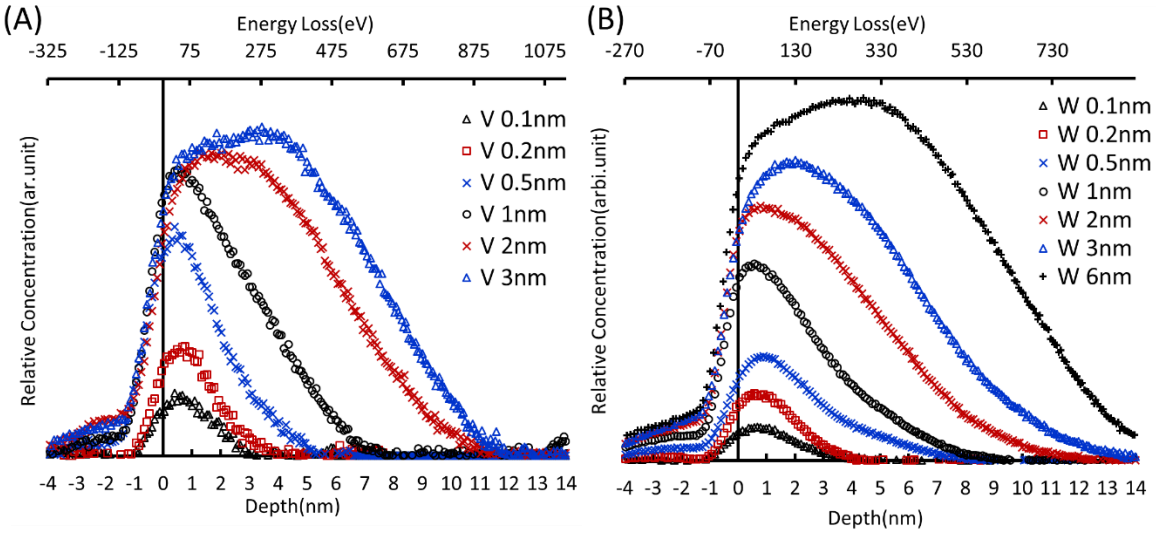

Figure 6- 4. Concentration depth profile of Vanadium (A) and Tungsten (B) showing the distribution of element in the BHJ layer with the zero mark indicating the outermost surface of the samples

A noticeable penetration of both V and W can be derived from Figure 6-4 and the metal oxides molecules are assumed to be the island-like forming on top of BHJ, which has been previously discussed in Chapter 3. In parallel comparison, after evaporating 0.1 nm of V_2O_5, V can be found over a depth range of ~3 nm. Upon the same thickness, the evaporation of WO_3 yields a similar depth of distribution. Subsequently, the 1 nm V_2O_5/BHJ sample illustrated a depth of V of ~6.0 nm, while in a WO_3/BHJ sample, W showed a distribution of ~7 nm. With more than 2 nm V_2O_5 deposited onto BHJ, the peak height was constant and a flat distribution was profiled in the 2 nm sample, indicating the surface is fully covered within a 1–2 nm V_2O_5 deposition. By contrast, the smallest deposition thickness of WO_3 completely covering the surface is between 3–6 nm in terms of the distribution of W peak, which turns flat after more than 3 nm of deposition. Both V_2O_5 and WO_3 illustrate a heavy diffusion of the TMO particles into polymer BHJ, but the surface coverage rate is different, which will be further investigated with topography characterisation.

6.4.4. Observation of V_2O_5 and WO_3 Distributions upon BHJ Surface

Scanning Auger Microscopy (SAM) was applied to achieve a topographical analysis of the

formation of V_2O_5 and WO_3 onto BHJ. The SAM images and elemental mapping at given spots for 0.3 nm V_2O_5/BHJ and 0.3 nm WO_3/BHJ samples are shown in Figure 6-5(A) and (B). The mapping of V and W with a resolution up to 5 nm is shown in Figure 6-5(C).

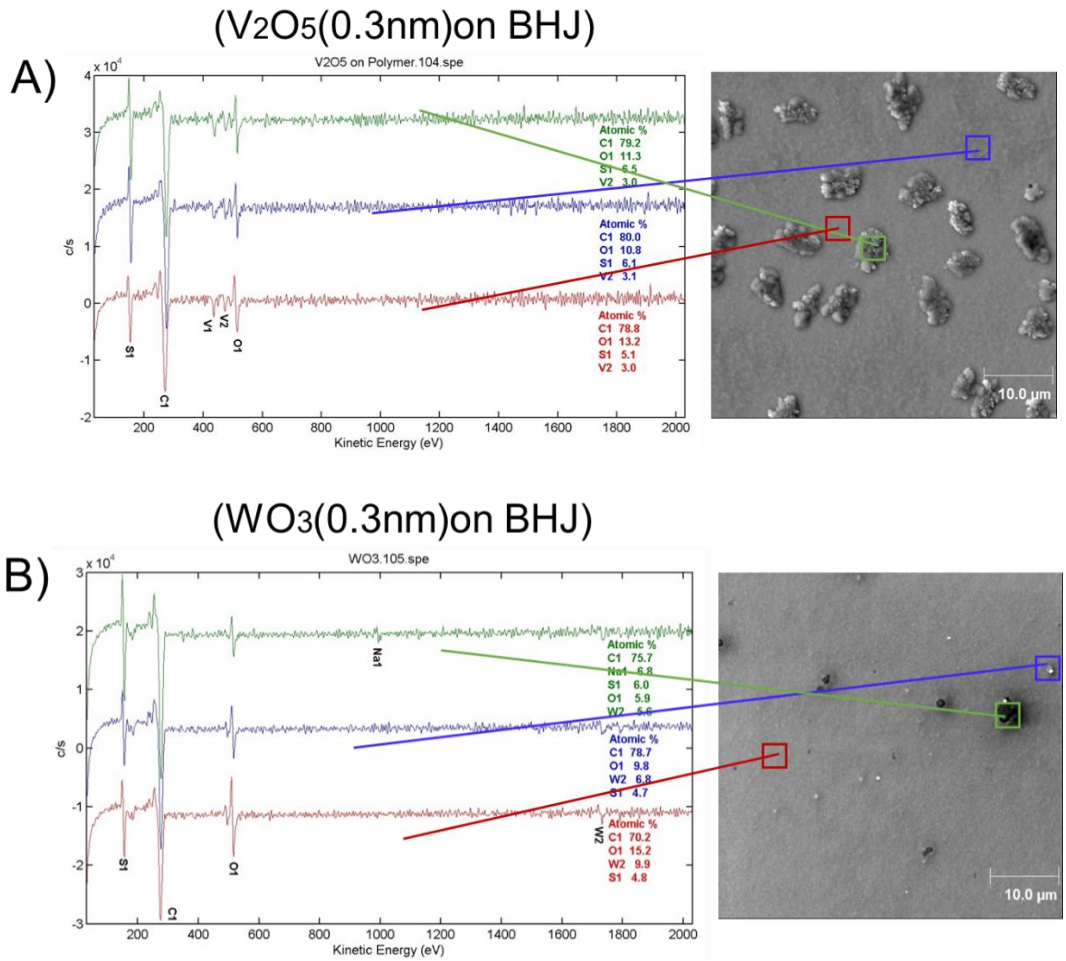

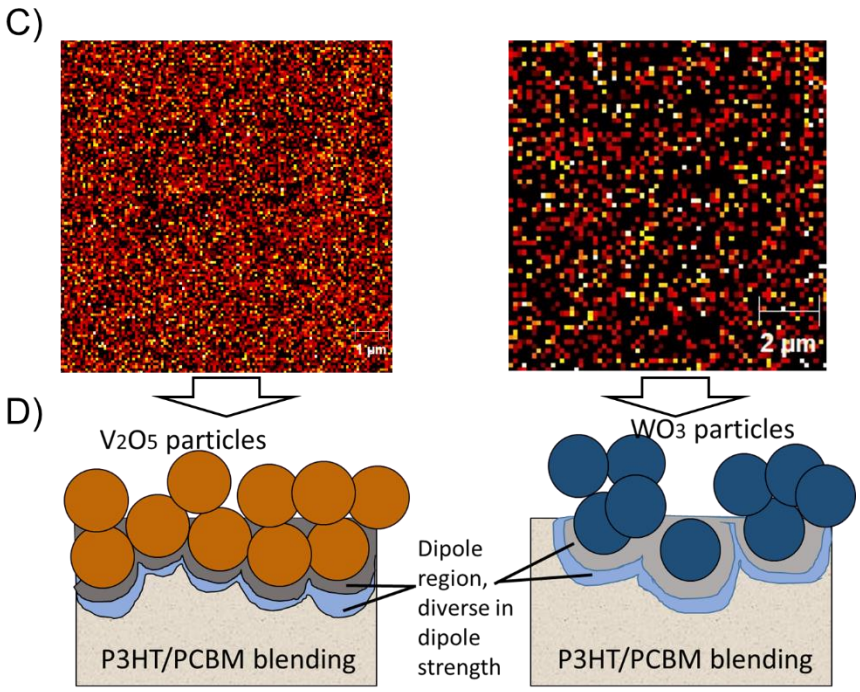

Figure 6- 5. (A) The AE spectra of selected points on 0.3nm V_2O_5/BHJ sample; (B) The AE spectra of selected points on 0.3nm WO_3/BHJ sample Right: (C) The elemental mapping of V (left) and W (right) on the correspondent samples over a 100 υm^2 area of SEM image, the resolution is up to 5nm. The scale on left Figure is 1 υm and on right Figure is 2 υm. (D) The illustration of V_2O_5 (left) and WO_3 (right) forming on BHJ surface of the same samples

Figure 6-5(A) and (B) also shows the AES survey scans of V_2O_5 and WO_3 on BHJ. The surface has not been fully covered with 0.3 nm thickness deposition. The information derived from Figure 6-5(C) is the elemental mapping of V (left) and W (right). Upon 0.3 nm evaporation thickness, both V_2O_5 and WO_3 reveal a uniform distribution on polymer BHJ (across all samples). However, the surface coverage of V_2O_5 is much higher than that of WO_3. This suggests that the WO_3 particles tend to agglomerate when deposited on BHJ surface due to the higher surface energy[18]. The difference in distributions of such metal oxides can cause differences in the formation of interfaces.

6.4.5. Decomposition and Analysis of MIES/UPS Spectra

a) The Observation and Analysis of MIES/UPS of the V_2O_5/BHJ Samples

Figure 6-6 illustrates the raw UP and MIE spectra of V_2O_5/polymer BHJ samples. The secondary electron cascade and valence electron region of UPS are shown in Figure 6-6(A) and (B) respectively. The valence electron spectra of MIES are shown in Figure 6-6(C). A shift to the lower binding energy scale of the secondary electron peak onset was observed from UPS with the increasing amount of V_2O_5. The MIE spectra exhibits energy distribution peaking at 6.4 eV with a minor amount of V_2O_5, which diminishes with the escalation of deposition quantity. The peaks can be assigned to the proportion of polymer BHJ.

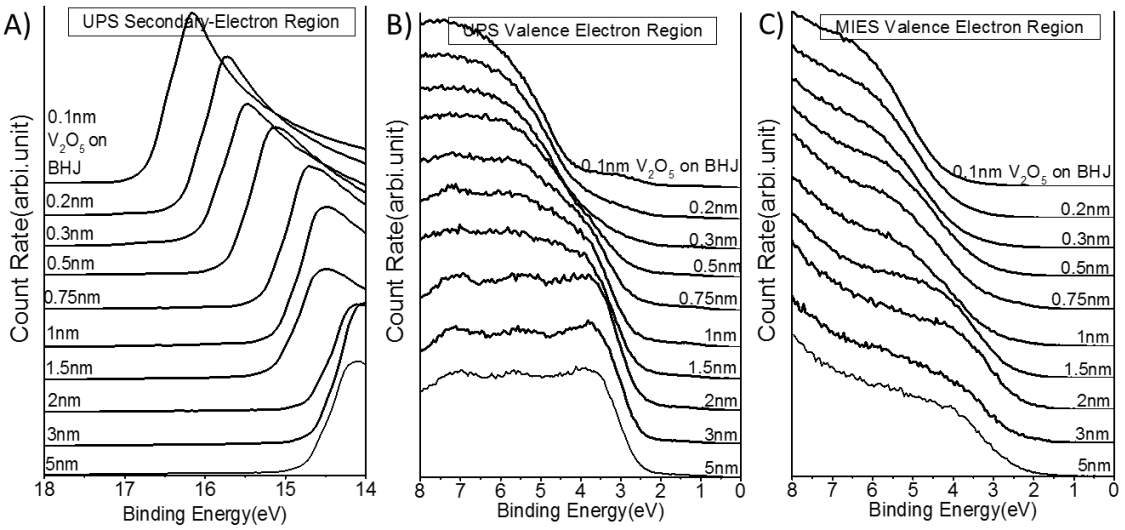

Figure 6- 6. (A) The secondary electron cascade of UPS of V_2O_5/BHJ samples; (B) The valence electron region of UPS of the same samples; (C) The valence electron region of MIES of the samples

b) The Observation and Analysis of MIES/UPS of the WO_3/BHJ Samples

The features of the secondary electron and valence electron regions of WO_3/BHJ samples from minor disposition to high surface coverage are shown in Figure 6-7(A) and (B). The valence electron region of MIES is shown in Figure 6-7(C). Similar to the V_2O_5/BHJ samples, the secondary electron peak onset shifts to a low energy region with the increasing amount of WO_3. Meanwhile, the shape of the valence electron spectra of both UPS and MIES changes gradually. Apparent energy distribution peaking at 4 eV occurred and began to grow from UPS with the increasing amount of WO_3. The MIE spectra are rather similar to those of V_2O_5/BHJ.

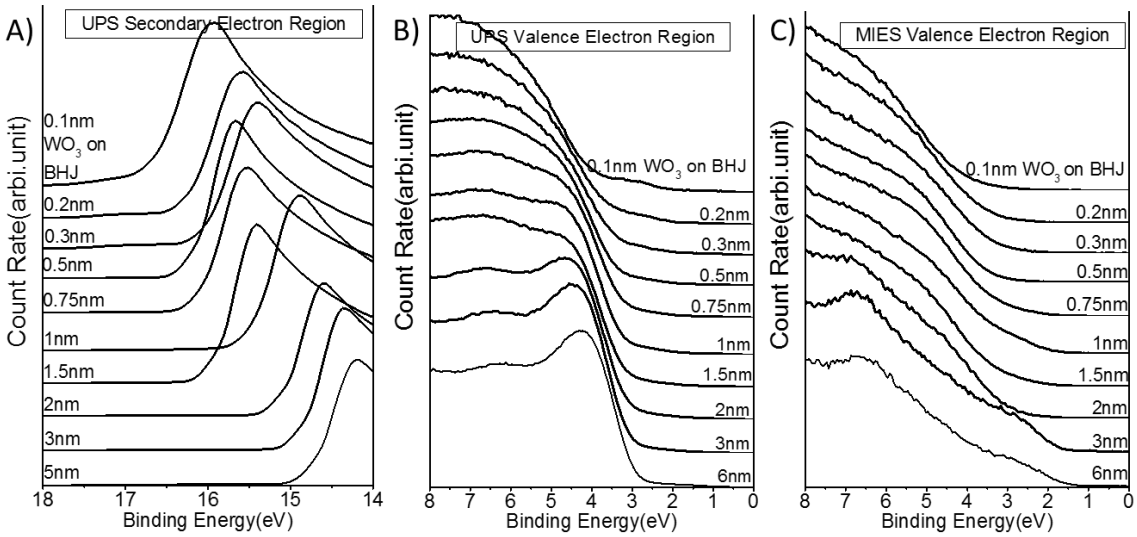

Figure 6- 7. (A) The secondary electron cascade of UPS of WO_3/BHJ samples; (B) The valence electron region of UPS of the same samples; (C) The valence electron region of MIES of the samples

c) Electrical Properties of V_2O_5/BHJ and WO_3/BHJ Interfaces

The WF/ϕ derived from the peak onset of secondary electron cascade of UPS is plotted in Figure 6-8(A). A noticeable modification[32] upon the WF of both V_2O_5 and WO_3 deposition onto BHJ is exhibited. The V_2O_5/BHJ sample reveals an increase from approximately 4.7 eV of 0.1 nm to 6.9 eV of 5 nm thickness sample while the WF of WO_3/BHJ sample ascends from 4.6 eV to 6.7 eV of 6 nm. The changes in WF reveal a dipolar complex, thus a p-type doping effect of deposited metal oxides upon the BHJ [33, 34] was observed. The valence electron spectra are further studied for identifying the comprising compounds.

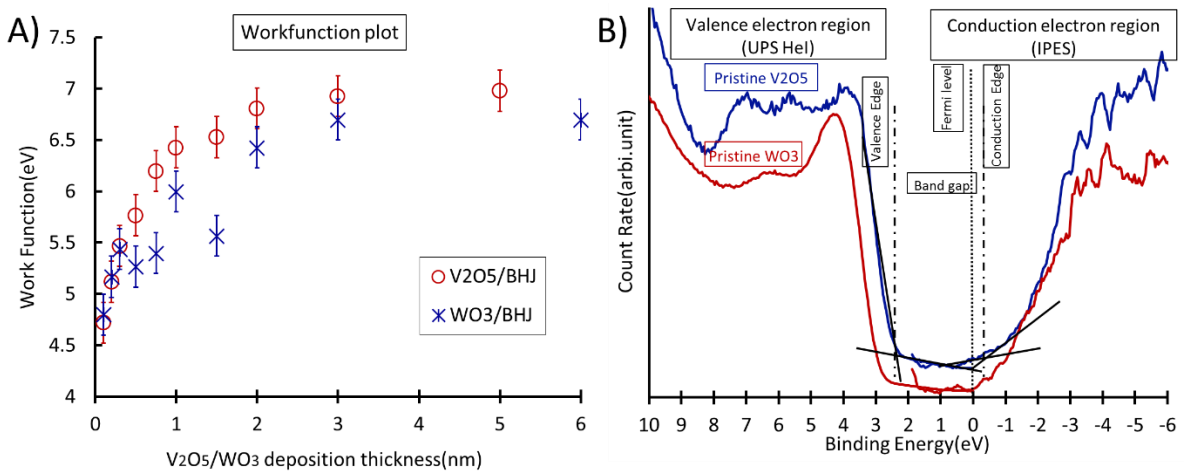

Figure 6- 8. (A) The WF of V_2O_5 and WO_3/BHJ across a range of deposition thickness; (B) The UP valence electron and IPE spectra of pristine V_2O_5 and WO_3

The characteristics of electrical properties of pristine BHJ and metal oxides are needed to comprise the energy level diagram at the interfaces. Therefore, the samples including 8 nm V_2O_5 and WO_3 on Silicon wafer were investigated with IPES and UPS for the WF, E_{CB} and E_{VB} pristinely. The valence electron and conduction electron spectra are shown in Figure 6-8(B). The WF/ϕ, E_{VB}, E_{CB} and band gap (E_g) are plotted in Table 6-1 with an error bar of ±0.1 eV. Also included are the electronic parameters for P3HT, $PC_{61}BM$ and the blended samples for reconstructing the energy level alignment (from Chapter 3). The characteristics obtained are also similar to Meyer[14]'s work.

Sample	**WF(eV)** **±0.1eV**	**E_{HOMO}/ E_{VB} (eV)** **±0.1eV**	**E_{LUMO}/ E_{CB} (eV)** **±0.1eV**	**E_g (eV)** **±0.2eV**
P3HT(c.3)	3.6	1.1	1.6	2.7
$PC_{61}BM$(c.3)	3.9	1.6	1.0	2.6
P3HT/PCBM(c.3)	3.7	1.2	1.5	2.7
V_2O_5	6.9	2.5	0.3	2.8
WO_3	6.7	2.8	0.5	3.3

Table 6-1. The plots of WF, E_{HOMO}, E_{LUMO}, E_{VB}, E_{CB} and E_g of pristine samples. Note that the conduction and valence energy representing the energy difference from the Fermi level are

absolute in the table

d) Decomposition of Valence Electron Region of MIE/UPS Spectra

The valence electron spectra of MIES and UPS illustrate a mix of valence electron states from different components. The principles are similar to that of the MoO_3/BHJ discussed in Chapter 3. Thus, the spectra were decomposed with a mathematical method for identifying the consisting components and related weighting factors. SVD analysis was first conducted in-group on the UP/MIE spectra of V_2O_5/WO_3 on BHJ samples, and the methodology was the same as that shown in Chapter 3. From the decomposition, a third spectrum similar to the pristine polymer BHJ, featuring a shift in energy scale, was identified to fit the measured spectra. The nature was found in the UP and MIE spectra of both V_2O_5/BHJ and WO_3/BHJ samples. The decomposition of UPS of V_2O_5/BHJ interfaces is shown in Figure 6-9. The spectrum Ref. A in Figure6-9(A) from different groups exhibits high similarity to pristine V_2O_5 in Figure 6-9(A), while Ref. B in Figure 6-9(B) reveals the same features with pristine BHJ. Ref. C can be assigned to BHJ spectrum, but is subjected to dipolar electric bias which causes energy shift.

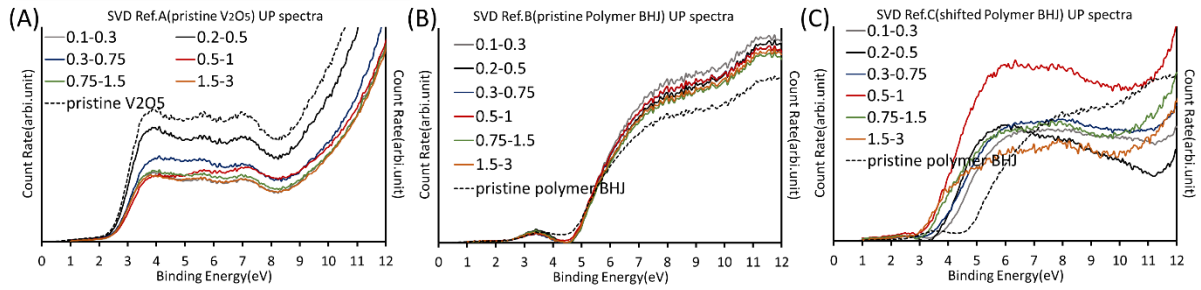

Figure 6- 9. (A) Reference spectrum A from different group features similar to pristine V_2O_5; (B) Reference spectrum B behaves as pristine BHJ; (C) Reference spectrum C as BHJ but shifts on energy scale

However, it is important to note that Ref. C shifts by a different energetic step across a variety of groups. The energy shift is stronger with a higher deposition of TMO on BHJ. As discussed in Chapter 5, due to the limits of SVD, weighted shifting method (WSM) were used for fitting the measured spectra. In this chapter, the decomposition equation has been modified as follows.

$$S_{meas}^{(i)} = \sum_{j=0}^{n} a_j^{(i)} \times S_{BHJ}\left(E + j \cdot \Delta E\right) + b \cdot S_{V_2O_5} \quad \text{with} \quad \sum_j a_j^{(i)} + b = 1$$ Equation 6-1

$$S_{meas}^{(i)} = \sum_{j=0}^{n} a_j^{(i)} \times S_{BHJ}\left(E + j \cdot \Delta E\right) + b \cdot S_{WO_3} \quad \text{with} \quad \sum_j a_j^{(i)} + b = 1$$ Equation 6-2

$$\Delta E_{mean}^{(i)} = \sum_{j=0}^{n} a_j^{(i)} \cdot j \cdot \Delta E$$

$S_{meas}^{(i)}$: The measured spectrum i

S_{BHJ} : The spectrum of the pristine BHJ layer

$S_{V_2O_5}$ and S_{WO_3} : The spectra of the samples with 8 nm V_2O_5 and WO_3 on Si individually for pristine reference

$a_j^{(i)}$: The weighting factors

$\Delta E_{mean}^{(i)}$: the mean shift for spectrum i

ΔE : The stepwise energy shift, which was set to 0.1eV

The electronic properties of pristine materials are included. The stepwise energy shift was set to 0.1 eV.

In Figure 6-10(A), the weighing factors of both BHJ and V_2O_5 and the mean energy shift from UP spectra are shown. The decomposition results of MIE spectra are shown in Figure 6-10(C). Figure 6-10(B) and (D) show the distribution of energy shift of UP and MIES spectra across the range respectively, from which the maximum energy shift of BHJ is observed as 2.5 eV in UP spectra.

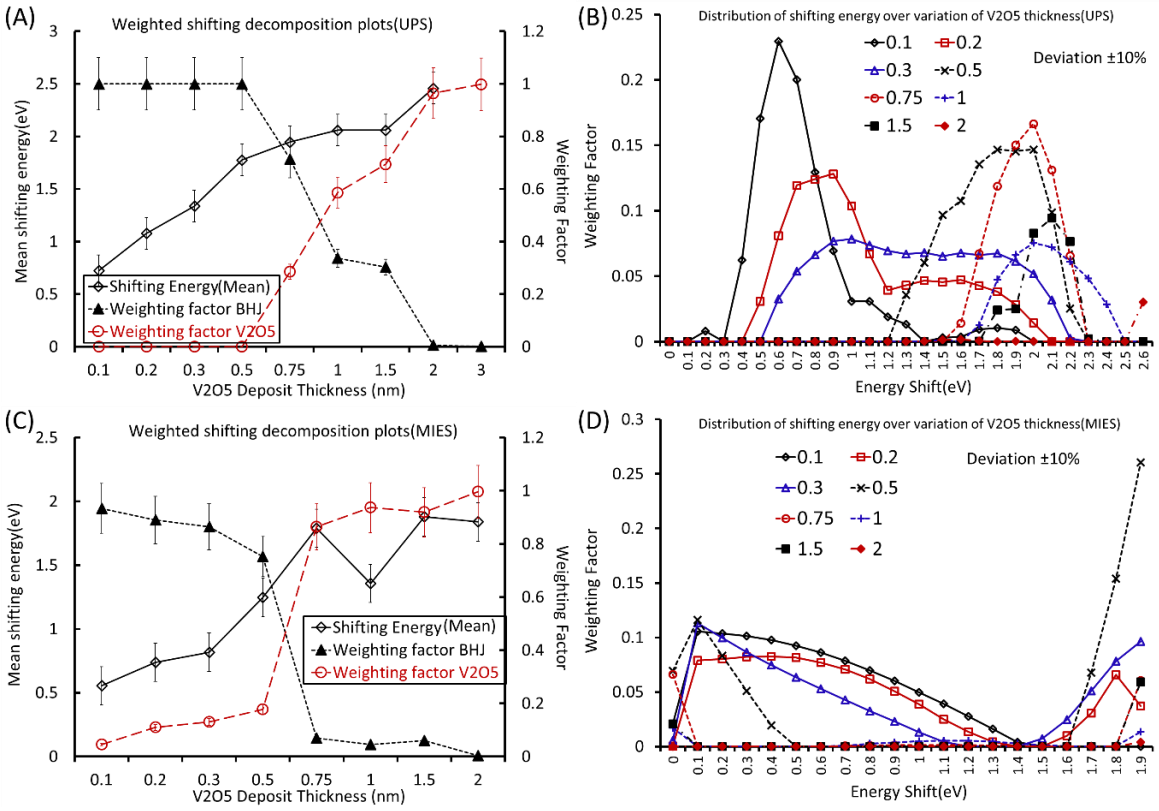

Figure 6- 10. (A)(C) Weighting factor of BHJ and V_2O_5 and the weighted shifting energy of UPS and MIES; (B)(D) Distribution of energy shifts of the polymer BHJ from UPS and MIES; Note that after 1nm, the V_2O_5 has covered the surface thus the weighing factor of BHJ in MIES is not observed after 1nm.

In Figure 6-10(A), up to a V_2O_5 thickness of 1 nm, a weighting factor of at least 0.32 of shifted polymer BHJ is observed and the energy shift levels at 2.0 ±0.1 eV, while the fraction of V_2O_5 weights about 0.68. Subsequently, the mean energy shift (ΔE^i_{mean}) peaks at 2.4 ± 0.1 eV with 3 nm V_2O_5. It can be seen either the ΔE^i_{mean} or maximum energy shift (ΔE^i_{Max}) increases with the increasing amount of V_2O_5 deposition.

The ΔE^i_{mean} and weighting factors of components for fitting the MIE spectra can be derived from Figure 6-10(C). The weighting factor of V_2O_5 levels at 0.96 ±10% and has approached unity, thus determining that full coverage of the BHJ with V_2O_5 can be achieved by a 1–1.5 nm deposition. A parallel increase of ΔE^i_{mean} with the increasing amount of V_2O_5 evaporation was determined. It can be seen that the fitting method resulted in a small degree of deviation and

that the energy shift of BHJ still showed up after 1.5 nm V_2O_5, shown in Figure 6-10(C).

The results of the decomposition upon valence electron region of UPS and MIES of WO_3/BHJ samples are shown in Figure 6-11. Weighing factors of WO_3 and BHJ and the weighted shifting energy from UP/MIE spectra are shown in Figure 6-11(A) and (C) and the distribution of energy shift in Figure 6-11(B) and (D).

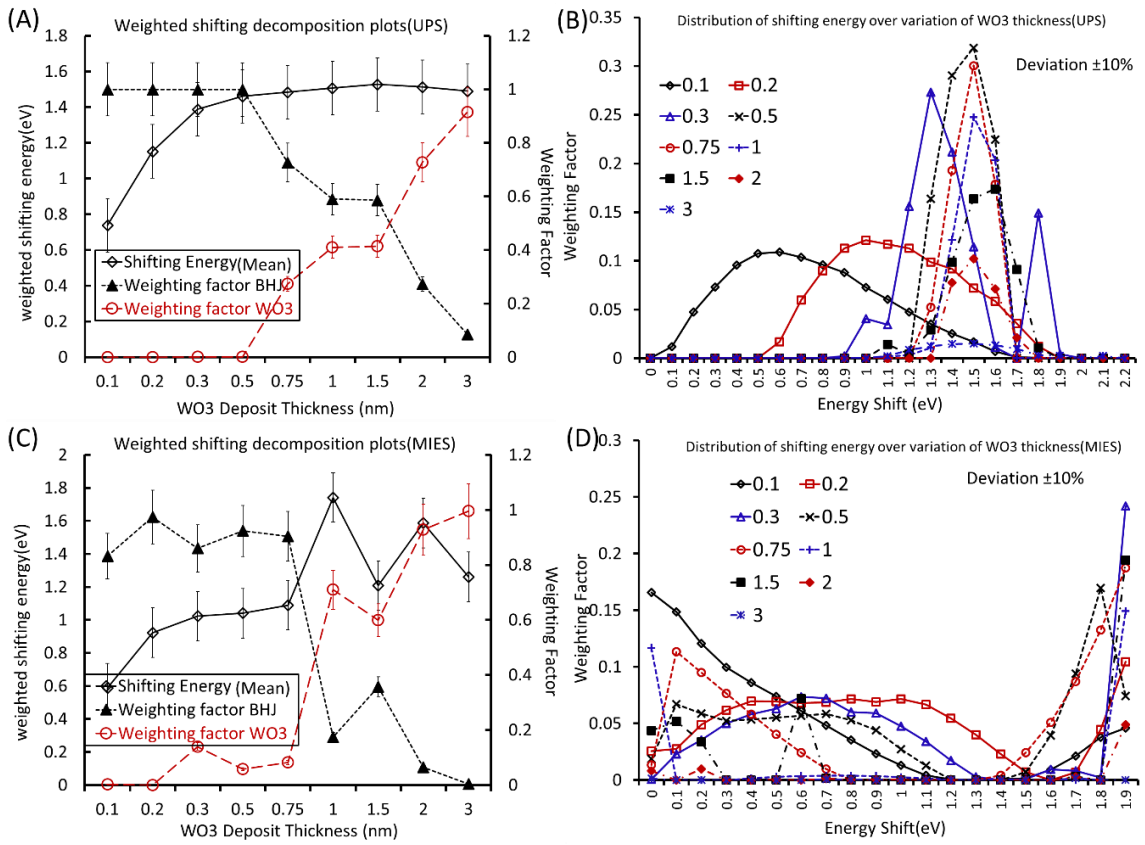

Figure 6- 11. (A)(C) Weighting factor of BHJ and WO_3 and the weighted shifting energy of UPS and MIES; (B)(D) Distribution of shifting energy of the polymer BHJ from UPS and MIES

In Figure 6-11(A), up to a WO_3 thickness of 1 nm, the ΔE^i_{mean} levels at 1.6 ±0.1 eV of UPS, which remains constant with the increase of WO_3 deposition. Under the same circumstance, a weighting factor of 0.6 of BHJ is determined. The MIES result, shown in Figure 6-11(C), reveals a weighting factor of 0.7 of WO_3 with 1 nm thickness, which rises to approximately 0.9 with 3 nm WO_3. A closed layer of WO_3 on BHJ surface can form with at least 3 nm depositions, which is identical to the NICISS result. The ΔE^i_{mean} and ΔE^i_{Max} rise due to the escalation of the deposition thickness of WO_3. However, the dipole strength related to the energy shift at the

WO_3/BHJ interface is weaker than that of V_2O_5/BHJ. This will be discussed in Chapter 6.3.8.

The reason for the formation of such a dipole at the TMOs/BHJ interface is as follows. The electron immigrates from polymer BHJ to TMOs due to the energy level alignment[35]. Thus, the dipole sides at positive polarity, pointing towards the metal oxides.

6.4.6. Work Function Reconstitution and Reconstruction of Energy Levels at the Interfaces

The method of WF reconstitution[36] was applied in Chapter 3 for the purpose of verifying the decomposing and fitting procedure. The algorithm is based on the convolution of components as in Equation 3-2: the pristine BHJ, the BHJ but subject to be shifted electronically at the interface, and the TMOs spectra with their individual weighting factor. The fittings of WF of V_2O_5/BHJ and WO_3/BHJ are individually shown in Figure 6-12(A) and (B) respectively.

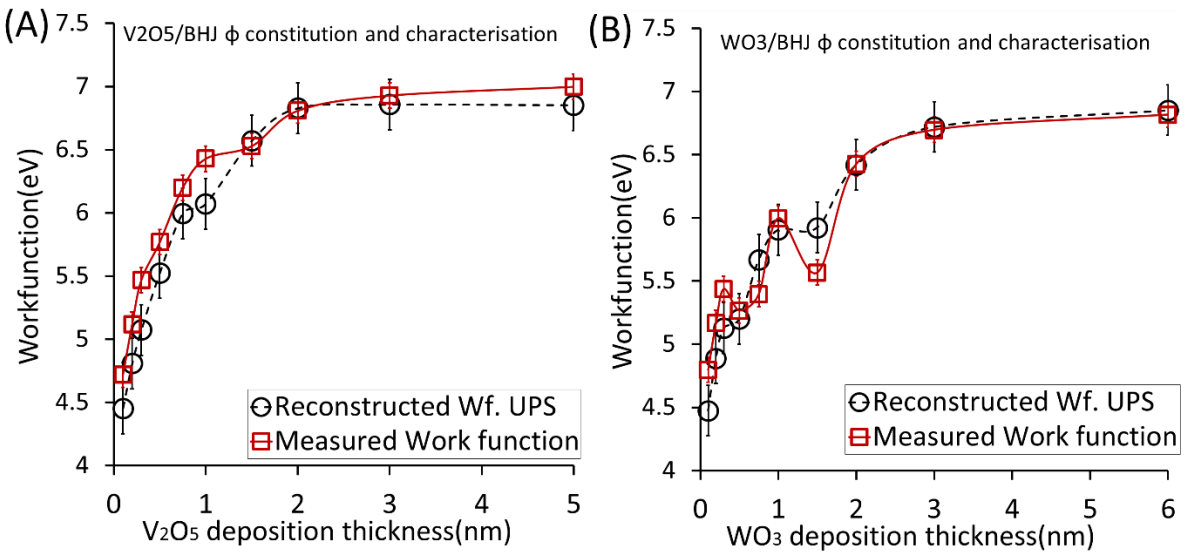

Figure 6- 12. Measured and reconstructed WF for (A) V_2O_5 and (B) WO_3 thicknesses on P3HT/$PC_{61}BM$

The reconstructed WF fits the measured WF reasonably well within error bars for V_2O_5/BHJ and WO_3/BHJ samples. Given that the weighting factors are calculated from the decomposition upon valance electron spectra, and thus representing the interface dipole energy, the constitution of WF can be considered an explanatory demonstration that the root cause of

modification of WF upon TMO deposition is due to the interface dipole complex.

Given that the quantities of electric properties of V_2O_5 and BHJ have been collected (see Table 6-1) and the intermediate BHJ spectra with energy shift are shown, a comprehension of the energy levels at the V_2O_5/BHJ interface can be further achieved. The WF/ϕ, E_{HOMO}/E_{LUMO} of BHJ, E_{VB}/E_{CB} of V_2O_5 is included in Table 6-1. Figure 6-10(B) shows the weighting factor of shifted BHJ spectra from UPS. Thus, the reconstruction of energy levels at the V_2O_5/BHJ interface across a variety of V_2O_5 thickness is shown in Figure 6-13, which abides by the mode of MoO_3/BHJ samples. The zero mark on the horizontal axis indicates the region of polymer BHJ with no deposition of V_2O_5. Thus, the left side can be assigned to the inner part of the pristine BHJ while the right side represents the occurrence of V_2O_5 with a range of deposition thicknesses.

It was noted that no energy gap or barrier was seen at the V_2O_5/BHJ interface with more than 0.2 nm V_2O_5 deposited. The E_{HOMO} of BHJ with maximum shifting energy has exceeded the E_{CB} of V_2O_5 due to the deposition of V_2O_5 generating a strong dipole at the interface.

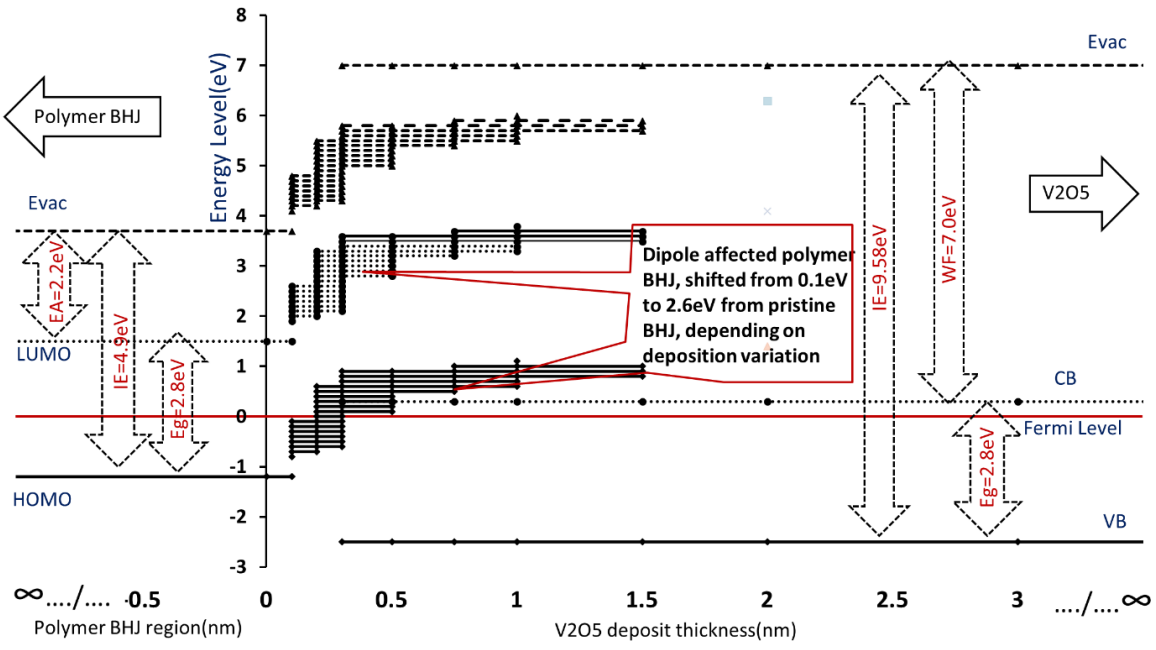

Figure 6- 13. The reconstruction of interface energy bands of pristine polymer BHJ, energy-shifted BHJ and pristine V_2O_5 upon variation of deposition thickness

Regarding the energetic values of the energy levels of the WO_3/BHJ samples, plotted in Table

6-1 and Figure 6-11(B), the energy levels at the interface with an increase in WO_3 layer thickness are displayed in Figure 6-14. In contrast, a prerequisite of depositing at least 1 nm WO_3 on BHJ is necessary to eliminate the energy gap between HOMO of intermediate BHJ and CB of WO_3. Given that the dipole here is weaker than that of V_2O_5, the HOMO of shifting BHJ with a highest energy is just aligned with the CB of WO_3.

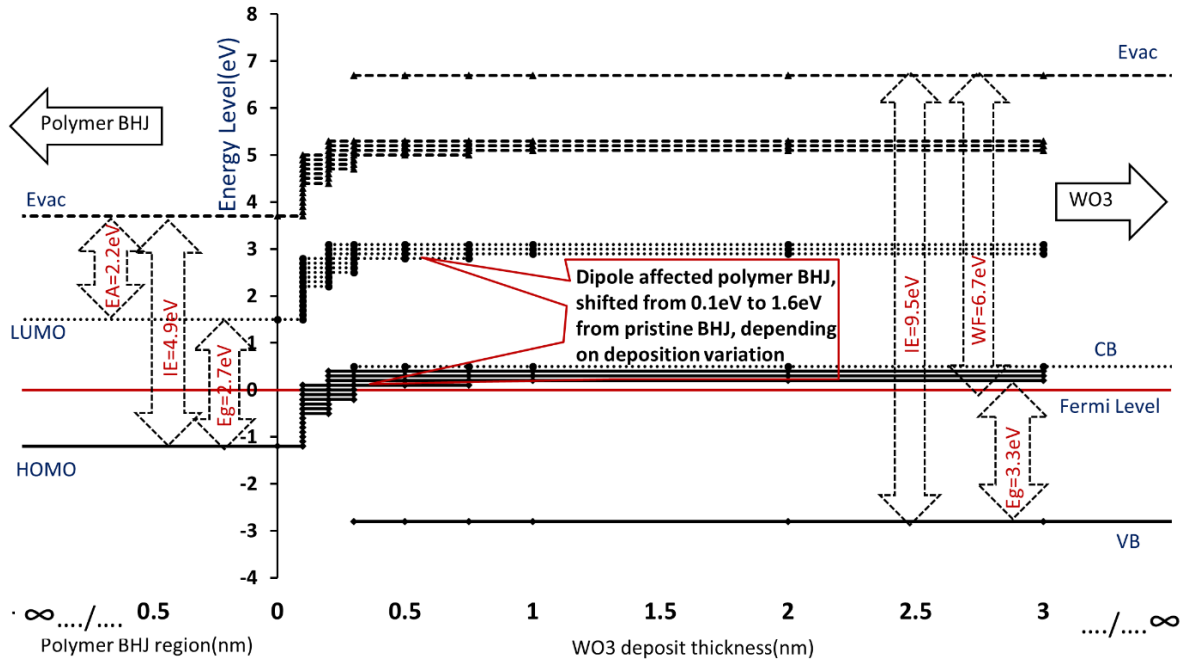

Figure 6- 14. The reconstruction of interface energy bands of pristine polymer BHJ, energy-shifted BHJ and pristine WO_3 upon variation of deposition thickness

6.4.7. Implication for the Operation of Charge Transfer over the Interfaces

A specific quantity of V_2O_5 will be evaporated onto polymer BHJ in a polymer-based solar cell when V_2O_5 serves as an ABL. Therefore, the electronic energy levels and the charge transfer under the circumstance will be discussed in this chapter. For reference, Figure 6-15 shows the energy level schematics and charge transfer at an interface of BHJ with 1 nm thickness V_2O_5. In Figure 6-10(B) and Figure 6-13, a range of BHJ spectra with different energy shift representing intermediate energy states have been observed and characterised. The energy shift was determined and ranges from 1.8 eV to 2.4 eV. Thus, the energy levels are shown and all the electronic parameters are taken from measured outcomes. In the schematics, the hole is

capable of transferring from HOMO of BHJ bulk to the intermediate HOMO levels of BHJ due to the energy shift, after which, hole transition from BHJ to the CB of V_2O_5 can be achieved because the energy gap in-between has been eliminated by dipole. Consequently, the charge injection/extraction mechanism[34] can be energetically supported. The charge transfer efficiency is expected to boost, thus improving the performance of the device[37].

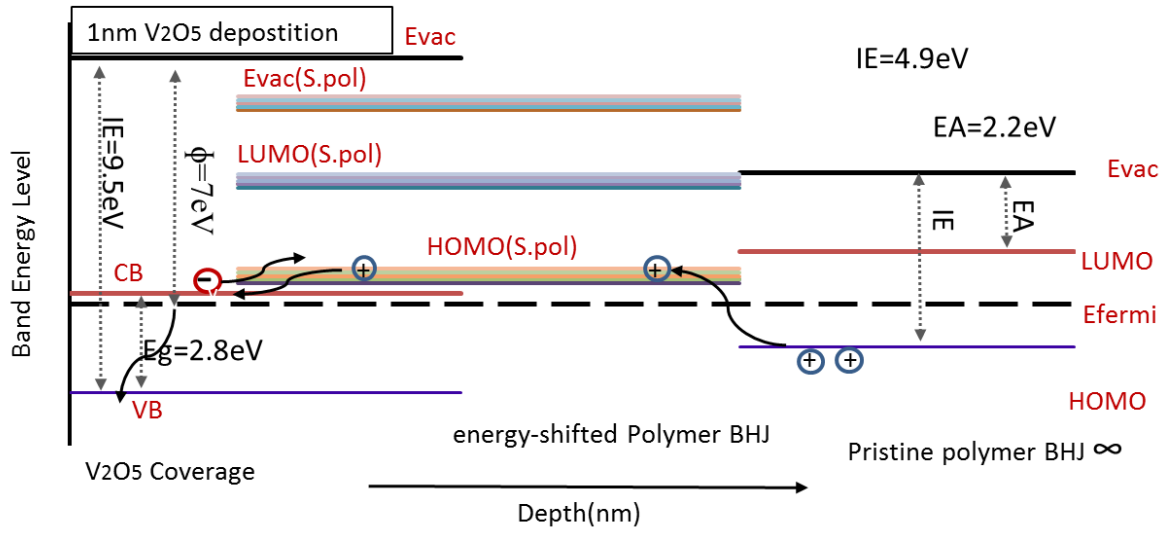

Figure 6- 15. The interface energy level structure of 1nm V_2O_5 on polymer BHJ and the illustration of charge transfer

An estimation of charge transfer over the WO_3/BHJ sample is shown in Figure 6-16. An example of 1 nm WO_3 on BHJ has been discussed. By comparison, the maximum energy shift is now levelling at 1.6 eV, resulting in an energy gap of approximately 0.2 eV to the CB of WO_3. Given that hole trap can occur at such interface[38], which leads to charge loss, the charge extraction/injection mechanism is not appropriately supported with the given WO_3 thickness. The favourable charge transfer only establishes with at least 3 nm WO_3 deposited on BHJ.

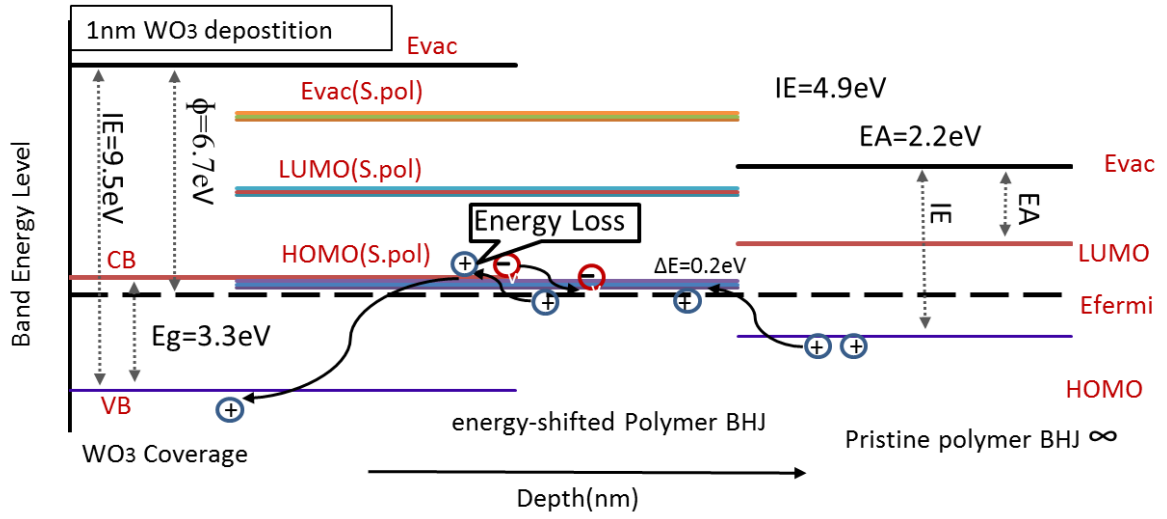

Figure 6- 16. The interface energy level structure of 1nm WO_3 on polymer BHJ and the illustration of charge transfer

6.4.8. Difference of the Dipole Forming and Surface Coverage among MoO_3, V_2O_5 and WO_3

The comparison of the dipoles forming at different interfaces including MoO_3/BHJ, V_2O_5/BHJ WO_3/BHJ is further discussed in this section. With abundant deposition thickness upon BHJ, the energy shift due to the interface dipoles is favourable for charge injection/extraction transport. The minimum deposition amount of these metal oxides for a closed surface layer and effective transport are shown individually in Table 6-2. The mean energy shift is included. The mean energy shift are from Figure 6-10(A) and Figure 6-11(A).

Metal Oxide On BHJ	**Minimum D for charge extraction/injection**	**Minimum D for a closed layer**	**D where the mean energy shift peaks**	**The mean energy shift peak(eV)**
MoO_3	0.75 nm	1~2 nm	3nm	2.0 ± 0.1
V_2O_5	0.5 nm	1 nm	2nm	2.4 ± 0.1
WO_3	2 nm	3 nm	1.5nm	1.6 ± 0.1

Table 6-2. The thickness of MoO_3, V_2O_5 and WO_3 to form a closed layer and charge extraction/injection transport. The thicknesses where mean energy shift peaks, are illustrated. (D: Thickness)

It is obvious the dipole forming at the V_2O_5/BHJ interface yields the largest energy shift while WO_3/BHJ provides the least energy shift. The cause of the difference can be addressed as follows:

a) Given that the dipole originates from the difference of WF of TMOs and polymer BHJ[19], the dipole strength relates to the pristine WF of TMOs. V_2O_5 possesses the highest WF at 6.9–7.0 eV, while that of MoO_3 is 6.8 eV and that of pristine WO_3 levels at 6.6–6.7 eV. The dipole strength is directly proportionate to the characterised WF of metal oxides.

b) The dipole forming at the interface can be related to the surface coverage of the metal oxides due to the accumulation of single dipole at the direction in parallel to the interface, which was described in Figure 3-9. The formation of a closed V_2O_5 layer requires less deposition than that of others; 3 nm WO_3 is requisite to cover the surface. The difference in the surface coverage rate is due to the difference of surface energy of the metal oxides. As stated[18], the surface energies of MoO_3 and V_2O_5 are 70 mj/m^2 and 80 mj/m^2 respectively. For WO_3, it is 100 mj/m^2. A higher surface energy leads to the occurrence of agglomeration of such metal oxides, by which the surface coverage can be postponed.

Finally, but importantly, in a polymer-based solar cell device performance can also strongly depend on the conductivity[39], transmittance[40] and amorphous states[41, 42] of these HTL metal oxides in addition to the interface dipole energy. Cell performance using WO_3 as an ABL is non-competitive compared to that using MoO_3[43]. The dipole energy forming at the interface could be one of the reasons. A selection of the materials for the buffer layer in polymer-based devices and the applied thickness has to be made with considerable thought.

6.5. Conclusion

In this chapter the dipole forming at the individual V_2O_5/P3HT:PCBM BHJ and WO_3/BHJ interfaces has been studied. The energy shift caused by the dipole can be seen from the shift of C and O components from XPS. The NICISS shows a penetration of the metal oxides into polymer BHJ, thus the mixing phase to form interface was determined. The energy levels and intermediate energy states at such interfaces have also been characterised from MIES and UPS.

In light of this, the charge transfer over the interface as a function of deposition thicknesses has also been discussed, as were differences in the interfaces and dipole strength among all the metal oxides. The cause of the variation has been identified and the potential implication on a device has been highlighted.

Reference

1. Sharma, A., et al., *Effect of indium and tin contamination on the efficiency and electronic properties of organic bulk hetero-junction solar cells.* Solar Energy Materials and Solar Cells, 2011. **95**(12): p. 3251-3255.
2. Liu, R., S.T. Lee, and B. Sun, *13.8% Efficiency hybrid Si/organic heterojunction solar cells with MoO3 film as antireflection and inversion induced layer.* Adv Mater, 2014. **26**(34): p. 6007-6012.
3. Elumalai, N.K., et al., *Enhancing the stability of polymer solar cells by improving the conductivity of the nanostructured MoO3 hole-transport layer.* Phys Chem Chem Phys, 2013. **15**(18): p. 6831-6841.
4. Zhang, Y., S. Yuan, and W. Liu, *Inverted organic solar cells employing RGO/TiOx composite films as electron transport layers.* Electrochimica Acta, 2014. **143**: p. 18-22.
5. Zhang, F., et al., *Recent development of the inverted configuration organic solar cells.* Solar Energy Materials and Solar Cells, 2011. **95**(7): p. 1785-1799.
6. Stubhan, T., et al., *High shunt resistance in polymer solar cells comprising a MoO3 hole extraction layer processed from nanoparticle suspension.* Applied Physics Letters, 2011. **98**: p. 253308.
7. Wang, H.-Q., et al., *Nanocrystal V2O5 thin film as hole-extraction layer in normal architecture organic solar cells.* Organic Electronics, 2012. **13**(12): p. 3014-3021.
8. Galatsis, K., et al., *Sol-Gel prepared MoO3-WO3 thin-films for O2 gas sensing.* Sensors and Actuators B, 2001. **77**: p. 478-483.
9. Nakayama, Y., et al., *Origins of Improved Hole-Injection Efficiency by the Deposition of MoO3on the Polymeric Semiconductor Poly(dioctylfluorene-alt-benzothiadiazole).* Advanced Functional Materials, 2009. **19**(23): p. 3746-3752.
10. Haemers, J., E. Baetens, and J. Vennik, *On the electrical conductivity of V2O5 single crystals.* Applications and materials science, 1973. **20**(1): p. 381-386.
11. Papaefthimiou, S., G. Leftheriotis, and P. Yianoulis, *Study of electrochromic cells incorporating WO3, MoO3, WO3-MoO3 and V2O5 coatings.* Thin Solid Films, 1999. **343-344**(1): p. 183-186.
12. Ozer, N. and C.M. Lampert, *Electrochromic performance of sol-gel deposited WO3–V2O5 films.* Thin Solid Films, 1999. **349**(1-2): p. 205-211.
13. Kröger, M., et al., *Role of the deep-lying electronic states of MoO3 in the enhancement of hole-injection in organic thin films.* Applied Physics Letters, 2009. **95**(12): p. 123301.
14. Meyer, J., et al., *Transition metal oxides for organic electronics: energetics, device physics and applications.* Adv Mater, 2012. **24**(40): p. 5408-5427.
15. Chen, S., et al., *Metal oxides for interface engineering in polymer solar cells.* Journal of Materials Chemistry, 2012. **22**(46): p. 24202.
16. Meyer, J. and A. Kahn, *Electronic structure of molybdenum-oxide films and associated charge injection mechanisms in organic devices.* Journal of Photonics for Energy, 2011. **1**(1): p. 011109.
17. Meyer, J., et al., *Charge generation layers comprising transition metal-oxide/organic interfaces: Electronic structure and charge generation mechanism.* Applied Physics Letters, 2010. **96**(19): p. 193302.
18. Mitchell, B.S., *An Introduction to Materials Engineering and Science: For Chemical and Materials Engineers.* Book, 2004.
19. Terán-Escobar, G., et al., *Low-temperature, solution-processed, layered V2O5 hydrate as the hole-transport layer for stable organic solar cells.* Energy & Environmental Science, 2013. **6**(10): p. 3088.
20. Wu, J., et al., *Role of solution-processed V2O5 in P3HT:PCBM based inverted polymer solar cells.*

Synthetic Metals, 2013. **170**: p. 7-10.

21. Tao, C., et al., *Role of tungsten oxide in inverted polymer solar cells.* APPLIED PHYSICS LETTERS, 2009. **94**.
22. Chen, Y. and S. Ruan, *Highly efficient ITO-free polymer solar cells based on metal resonant microcavity using WO3/Au/WO3 as transparent electrodes.* Organic Electronics, 2014. **15**(7): p. 1545-1555.
23. Silversmit, G., et al., *Determination of the V2p XPS Binding Energies for Different Vanadium Oxidation States (V5+ to V0+).* Journal of Electron Spectroscopy, 2004. **135**: p. 167-175.
24. Mendialdua, J., R. Casanova, and Y. Barbaux, *XPS studies of V2O5, V6O13 , VO2 and V2O3* Journal of Electron Spectroscopy and Related Phenomena, 1995. **71**: p. 249-261.
25. Scudiero, L., Y. Shen, and M. Gupta, *Effect of light illumination and temperature on P3HT films, n-type Si, and ITO.* Applied Surface Science, 2014. **11**: p. 085.
26. Schmerl, N. and G. Andersson, *A layered structure at the surface of P3HT/PCBM blends.* Phys Chem Chem Phys, 2011. **13**(33): p. 14993-15002.
27. Zhang, Z., et al., *Co3O4 Hollow Nanoparticles and Co Organic Complexes Highly Dispersed on N-Doped Graphene: An Efficient Cathode Catalyst for Li-O2 Batteries.* Particle Systems Characterization, 2015. **32**(6): p. 680-685.
28. Yin, Y., et al., *Dipole Formation at the MoO3/Conjugated Polymer Interface.* Advanced Functional Materials, 2018. **28**(46): p. 1802825-1802835.
29. Prześniak-Welenc, M., et al., *Electrical conductivity and relaxation processes in V2O5 nanorods prepared by sol-gel method: Electrical conductivity and relaxation processes in V2O5 nanorods.* Phys. Status Solidi B, 2015. **252**(9): p. 2111–2116.
30. Jeon, I., et al., *Air-processed inverted organic solar cells utilizing a 2-aminoethanol-stabilized ZnO nanoparticle electron transport layer that requires no thermal annealing.* J. Mater. Chem. A, 2014. **2**: p. 18754-18760.
31. Ghoreishi, K.B., et al., *Enhanced Catalyst Activity of WO3 Using Polypyrrole as Support for Acidic Esterification of Glycerol with Acetic Acid.* Journal of Chemistry, 2013. **2013**: p. 10.
32. Mansour, A.E., et al., *Facile Doping and Work-Function Modification of Few-Layer Graphene Using Molecular Oxidants and Reductants.* Advanced Functional Materials, 2017. **27**(7).
33. Meyer, J., et al., *Metal oxide induced charge transfer doping and band alignment of graphene electrodes for efficient organic light emitting diodes.* Sci Rep, 2014. **4**: p. 5380.
34. Hamwi, S., et al., *p-type doping efficiency of MoO3 in organic hole transport materials.* Applied Physics Letters, 2009. **94**(25): p. 253307.
35. Meyer, J., et al., *Electronic structure of Vanadium pentoxide: An efficient hole injector for organic electronic materials.* Journal of Applied Physics, 2011. **110**(3): p. 033710.
36. Berlich, A., Y. Liu, and H. Morgner, *Growth of nickel nanoparticles on NiO/Ni(001): Evidence of adsorbed oxygen on metal particles by metastable induced electron spectroscopy (MIES).* Surface Science, 2008. **602**(24): p. 3737-3744.
37. Lin, C.F., et al., *High photoelectric conversion efficiency of metal phthalocyanine/fullerene heterojunction photovoltaic device.* Int J Mol Sci, 2011. **12**(1): p. 476-505.
38. Stolterfoht, M., et al., *Charge Transport without Recombination in Organic Solar Cells and Photodiodes.* The Journal of Physical Chemistry C, 2015. **119**(48): p. 26866-26874.
39. Godoy, A., et al., *Effects of the buffer layer inserted between the transparent conductive oxide anode and the organic electron donor.* Solar Energy Materials and Solar Cells, 2009. **49**(4): p. 648-654.
40. Yua, W., et al., *Highly efficient and high transmittance semitransparent polymer solar cells with one-*

dimensional photonic crystals as distributed Bragg reflectors. Organic Electronics, 2013. **15**(2): p. 470-477.

41. Ramans, G.M., et al., *Structure of amorphous thin films of WO3 and MoO3.* Journal of Non-Crystalline Solids, 1987. **90**(1-3): p. 637-640.
42. Siokou, A., et al., *Effect of the tungsten and molybdenum oxidation states on the thermal coloration of amorphous WO3 and MoO3 films.* Surface Science, 2001. **482-485**(1): p. 294-299.
43. Gerling, L., et al., *Characterization of Transition Metal Oxide/Silicon Heterojunctions for Solar Cell Applications.* Applied Sciences, 2015. **5**(4): p. 695-705.

Chapter 7. Influence of Moisture on the Energy Level Alignment at the V_2O_5/BHJ and WO_3/BHJ Interfaces

7.1. Abstract

Electron spectroscopy was applied to investigate the chemical and electronic properties of the interfaces formed at V_2O_5 and WO_3/P3HT:$PC_{61}BM$ BHJ as a consequence of air exposure. Over an exposure of 36 hrs, H_2O and other residues are adsorbed on the sample surface and also penetrate to the interface. H_2O molecules diminish the workfunction of the metal oxides and also encounter the dipolar orientation at such interfaces, significantly deteriorating dipole strength. It was also found that the polymer BHJ is oxidised due to the air exposure. Subsequently, the energy band structure at the metal oxides/BHJ interface is altered. The change of energy level positioning and diminishing of the dipole lead to the misalignment of energy levels which is predicted to decline the charge transfer. The nature of the interface across a range of air exposure durations is discussed in this chapter.

7.2. Introduction and Research Aim

The interfaces forming at the boundary of high WF metal oxides, V_2O_5, WO_3 and a polymer BHJ substrate-P3HT:$PC_{61}BM$, were investigated and the formation of dipoles at the interface characterised with multiple photoelectron spectroscopy. Dipole strength significantly influences the charge transfer in a polymer-based solar cell [1, 2] using V_2O_5 or WO_3 as an ABL. Therefore, from the perspective of operation of devices it is of important to understand the stabilisation of such dipoles during fabrication.

The electrical properties of pristine V_2O_5 and WO_3 have been reported[2]. The WF of V_2O_5 was characterised as 7.0 eV[1], while the IE was assigned to 9.5 eV. The WF and IE for WO_3 were 6.7 eV and 9.8 eV respectively[3]. In Chapter 6, the WF and IE of V_2O_5 and WO_3 were measured and also approached the reported values. Such high WF and IE can lead to significant dipole strength of ~2 eV to support the charge transfer over the interface of metal oxides and polymer BHJ [4-6]. However, the range of the electrical properties of these metal oxides has

previously been measured when other means of processing are adopted [7, 8]. The WF of V_2O_5 is thus reported as 5.2 eV[9] after air exposure, while the WF of an exposed WO_3 film has been characterised as 5.0 eV[10]. An energetic difference of ~1.6 eV of WF would noticeably influence dipole strength. Therefore, the influence of air exposure on the interface and dipole of V_2O_5/BHJ and WO_3/BHJ is studied as such exposure is inevitable during commercialised device fabrication.

The influence of air exposure on the MoO_3/BHJ interface was shown in Chapter 4, where the invasion of H_2O was determined to orient freely and encounter the interface dipole. Thus, the overall dipole strength is diminished. Due to the similarity of the electrical properties of these metal oxides, a similar nature is assumed for the V_2O_5/BHJ and WO_3/BHJ interfaces once the samples are exposed. Photoelectron spectroscopy was employed for chemical and electrical characterisation and ion scattering spectroscopy was applied to profile the elemental distribution. This chapter first aims to show how the air exposure affects the electrical performance of V_2O_5 and WO_3 and which atmospheric compounds cause the most impact. Thus, the change upon dipole at such interfaces can be determined as a function of air exposure. The charge transfer over the interfaces is also discussed later.

7.3. Sample Preparation and Treatment

High purity P3HT and $PC_{61}BM$ were blended as described in Chapter 2 and spin-coated on Si substrate. All samples were made in the same batch, thus they have a relatively identical nature. The evaporation of V_2O_5 and WO_3 was processed individually on the substrates. The details of BHJ fabrication and physical vapour deposition of these TMOs are discussed in Chapter 2. The evaporation was processed synchronously to maintain the uniformity of samples. Air exposure was proceeded and periodically controlled, as shown Figure 7-1.

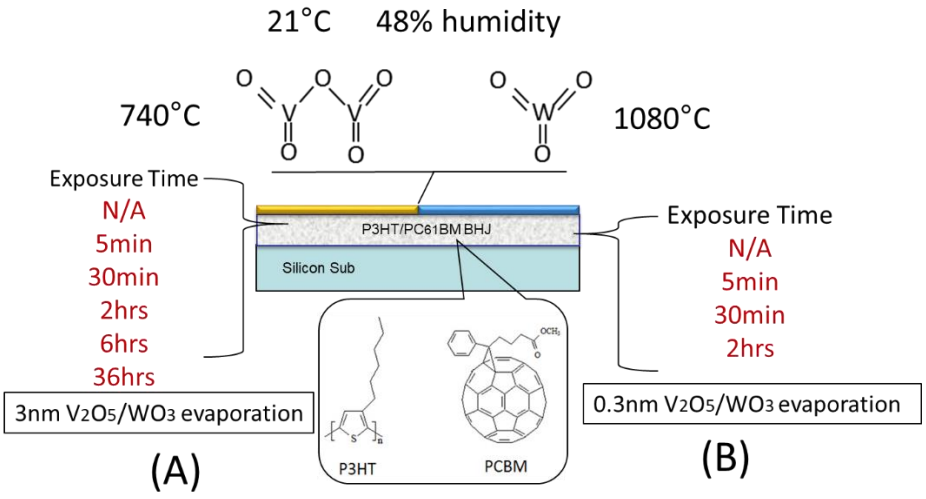

Figure 7- 1. Sample structure of V_2O_5/BHJ and WO_3/BHJ and air exposure treatments on respectively 3nm TMOs (A) and 0.3nm TMOs (B) on BHJ

As discussed in the MoO_3 work in Chapter 4, samples were made with two metal oxide layer thicknesses. The 3 nm thickness layers were fabricated to investigate the electric properties of TMO only due to the measuring depth of UPS[11], while measurement on 0.3 nm thickness samples characterise the changes over TMO/BHJ interface. Thus, analysis of the interface including a characterisation of the dipole can be achieved across a range of exposure times. The samples were exposed to atmosphere in lab conditions at approximately 21° C with 50% humidity. The controllable exposure time ranged from 5 mins to 36 hrs for 3 nm samples, and 5 mins to 2 hrs for 0.3 nm samples. All measurements were processed under UHV ($<10^{-9}$ mbar) after the samples had been introduced into the analysis chamber.

7.4. Results and discussion

7.4.1. Chemical Characteristics and Valence States Shift of the Air-exposed V_2O_5/BHJ Interface

To characterise the chemical and elemental valence state change of the V_2O_5/P3HT:PCBM interface which was exposed to air for a variety of exposure durations, the high-resolution scan of XPS of V, S, C and O was processed on 3 nm deposition thickness samples at a pass energy of 10 eV. The spectra are illustrated in Figure 7-2(A), (B) and (C). The energy position of C

and O of a given proportion of BHJ is shown in Figure 7-2(D). The calculated O concentration of the adsorbed proportion of H_2O and O_2 upon exposure is shown in Figure 7-2(E).

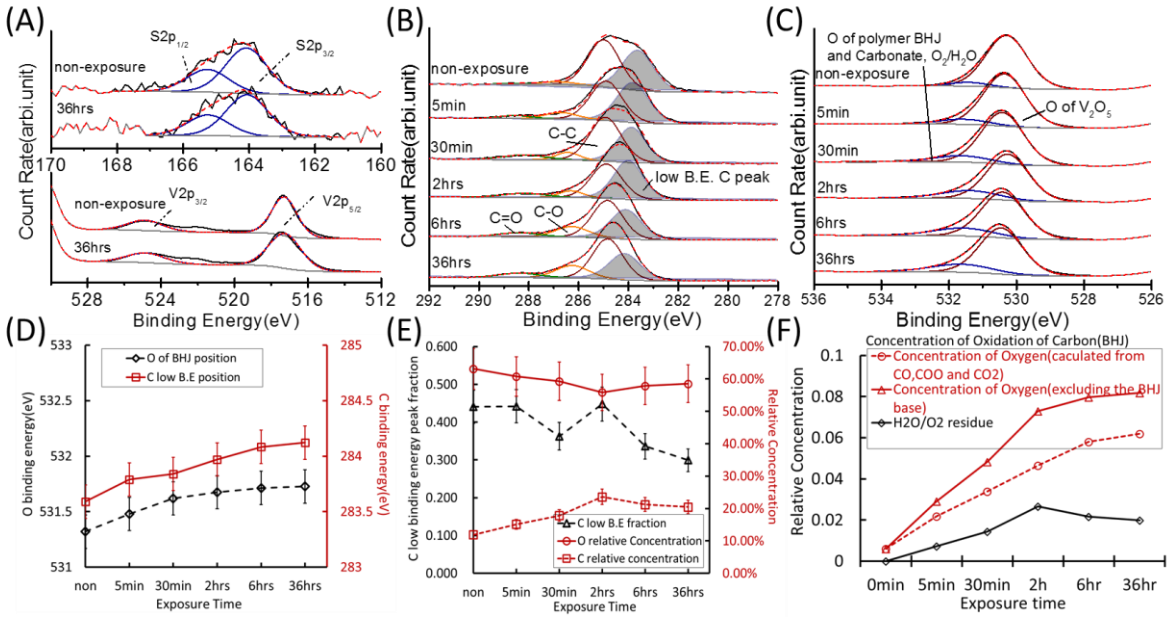

Figure 7- 2. (A)(B)(C) High-resolution scan of S, V, C and O; (D) O of BHJ and C low binding energy peak position; (E) The fraction of C low binding energy peak in contribution of C, the elemental concentration of C and O; (F) The calculation of the concentration of O from adsorbent-H_2O and O_2 as a function of exposure time

Upon exposure for up to 36 hrs, no obvious energetic change of V and S was identified in Figure 7-2(A). The $V2p_{5/2}$ peak being assigned as pristine V_2O_5 is fitted at 517.1 ± 0.15 eV[12, 13] with a doublet $V2p_{3/2}$, while the $S2p_{3/2}$ was found at 164.0 ± 0.15 eV[14, 15] of both non-exposed and 168 hrs exposed samples. The occurrence of S is attributed to the thiophene of P3HT[16]. Therefore, V_2O_5 was not reduced through the exposure. Thus, the conclusion made is contradictory to those previously reported[2]. In Figure 7-2(B), the fitting of C results in four individual peaks. The C-C peak was identified as 285.0 ± 0.15 eV, while the C-O/Sp2 peaks were identified as 286.3 ± 0.15 eV[17, 18]. COO/Sp3 peak was thus allocated at 288.3 ± 0.15 eV[17]. The intensity of oxidised C peak (C-O and COO) slightly increases, which is parallel to the escalation of exposure time. In Figure 7-2(E), the concentration of C was found to have slightly increased with increasing exposure time, the nature is not clear because the increase was not found in MoO_3 and WO_3. It can be Vanadium carbide or else. This is an

indication that either the polymer BHJ is oxidised or hydrocarbon is adsorbed into the surface due to the exposure. The non-exposed V_2O_5/BHJ sample exhibited a low binding energy C peak, which was found at 283.6 ± 0.15 eV. The specific C was assigned to the formation of a diploe at the V_2O_5/BHJ interface in Chapter 6. It can be derived from Figure 7-2(B), (D) and (E), wherein upon exposure for 36 hrs the C peak shifted from 283.6 eV to 284.2 eV, of which the fraction declines from 0.45 to 0.32. Thus, dipole strength at the interface diminishes due to air exposure.

Two peaks were identified by fitting the O peak and are shown in Figure 7-2(C). The one levelling at 530.3 ± 0.15 eV is relevant to V_2O_5[19], which is rather stable during air exposure. The other peak, found across a range from 531.3 to 531.7, can be assigned to O of the BHJ[20] which is subjected to the dipole bias. Similar to the trend of low binding energy C peak, the energy of this O peak increased with increasing exposure time. The extrapolation of concentration of O which is assigned to the adsorption of H_2O and O_2 has been made by subtracting the overall increasing of O and the O contribution to oxidation of BHJ. In Figure 7-2(F), it can be seen that the H_2O/O_2 increased within 2 hrs of exposure, after which it stabilised, indicating the adsorption of H_2O/O_2 can be saturated. Meanwhile, the oxidation of BHJ occurs constantly.

7.4.2. Chemical Characteristics and Valence States Shift of the Air-exposed WO_3/BHJ Interface

Figure 7-3 shows the high-resolution scans of Tungsten (W), S, C and O of 3 nm deposition thickness WO_3/BHJ samples across a variety of exposure times. The plot of C and O related to the dipole is shown in Figure 7-3(D). The elemental concentration is shown in Figure 7-3(E), while the residue of H_2O/O_2 adsorption is shown in Figure 7-3(F).

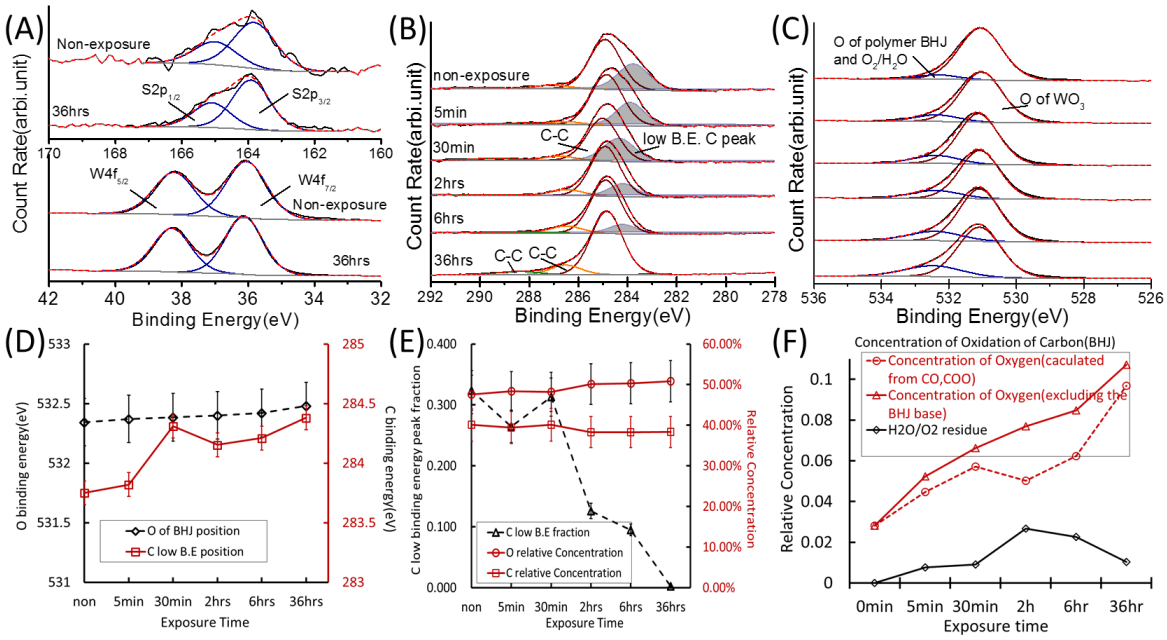

Figure 7- 3. (A)(B)(C) High-resolution scan of S, W, C and O; (D) O of BHJ and C low binding energy peak position; (E) The fraction of C low binding energy peak in contribution of C, the elemental concentration of C and O; (F) The calculation of the concentration of O from adsorbent-H_2O and O_2 as a function of exposure time

Similar to V_2O_5/BHJ upon exposure, no reduction of WO_3 or chemical change of P3HT:$PC_{61}BM$ was observed. $W4f_{7/2}$ energy distribution peaking at 36.0 ± 0.15 eV did not show any shift. Meanwhile, the $S2p_{3/2}$ peak was consistently situated at 164.0 ±0.15 eV among the samples. The C-O/Sp2 and COO/Sp3, which are individually fitted at 286.4 ±0.15 eV and 288.3 ±0.15 eV respectively, increase upon air exposure due to oxidation of the polymer BHJ. In Figure 7-3(B) and (D), the low binding energy C peak shifts from 283.8 to 284.3 in the 6 hrs exposed sample, after which it is hard to identify. The fraction declines synchronously from 0.32 to 0.13. Moreover, the O assigned to BHJ illustrates an energy shift from 532.2 eV to 532.8 eV within 36 hrs of exposure. These changes can be regarded as an indication of the decline of the interface dipole upon exposure. This nature is rather similar to that of the dipole forming at V_2O_5 and MoO_3/BHJ interfaces.

The relative concentration of O in Figure 7-3(E) increases from 46% to 49%, while that of C declines. Thus, it can be determined that no hydrocarbon or similar compounds have been adsorbed. By extrapolating the relative concentration of O owing to the H_2O and O_2, the

adsorption of such compounds peaks at around 2 hrs exposure time. The result is shown in Figure 7-3(F).

The adsorption of hydrocarbon, H_2O and O_2 was found in V_2O_5/BHJ samples, while only H_2O and O_2 were adsorbed in WO_3/BHJ samples. This could be due to the surface energy of V_2O_5 and WO_3 discussed in Chapter 6. The dipole forming at such interfaces shows a similar decreasing trend upon exposure.

7.4.3. Elemental Depth Distribution of Air-exposed V_2O_5/BHJ and WO_3/BHJ Interface

The NICISS was processed on non-exposed and 36 hrs exposed 3 nm V_2O_5/BHJ and 3 nm WO_3/BHJ samples for further investigation into the chemical properties and distribution over the interface. The results illustrating the distribution of V and W via certain depth (up to 15 nm) are shown in Figure 7-4. The scale of energy loss is also included.

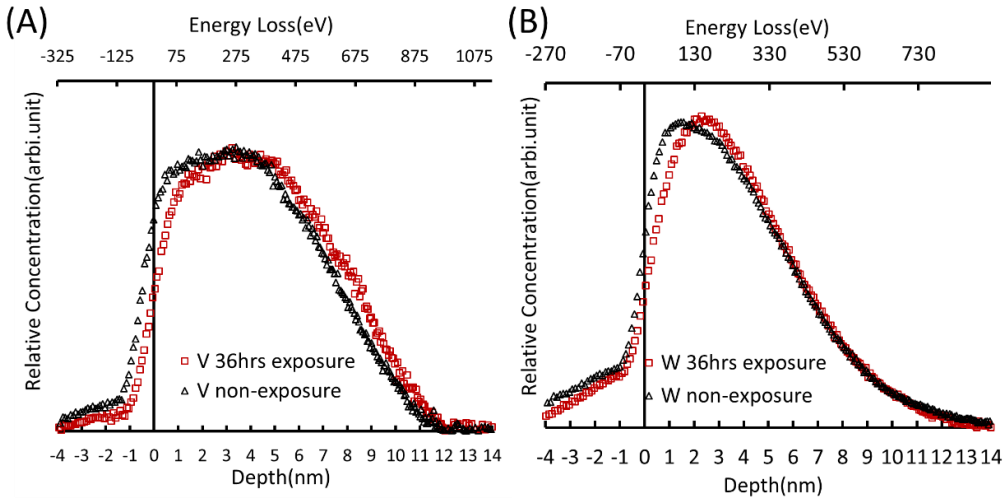

Figure 7- 4. The NICISS results of V and W upon V_2O_5/BHJ and WO_3/BHJ, The results include the samples before and after exposure to air. The duration was up to 36 hours

The penetration of V_2O_5 and WO_3 into polymer BHJ can be observed due to the distribution over a range of ~8 nm upon 3 nm metal oxides evaporation, and the gradient of the V and W concentration depth profile at the surface is much steeper than that of the TMOs/BHJ interface side. Upon air exposure of the samples, the concentration of V at the surface slightly decreases and shifts by ~0.8 nm into BHJ, while that of W shifts by ~0.9 nm. Thus, it can be determined

from the perspective of chemical distribution via depth that the compounds from atmosphere, mostly moisture, are adsorbed on the TMO/BHJ sample surface. The shift of the peak from the spectra is in agreement with that of the MoO_3/BHJ interface exposed to air in Chapter 4.

7.4.4. Decomposition and Analysis of MIES/UPS Spectra

a) The Analysis of MIES/UPS of 3nm V_2O_5/BHJ and WO_3/BHJ with Exposure

UPS and MIES measurement was conducted to characterise the change of electronic properties of V_2O_5 and WO_3 upon various exposure durations. The information can be derived from Figure 7-5(A) and (B). Figure 7-5(D) and (E) shows the secondary electron and the valence electron region of 3 nm V_2O_5/BHJ and WO_3/BHJ from UPS. The IPES was performed on samples to identify the conduction electron states, shown in the right side of Figure 7-5(B) and (E). The valence electron region of MIES is shown in Figure 7-5(C) and (F).

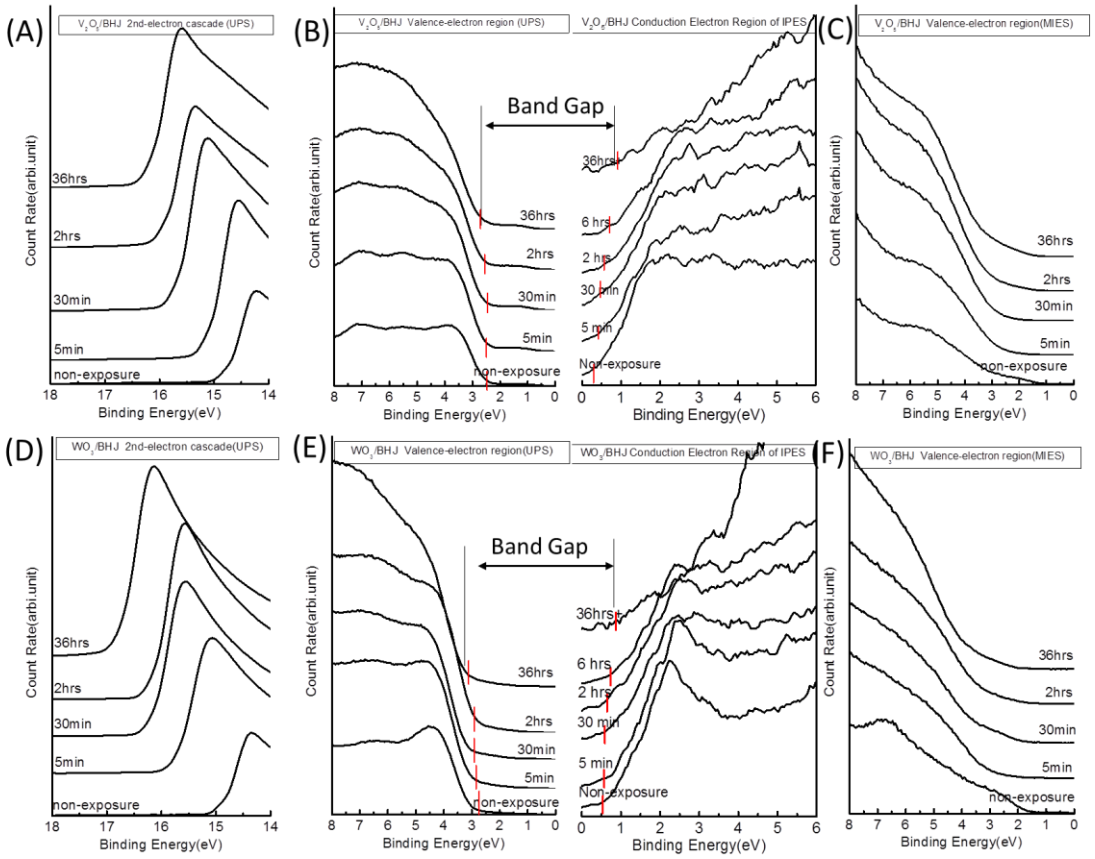

Figure 7- 5. (A),(D) The secondary electron cascade of UPS of V_2O_5/BHJ and WO_3/BHJ; (B),(E) The valence electron and conduction electron region of UPS and IPES of V_2O_5/BHJ

and WO_3/BHJ samples; (C),(F) The valence electron region of MIES of V_2O_5/BHJ and WO_3/BHJ

A shift of the second electron peaks on the binding energy scale of UPS was observed in both V_2O_5/BHJ and WO_3/BHJ samples. The V_2O_5/BHJ shifted from approximately 14.4 ± 0.1 eV in non-exposed condition to 16.0 ± 0.1 eV after 36 hrs exposure. In comparison, the insertion of peak on energy scale for WO_3/BHJ was at 14.7 eV in a non-exposed condition and shifted to 16.4 eV within the error bar after 36 hrs exposure. The valence electron states of UPS for the V_2O_5/BHJ samples are shown in Figure 7-5(B); an energy distribution peaking at ~6.5 eV grows as exposure time increases. This also occurred for the WO_3/BHJ samples, as shown in Figure 7-5(E). As stated[21, 22], the energy state approximating at 6.5 eV was assigned to the occurrence of moisture (H_2O/OH^-) 1 π state on these kinds of metal oxides. The similarity has also been found in the MoO_3/BHJ work in Chapter 4 (see Figure 4-5(B)). In addition, a shift of the conduction electron peak edge was observed, indicating an energy shift in the conduction state of TMO/BHJ due to exposure. As illustrated in Figure 7-5(C) and (F), the feature exhibited in the valence electron region of MIES revealed a shift relative to the energy scale as well. Subsequently, the changes upon WF, E_{VB} and E_{CB} were determined and the plots are shown in Figure 7-6. The E_g was calculated and is included. The extrapolation is described in the Chapter 2.

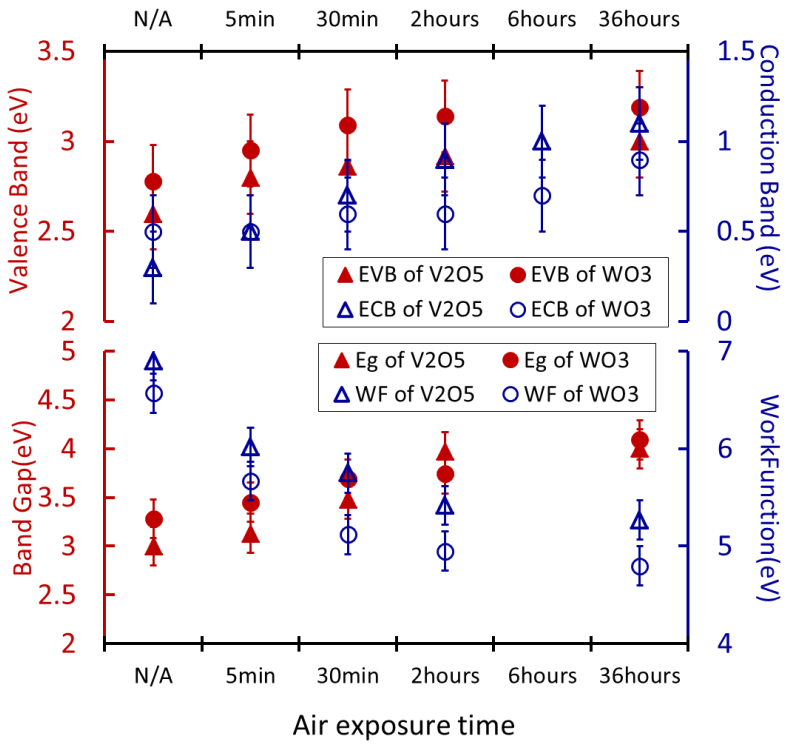

Figure 7- 6. Up: plots of E_{CB} and E_{VB} of V_2O_5 and WO_3/BHJ samples as a function of exposure time; Down: the WF and E_g of the set of sample

The WF derived from the bottom of Figure 7-6 decreases with increasing exposure time of the samples. The WF of non-exposed V_2O_5 sample levels was 6.9 ± 0.1 eV, which decreased to 6.0 ± 0.1 eV after 5 mins exposure and further decreased to 5.2 ± 0.1 eV after 36 hrs exposure. For WO_3 samples, the WF declined from pristinely 6.7 ± 0.1 eV to 4.8 ± 0.1 eV after 36 hrs exposure. The E_{VB} of V_2O_5/BHJ shown at the top of Figure 7-6 exhibits a gradual increase from 2.5 ± 0.1 eV to 2.9 ± 0.1 eV, while the E_{VB} of WO_3 increased from 2.8 ± 0.1 eV to 3.1 ± 0.1 eV. The E_{CB} of V_2O_5/BHJ showed a similar trend, increasing from 0.3 ± 0.1 eV at non-exposed to 1.0 ± 0.1 eV after 36 hrs exposure. The E_{CB} of WO_3/BHJ showed a smaller increase from 0.5 ± 0.1 eV to 0.9 ± 0.1 eV. It is noteworthy that, upon the exposure, the peak exhibiting at 2 eV of conduction electron spectra is being destructed which is assumed to be a metallic feature of such metal oxides.

It can be determined that the E_g of the two materials significantly broadened with air exposure. The nature is similar with that of MoO_3 described in Chapter 4. The electrical parameters including WF, E_{VB}, E_{CB} and E_g are detailed in Table 7-1. The E_g of V_2O_5 and WO_3 broadened

by 1.1 eV and 0.7 eV respectively. As described, the significant increase in E_g due to the air exposure can cause a sharp decline in the conductivity across the metal oxide layers[23, 24].

Sample	**WF(eV)±0.1**	**E_{HOMO}/ E_{VB} (eV)±0.1**	**E_{LUMO}/ E_{CB} (eV)±0.1**	**E_g (eV)±0.2**
Pristine V_2O_5	6.9	2.5	0.3	2.8
Exposed V_2O_5	5.2	2.9	1.0	3.9
Pristine WO_3	6.7	2.8	0.5	3.3
Exposed WO_3	4.8	3.1	0.9	4.0

Table 7-1. The plots of electrical properties of pristine V_2O_5/WO_3 and the same samples which have been exposed for more than 36hrs.

To determine which components from air cause the change in either valence electron features or WF, pristine samples of V_2O_5 and WO_3 on Si substrate were exposed to atmosphere (21 ℃, 48% humidity), dry N_2 (98%+) and dry air (98%) individually for 30 mins each. As seen in Figure 7-7, exposing the samples to a level of H_2O from the atmosphere causes major reduction of WF and shift of E_{VB}. The exposure to dry N_2 and dry air was with a small degree of moisture from the supplier gas line. Thus, the minor shifts of the spectra on the energy scale are mostly from such residues.

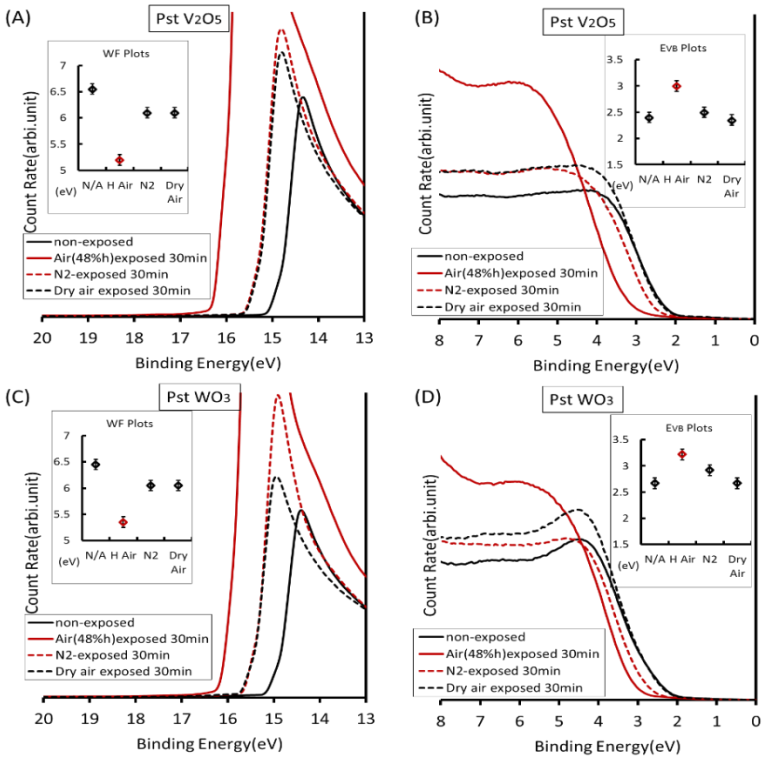

Figure 7- 7. (A) (B) The secondary-electron and valence electron regions of the pristine V_2O_5 sample exposed to different ambient; (C) (D) The secondary-electron and valence electron regions of the pristine WO_3 sample exposed to different ambient

b) Decomposition of Valence Electron Region of MIE/UP Spectra of 3nm V_2O_5/BHJ

To investigate the occurrence of components of V_2O_5/BHJ samples during air exposure, SVD was applied for decomposing the valence electron region of the MIES/UP spectra. The reference spectra and correspondent weighting factors were addressed and are shown in Figure 7-8. Due to the difference in probing depth of UPS and MIES, the weighting factor observed for exposed V_2O_5 is different. The similar nature has been further found in WO_3/BHJ samples.

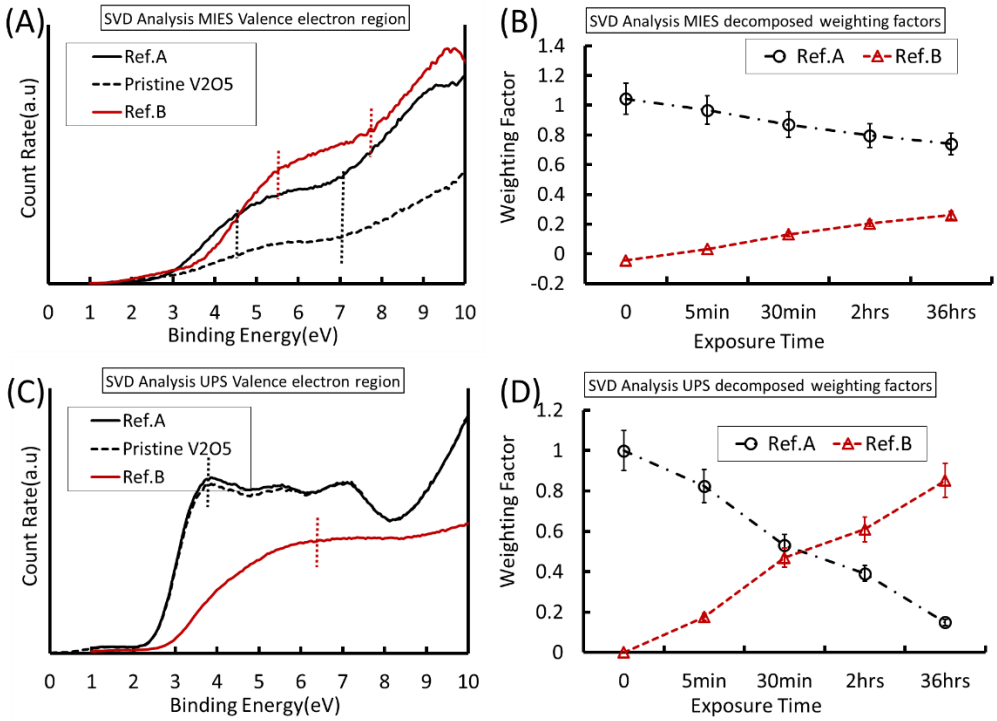

Figure 7- 8. (A)(C) The decomposed MIE and UP spectra using SVD method and the comparison with non-exposed V_2O_5 spectrum; (B)(D) The weighting factors of individual reference spectra of analysed MIES and UPS

Figure 7-8(A) shows the two reference spectra with a spectrum of the non-exposed pristine V_2O_5 (Ref. V_2O_5) which are required to fit the MIE spectra of V_2O_5/BHJ. The reference spectrum A (Ref. A) can be assigned to non-exposed V_2O_5 due to the same feature across the valence region, and reference spectrum B (Ref. B) can be assigned to V_2O_5·H_2O[21, 25] in terms of the OH^- peak exhibiting at around 5.6 eV. The normalised weighting factors of reference spectra are shown in Figure 7-8(B). V_2O_5·H_2O (Ref. B) reveals an increase from 0 to 0.27 after 36 hrs exposure, while the pristine V_2O_5 shows an opposite trend. The decomposition of UP spectra results in the identification of two reference spectra, shown in Figure 7-8(C). Referring to the pristine V_2O_5 spectrum, Ref. A is thus approximated to pristine V_2O_5. Ref. B exhibits an energy peak of ~6.5 eV, which is then related to metal oxide containing 1 π OH^- energy state as reported[21]. The relative weighting factors are shown in Figure 7-8(D), which reveals a parallel trend as MIES. Ref. B (V_2O_5·H_2O) increases noticeably from 0 to 0.18 after 5 mins exposure and by far dominates the weighing factor after 2 hrs exposure, with the weighting factor peaking at 0.82 after 36 hrs exposure.

c) Decomposition of Valence Electron Region of MIE/UP Spectra of 3nm WO_3/BHJ

The decomposition of valence electron region of the MIE/UP spectra of WO_3/BHJ samples upon exposure and the weighting factors of reference spectra are shown in Figure 7-9.

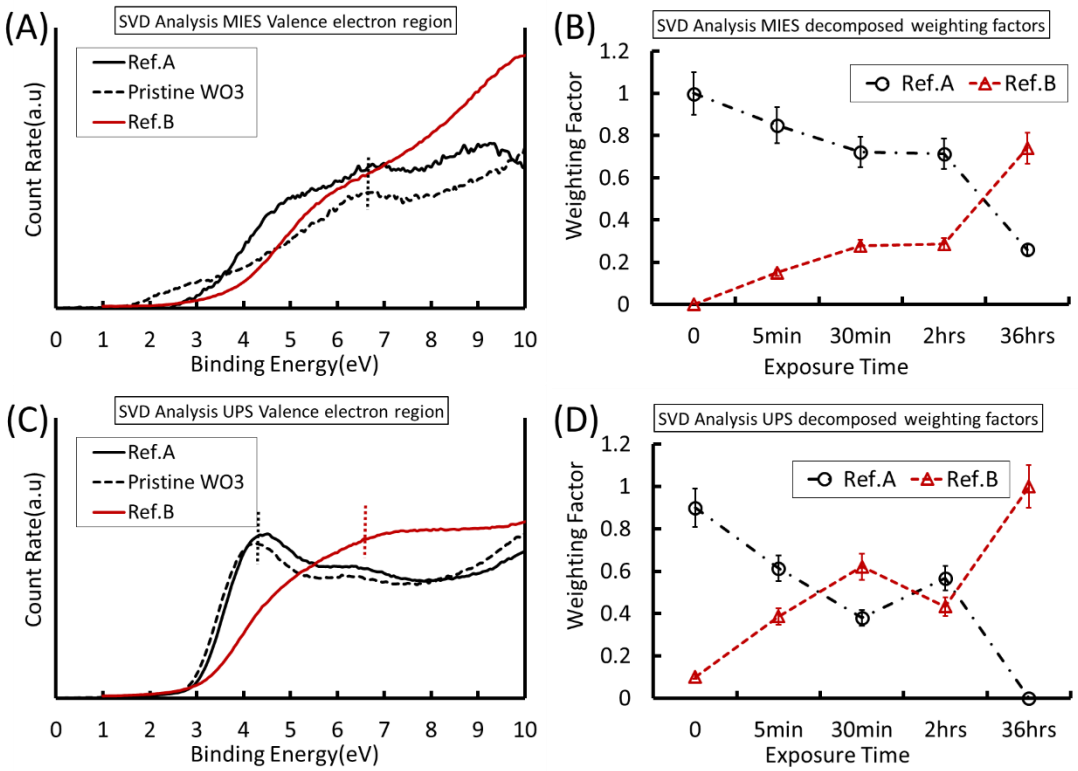

Figure 7- 9. (A)(C) The decomposed MIE and UP spectra using SVD method and the comparison with non-exposed WO_3 spectrum; (B)(D) The weighting factors of individual reference spectra of analysed MIES and UPS

By comparing the features of the MIE spectra in Figure 7-9(A), Ref. A can be identified as non-exposed WO_3, while Ref. B represents the occurrence of WO_3·H_2O. The weighting factor of Ref. B illustrates an escalation to ~0.18 after 5 mins exposure and 0.32 after 2 hrs exposure, after which a rapid increase to 0.77 after 36 hrs exposure was observed. Meanwhile, regarding the decomposition upon valence electron region of UPS in Figure 7-9(C), Ref. A here was assigned to pristine WO_3 due to the similar features. Thus, Ref. B corresponds to WO_3·H_2O because the energy state approximating at 6.5 eV was seen. The weighting factor of Ref. B shows an upwards trend, which levels at 0.62 after approximately 30 mins exposure, then fluctuates to 0.48 and finally maximises at 0.98 after 36 hrs exposure.

d) Influence of Moisture on Dipole Forming at Interfaces

The WSM upon UP spectra was applied here for characterising the dipole energy at V_2O_5/BHJ and WO_3/BHJ interface which was adopted in Chapter 6. The technique allows identifying energy shift on the x-axis for a given spectrum. The decomposition was used on the batch of samples with 0.3 nm deposition thickness for observation of the interface. The algorithm can be modified as the following equation. The set of processed spectra includes the samples that are pristine and also individually exposed to air for 5 mins, 30 mins and 2 hrs.

$$S_{meas}^{(i)} = \sum_{j=0}^{n} a_j^{(i)} \times S_{BHJ}\left(E + j \cdot \Delta E\right) + b \cdot S_{MTOs} + c \cdot S_{e-MTOs} \quad \text{with} \quad \sum_j a_j^{(i)} + b + c = 1$$
$$\Delta E_{mean}^{(i)} = \sum_{j=0}^{n} a_j^{(i)} \cdot j \cdot \Delta E \qquad \text{Equation 7-1}$$

S_{BHJ} : the spectrum of the BHJ layer

S_{TMOs} : pristine V_2O_5 and WO_3 spectra shown in Figure 7-8(C) and 7-9(C) for reference

$S_{e\text{-}TMOs}$: exposed V_2O_5 and WO_3 spectra shown in Figure 7-8(C) and 7-9(C) from SVD

ΔE : an energy increment

$j \cdot \Delta E$: an integer multiple of the energy increment for which S_{BHJ} is shifted in applying Equation 7-1

$\Delta E_{mean}^{(i)}$: the mean shift for spectrum i. $\Delta E_{mean}^{(i)}$ is a consequence of the dipole formed at the TMOs/BHJ interface with evidence for such diploe formation.

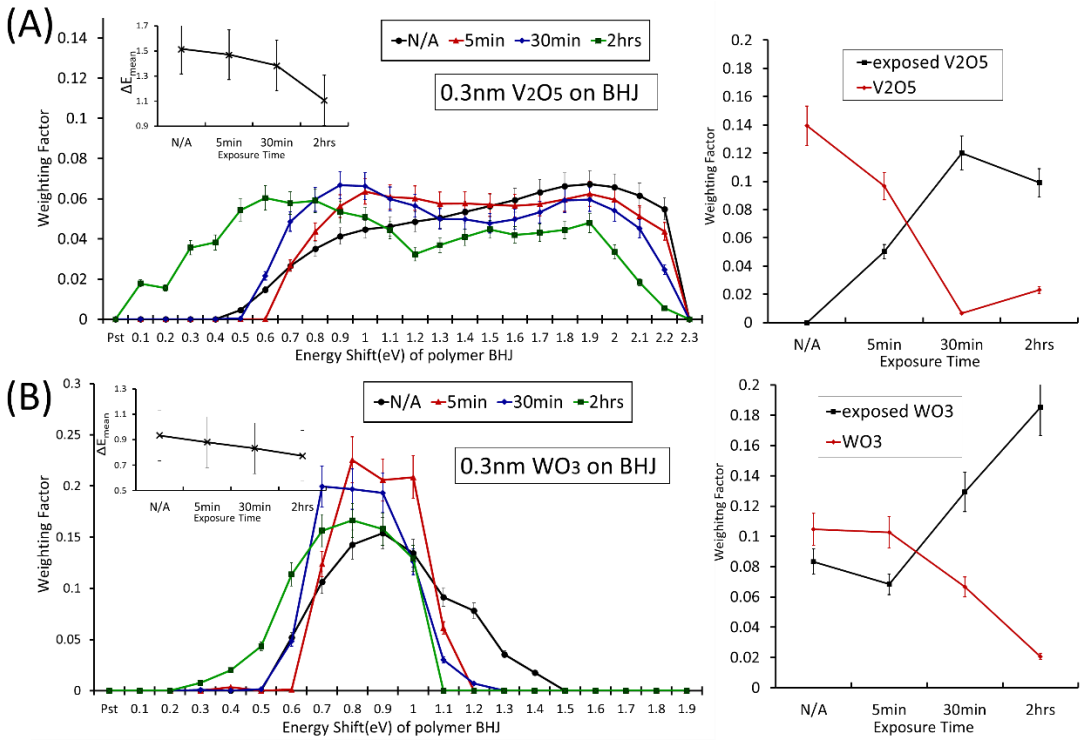

Figure 7- 10. (A) Left: weighting factor of the polymer BHJ energy shift of UPS, Right: weighting factor of the pristine and exposed V_2O_5 reference spectra of UPS; The results are based on 0.3nm V_2O_5/BHJ sample; (B) Left: weighting factor of the polymer BHJ energy shift of UPS, Right: weighting factor of the pristine and exposed WO_3 reference spectra of UPS; The results are based on 0.3nm WO_3/BHJ sample

The weighting factor of energy shift of polymer BHJ of 0.3 nm V_2O_5/BHJ and WO_3/BHJ samples after various exposures are shown in Figure 7-10, with the proportions of pristine V_2O_5/WO_3 and exposed V_2O_5/WO_3 illustrated. The distribution of energy shift shows a trend to lower binding energies with increased exposure time for both V_2O_5 and WO_3 on BHJ. The mean shifting energies are shown as insets, which shift from 1.5 ± 0.1 eV to 1.1 ± 0.1 eV of V_2O_5/BHJ and decline from 0.9 ± 0.1 eV to 0.7 ± 0.1 eV for WO_3. Given this, an obvious decline upon dipole strength at such interfaces can be determined. The cause of the energetic changes on the formed interfaces with BHJ are summarised as follows:

a) As discussed in Chapter 2 and Chapter 4, the determination of WF from secondary electron cascade relies on the dipole situated at the outermost layer. The dipole can be altered due to the attaching of mainly H_2O which encounters the dipolar electrostatic field. Therefore,

a noticeable change of WF was observed. However, this dipole does not represent the dipole forming at the TMO/BHJ interface. Thus, a direct analysis on the valence electron region is required.

b) The shift of low binding energy C peak from XPS can be regarded as an indication of the interface dipole strength, which declines with air exposure. The outcome was thus verified with the observation of actual dipole strength by decomposing the UPS valence electron states.

c) Given the nature of H_2O dielectric[21, 25], it is likely to penetrate into the sample. The H_2O molecules can free-orient at the interface, redirecting the electron encountering the dipoles. For this reason, the dipole forming at the interface will be significantly weakened.

7.4.5. Estimation for the Change in BHJ/V_2O_5 and BHJ/WO_3 Interface Dipole

The influence of air exposure upon the charge transfer over the metal oxide/BHJ interface can be further discussed by modelling the energy level diagram. Figure 7-11 shows a schematic of the energy gap between the CB of V_2O_5 and HOMO of BHJ and the maximum energy shift (ΔE_{max}) of BHJ as a consequence of air exposure. The inset provides with a comparison with the WO_3/BHJ interface. The reasons for this are summarised as follows:

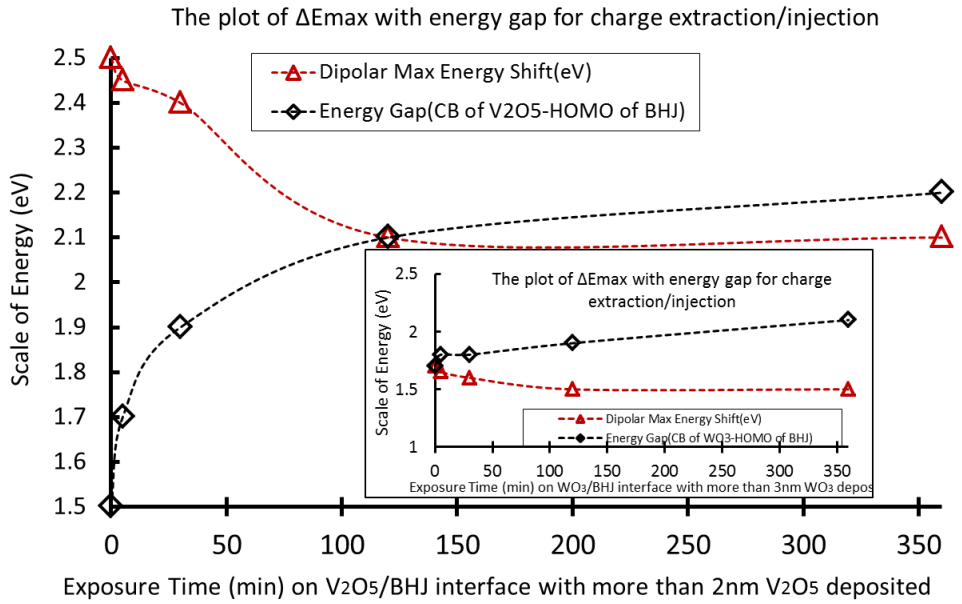

Figure 7- 11. The plot of maximum energy shift and the energy gap between CB of V_2O_5 and HOMO of BHJ, the inset illustrates the energy gap of WO_3/BHJ sample experiencing air exposure

a) As described in Chapter 6, the dipole forming at the V_2O_5/BHJ interface is strong enough to support the charge extraction/injection mechanism[26, 27]. Upon the air exposure the dipole is being destructed, thus the energy shift of BHJ at the interface declines, while the CB of air-exposed V_2O_5 keeps broadening from the equilibrium E_f. In Chapter 6, the ΔE_{max} was determined as 2.5 eV with more than 2 nm V_2O_5 on BHJ and the energy gap between the HOMO of pristine BHJ and CB of V_2O_5 levels at 1.5 eV which has been exceeded. However, upon air exposure the E_{CB} shifts according to the result in Figure 7-6, while the ΔE_{max} declines in terms of Figure 7-10(A). Given this, the changing trend of ΔE_{max} and the energy gap between the HOMO of BHJ and CB of exposed-V_2O_5 is shown in Figure 7-11. It is worth noting that after 2 hrs (120 mins) exposure, the energy bands no longer align, resulting in the occurrence of energy barrier. Therefore, a rapid decline of the charge transfer efficiency over the interface can be assumed. With ongoing exposure, the energy gap even increases, leading to a hole-trap[28, 29].

Conversely, the ΔE_{max} determined in Chapter 6 of the WO_3/BHJ interface is just sufficient for aligning the HOMO of BHJ and CB of WO_3. As such, upon increase of E_{CB}

of WO_3 and decline of ΔE_{max} under the circumstance of exposure, the energy gap immediately occurs, destructing the charge transfer.

b) Dielectric as H_2O into TMOs layer would significantly increase the band gap of such metal oxides. The conductivity[30] of V_2O_5 and WO_3 can be easily affected. Thus, higher R_s of both V_2O_5 and WO_3 layers is predicted, which reduces the charge mobility [31, 32] across the layers. The findings of this work have strong implications for devices using V_2O_5, WO_3 or similar metal oxides to form interfaces with polymer/fullerene. Even a short period of exposure to atmosphere can cause noticeable changes in electric properties of the TMOs/polymer interface.

7.4.6. Oxidation of BHJ upon Air Exposure at the Interface of $MoO_3/V_2O_5/WO_3$ on Polymer BHJ

On a V_2O_5/conjugate BHJ sample, adsorption of hydrocarbon (C_mH_n) can be observed on the surface in addition to the invasion of H_2O/O_2. For the WO_3/BHJ sample, only the adsorption of H_2O/O_2 was seen. Oxidation of polymer BHJ at both interfaces was observed, while in Chapter 4 oxidation of BHJ at the interface of MoO_3/BHJ was confirmed. Since the oxidation was not observed on pristine BHJ only, where interface dipole did not present. The dipole at the interfaces of metal oxides and BHJ alters the oxidation potential, thus the BHJ is prone to oxidise. This nature has been discussed in Chapter 4. A comparison of the oxidised species between the various metal oxides interfaces as a function of exposure time was made and is shown in Figure 7-12. The inset illustrates the weighted oxidation states.

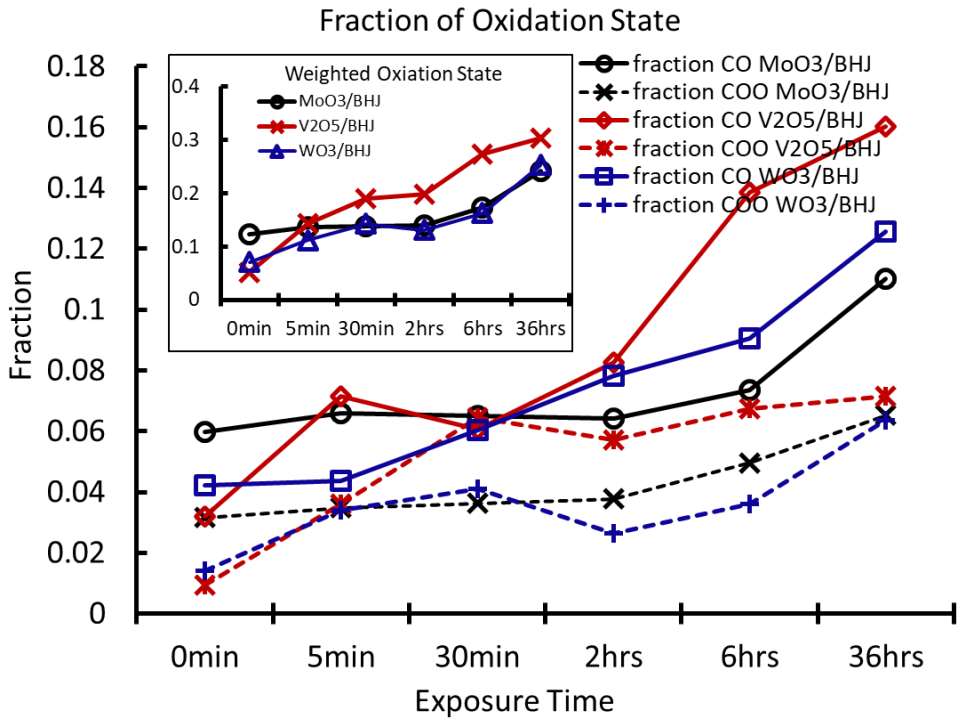

Figure 7- 12. The oxidation states of polymer BHJ at the TMOs/BHJ interface as a function of exposure time, the insets illustrate the weighted oxidation fraction by a calculation of the carbon-oxygen ratio

Apparently, the BHJ is more oxidised at the V_2O_5/BHJ interface due to the higher fraction of C-O and COO across the exposure duration. In Chapters 3 and 6, the maximum dipole strength forming at V_2O_5/BHJ interface is higher than that of the MoO_3/BHJ interface by 0.4 eV and that of the WO_3/BHJ interface by 0.9 eV. Due to the fact that the dipole has a potential to accelerate the oxidation of polymer BHJ, the most oxidised state for V_2O_5/BHJ can be assigned to the strongest interface dipole. Besides, the maximised dipole strength at the MoO_3/BHJ interface is higher than that of the WO_3/BHJ by 0.5 eV. A hypothesis is proposed that upon 3 nm deposition thickness the WO_3 forms an uneven layer in comparison with MoO_3, and the H_2O reaches the interface more easily. Under these circumstances, more BHJ is exposed to moisture, leading to a higher oxidation state.

7.5. Conclusion

No obvious chemical change of V_2O_5 or WO_3 was observed upon exposure to air. Instead, the

adsorption of mainly H_2O from atmosphere was seen, which reduces the WF of metal oxides and alters the valence and conduction states. Meanwhile, the conjugate polymer BHJ at the interfaces with these metal oxides was oxidised. The H_2O also penetrated and approached the interfaces and diminished the dipole strength. Thus, the positioning of the energy levels at interface can be influenced which creates obstruction towards charge transport over the interface. The estimation of charge transfer as a consequence of air exposure has also been discussed.

Reference

1. Meyer, J., et al., *Electronic structure of Vanadium pentoxide: An efficient hole injector for organic electronic materials.* Journal of Applied Physics, 2011. **110**(3): p. 033710.
2. Meyer, J., et al., *Transition metal oxides for organic electronics: energetics, device physics and applications.* Adv Mater, 2012. **24**(40): p. 5408-5427.
3. Meyer, J., et al., *Charge generation layers comprising transition metal-oxide/organic interfaces: Electronic structure and charge generation mechanism.* Applied Physics Letters, 2010. **96**(19): p. 193302.
4. Meyer, J., et al., *Metal oxide induced charge transfer doping and band alignment of graphene electrodes for efficient organic light emitting diodes.* Sci Rep, 2014. **4**: p. 5380.
5. Irfan, et al., *Strong interface p-doping and band bending in C60 on MoOx.* Organic Electronics, 2011. **12**(9): p. 1588-1593.
6. Hamwi, S., et al., *p-type doping efficiency of MoO3 in organic hole transport materials.* Applied Physics Letters, 2009. **94**(25): p. 253307.
7. Chen, S., et al., *Metal oxides for interface engineering in polymer solar cells.* Journal of Materials Chemistry, 2012. **22**(46): p. 24202.
8. White, R.T., E.S. Thibau, and Z.H. Lu, *Interface Structure of MoO3 on Organic Semiconductors.* Sci Rep, 2016. **6**: p. 21109.
9. Wang, H.-Q., et al., *Nanocrystal V2O5 thin film as hole-extraction layer in normal architecture organic solar cells.* Organic Electronics, 2012. **13**(12): p. 3014-3021.
10. Lin, J., et al., *Understanding the photoelectrochemical properties of a reduced graphene oxide–WO3 heterojunction photoanode for efficient solar-light-driven overall water splitting.* RSC Advances, 2013(24).
11. Ozawa, R., et al., *Angle-resolved UPS study of the oxygen-induced 2 × 1 surface of Cu(110).* Surface Science, 1996. **346**: p. 237-242.
12. Mendialdua, J., R. Casanova, and Y. Barbaux, *XPS studies of V2O5, V6O13 , VO2 and V2O3* Journal of Electron Spectroscopy and Related Phenomena, 1995. **71**: p. 249-261.
13. Adil, S.F., et al., *Vanadia supported on nickel manganese oxide nanocatalysts for the catalytic oxidation of aromatic alcohols.* Nanoscale Res Lett 2015. **10**(52).
14. Moon, B.J., et al., *In situ modulation of the vertical distribution in a blend of P3HT and PC(60)BM via the addition of a composition gradient inducer.* Nanoscale, 2014. **6**(4): p. 2440-2446.
15. Cheng, P., Y. Li, and X. Zhan, *A DMF-assisted solution process boosts the efficiency in P3HT:PCBM solar cells up to 5.31%.* Nanotechnology, 2013. **24**(48): p. 484008.
16. Scudiero, L., Y. Shen, and M.C. Gupta, *Effect of light illumination and temperature on P3HT films, n-type Si, and ITO.* Applied Surface Science, 2014. **292**: p. 100-106.
17. Zhao, M., et al., *Effect of nitrogen atomic percentage on N+-bombarded MWCNTs in cytocompatibility and hemocompatibility.* Nanoscale Res Lett, 2014. **9**(1): p. 142.
18. Mortazavi, S.Z., et al., *Generation of various carbon nanostructures in water using IR/UV laser ablation.* Journal of Physics D: Applied Physics, 2013. **46**(16): p. 165303.
19. Prześniak-Welenc, M., et al., *Electrical conductivity and relaxation processes in V2O5 nanorods prepared by sol-gel method: Electrical conductivity and relaxation processes in V2O5 nanorods.* Phys. Status Solidi B, 2015. **252**(9): p. 2111–2116.
20. Chi, D., et al., *High efficiency P3HT:PCBM solar cells with an inserted PCBM layer.* J. Mater. Chem. C,

2014. **2**: p. 4383-4387.

21. Krischok, S., et al., *H2O interaction with bare and Li-precovered TiO2: studies with electon-spectroscopy(MIES and UPS HEI and HEII).* Surface Science, 2001. **495**: p. 8-18.
22. Krischok, S. and H.V. Kempter, *The chemisorption of H2O and CO2 on TiO2 surfaces: studies with MIES and UPS (HeI/II).* Surface Science, 2002. **507-510**: p. 69-73.
23. Choi, W.S., *Wide band gap tunability in complex transition metal oxides by site-specific substitution* Diploma Thesis.
24. Benramache, S., O. Belahssen, and H.B. Temam, *Effect of band gap energy on the electrical conductivity in doped ZnO thin film.* Journal of Semiconductors, 2014. **35**(7).
25. Volgmann, K., F. Voigts, and W. Maus-Friedrichs, *The interaction of H2O molecules with iron films studied with MIES, UPS and XPS.* Surface Science, 2012. **606**: p. 858-864.
26. Meyer, J. and A. Kahn, *Electronic structure of molybdenum-oxide films and associated charge injection mechanisms in organic devices.* Journal of Photonics for Energy, 2011. **1**(1): p. 011109.
27. Zeng, W., et al., *The effect of the hole injection layer on the performance of single layer organic light-emitting diodes.* Journal of Applied Physics, 2014. **116**(22).
28. Harding, M.J., et al., *Variations in Hole Injection due to Fast and Slow Interfacial Traps in Polymer Light-Emitting Diodes with Interlayers.* Advanced Functional Materials, 2010. **20**(1): p. 119-130.
29. BORSENBERGER, P.M. and W.T. GRUENBAUM, *Hole Trapping in Molecularly Doped Polymers.* BORSENBERGER ET AL, 1998(352).
30. Shaheen, A., W. Zia, and M.S. Anwar, *Band Structure and Electrical Conductivity in Semiconductors.* Phd Thesis, 2010.
31. Fu, B., et al., *High Charge Carrier Mobility, Low Band Gap Donor–Acceptor Benzothiadiazole-oligothiophene Based Polymeric Semiconductors.* Chem. Mater, 2012. **24**(21): p. 4123–4133.
32. Liu, T., M. Dupuis, and C. Li, *Band Structure Engineering: Insights from Defects, Band Gap, and Electron Mobility, from Study of Magnesium Tantalate.* J. Phys. Chem. C, 2016. **120**(13): p. 6930–6937.

Chapter 8. Characterisation of Dipole Forming at MoO_3/TQ1:$PC_{71}BM$ Interface and the Influence of Air Exposure

8.1. Abstract

In this chapter, the capability of charge extraction/injection of MoO_3 is demonstrated when working as anode buffer layer to form interfaces with TQ1:$PC_{71}BM$ bulk heterojunction. First, X-ray photoemission and neutral impact collision ion scattering spectroscopy (NICISS) characterised the chemical properties and elemental distributions of given interfaces. Metastable induced electron spectroscopy was then applied to determine the minimum MoO_3 deposition thickness forming a closed layer on TQ1:$PC_{71}BM$ BHJ. The distribution of intermediate energy states—related to dipole strength at the interface—were determined by UV-photoelectron spectroscopy through a series of mathematical algorithm decompositions. Dipole strength was determined to maximise at 2.4eV with more than 2nm MoO_3 deposition. The SVD algorithm was also processed on the MoO_3/BHJ samples subjected to air exposure. The decrease of dipole energy was identified as a function of exposure and quantified energy shift.

8.2. Introduction and Research Aim

The polymer-fullerene bulk heterojunction formed with TQ1 and $PC_{71}BM$ has been developed and applied on polymer-based solar devices [1-4]. Further, it has been reported that devices using donor TQ1 demonstrate a higher efficiency than P3HT [5] and the external quantum efficiency (EQE) of TQ1 surpasses P3HT [6], as measured by Fourier-transform photocurrent spectroscopy. The charge mobility of donor TQ1 is competitive with P3HT [7]. Thus, the advantage of TQ1 as donor material has been attributed to its stable phase [8] and lower recombination rate [9]. Additionally, as acceptor fullerene, $PC_{71}BM$ displays a higher photon absorption than $PC_{61}BM$ [10], while other properties illustrate a similarity between each other. TQ1:$PC_{71}BM$ BHJ has attracted the researchers' attention due to their advantages.

The polymer solar cell using TQ1:$PC_{71}BM$ BHJ has a conventional structure based on MoO_3 as anode buffer layer. While energy levels of LUMO/HOMO of given polymer BHJ and

CB/VB of MoO_3 have previously been characterised [11-14], the interface of MoO_3/TQ1:$PC_{71}BM$ and the dipole forming the interface have not yet been studied. In Chapter 3, the dipole was demonstrated to have a significant impact on charge transfer over the interface, whereas in this chapter, the full energy level diagram will be determined. Further, the influence of moisture from air exposure on the properties of MoO_3 and the dipole at the interface was demonstrated in Chapter 4. The same procedure is adopted here for an observation on the change of dipole at MoO_3/TQ1:$PC_{71}BM$ interface, from which the charge transfer resulting from air exposure can be predicted.

First, it will be shown that a minimum deposition thickness of MoO_3 is required to form a closed layer on TQ1:$PC_{71}BM$. Second, it will be demonstrated that dipole strength alters across variations of deposition. The decline of dipole strength at interfaces due to air exposure will also be exhibited. Electron spectroscopy analyses of the electronic properties of the interface and ion scattering spectroscopy can be used to determine elemental distribution across the interface up to a certain thickness.

8.3. Sample Preparation

TQ1 (Poly[[2,3-bis(3-octyloxyphenyl)-5,8-quinoxalinediyl]-2,5-thiophenediyl]) and $PC_{71}BM$ ([6,6]-Phenyl C71 butyric acid methyl ester) are blended in CB:ODCB solvent as described in chapter 2. After which the solution was spin-coated onto Si substrate and then dried in an oven. A range of MoO_3 thickness of deposition was conducted as 0.2, 0.5, 1, 1.5, 2, 3 nm. The maximum 3nm deposition thickness of MoO_3 would provide with a closed layer in terms of the demonstration from chapter 3. The samples were transferred from PVD chamber directly to the analysis chamber for applying spectroscopy thus reaction with oxygen and moisture was avoided during the transferring.

In the section of air exposure, the MoO_3 was deposited at a thickness of 0.3nm on the TQ1:$PC_{71}BM$ BHJ for a clear observation over the interfaces. The exposure time was set to 5min, 30min, 2hrs and 6hrs. After exposure, the sample was transferred immediately to the UHV analysis chamber for measurement with UPS. The analysis of electrical properties based

on secondary electron and valence electron states are thus made. The details of applying UPS are described in the experimental chapter.

8.4. Results and Discussion

8.4.1. Chemical Composition and Distribution of MoO_3/TQ1:$PC_{71}BM$ Interface

Only the fittings of high resolution XP spectra of C and O are provided in Figure 8-1(A) and (B), including the sample with 0.2, 1, 2.2 and 3nm MoO_3 thicknesses. The fitting of Mo, S and N does not show obvious change on the energy scale because of deposition thickness. In Figure 8-1(C), the nature of O from BHJ and relative concentration of Mo are illustrated. The energy position and fraction of C, which has been determined as the proportion of BHJ experiencing dipolar bias [15], are shown in Figure 8-1(D).

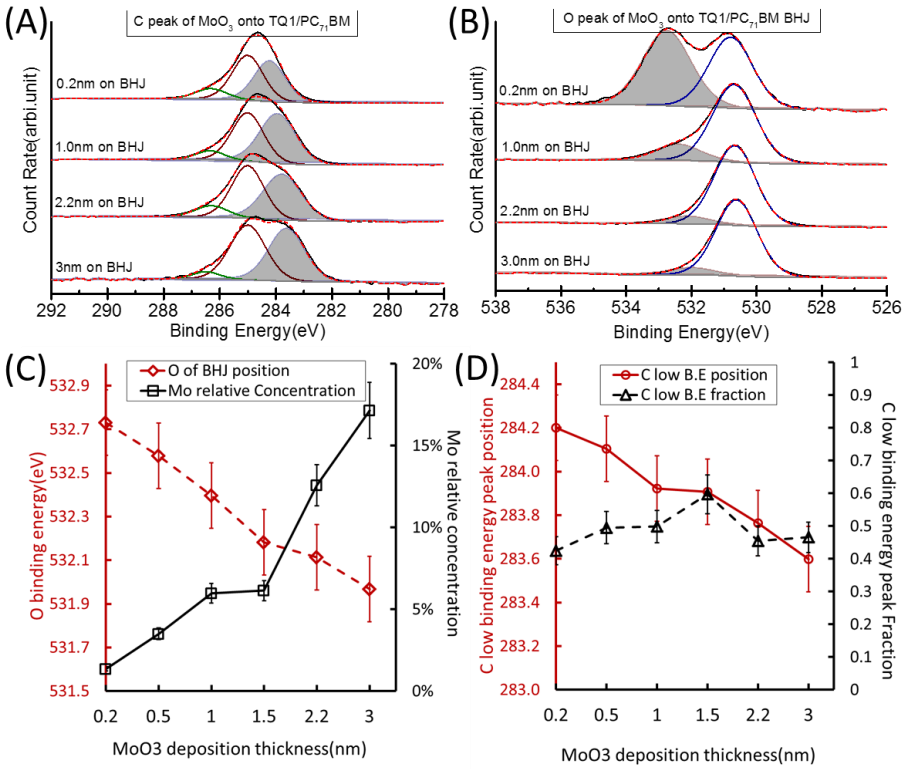

Figure 8- 1. (A)(B) The fittings of C and O of XP spectra of the given samples; (C) The illustration of O of the fraction of BHJ and quantification of Mo; (D) The position and fraction the C which levels at lower binding energy

The fitting of C results in four individual peaks. The energy position of C-O and C-O peaks

are, respectively 286.7 ± 0.2eV [16, 17] and 288.0 ± 0.2eV [18], in terms of the finding of C-C peak at 285.0 ± 0.2eV, with no processed calibration. Another C peak, ranging from 283.4 to 284.1eV, has also been determined. Due to the exclusion of chemical shift and sample charging, the origin of the low binding energy C peak can be assigned to the proportion of polymer BHJ[15]. Additionally, TQ1:$PC_{71}BM$ BHJ is subjected to an electric bias within the interface dipole. This is consistent with the finding of P3HT:PCBM BHJ described in Chapter 3. In Figure 8-1(B), two peaks are used for fitting the O peak. The O peak of MoO_3 levels at 530.5 ± 0.2eV [19], while the other one is fitted at 533.0 ± 0.2eV of 0.2nm MoO_3/BHJ sample, which can be assigned to O of polymer BHJ ($PC_{71}BM$ fraction). In Figure 8-1(D), the energy positions of both C and O related to BHJ, exhibit an energy shift to lower energy position, maximising at approximately 0.7 eV. The nature was discussed in Chapter 3, where the difference of energy shift among the samples was due to the change of mean dipole strength at the interface, enlarging with the increase of MoO_3 deposition thickness.

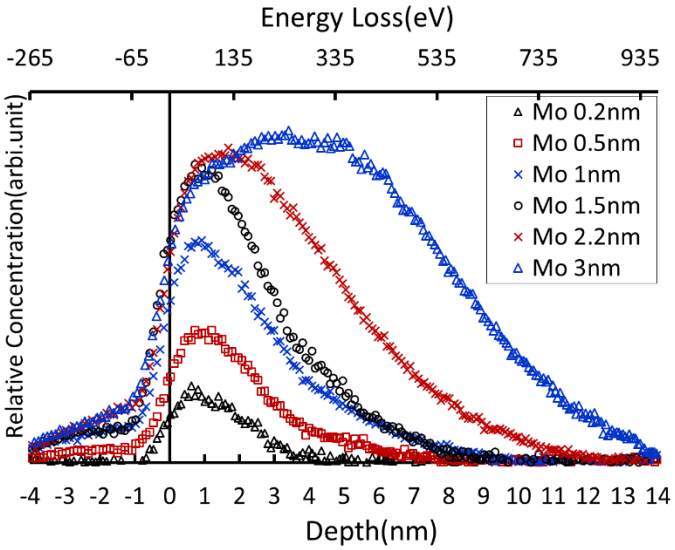

Figure 8- 2. The depth profile of Mo as the result of a range of deposition thickness

The information of the distribution of elements can be derived from Figure 8-2, in which the distribution of Mo scaled with certain depth into the BHJ substrate is quantified at the atomic level. The gradient of Mo distribution at the side of the outermost layer is much higher than the side towards the bulk, indicating a heavy diffusion of MoO_3 into the polymer BHJ [15, 20]. Chapters 3 and 6 demonstrated similar findings, with a penetration of TMOs into BHJ. A

deposition thickness of 0.2nm MoO_3 yields a distribution of around 3nm MoO_3 into BHJ. Meanwhile, the MoO_3 penetrates as deep as 8nm with 1nm thickness. As such, it can be determined that a high deposition amount of MoO_3 will produce a deeper penetration of MoO_3 into the BHJ. The surface coverage of MoO_3 as a function of deposition thicknesses is extrapolated in Figure 8-2, as the peak height of Mo contribution did not increase beyond the deposition of 1.5nm MoO3. The alternative method for determining the surface coverage of MoO_3 on BHJ is shown later with a combination of MIES analysis.

8.4.2. Decomposition and Analysis of MIES/UPS Spectra

a) The Observation and Analysis of MIES/UPS of the MoO_3/BHJ samples

In Figure 8-3(A) and (B), the secondary electron and valence electron regions of UPS are displayed. The valence electron state of MIES is illustrated in Figure 8-3(C). The secondary electron peak onset shifts from 16.5 $\pm$0.1eV of 0.2nm to 14.5 $\pm$0.1eV of 3nm by processing Equation 2-4, indicating a change upon WF as a function of MoO_3 thicknesses. The valence electron region of UPS displays a growing peak positioning at 3.8eV, relative to the occurrence of MoO_3. Both shapes of UPS and MIES valence electron peaks change gradually. The WF derived from UPS secondary electron cascade is plotted in Figure 8-3(D), with characterisation of a pristine polymer BHJ, increasing from 3.9 $\pm$0.1eV zero thickness to 6.5 $\pm$0.1eV deposition. The change in WF can be attributed to electrical interaction, due to the dipole formed at the MoO_3/BHJ interface, which can in turn be altered by tuning the fraction of given components at interface [21, 22]. The origin is explained next.

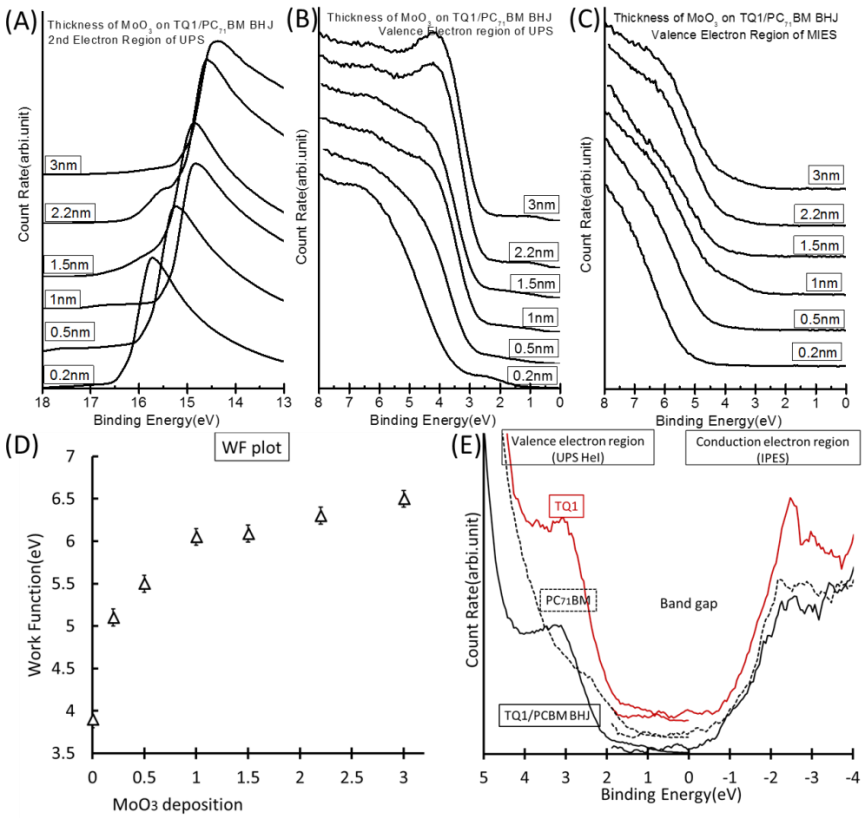

Figure 8- 3. (A) (B) The secondary electron cascades and valence electron spectra from UPS of the samples; (C) The valence electron spectra from MIES; (D) The plots of WF and EVB as a function of thicknesses of MoO_3; (E) The valence electron and conduction electron spectra respectively from UPS and IPES of the polymer- fullerene substrate

The outcomes of UPS and IPES of pristine polymer BHJ substrates including TQ1, $PC_{71}BM$ and BHJ are added in Figure 8-4(E), for further consideration of the energy level diagram. The E_{LUMO}, E_{HOMO} and WF of active layer materials are presented in Table 8-1. The BHJ represents a dipolar complex of two organic materials [11], which is considered an entirety.

Sample	**WF/ϕ(eV)±0.1**	**E_{HOMO}/ E_{VB} (eV)±0.1**	**E_{LUMO}/ E_{CB} (eV)±0.1**	**E_g (eV)±0.2**
TQ1	3.6	0.8	1.2	2.0
$PC_{71}BM$	4.1	1.6	0.8	2.4
TQ1:$PC_{71}BM$ BHJ	3.9	1.0	1.2	2.2

Table 8-1. Plots of WF, E_{HOMO}, E_{LUMO}, E_{VB}, E_{CB} and band gap (E_g) of pristine polymer BHJ

b) Decomposition of valence electron region of MIE/UP spectra

Similar to the procedure described in Chapter 3, valence electron regions of MIES and UPS were decomposed using Equation 2-6 to identify components at the outermost surface and outermost interface, respectively. The decomposition was processed in groups, which is also detailed in Chapter 3. The outcome shows the identification of the spectra of respectively pristine MoO_3, pristine polymer BHJ and polymer BHJ, although shifted to lower binding energy by 1.0-1.7eV. Both UPS and MIES illustrate similar developments, with the identified reference spectra provided in Figure 8-4. The legend indicates the decomposition group containing a range of MoO_3 thicknesses. For example, '02, 05, 10' means a group covering 0.2nm, 0.5nm and 1nm samples for processing SVD. As a consequence of MoO_3 deposited on TQ1:$PC_{71}BM$ BHJ, it can be determined that alignment of Fermi level of the components causes an electron flow at the interface, generating a static electrical dipole [23, 24]. The dipole works as an electrical bias, causing the energy shift of polymer BHJ [15]. Therefore, within the dipole moment, the electrical properties of such organics can be shifted. The result is similar to the MoO_3/P3HT:$PC_{61}BM$ interface.

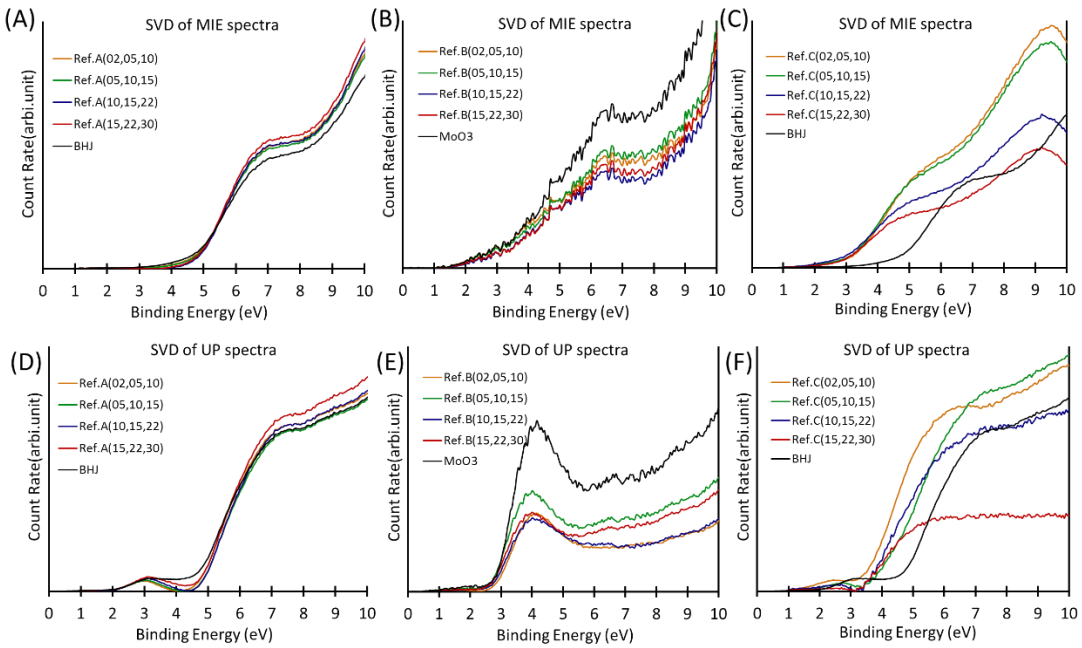

Figure 8- 4. (A),(B),(C) The reference spectra found from SVD of MIES and the comparisons with pristine BHJ and MoO_3 spectra. The fittings were made among the groups covering a range of thickness of MoO_3, which is indicated as labelled; (D),(E),(F) The reference spectra

found from SVD of UPS and the comparisons with pristine BHJ and MoO_3 spectra. It can be seen from the decomposition of MIES and UPS, Ref. C shows a rather similar feature and shape as the pristine BHJ but shifted on the energy scale

The valence spectra can be further decomposed through Equation 3-1 by using the measured spectra and updating ingredient spectrum of P3HT:$PC_{61}BM$ BHJ to TQ1:$PC_{71}BM$ BHJ. The weighting factors of BHJ energy shift from MIES and UPS are shown in Figure 8-5(A) and (B). The mean energy shift using Equation 3-1 and the weighting factors of components are also illustrated in Figure 8-5(C) and (D). A distribution of dipoles is located at the interface between MoO_3 and BHJ. The distribution of BHJ energy shift due to dipole of both MIES and UPS demonstrates an increasing trend, with more MoO_3 deposited. The energy shift of UPS maximised at approximately 2.4 $\pm$0.1 eV. The weighting factor of MoO_3 can be derived from Figure 8-5(C), which shows an initial sharp increase followed by saturation at 0.9 with 1-1.5nm MoO_3 thickness. Combining with the outcome from NICSS, it can be determined a closed MoO_3 layer on TQ1:$PC_{71}BM$ surface is established with a deposition thickness between 1nm and 1.5nm. The mean energy shift (ΔE_{mean}) from MIES and UPS can be observed from Figure 8-5(C) and (D), with increasing amounts of MoO_3 induced by evaporation. For MIES, the ΔE_{mean} maximised at 1.8eV, and for UPS, it was 2.2eV.

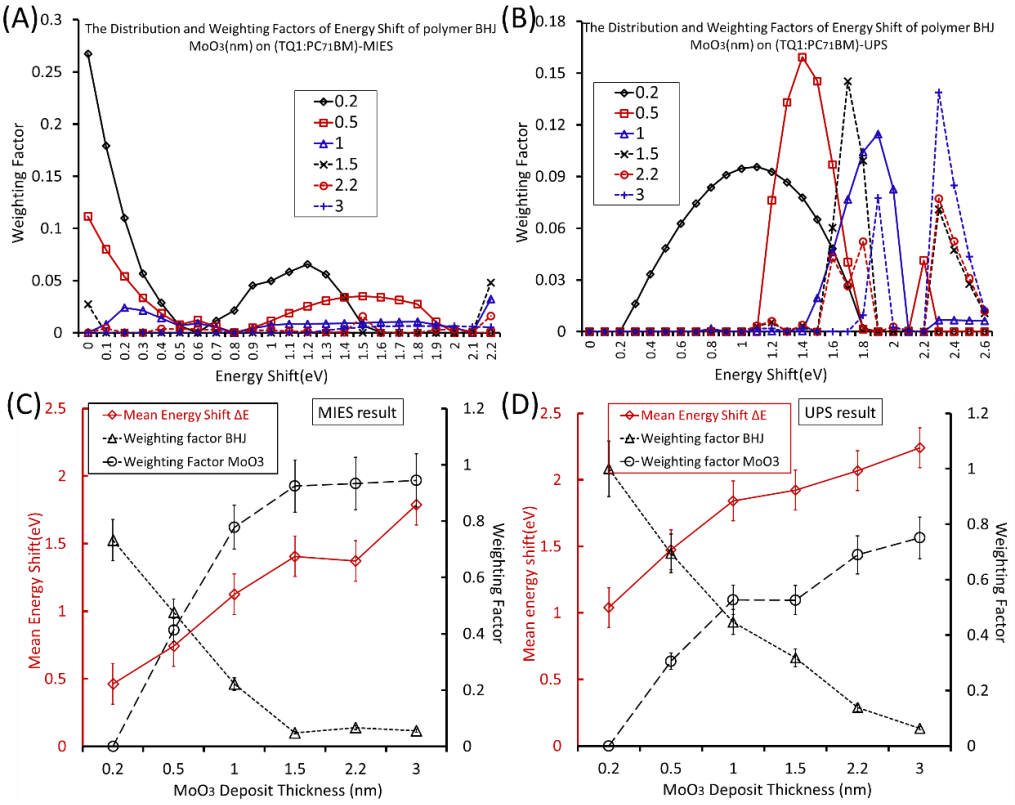

Figure 8- 5. (A)(B) The distribution of energy shift of polymer BHJ within the dipole moment from MIES and UPS; (C)(D) The plot of mean energy shift, weighting factors of BHJ and MoO_3 form MIES and UPS

8.4.3. Reconstruction of Energy Level Diagram at the MoO_3/TQ1:$PC_{71}BM$ Interface

First, a reconstruction of the WF of all samples has been achieved using Equation 3-2. The constituted WF is close to the measured WF. This result is provided in Figure 8-6(A). The diagram represents full energy levels at the MoO_3/TQ1:$PC_{71}BM$ interface as a function of certain MoO_3 thicknesses. All electrical parameters are associated in Tables 3-1 and 8-1, and Figure 8-5(B). The diagram offers insight into the relation between MoO_3 deposition amount of and interface dipole strength.

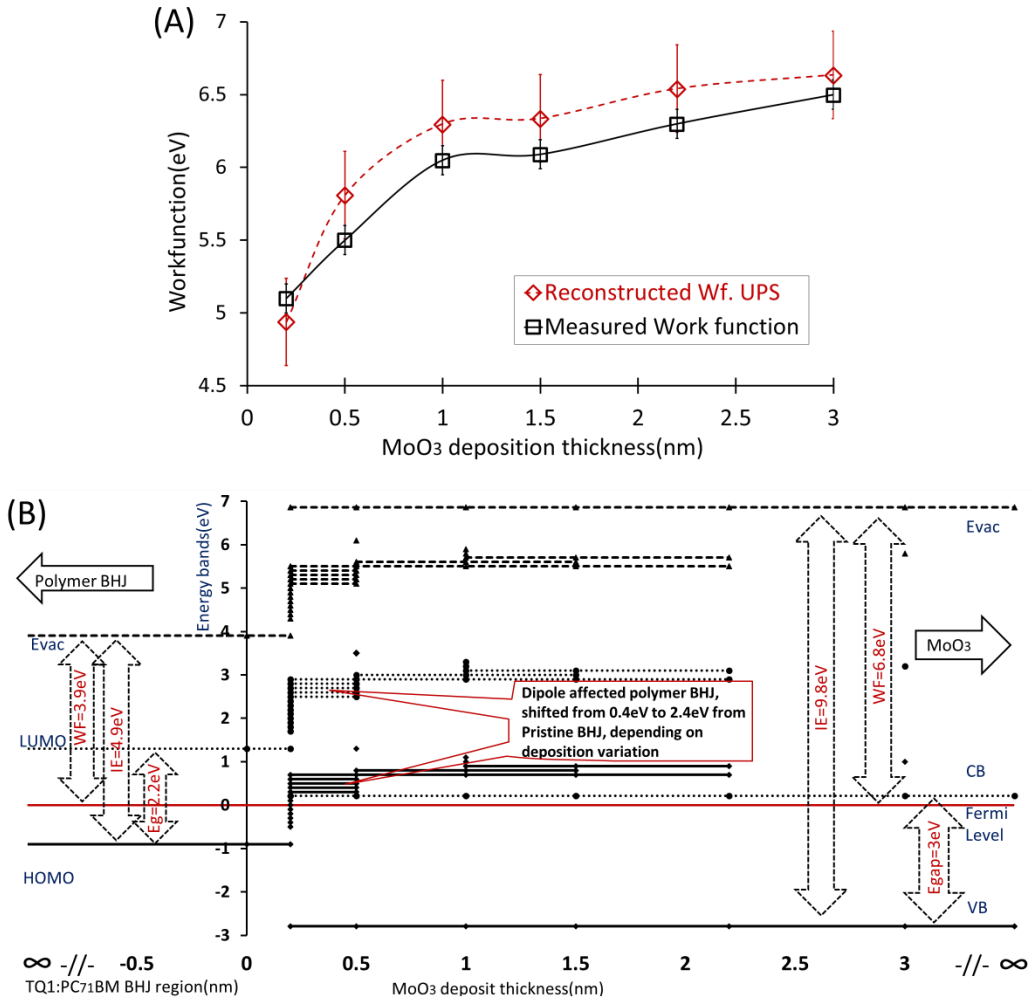

Figure 8- 6. (A) The fitting of WF using the analysis of decomposition components in comparison with the measured WF; (B)The reconstruction of interface energy bands of pristine polymer BHJ, energy-shifted BHJ and pristine MoO_3 as a function of MoO_3 deposition thicknesses

The section of pristine polymer BHJ is located at the left side of Figure 8-6(B), from the zero mark on the horizontal axis. The vertical axis represents the positioning of energy levels. The direction to the right side on the horizontal axis represents the interface of the MoO_3 layer to the BHJ layer, with increasing distance from the BHJ. The layer thickness means the value for an energy level is shown with a certain thickness of MoO_3 deposition. A mixed region of MoO_3 and BHJ has been identified due to the penetration, considered the prerequisite of dipole formation. The electrical properties, such as E_{HOMO}, E_{LUMO} of BHJ within the dipole moment, are shown as shifted BHJ at the interface.

It also can be derived from Figure 8-6(B) that insufficient MoO_3 thickness (e.g., less than 0.5nm) will result in dipole strength at the interface incapable of supporting the charge injection/extraction transport mechanism [25, 26] due to mismatching HOMO of BHJ and CB of MoO_3. Therefore, a loss of the charge efficiency across the interface can be expected.

8.4.4. Comparison between the BHJ of TQ1:$PC_{71}BM$ and P3HT:$PC_{61}BM$ with MoO_3

The comparison of the dipoles forming at the interfaces of MoO_3/TQ1:$PC_{71}BM$ and MoO_3/P3HT:$PC_{61}BM$ is based on NICISS results (see Figures 3-3 and 8-2) and the energy shift of BHJ at such interfaces (see Figures 3-8 and 8-4). The same thickness of MoO_3 yields a deeper penetration of MoO_3 into the P3HT:$PC_{61}BM$ BHJ than TQ1:$PC_{71}BM$. The closed MoO_3 layer on the outermost BHJ surface is formed with similar deposition thickness (>1nm). This results in a more condensed layer of MoO_3 forming at the interface of TQ1:$PC_{71}BM$ BHJ than P3HT:$PC_{61}BM$, which was also previously observed by Carle [8]. The distribution of BHJ energy shift, maximum energy shift and mean energy shift from the related figures demonstrate that with the same MoO_3 thickness, the dipole strength forming at the interface of MoO_3/TQ1:$PC_{71}BM$ is higher than that of MoO_3/P3HT:$PC_{61}BM$. The roots of the difference of dipoles and the nature is illustrated in Figure 8-7.

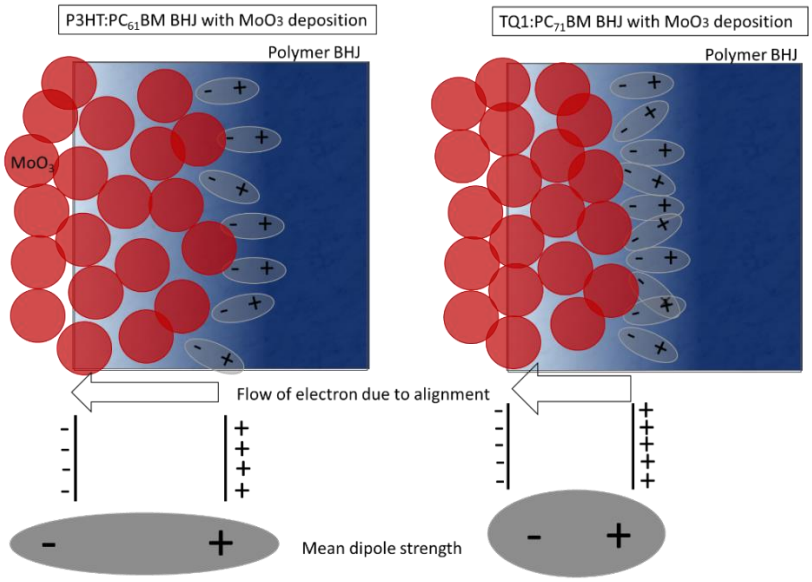

Figure 8- 7. The illustration of dipole strength based on the analysis at the interfaces of

different polymer BHJ covered with MoO_3

The interface dipole can be considered as an accumulation of individual dipole, which has an electric performance at the horizontal direction. The dipole functioning at the vertical direction in Figure 8-7 is likely to cancel each out because such dipole is highly related to the contact of the BHJ and metal oxide to form an interface. If the local dipole vectors are in opposite direction, they will be cancelled. Therefore, in a MoO_3/TQ1:$PC_{71}BM$ system, an interface with a more condensed MoO_3 layer within the same vertical area can generate higher dipole energy due to a more intense distribution of MoO_3 functioning at the horizontal direction. On the contrary, where there is less penetration of MoO_3, the dipole region becomes narrower. However, the interface dipole strength is unlikely to be affected by the dipole region.

8.4.5. Influence of Air Exposure on MoO_3/TQ1:$PC_{71}BM$ Interface

A similar procedure investigating the change of dipole strength at the interface of MoO_3/TQ1:$PC_{71}BM$ as a function of air exposure was processed. The methodology is detailed in Chapter 4. A sample of 0.3nm MoO_3/TQ1:$PC_{71}BM$ was exposed to air for a range of durations (5 mins, 30 mins, 2 hrs, 6 hrs). The UPS valence spectra were decomposed using Equation 4-1 and presented in Figure 8-8(A) inset. The energy shift of BHJ is also shown in Figure 8-8(A) due to variance in exposure time. Distributions of weighting factors for energy shift demonstrate movement to lower binding energies with increasing exposure time. In Figure 8-8(B), the ΔE_{mean} levels are illustrated, along with weighting factors of BHJ and MoO_3. The ΔE_{mean} levels at 1.3 ± 0.1 eV shift to 0.6 ± 0.1eV after six hours exposure. The root has been addressed in Chapter 4, which demonstrated that the re-orientation of H_2O dielectric at the interface encounters with the existing dipole, weakening the dipole strength.

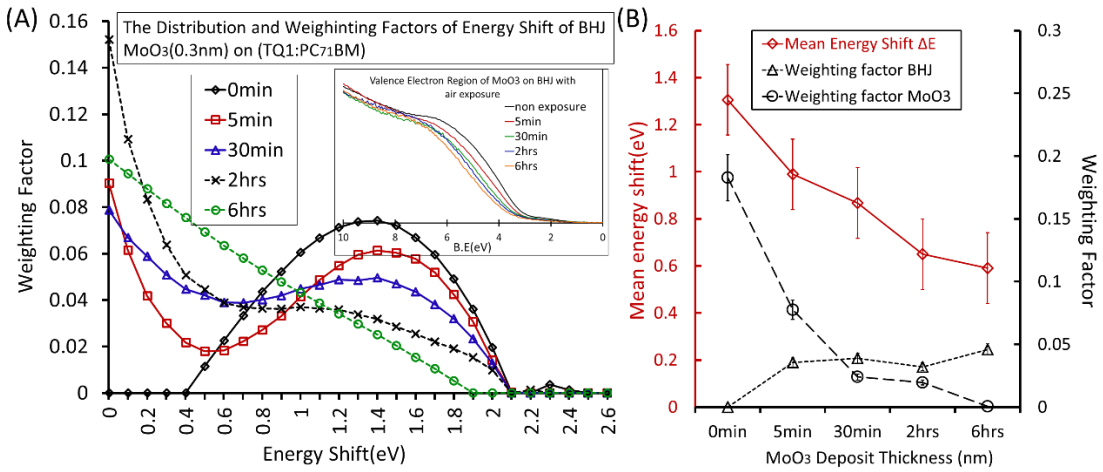

Figure 8- 8. (A) The distribution of energy shift of polymer BHJ as a function of air exposure time upon the 0.3nm MoO_3 on TQ1LPC_{71}BM BHJ, the inset shows the raw valence spectra before decomposition; (B) The mean energy shift, the weighting factors of BHJ and MoO_3

A simulation of MoO_3/BHJ interface with more than 2nm MoO_3 thickness is shown in Figure 8-9. The energy gap between CB of pristine MoO_3 and HOMO of BHJ levels at 1.3eV and the maximum energy shift of BHJ ΔE^{i}_{Max} has been identified to be 2.4eV. It can be observed that after approximately 65 minutes exposure, the CB of MoO_3 and HOMO of BHJ no longer align because the energy gap overtakes the ΔE^{i}_{Max}. The consequent mismatching of energy levels results in charge loss at the interface. The charge loss increases with longer exposure time, while the interface can be turned into a hole-trapping interface [27-29].

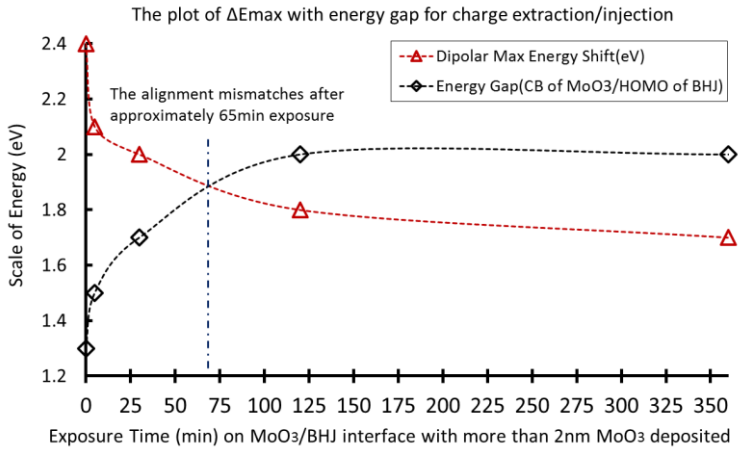

Figure 8- 9. The plot of maximum energy shift and the energy gap between the HOMO of BHJ subjected to energy shift and the CB of MoO_3, the x-axis is the exposure time in min

8.5. Conclusion

No chemical change is observed upon evaporation of MoO_3 onto the BHJ formed by TQ1 and $PC_{71}BM$. The MoO_3 penetrates deep into the BHJ to form an interface and the penetration depth escalates with greater MoO_3 deposits. The dipole strength at the interface as a function of MoO_3 deposition has been characterised. It can be determined that dipole strength increases with greater MoO_3 evaporation. Energy levels of occupied and unoccupied states have been determined, including the development of a full diagram of the electronic states at the MoO_3/BHJ interface. Due to air exposure and the accompanying moisture contact, dipole strength declines. The alignment and mismatching of energy levels as a consequence of exposure durations was illustrated and finally, implications for the performance of photovoltaic devices were discussed.

Reference

1. Lindqvist, C., et al., *Fullerene mixtures enhance the thermal stability of a non-crystalline polymer solar cell blend.* Applied Physics Letters, 2014. **104**(15): p. 153301.
2. Zhu, H., M.B. Johansson, and E.M.J. Johansson, *The Effect of Dopant-Free Hole-TransportPolymers on Charge Generation and Recombination in Cesium-Bismuth–Iodide Solar Cells.* ChemSusChem, 2018. **11**(1114–1120).
3. Wang, F., Z.a. Tan, and Y. Li, *Solution-processable metal oxides/chelates as electrode buffer layers for efficient and stable polymer solar cells.* Energy & Environmental Science, 2015. **8**(4): p. 1059-1091.
4. George, Z., et al., *Two-in-one: cathode modification and improved solar cell blend stability through addition of modified fullerenes.* Journal of Materials Chemistry A, 2016. **4**(7): p. 2663-2669.
5. Hansson, R., et al., *Photo-degradation in air of the active layer components in a thiophene-quinoxaline copolymer:fullerene solar cell.* Phys Chem Chem Phys, 2016. **18**(16): p. 11132-11138.
6. Vandewal, K., K. Tvingstedt, and O. Inganäs, *Polarization anisotropy of charge transfer absorption and emission of aligned polymer:fullerene blend films.* Physical Review B, 2012. **86**(3).
7. Kleinschmidt, A.T., S.E. Root, and D.J. Lipomi, *Poly(3-hexylthiophene) (P3HT): fruit fly or outlier in organic solar cell research?* Journal of Materials Chemistry A, 2017. **5**(23): p. 11396-11400.
8. Carlé, J.E., et al., *Fused thiophene/quinoxaline low band gap polymers for photovoltaic's with increased photochemical stability.* Solar Energy Materials and Solar Cells, 2011. **95**(12): p. 3222-3226.
9. Kulshreshtha, C., et al., *Excitation Intensity Dependent Carrier Dynamics of Chalcogen Heteroatoms in Medium-Bandgap Polymer Solar Cells.* Sci Rep, 2017. **7**(1): p. 836.
10. Xia, Y., et al., *Pyramid shape of polymer solar cells: a simple solution to triple efficiency.* Journal of Physics D: Applied Physics, 2013. **46**(30): p. 305101.
11. Park, S., et al., *The origin of high PCE in PTB7 based photovoltaics: proper charge neutrality level and free energy of charge separation at PTB7/PC71BM interface.* Sci Rep, 2016. **6**: p. 35262.
12. Bao, Q., et al., *Intermixing Effect on Electronic Structures of TQ1:PC71BM Bulk Heterojunction in Organic Photovoltaics.* Soalr RRL, 2017. **1**(10).
13. Nakayama, Y., et al., *Origins of Improved Hole-Injection Efficiency by the Deposition of MoO3on the Polymeric Semiconductor Poly(dioctylfluorene-alt-benzothiadiazole).* Advanced Functional Materials, 2009. **19**(23): p. 3746-3752.
14. Hamwi, S., et al., *p-type doping efficiency of MoO3 in organic hole transport materials.* Applied Physics Letters, 2009. **94**(25): p. 253307.
15. Yin, Y., et al., *Dipole Formation at the MoO3/Conjugated Polymer Interface.* Advanced Functional Materials, 2018. **28**(46): p. 1802825-1802835.
16. Zhu, H., et al., *A Novel Metal-Organic Framework Route to Embed Co Nanoparticles into Multi-Walled Carbon Nanotubes for Effective Oxygen Reduction in Alkaline Media.* Catalysts, 2017. **7**(12): p. 364.
17. Mortazavi, S.Z., et al., *Generation of various carbon nanostructures in water using IR/UV laser ablation.* Journal of Physics D Applied Physics, 2013. **46**: p. 165303.
18. Zai, J., et al., *3D Hierarchical Co-Al Layered Double Hydroxides with Long-term Stabilities and High Rate Performances in Supercapacitors.* Nano-Micro Lett., 2017. **9**(21).
19. Wang, J., et al., *Facile synthesis of ultrasmall monodisperse "raisin–bun"-type MoO3/SiO2 nanocomposites with enhanced catalytic properties.* Nanoscale, 2013(11).
20. Andersson, G.G. and C. Ridings, *Ion scattering studies of molecular structure at liquid surfaces with*

applications in industrial and biological systems. Chem Rev, 2014. **114**(17): p. 8361-8387.

21. Sharma, A., et al., *Invisible high workfunction materials on heterogeneous surfaces.* Applied Surface Science, 2015. **327**: p. 22-26.
22. Ma, H., et al., *Interface Engineering for Organic Electronics.* Advanced Functional Materials, 2010. **20**(9): p. 1371-1388.
23. Lee, C.S., et al., *Interface dipole at metal-organic interfaces: Contribution of metal induced interface states.* Applied Physics Letters, 2009. **94**(11): p. 113304.
24. Wu, Q.-H., et al., *Electronic structure of MoO3−x/graphene interface.* Carbon, 2013. **65**: p. 46-52.
25. Meyer, J. and A. Kahn, *Electronic structure of molybdenum-oxide films and associated charge injection mechanisms in organic devices.* Journal of Photonics for Energy, 2011. **1**(1): p. 011109.
26. Meyer, J., et al., *Metal oxide induced charge transfer doping and band alignment of graphene electrodes for efficient organic light emitting diodes.* Sci Rep, 2014. **4**: p. 5380.
27. BORSENBERGER, P.M. and W.T. GRUENBAUM, *Hole Trapping in Molecularly Doped Polymers.* Journal of Polymer Science: Part B, 1999. **37**: p. 349–356.
28. Ohkita, H., et al., *Direct observation of the carbazole hole trap in polymer solid films by the charge-resonance band.* Chemical Physics Letters, 1996. **263**: p. 602-606.
29. Harding, M.J., et al., *Variations in Hole Injection due to Fast and Slow Interfacial Traps in Polymer Light-Emitting Diodes with Interlayers.* Advanced Functional Materials, 2010. **20**(1): p. 119-130.

Chapter 9. Conclusion and Future Work

9.1. Conclusion

9.1.1. Interfaces Formed with High WF Metal Oxides and P3HT:$PC_{61}BM$ BHJ

High WF transition metal oxides—MoO_3, V_2O_5 and WO_3—have been respectively deposited onto the conjugated polymer P3HT:$PC_{61}BM$. Upon evaporation, no new chemical species were found. Core electron spectroscopy showed a species of C component energetically biased at the interface due to the formation of dipole. The dipole strength and its electrical distribution were further determined by analysing the valence electron spectra and employing a decomposition algorithm. A full diagram of the electronic states at the TMOs/BHJ interfaces has been developed and the mechanism of charge transfer has been discussed.

Difference in the surface coverage rate among MoO_3, V_2O_5 and WO_3 was observed, as was the energy difference of the dipoles among the interfaces of these TMOs and the distinct BHJ layer. The deposition of V_2O_5 on BHJ yielded an interface dipole of a maximise energy of 2.5 eV. For MoO_3/BHJ and WO_3/BHJ, this was 2.2 eV and 1.6 eV, respectively.

9.1.2. Influence of Air Exposure on the Interfaces with High WF Metal Oxides and P3HT:$PC_{61}BM$ BHJ

The properties of the interfaces of high WF transition metal oxides MoO_3, V_2O_5 and WO_3 and the conjugate polymer BHJ as a consequence of air exposure have been investigated. The invasion of mainly moisture from atmosphere enormously reduced the WF of the metal oxides and broadened their band gaps. Decline of the dipole strength at the interfaces was further determined, resulting in a degradation of the charge transfer over the interfaces.

For a MoO_3/BHJ interface, the mismatching of energy levels and degradation of transport efficiency occurred after 30 mins exposure. For a V_2O_5/BHJ interface, similar changes affected the charge transfer after 120 mins exposure. For a WO_3/BHJ interface, these changes occurred instantly.

9.1.3. Effect of Vacuum Annealing on the Interfaces Formed with MoO_3 and P3HT:$PC_{61}BM$ BHJ

The simulation of annealing process upon BHJ and high WF MoO_3 during the fabrication has been performed. A sharp interface with a less elemental-mixing phase was found with the pre-annealing upon BHJ before depositing the MoO_3. A robust surface of P3HT:PC_{61}BM BHJ can be achieved due to the pre-annealing. The dipole region is reduced; however, the dipole strength remains unchanged.

On the other hand, post-annealing upon the interfaces formed with MoO_3/BHJ drives the MoO_3 into the BHJ bulk. The regions of mixed compounds were increased. Therefore, the interface regions are broadened. Meanwhile, the thermal annealing significantly reduced the WF of MoO_3 by creating a proportion of oxygen vacancies. In these circumstances, the dipole strength can be declined. Changes upon the energy level schematics at the interfaces as a function of annealing processes were shown and the mechanism of charge transfer was further modelled.

9.1.4. Interface Formed with MoO_3 and TQ1:PC_{71}BM BHJ and the Influence of Air Exposure on the Interface

The interface of MoO_3/TQ1:PC_{71}BM BHJ has been further studied. The outcomes derived from the work are the characterisation of dipole strength forming at the interface as a function of deposition thicknesses. Comparing to the dipole adjacent with P3HT:PC_{61}BM BHJ, a stronger dipole maximised at 2.4 eV was observed. Other findings including the minimum deposition amount of 1–1.5 nm MoO_3 to form a closed layer onto TQ1:PC_{71}BM BHJ surface have been shown.

The air exposure was applied to such an interface while the dipole was characterised. The dipole was reduced as a consequence of H_2O penetration and encountering in the energetic direction. It was calculated that after ~65 mins, the mismatching of energy level occurs which can noticeably retard the charge transfer.

The procedure developed in the present work for analysing of core and valence electron spectra shows directly that a dipole is formed at the TMOs/BHJ interfaces. Moreover, this approach can be applied to any organic/inorganic interface that requires an essential characterisation of the interfacial energy bands structure and importantly, can also be applied on interfaces which have been annealing or exposed to air and has applications well beyond OPV's as it provides an effective way to characterise the dipoles forming at these interfaces.

9.2. Future Work

The work shows a strong dipole forms at the high WF metal oxides and conjugate polymer-fullerene interface, which makes the energy structure energetically favourable for charge extraction/injection transport. The mechanism has been fully investigated. However, the influence on the performance of a real device has not been tested. Therefore, further experiments need to be conducted using the full structure of a polymer-based solar cell. The structure has been designed as an Ag/MoO_3/P3HT:$PC_{61}BM$ BHJ/ZnO/ITO layered cell. The J-V curve under AM1.5 solar radiation will be characterised with a range of MoO_3 thicknesses. Cell performance will be analysed with an assumption of the interfacial energy diagram.

It was assumed that by spin-coating the P3HT:$PC_{61}BM$ BHJ onto a MoO_3 substrate the mixing of compounds can be significantly minimised. The interface and dipole formation will be correspondently altered. Characterisation of such dipoles is scheduled to be conducted. Further work, such as investigating the interfaces with a range of thicknesses of BHJ onto MoO_3, can be implemented. The swapping of deposition consequence of MoO_3 and polymer BHJ layer commonly occurs in different fabrication procedures.

This thesis has focused on the interface of HTL/polymer BHJ. Other interfaces forming at different distinct layers, for example, polymer/fullerene, polymer/polymer and polymer/ETL, and the relevant dipole formation have not been fully studied. Such interfaces also play an important role in the charge transport and promotion of the PCE of a device. Thus, investigations into these should be undertaken.

The thermal evaporation method was applied in this thesis for depositing the metal oxides. It has been shown that the low-temperature sol-gel and solution process can be alternatives which have been commonly adopted due to their harmlessness to organic substrate and convenience for processing. However, it can be expected that the TMO layer inevitably adsorbs moisture during these deposition methods. Consequently, the energy level diagram at the interface can refer to the work presented in Chapter 4. Investigations into such interfaces using low-temperature deposition methods should be conducted to achieve a better understanding of the transporting mechanism. Moreover, a variety of the concentrations of the gel and solution will need to be examined. MIES would be employed for observing the energy shift at the outermost layer and the surface coverage. Meanwhile, UPS would characterise the dipole at the interfaces. NICISS can further investigate the chemical distribution across the interface. The results of such research would be of interests to the researchers using a range of low-temperature methods.

The annealing process in this thesis was conducted under UHV conditions. Conversely, researchers have found the reduction of MoO_3 does not present with an O_2 ambient. There could be further study done on the interface of MoO_3/BHJ annealed with abundant O_2. The O_2 ambient can be created in a gas flooding chamber. However, a risk might arise in that the filament of electron beam heating would be oxidised due to the presence of O_2. Also, the flood of O_2 has a potential to oxidise the mineral oil for turbo bearing.

The resolution (energy step) for decomposing the valence electron spectra was set to 0.05 eV, producing an error bar of 0.1 eV of characterising the energy shift. A finer energy step to decompose the spectra should be used in future studies. In this way, the characterisation of energy shifts would be more accurate. Therefore, an optimised calculation algorithm and powerful processor needs to be developed for fitting the spectra.